UNIVERSITY OF OKLAHOMA

GRADUATE COLLEGE

# RESERVOIR CHARACTERIZATION AND MODELING OF A CRETACEOUS TRIPLE POROSITY CARBONATE RESERVOIR CONTRIBUTION OF PORE TYPES TO HYDROCARBON PORE VOLUME AND PRODUCTION, CAMPECHE SOUND, GULF OF MEXICO

A DISSERTATION
SUBMITTED TO THE GRADUATE FACULTY

in partial fulfillment of the requirements for the

Degree of

DOCTOR OF PHILOSOPHY

By

ANTONIO CERVANTES VELAZQUEZ
Norman, Oklahoma
2019

# RESERVOIR CHARACTERIZATION AND MODELING OF A CRETACEOUS TRIPLE POROSITY CARBONATE RESERVOIR: CONTRIBUTION OF PORE TYPES TO HYDROCARBON VOLUME AND PRODUCTION, CAMPECHE SOUND, GULF OF MEXICO

A DISSERTATION APPROVED FOR THE
CONOCOPHILLIPS SCHOOL OF GEOLOGY AND GEOPHYSICS

BY

Dr. Roger M. Slatt, Chair

Dr. Kurt J. Marfurt

Dr. Richard D. Elmore

Dr. Shankar Mitra

Dr. Zulfiquar A. Reza

*To my beloved wife Orquídea and my adored daughters Blenda and Rebeca*

# Acknowledgements

I would like to thank Dr. Slatt for all his patience and guideance during my time working on my dissertation.

I am very grateful to the members of my committee for their patience and support. Dr. Mitra for all his advising about the structural setting on my study area. To Dr. Marfurt for their classes and a lot of advising on the complexity of the attributes and machine learning. Dr. Reza, for all his patience and advising related to the integration of a static geo-cellular model oriented to simulation. To Dr. Elmore and his excellent diagenesis class. I would like to thank Dr. Pranter for giving me the opportunity to be in OU

I would like to thank Pemex Exploration and Production Co. for their support for this research. I would also like to show my gratitude to the National Council of Science and Technology (CONACyT) for the scholarship awarded under contract with the Energy Bureau of Mexico (Sener).

I would like to thank my fellow graduate students for their feedback, cooperation and of course friendship. There are so many that I fear to forget somebody.

I am also grateful to the always supportive and kind to the ConocoPhillips School of Geology and Geophysics staff.

Last but not least, I would like to thank my family: my wife Orquidea and to my daughters Blenda and Rebeca for supporting me spiritually throughout writing this dissertation.

# Table of Contents

# List of Tables

# List of Figures

## Abstract

Campeche Sound, located southeast of the continental shelf in the Gulf of Mexico. represents about 80% of the national hydrocarbons production of Mexico, and comprises several giant oilfields, including Cantarell and Ku-Zaap-Maloob. The reservoir rock was deposited during the Cretaceous over the Yucatan Slope and is divided into Upper, Middle, and Lower Cretaceous. The main reservoir rocks are carbonate debris flow facies in the Upper Cretaceous. The formation was diagenetically altered by dolomitization, dissolution, and fracturing processes. All these processes were related to a compressional tectonic regime.

Dolomitization in this area is a major control on porosity. When dolomitization exists porosity is improved and is divided into three kinds: matrix, fracture and vug porosity. Fracture and vug porosities are the main productive porosities because they increase connectivity among porous voids. Dolomitization is not homogeneous in the Cretaceous rocks in the study area, which is an important difference with the major fields cited above. Dolomitization is present in the upper and middle part of the Upper Cretaceous and in the Middle Cretaceous, but not in the Lower Cretaceous. The lower part of the Upper Cretaceous is not completely dolomitized in the study area. This heterogeneity in the porosity, and consequently in the permeability, could form vertical barriers to the flow, and it could increase the mobility of fluid movement in the aquifer in the zone, creating early irruptions of water during the production of the future wells.

To characterize these complex fields and plan their development, I developed an integrated workflow. The ultimate objective of this research was a 3D-cellular model that represented all the geological complexities identified in the fields through well and seismic data. The first part of this workflow described in Chapter 1, is to define the architecture and structure of the fields. The resulting structural model was supported by the interpretation of a 3D depth

migrated seismic integrated data with previous studies in nearby fields describing lithofacies and stratigraphical units to subdivide the model based on lithology supported by image well-logs and core reports.

In Chapter 2, I focus on the internal distribution of the dolomitized facies in the field. I evaluated different seismic attributes and selected the ones that on both time and depth-migrated best-differentiated dolomite from limestone. Then, I incorporated them into machine learning processes to identify the process that gave us a result that was closer to the expected geology in the area.

In Chapter 3, I use Nuclear Magnetic Resonance (NMR) and image logs, I estimated a dual-porosity petrophysical model. This model was then used as a parameter to select a method from those proposed by other authors to estimate dual-porosity based on basic well-logs. The selected method can be applied to future wells in the area. Then, I distributed the petrophysical properties using geostatistical methods based on the lithofacies described in chapter one. I used the dolomitization trends estimated in chapter 2, as a second variable into the geostatistical process.

The result was a 3D model, which identified sweet spots to locate new development wells, estimate original volumes and, make simulations of the production of the fields.

# Introduction to Chapter 1

In this chapter, I address the geological structural model, facies characterization and the stratigraphic model. These elements form the outer part of our geological 3D model, delimiting the horizontal limit of the reservoir by the faults and closures of the structures. Beside of this, understanding the structural geology is useful to orient future seismic-structural interpretations in the zone, and it allows correlates properties, such as porosity, with structural features.

The stratigraphic model is useful to delimit our reservoir vertically. The stratigraphic model was stated through the characterization of the facies presented in the proposed units, and the response of the photoelectric well-log because this log is useful to distinguish limestone from dolostone.

Furthermore, I tried two machine learning methods to automate facies interpretation from basic well-logs. The objective of try these methods was to have a tool to bolster facies interpretation prescinding from cores and expensive special logs as image well-logs in future wells.

The results of this chapter were the base to build the final comprehensive model.

# Chapter 1: Stratigraphy and Structural Characteristics of Cretaceous Carbonates, Campeche Sound, Gulf of Mexico

Antonio Cervantes-Velazquez and Roger M. Slatt

ConocoPhillips School of Geology and Geophysics, University of Oklahoma, Norman, Oklahoma

## Abstract

Campeche Sound located southeast of the continental shelf in the Gulf of Mexico. represents about 80% of the national hydrocarbons production of Mexico, and comprises several giant oilfields, including Cantarell and Ku-Zaap-Maloob. The reservoir rock was deposited on the Yucatan Slope in the Cretaceous and is divided among Upper, Middle, and Lower Cretaceous. The main reservoir rocks are Upper Cretaceous carbonate debris flow facies. The formation was diagenetically altered by dolomitization, dissolution, and fracturing processes. All these processes were related to a compressional tectonic regime.

Dolomitization in this area is a major control on porosity. When dolomitization exists, porosity is improved and is diversified into three kinds of porosity: matrix, fracture and vug porosity. Fracture and vug porosities are the main productive kind of porosities because they increase connectivity and porous voids. Dolomitization is not homogeneous in all the Cretaceous column in the study area and is an important difference with the major fields cited above. Dolomitization is present in the upper and middle part of Upper Cretaceous and in the Middle Cretaceous, but not in Lower Cretaceous. The lower part of Upper Cretaceous is not completely dolomized in the study zone. This heterogeneity could form vertical barriers to the flow, and it could increase the mobility of the aquifer in the zone.

The study area includes three anticlinal structures formed by thrust faults, resulting in three oil fields, denoted from north to south as fields A, B, and C. The structural trend of the thrusts is oriented east-west with a dip towards the south for fields A and C. However, the thrust for field B is dipping towards the north. The dip-orientation for the thrust-faults is North for the analog fields. Another structural difference with the analog fields is the presence of salt extruding through the Cretaceous column in some parts of the study area.

Low oil gravity is a distinctive feature for the study area. Analog fields have a gravity of 21° API, while the fields in the study area have 11° API. For this gravity, the viscosity is increased which increases the difficulty to produce from these fields. A combination of heterogeneous dolomized zones with low gravity oil generates a challenge for production. Attention is needed to characterize the porosity controls as dolomitization, and structural features are important for an effective production planning.

Because of the complexity of the structural framework along with the complexity of the lithofacies as controls of reservoir quality, in this study, we are proposing an integrated approach to incorporate the structural framework in the area with a 3D model derived from seismic interpretation and facies description in the wells from image logs. A facies distribution in the wells based on K-mean and Artificial Neural Net algorithms were also performed, to evaluate its utility in a scenario where electric well-logs are available as an input, but no image-logs. Seismic interpretation of faults was facilitated through a process of skeletonization. The resulting 3D cell-model is a trustful base for a posterior population of petrophysical properties controlled by stratigraphy and structural geology.

# Introduction

Campeche Sound, located offshore on the continental shelf of the Gulf of Mexico, is the most important petroliferous region in Mexico, and includes the giant Upper Cretaceous carbonate reservoirs of Cantarell, Sihil, Ku, Zaap, and Maloob oil fields. Campeche Sound production represents close to 80% of the national production of Mexico (Acevedo, 1980; Santiago and Baro, 1992; Guzman and Marquez-Dominguez, 2001; Figure 1-1). Our study area is focused on three fields in the neighborhood of the mentioned fields. These fields have a complex porous system derived from a diagenesis process that altered through a sequence of dolomitization, dissolution, and fracturing. However, the fields in the study area exhibit significant vertical and lateral diagenetic heterogeneity in the Cretaceous column. Because diagenesis could be a key in generating secondary porosity, understanding the diagenesis and quantitatively mapping the stratigraphic and structural trends is critical to planning the development of these fields.

The study area includes three fields, from north to south field A, B, and C, (Figure 1-2). The fields A and B are each associated with a thrust fault. And every thrust-fault has an associated anticline that forms the trap for the fields. Every one of this fields has been drilled by an exploration-well, wells A-1 and B-1.

The C field is composed of three anticlines. The north and center anticlines are associated to a sub-thrust-faults that branch from the main thrust fault. The south anticline of this field is associated directly with the main thrust-fault, this field contains two wells, one in the center anticline, well C-1, and, another in the south anticline, well C-DL1.

The research questions for this work are next: What is the configuration of the top and base of the reservoir? What are the primary and secondary faults that control the properties

distribution? What is the architectural style for this zone and how it related to the structural history defined by Mitra et al. (2003, 2005)? How can be identified the lithofacies and the units that form the reservoir? Can we predict the facies with a machine learning approach? What sedimentary model could represent this reservoir? Can the stratigraphic model proposed by Angeles-Aquino (2006) be subdivided to fit the observed facies? To solve these questions, we applied a comprehensive workflow that includes seismic interpretation, structural modeling, identification of facies from photographs and reports of cores along with image logs, and identification of stratigraphic units.

# Geological setting

## Structural Geology

Physiographically, the study area is in southeast Mexico in the Pilar de Akal Horst. The Pilar de Akal Horst is part of the folded structural belt of the Sierra de Chiapas-Reforma-Akal (Figure 1-3). The Reforma-Akal section is only known by subsurface data, while the Sierra de Chiapas has outcrops on shore. The Pilar de Akal Horst is, economically, the most important petroliferous zone in the Mexican Gulf of Mexico. The horst is bounded by the Comalcalco, Frontera, and Macuspana faults (Angeles-Aquino, 2006).

Tectonically this zone is very complex because it is near to the convergence of North America, Caribbean, and Cocos plates (Figure 1-3). The North American plate has a relative movement westward to the Caribbean plate, while the Cocos plate has a relative motion toward the northwest, moving in the opposite direction to that of the Caribbean and North America plates (Padilla y Sanchez, 2007). The surrounding major tectonic features include the Sierra de Chiapas foldbelt, Macuspana and Comalcalco basins, and the submarine Campeche fold belt. From Paleocene through Early Miocene, the east-west translation between the Caribbean and

North American plates removed the Chortis block in an easterly direction, thus, generating basement compressive deformation, including thrusting and folding farther to the northeast in the study area (Pindell and Miranda, 2011).

The Campeche Sound was a passive-margin regime during the Late Cretaceous to Early Cenozoic. This extensional tectonic setting lasted from the early Jurassic to the late Jurassic (Murillo-Muñeton, et al., 2002). However, major tectonic deformation occurred during the late Oligocene to Miocene when compression and strike-slip faulting took place (Murillo-Muñeton, et al., 2002). A final transtensional tectonic event that resulted in extensive normal faulting affected this region during Pliocene-Pleistocene (Murillo-Muñeton, et al. 2002). These late Cenozoic tectonic processes were the responsible mechanisms for the origin of the fracture systems in this oil field (Murillo-Muñeton, et al., 2002).

Mitra et al. (2005, 2006) provide a structural analysis of the nearby Cantarell, Sihil, Ku, Zaap, and Maloob fields. These analyses identify three main episodes of deformation: (1) a Jurassic to Early Cretaceous extensional event, (2) a Miocene compressive phase, during which the main trap-forming structures were formed; and (3) a Pliocene to Holocene extensional event, resulting in several listric growth faults.

## Regional Stratigraphy

Angeles-Aquino (2006) describes the stratigraphy, identifying the main units from the Jurassic to the Cenozoic, dividing the reservoir in the study into Upper, Middle, and Lower Cretaceous intervals (Figure 1-4). Furthermore, Angeles-Aquino (2006) describes a transgression during the Early and Middle Cretaceous that covered the continent located to the southwest,

where rising sea level that modified the environment, generating basin and slope sequences. These sequences are represented by bentonitic mudstone, intraclastic mudstone to wackestone, and micro-dolomites. During Upper Cretaceous time, the Yucatan platform was exposed and subsquently eroded, generating carbonaceous mass transport deposits and aprons. The lithology for this sequence is represented by a calcareous breccia formed by exoclasts composed of mudstone-wackestones, and dolomites.

*Lower Cretaceous*

The predominant lithology of the Lower Cretaceous zone is a bentonite-rich, greenish-gray limestone mudstone [Dunham (1962) classification] that is slightly dolomitic and includes carbonate incraclasts and exoclasts. The zone has been altered by dolomitization, silicification, and pressure-solution processes (stylolites) (F. J. Angeles-Aquino, 2006).

*Middle Cretaceous*

The Middle Cretaceous zone is represented by mudstone to wackestone whose intraclasts are exoclasts, intraclasts, bioclasts. In this formation are a presence of bentonite It has light gray intercalated bodies of crystalline dolomite with laminations of dark gray shale and greenish gray bentonite. Accessory minerals present are pyrite, flint, anhydrite, authigenic quartz, and bentonite. The zone has undergone dolomitization and silicification (F. J. Angeles-Aquino, 2006).

*Upper Cretaceous.*

During Maastrichtian time, the Yucatan Peninsula represented a broad, relatively stable carbonate platform that extended to the area of the Sierra de Chiapas. Adjacent to this carbonate system, an extensive belt of "slope" carbonate breccias has been widely documented in outcrops of the Sierra de Chiapas and offshore Campeche (

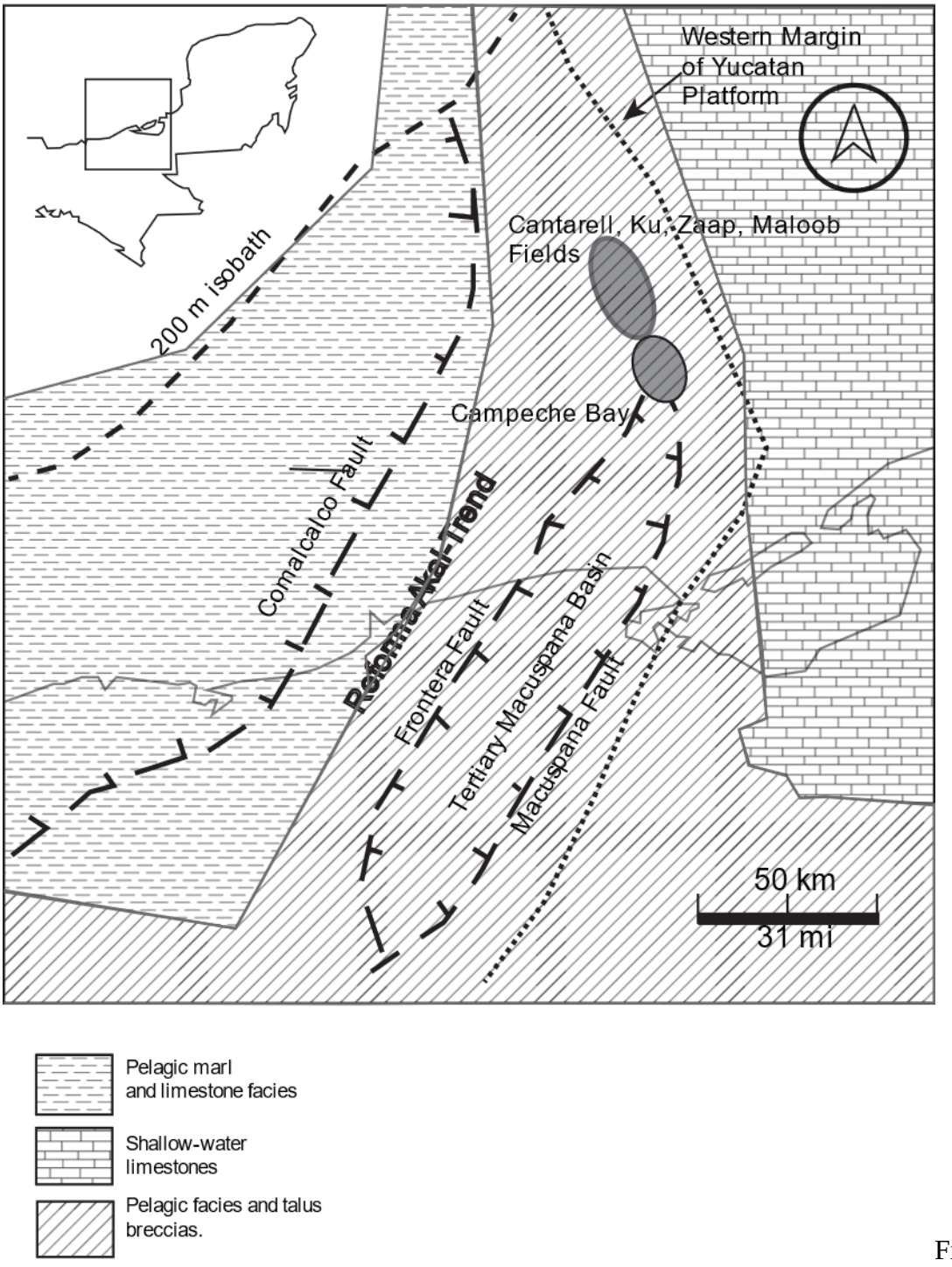


Figure 1--5)

(Murillo-Muñeton, et al. 2002). The upper Cretaceous zone corresponds to a breccia consisting of dolomitized, calcareous, angular fragments of diverse sizes cemented by a beige carbonate mudstone (Murillo-Muñeton, et al. 2002). The breccia in the study area has a brown color caused

by oil staining. The zone changes laterally to shaly limestone and in the southwestern part of the study area, the breccia changes to calcareous shale (Cantu-Chapa and Landeros-Flores 2001). The origin of the carbonate breccias is either due to solution-collapse related to subaerial exposure, deposition of talus in a deep-water setting (Angeles-Aquino, et al., 1992; Limon-Gonzalez, et al., 1994) or it was formed for the meteorite impact in the Chicxulub zone (Grajales-Nishimura et al., 1994). This formation is considered the main reservoir rock in the area. When this formation has been altered by dolomitization, dissolution, and fracturing porosity and permeability increase, otherwise the rock has poor porosity characteristics. Particularly for the reservoir objective of this study, these characteristics define if a well is going to have an adequate production.

Since the structural framework could be along with the facies controls on reservoir quality, in this study, we are proposing an integrated approach. In this approach, the structural frame was incorporated in a 3D model derived from seismic interpretation, and a stratigraphic subdivision was also included. This stratigraphic subdivision was based on facies content. The facies were described in the wells from image logs and, eight reports of cores from four wells in the study area. A facies distribution in the wells based on K-mean and Artificial Neural Net algorithms were also performed, to evaluate its utility in a scenario where electric logs (resistivity, sonic, gamma ray, photoelectric log) are available as an input, but no image-logs. Seismic interpretation of faults was facilitated through a process of skeletonization that gave a better definition to map faults.

## Methodology

Reservoir characterization consists of translating geological characteristics of the reservoirs into a numerical model. This numerical model must be able to simulate the flow patterns, and to establish and optimize the development plan for the reservoir (Sinha et al., 2017; Zapata et al., 2016).

The decisions about the development plan must be made based on an adequately characterized reservoir model. “The highest levels of uncertainty generally involve complexity-deformed reservoirs where either the exploitation or the avoidance of structural heterogeneities (e.g. faults) is important” (Hennings, et al., 2000). Ideally, it would be best to have comprehensive models of reservoir architecture early in the drilling program; however, reservoir architecture depends on numerous variables, many of which are difficult or impossible to evaluate before extensive drilling (Hennings, et al., 2000).

To achieve a three-dimensional model, it is necessary to have reliable geological information. This information must be adequate and must be interpreted to be an input in building the numerical model. The interpreted information then becomes a structural, stratigraphic and sedimentological model. The structural model provides a geometric framework for the model and structural trends that could be useful in identifying possible properties distributions (Sinha et al., 2017). The stratigraphic model supports unit identification and helps to correlate properties in a vertical direction. The next methods address the questions stated for this research, based on a reservoir characterization approach.

The proposed workflow to improve seismic interpretation is based in the works of Jie et al., 2016, and is shown next. Seismic attributes are based on the quantification of the patterns identified between neighboring samples to extract subtle features valuable for interpretation (Jie et al., 2005). The first step was to apply principal component structure-oriented filtering to reject

random noise and sharpen the lateral edges of seismic amplitude data (Jie et al., 2005). Next, the eigenstructure coherence was calculated to highlight the discontinuities. Then, a Laplacian of a Gaussian filter was applied to the coherence attribute, this process sharpens the steeply dipping faults, attenuates the stratigraphic features parallel to the seismic reflectors, and skeletonizes the unconformity features subparallel to the reflectors (Machado et al., 2015). The last process to the seismic was skeletonize the filtered coherence attribute along with the fault planes (Jie, et al., 2017).

Determination of the structural interpretation of the top and the base of the reservoir and the faults.

To understand the structural geology of the study area, beside interpreting the base, the top of the reservoir and the top of the autochthonous salt. The main reservoir faults were delineated to the detachment zone of the main thrust fault. This extended interpretation purposes the information to understand the structural evolution and the relation with the events described by Mitra, et al. (2006). The faults and horizons were the input to create a 3D structural model based on volume. This structural method based on volume was presented by Souche, et al. (2013). This algorithm creates an implicit function that corresponds to the stratigraphic age of the formations (Souche, et al. 2013). This function is embedded and interpolated in an unstructured tetrahedral mesh for carrying and interpolating the implicit function using a 3d Boundary-Constrained-Delaunay mesh generator (Souche, et al. 2013). This mesh generator is constrained with the faults affecting the horizons, using the faults as internal boundaries.

The next step to generate the structural model is interpolating the values of the implicit function on the nodes of the tetrahedral mesh (Souche, et al. 2013). This interpolation is done using a linear least squares formulation, which will tend to minimize (1) the misfit between

interpolation data and the interpolated surfaces and (2) the variations of dip thickness of the layers (Souche, et al. 2013).

The last step of the algorithm generates surfaces representing every implicitly modeled horizon. The result is a 3D model that includes the modeled horizons, faults and zones. In this model, the inconsistencies of the interpretation can be visualized and brought back to the original interpretation to identify the inconsistencies and corrected. This process is repeated until achieving the most consistent interpretation. Because the resulting model is three-dimensional, cross sections in any direction can be generated and analyzed from the structural point of view.

The structural model based on volume is very useful in visualizing the structural events and giving consistency to the seismic interpretation, but still, a cell 3D grid is necessary to distribute properties and perform the reservoir simulation. The resulting modeled horizons and faults from the structural modeling were used as an input to build a 3D grid. This 3D grid was built in the traditional pillar-gridding technology. The grid was oriented to the direction of the main faults, keeping the cells deformation to the minimum and the cell volume values positive.

### *Facies Classification*

Photographs, and microphotographs from cores were used to classify the lithofacies. Then, these lithofacies core were adjusted to depth into the image well logs available. When the lithofacies patterns were identified in the cored intervals in the well logs, then, they were identified in the rest of the image log generating a lithofacies log. The resulting lithofacies log was used to feed a supervised neural net. Neural net tries were made based on different sets of well logs to test the accuracy compared with the results based on the interpretation. The log combination resulting in the neural net with the best accuracy was highlighted. The log combinations for the Neural Net tries were the next:

- Gamma-ray, resistivity.
- Gamma-ray, resistivity, and density.
- Gamma Ray, resistivity, density, and neutron porosity.
- Gamma-ray, resistivity, density, neutron porosity and photoelectric factor.

An index of dolomitization was calculated based on the values of the Photoelectric Factor using the values of dolomite and limestone from Gardner and Dumanoir (1980). These values were normalized in percentage, with 100% for the dolomite value 3.14 barns/electron, to 0% in the calcite value 5.08 barns/electron and was verified with the presences of dolomite from the photographs of the cores. In the same method used for the lithofacies estimation, an array of well-logs was used to generate a different dolomitization facies for the reservoir. These resulting dolomitic facies were verified with the previously estimated dolomitization index from PEF.

The Cretaceous stratigraphy described by Angeles-Aquino (2006) was subdivided to have a better control of the vertical distribution of the properties. The unit division was based on the continuity of the lithofacies identified in the cores and image logs and correlated with the response on the resistivity, gamma ray, porosity, density and PEF logs. These units were correlated between the wells to cover the stratigraphic variations of the reservoir. The late Cretaceous was divided into three units, the upper one is characterized by a calcareous micro breccia with semi-oriented clasts; the middle zone in the late Cretaceous is formed by a chaotic dolomized calcareous breccia with poor textural classification; the lower zone corresponds to a succession of mudstone to wackestone limestones, with occasional micro breccias (this unit could be dolomized). Middle Cretaceous strata was conserved as a unique unit and presents mudstone to wackestone limestone with intercalations of calcareous micro-breccias, which could

be dolomized. Early Cretaceous was also conserved as a unique unit too and is composed by mudstones mainly with occasional intercalation of microbreccias; this unit is not dolomized.

# Results and discussion

## Structural Geometry

Three-dimensional modeled surface of the tops of Late Cretaceous, Late Tithonian and Autochthonous salt are shown in Figure 1-6, 1-7 and, 1-8. The major structures correspond to anticlines with associated thrust faults on their front limb, and some are also cut by back thrusts. These anticlines change in trend from east-west for the northern anticline to northeast-southwest for the southern anticline. The detailed geometry of the faults and individual structures are described in detail next.

### *Thrust Faults*

The main detachment in the area is located below the top of the autochthonous salt. According to the stratigraphy proposed by Angeles-Aquino (2006), this salt corresponds to Callovian age rocks. All the main thrust faults that form the anticlines merge into this major detachment (Figure 1-9). The major frontal thrust is in the reservoir C, this thrust is showed in the Figure 1-10, which changes sharply from an approximate northwest-southeast trend to a north-northwest-south-southeast trend in the southern region. In the northern part of this thrust, there is a back-thrust delimiting the northern anticline of the reservoir C. This anticline is parallel to the main northwest-southwest oriented thrust fault-oriented. The sub-reservoir C thrust is a minor thrust associated to the major C reservoir thrust formed as a strand of the middle part of the main C reservoir thrust. The associated anticline to this sub-thrust is oriented east-west and

the discovery well C-1 is in this anticline. In the southern area, the anticline has low angle flanks, forming a plateau-like structure. In this structure the delineation well, C-DL1 was drilled. In the southwestern area, there is a set of normal faults oriented roughly north to south in the east zone and drifting to southwest-northeast.

The structure of reservoir B has the largest vertical displacement of the thrust fault, nearly 450 m (1470 ft). The thrust fault is oriented in the inverse sense of the other two main thrust faults and is also steepest. This orientation and steepness suggest that the thrust comes from the reactivation of a previous existent normal fault (Figure 1-9). The orientation of the thrust fault changes from north-northwest - south-southeast in the west to southwest to northeast in the east zone. The structure is limited to the north for a backthrust fault associated with the main fault thrust.

The northern structure is the structure of reservoir A. The reservoir A is composed by a main fault thrust to the north, forming an anticline with an orientation near to east to west. In this structure the well A discovered this reservoir and is the only well in the structure. In the western part of the structure the thrust has an orientation southwest to northeast. For the eastern part the thrust orientation is roughly west to east. This structure has a backthrust that is not well developed forming a minor fault.

*Field C structural system.*

The cross-section 3-3’ (Figure 1-10) cuts through the north anticline of reservoir C and passes through the north limb of the central anticline. The main thrust fault is detached below Callovian salt in a stepping detachment, probably shaped by previous normal faults. The main

fault is very steep on the zone, suggesting a reactivation of a Jurassic normal in the Tertiary age. The main fault presents a backthrust with less steepness than the main fault delimiting the north anticline to the southeast. The secondary thrust fault that forms the middle anticline can be observed in the cross-section too. This thrust fault has a shallower dip and trends asymptotically to the detachment zone at an inferior level to the main fault. This secondary thrust joins with the main fault thrust in the east area and changes its orientation to the main fault orientation. The secondary thrust has an associated backthrust fault, which is joined as a branch to the secondary fault associated with the central anticline. This associated fault is better observed in the 4-4' cross-section (Figure 1-10), where the section cuts transversally over the anticline. In this section the attachment surface can also be observed, to show a stepped character that could be related to the normal faults associated with the Gulf Opening aperture. In the southern part of the central anticline, the salt goes through to the Jurassic in the main fault zone. The fault plane in the zone is almost vertical. In the southern part illustrated by the 2-2' cross-section (Figure 1-10), the main fault is less visible, and the salt penetrates all the Upper Jurassic and Cretaceous stratigraphic column. In the southern part of the reservoir, C is limited by a normal fault.

*Field B structural system*

The reservoir B is the highest in the study area. The trap for this reservoir is composed of a thrust fault, that changes its orientation from northwest-southeast to southwest-northeast, almost at a right angle. The section running northwest-southeast forms the main anticline in the structure, reaching 3000 m (9840 ft) depth. The section running southwest-northeast of the main fault is associated with a minor anticline that is broken up in the east part by a salt dome that intrudes the Cretaceous column (Figure 1-11, Cross-section 6-6').

The main thrust has three backthrust faults associated with it. The nearest backthrust to the main fault is a fault of short extension and doesn't disrupt the continuity of the reservoir (Figure 1-11, Cross-section 5-5'). The next backthrust fault to the north is the most important associated fault and delimits the main anticline. This associated fault changes its direction from northwest-south on the west part to almost north-south for the east area. In the east area, this fault joins to the main fault in a perpendicular way, closing the anticline. The farthest associated backthrust fault is a minor fault and is not associated to the anticline.

The orientation of the dip for the main thrust is in the opposite direction of the general trend of the faults. A possible explanation for this could be sustained, relating the structural style existing before to the compressive phase in the zone (Figure 1-9). The aperture of the Gulf of Mexico was an extensive regime that generated normal faults in the early Jurassic. Many of this these faults could be reactivated as a reverse fault, generating thrusts at unconventional angles (Figure 1-9). These mechanisms have been observed in the area by Mitra, et al. (2006). The variation in thickness between the blocks supports this model because the column above the detachment is thickest in the hanging-wall block that in the footwall (Figure 1-9).

Where the main thrust turns to the direction southwest-northeast, a secondary anticline is formed that is separated from the main anticline of the main backthrust fault. In the eastern part of this anticline, a salt diapir intrudes through the formation, sealing the reservoir in this direction.

### *Substructure B*

There is a minor structure to the east of the salt diapir that is cored by salt and is delimited by a thrust fault and a backthrust fault (Figure 1-12). These faults are oriented

southwest-northeast, keeping a constant orientation. This structure has not been drilled but seismically is difficult to identify if the Cretaceous is present in this structure or corresponds to the top of the salt. The mechanism was interpreted as a thrust with a backthrust fault, in order with the structural style in the area, but this could be generated by salt movement also.

*Field A structural system*

The northern structure in the area is the Structure A shown on Figure 1-13, discovered by the well A-1. This structure is formed by a thrust fault that is thrusting to the north, and the orientation of the fault plane changes from southwest to northeast in the west part to northwest to southeast in the east part. The main thrust has an incipient backthrust associated in the south part of the associated anticline. The structure attains its maximum relief in the central section and has a long, gently dipping back limb and a short steep front limb.

In general, the structural style observed in the zone could evidence that the detachment zone is ductile according to the models proposed by Li (2016). From the Li (2016) experimental models, the resulting of a ductile detachment zone, as the autochthonous salt observed in our study area, results in detachment folds with forethrusts and backthrusts. These characteristics fit with our observations in the study zone.

## Stratigraphy

To control the thickness variation in the model, and understand the stratigraphy of the zone, thickness maps were generated using the tops of the formations identified in the wells. (Figure 1-16 to Figure 1-18). These maps were generated along the base of the well tops from the wells in the area. A description of the stratigraphic units is presented next.

### *Lower Cretaceous*

This unit is the lowest unit in the reservoir model. This unit is formed by mudstone and mudstone to mudstone-wackestone; occasionally micro-breccias are present with some intraparticle porosity. The thickness in this unit follows a general trend of increasing to the west of the area and decreasing to the north and the east. The thickness of this unit varies from 80 m (260 ft) to a maximum thickness of 300 m (980 ft), with a mean of 80 m (260 ft) and a standard deviation around 80 m (260 ft). This variation in thickness is the broadest in the analyzed units and could be being an indicator of this unit leveling the previous paleo-morphology related to the Gulf of Mexico opening. This interpretation can be supported based on the conditions in the Early Cretaceous described by Padilla y Sanchez (2007). In this work, the events that form this formation are interpreted as a result of a transgression and a stable tectonic setting combined with a slow subsidence rate. This tectonic setting began in the Tithonian and continued until the end of the early Neocomian (Berriasian) in the Early Cretaceous (Padilla y Sanchez, 2007). For the Late Neocomian (Hauterivian-Berriasian) and the upper part of Early Cretaceous (Aptian-Albian) subsidence speed was increased favoring the deposit of thick carbonaceous beds with a minor ratio of shales. For modeling purposes this unit was modeled as a unique unit divided into five layers with an average thickness of 37 m (120 ft).

### *Middle Cretaceous*

This unit is the next over the Early Cretaceous and is the thinnest unit in the reservoir. This unit is composed of mudstone and mudstone to wackestone with an organic material presence. In some parts intercalations of micro-breccias are present. The thickness of this unit varies in the study area from a minimum thickness of 77 m (250 ft) to a maximum of 151 m (495 ft). In a general trend, the thickness decreases to the north, and its maximum increases are toward the southeast of the area. The minimum thickness of this formation was drilled by the well A-1 with 105 m (344 ft) and a maximum drilled thickness of 137 m (450 ft) by the well C-DL1. For the Middle Cretaceous (Albian-Cenomanian) the subsidence continued for the Gulf of Mexico, at a constant speed for the entire basin (Padilla y Robles, 2007).

### *Upper Cretaceous*

This unit is the most complex in the reservoir and has the best characteristics of porosity and permeability. Because of the vertical variations inside of this unit, three subunits were proposed to characterize this part of the reservoir. These units are described next.

#### *Upper Cretaceous I*

This subunit is formed by intraclasts mudstone to wackestone, and generally is dolomized, except in the well C-DL1 where there is limestone only. Specifically, for the well C-DL1, this unit presents low porosity values and few secondary porosities associated with it. The maximum thickness was drilled by the well C-DL1 95 m (310 ft) and the minimum thickness was crossed by the well B-1 with 30 m (100 ft). This unit could correspond to the Turonian-Santonian age continuing with the same deposition of carbonates (Padilla y Sanchez, 2007). For

the Coniacian-Santonian there was an increment in the volcanic activity with bentonitic horizons reported in the marine sedimentation in the Gulf of Mexico (Padilla y Sanchez, 2007).

### *Upper Cretaceous II*

This subunit is the most important, containing the highest porosity values and the most abundant secondary porosity. This unit is composed of dolomized carbonate breccias, with open fractures and dissolution cavities (vugs). The maximum thickness for this subunit was penetrated by the well C-DL1 162 m (530 ft), and a minimum thickness of 67 m (220 ft) for the well A-1. This formation corresponds to the Campanian-Maastrichtian according to the work of Cantu-Chapa and Landeros-Flores (2001). The origin for this formation has been explained in numerous ways but there are two theories that are most accepted. The first theory declares the cause to be from the impact of a meteorite in the Chicxulub area forming the breccia (Grajales-Nishimura et al., 2000). The second theory says that the breccia was produced by the falling of carbonaceous fragments in the slope of the Campeche escarpment (Angeles-Aquino et al., 1992).

### *Upper Cretaceous III*

This subunit is formed by a microbreccia with a thickness of 5 m (16 ft) in the well C-1 to 28 m (90 ft) in the well A-1. This subunit generally is described as being part of the breccia of the subunit LC-II and is even considered as an evidence of a gradation of this unit (Grajales-Nishimura, et al., 2003). In this unit has been reported shocked quartz and coarser, altered granitic basement clasts (Grajales-Nishimura, et al., 2003). These components can relate the

origin of this unit to the Chicxulub impact. Economically this unit has low porosity and permeability values and is not considered a reservoir rock in the area.

## Lithofacies Characterization

After of the review of the photographs and microphotographs, and reports of cores, the facies were identified:

***Fine breccia***. - This lithofacies consists of heterogeneous dolomized, carbonate microbreccias. The assortment of the clasts is very regular, the sizes of the clasts varying from 10 to 20 mm. In the well-logs, this lithofacies is the main constituent unit in the Late Cretaceous III unit (Figure 1-19). Because this lithofacies is located only on the upper part of the Upper Cretaceous and is in the transition to the Paleogene clastic sediments, a possible origin for this unit could be related to the Chicxulub meteoritic impact same as the upper facies described by Grajales-Nishimura et al., 2000.

***Laminated fine breccia***. – This lithofacies is similar in composition to the fine breccia lithofacies but is not chaotic and contains laminations. This lithofacies is located in the Lower and the Middle Cretaceous and occasionally in the Upper Cretaceous (Figure 1-20). This lithofacies could be originated by gravitational deposits and could be related to the facies A, described by Mullins and Cook (1986). Where these facies are described as class-supported breccias. According to Mullins and Cook paper, these facies could be corresponding to outer carbonate apron deposits zone (Figure 1-20).

***Coarse breccia***. – A chaotic heterogeneous carbonate breccia composes this lithofacies, the size of the clasts varying between 2 m (7 ft) to 25 mm (1 inch). The sorting is poor. The fragments are constituted by fragments from the platform in lagoon facies and some reef

fragments. The porosity in this lithofacies is dominated by widened fractures, dissolution cavities (vugs) and, moldic porosity. This facies is always dolomized in the zone and is ubicated Late Cretaceous II unit (Figure 1-21). According to Mullins and Cook (1986), this facies corresponds to F facies, corresponding to megabreccias having how the mechanism of transport submarine-slides and are present mainly in the inner apron zone (Figure 1-20).

***Pelagic mudstone to wackestone***. – This lithofacies is formed by mudstone to wackestone limestones according to Dunham (1962) classification. The porosity corresponds to fractures mainly, but occasionally can be dolomitized with some minor vug porosity isolated. This lithofacies is founded in the base of the Late Cretaceous II and is not dolomized in the well C-DL1. This lithofacies is the main constituent in the Middle Cretaceous and Early Cretaceous unit (Figure 1-22). According to the model of Mullins and Cook (1986), these sediments corresponds to Facies G, composed by hemipelagic and pelagic sediments (Figure 1-20).

The pattern of these facies was identified in the image log for every well. This vertical lithofacies distribution was used to define the units that compose the 3D grid model.

To evaluate the relationship between porosity and lithofacies and dolomitic facies histograms were generated from the total porosity well log (Figure 1-21). In general from the porosity distribution we can observe that coarse breccia lithofacies have higher porosity values with a mean of 9%, the fine breccia lithofacies with a mean of 7%, fine laminated breccia with a mean porosity of 4% and the facies with the lower values was the mudstone-wackestone lithofacies with a mean porosity of 3%.

For dolomitic facies the higher porosities were for dolomite facies with a mean of 6% of porosity, then dolomitic limestone facies with a mean of 3% and the lower values were for limestone with a mean of porosity of 2% (Figure 1-22).

An integrated facies classification was performed, applying the interpretation of information from cores and image logs in the study area with two facies classification algorithms, each one including both unsupervised (K-means) workflows (Figure 1-26.) and supervised (Artificial Neural Network Analysis -ANN-) (Figure 1-27) methods.

The overall accuracy (number of correctly predicted facies/total testing facies) was 64.22% for K-means and was achieved for a four-classes lithofacies realization. The lithofacies were predicted with producer's accuracies (this is how often are interpreted facies correctly shown on the predicted facie) of 77.63%, 90.06%, 18.33%, 31.09% for the mudstone-wackestone, coarse breccia, fine breccia and, laminated breccia classes, respectively. The fine breccia facies was most misclassified for breccia (45/60). However, for stratigraphic position and for the values in resistivity logs it is possible to distinguish these facies. Laminated breccia was misclassified most often for breccia also (319/624). For mudstone-wackestone facie this trend stills and was misclassified by breccia 266 of 1417. Dolomitization heterogeneity may have been an important factor for this misclassification because well logs could be responsing mainly to the composition of the rock as PEF or fluid content or compacity as resistivity more than the texture of the facies. For K-means, the combination of gamma ray, resistivity and, neutron porosity wireline logs have proven to be the most accurate.

For ANN the overall accuracy was 69.89% for the same four facies. The resulting producer accuracy reaches 91.25% for mudstone-wackestone, 83.04% for breccia, 6.67% for fine breccia and, 23.88% for laminated breccia facies (figure 19). In a similar way than K-means for ANN fine breccia was the most misclassified (28/60). Producer accuracy for laminated breccia in ANN (23.88) have not a good performance as k-means (31.09%). However, ANN achieves a most equilibrated distribution between mudstone-wackestone and breccia, classifying 1293 of

1417 and 142 of 171 respectively where K-means classified 1100 of 14717 for mudstone-wackestone and 154 of 171 for breccia. Because these last two facies are the most abundant and important for production, ANN could be helpful to identify facies without image logs, when is complemented by the knowledge of stratigraphy in the zone.

## Conclusions

The studied fields are dominated by carbonaceous sediments including mudstone, mudstone to wackestone, coarse breccia and fine breccia. The coarse breccia lithofacies have the best reservoir characteristics. These sediments are altered by dolomitization, dissolution and fracturing. The occurrence of this lithofacies varies vertically being present in the mudstone and mudstone wackestone lithofacies in the Lower, Middle, and lower part of Upper Cretaceous; the fine breccia lithofacies are sporadically present in Lower, Middle and the upper part of Upper Cretaceous.

The dolomite presence vertically is limited to the Upper Cretaceous unit. Sub unit upper Cretaceous I is the only unit that is not dolomized as was observed in the well C-DL1. This becomes something remarkable, because if this formation is not dolomized, it could be a vertical barrier for the flow.

In the study area, the associated folds form three fields called from north to south, A, B, and C. The thrust faults have a general orientation east-west with a general dip to the south, although the thrust that forms the field B is oriented to the north. A possible explanation for this difference in structure orientation in field B can be supported by the inversion of previous structural regimes in the zone, which initially suffered an extensional deformation that formed

normal faults during the Jurassic, and in the Tertiary. These normal faults were reactivated under a compressional deformation, which their dip and azimuth in the present day as reverse faults

The structure of the reservoir A is characterized by a thrust fault that is thrusting to the north, and the orientation of the fault plane changes from southwest to northeast in the west side of the major anticline structure. In the east side of this reservoir, A anticline, the fault plane changes from a northwest to southeast orientation. The reservoir C is formed by three substructures and sub-thrusts that merge into a main thrust system located in the east side of this field. The main fault system is very steep in this zone, also suggesting a reactivation of a normal fault from Jurassic in the Tertiary compression.

The method of machine learning k-means and ANN have different results for facies classification. Apparently, dolomitization heterogeneity influenced the results for k-means masking the textural facies. ANN have a better performance identifying the main two facies, breccia and mudstone-wackestone. The two facies (fine breccia and laminated breccia) can be identified by stratigraphic position.

## Chapter 1 Figures

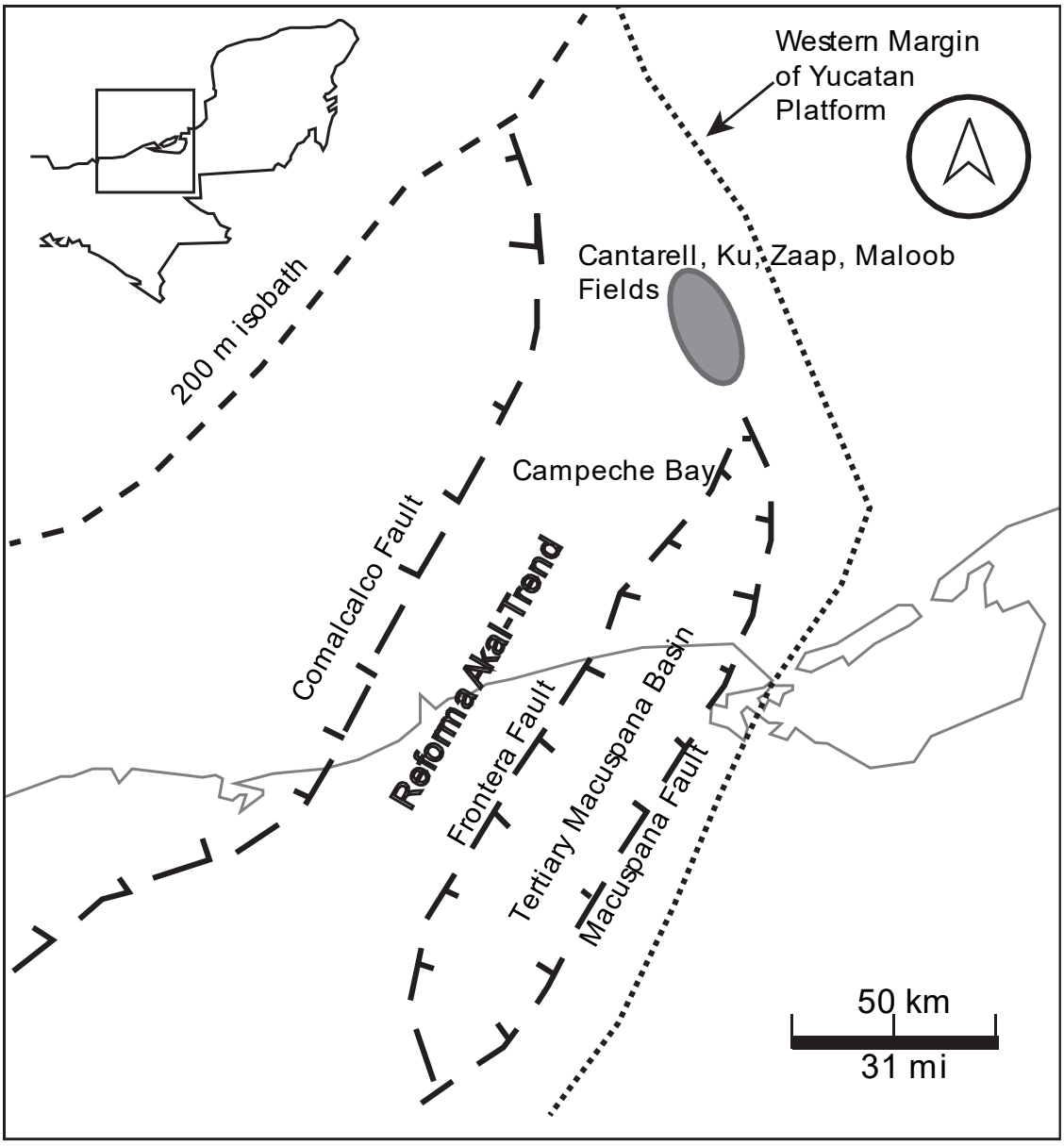


**Figure 1-1.** Location of the study area and the main structural features in the zone. Study area shares the geological history and some features with the major fields in the Gulf of Mexico, Cantarell, Ku, Maloob and, Zaap. (after Murillo-Muñeton, et al., 2007).

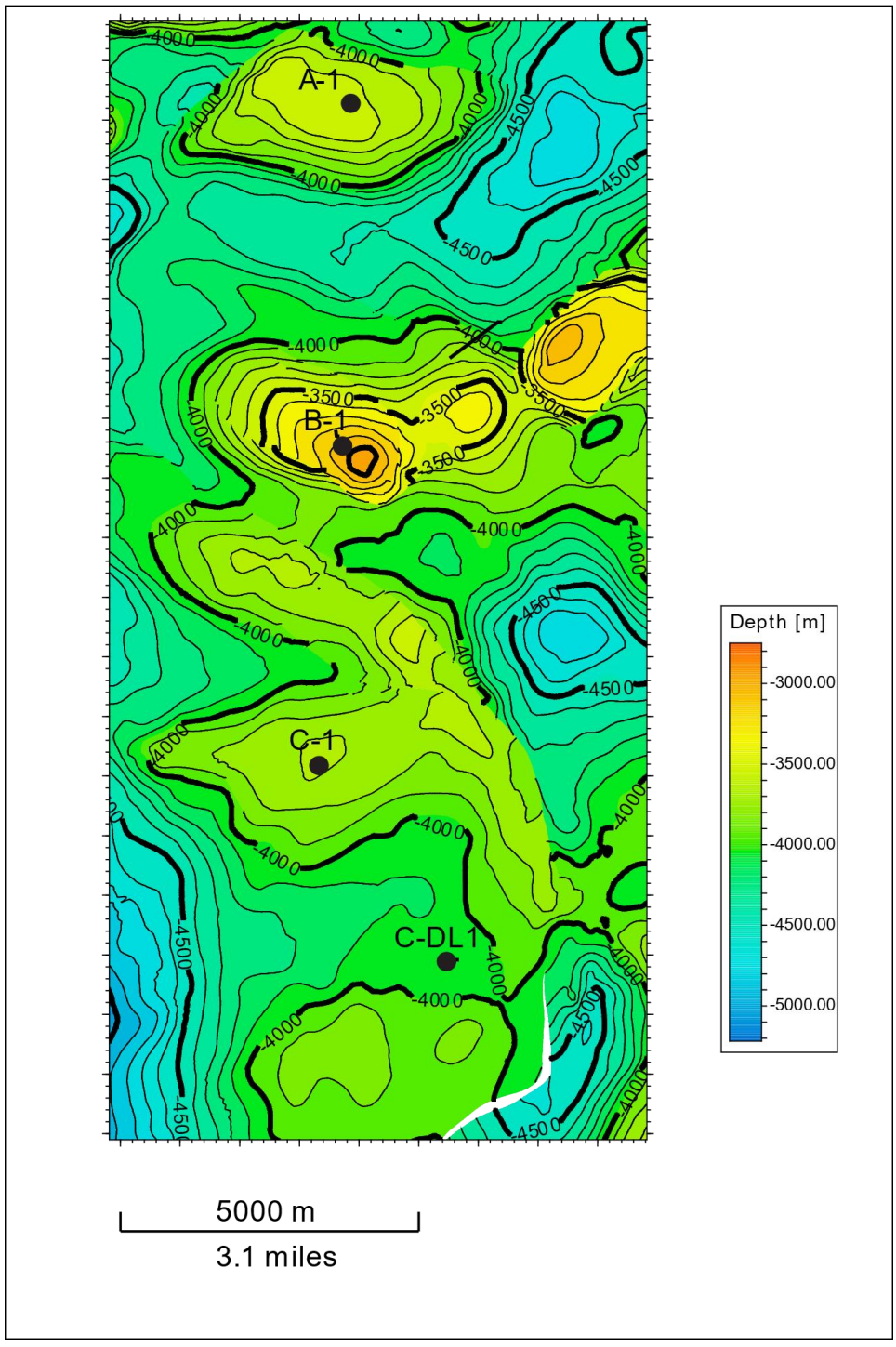


**Figure 1-2.** Top of the Cretaceous map showing the three oil fields in the study area, from north to south A, B, and C. Fields A and B are each related to one anticline, forming the traps for the fields. The C field is composed of three anticlines. In this map, the position of the wells is shown also. The wells are three exploration wells, A-1, B-1, and C-1 and, one delineation well, C-DL1.

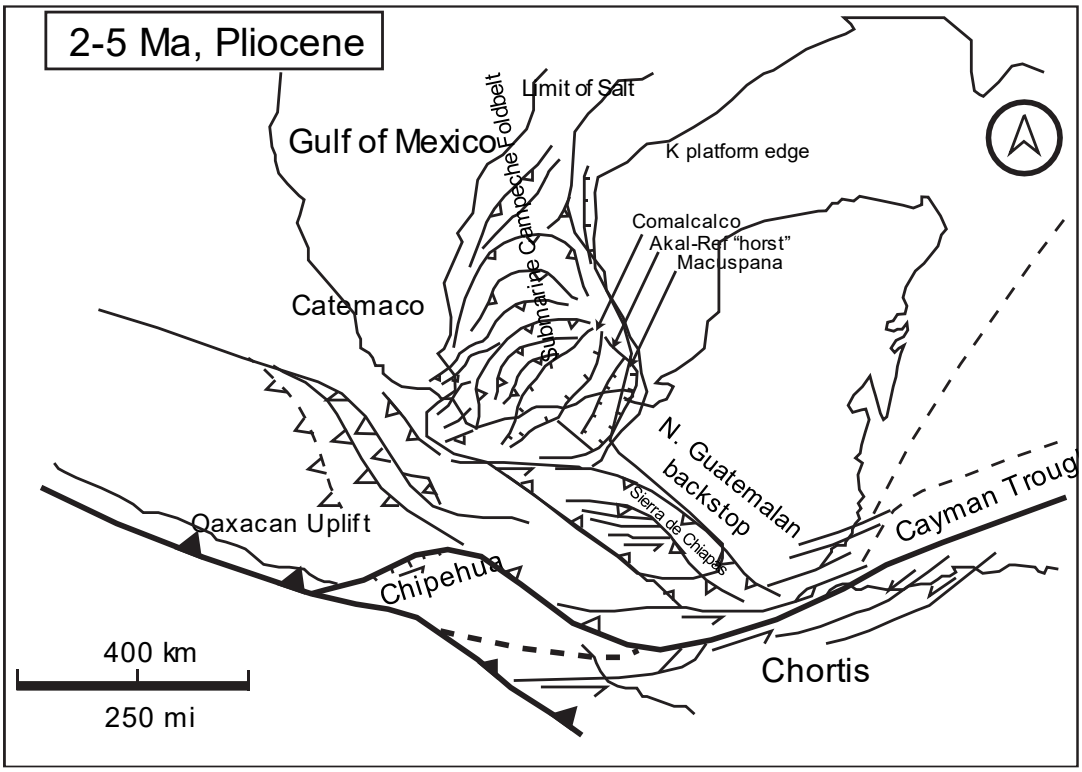


**Figure 1-3.** Tectonic setting during the Late Miocene-Pliocene, Chiapanecan deformation characterized by an E-W shear in Chiapas resulting in the opening of the Macuspana Basin and folding in the submarine Campeche Foldbelt. This is the primary time of the opening of the Comalcalco Basin (After Pindell & Miranda, 2011).

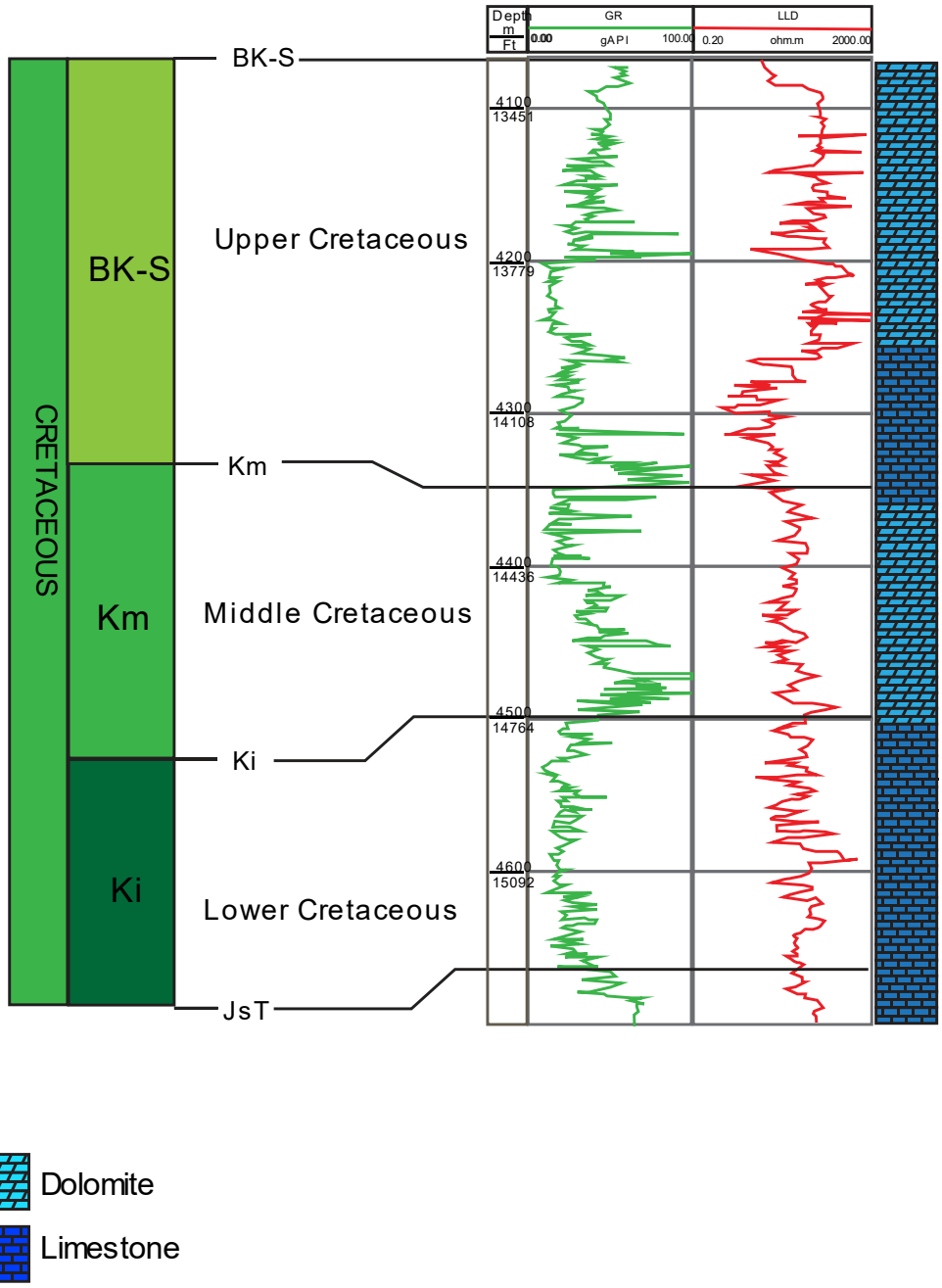


**Figure 1-4.** Stratigraphic section and corresponding well log response showing the reservoir rock ranging Lower Cretaceous to Upper Cretaceous. Dolomites generally exhibit better porosity ad permeability than limestones. Generally, more intense dolomitization occurs in the breccias of the Upper Cretaceous zone. In contrast, dolomitization in Middle and Lower Cretaceous is variable.

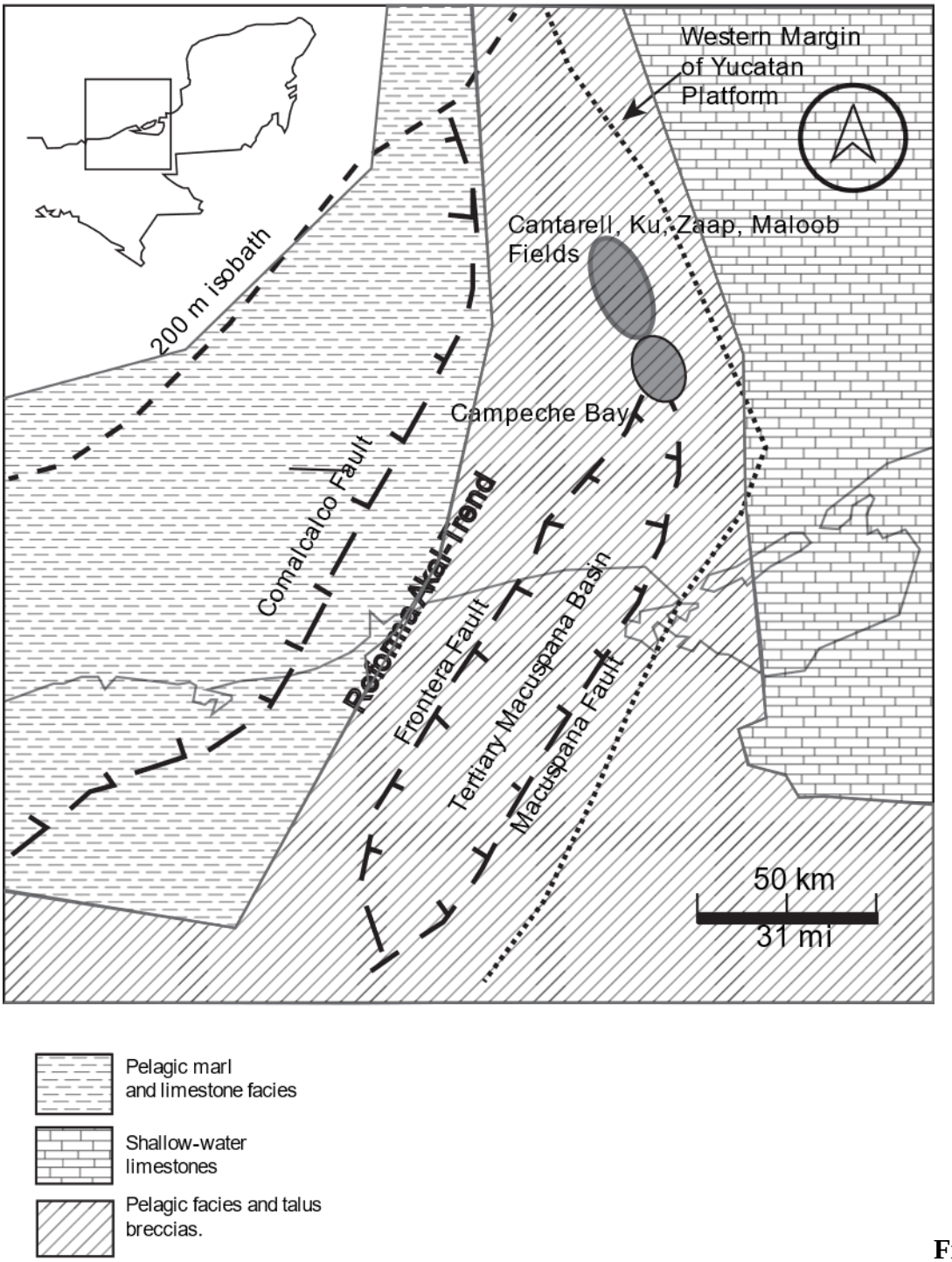


**Figure 1--5.**

**Figure 1-5.** Geologic setting at the end of the Maastrichtian in Southeastern Mexico showing extensive shallow-water sedimentation in the Yucatan Platform and in the Sierra de Chiapas. The main fields in the zone was in the slope where massive debris flow formed the main reservoir rock of the area. (After Murillo-Muñeton, et al., 2002).

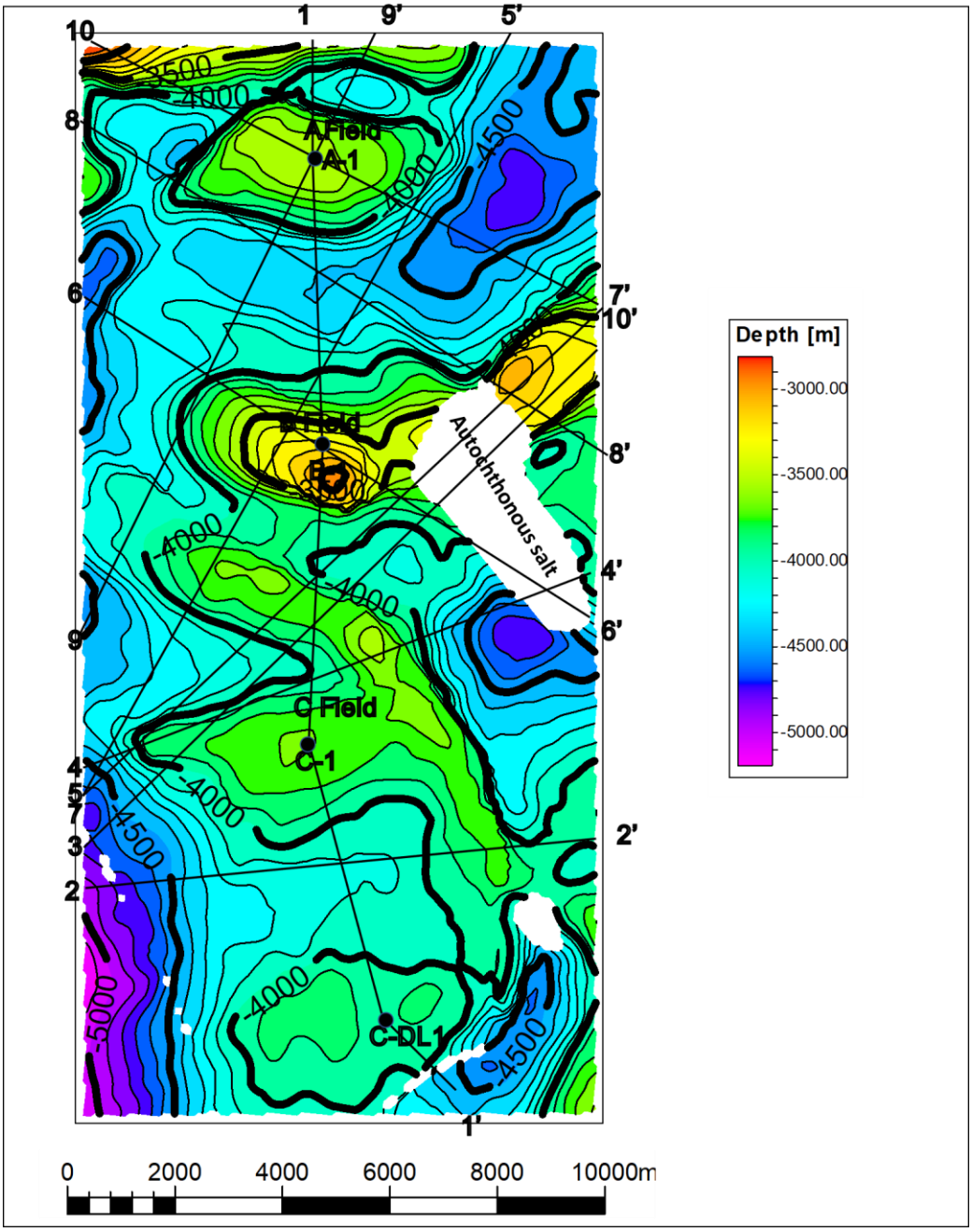


**Figure 1-6.** Structural contour map for the Upper Cretaceous surface. In general, the anticlines that form the fields A and B have its main axis oriented E-W. For the field C, the main anticline has an arcuate form that ramifies in three anticlinal sub-structures. Part of the autochthonous salt break through the East part of the B field, and on a small area on the East of field C. The analyzed cross-sections are shown.

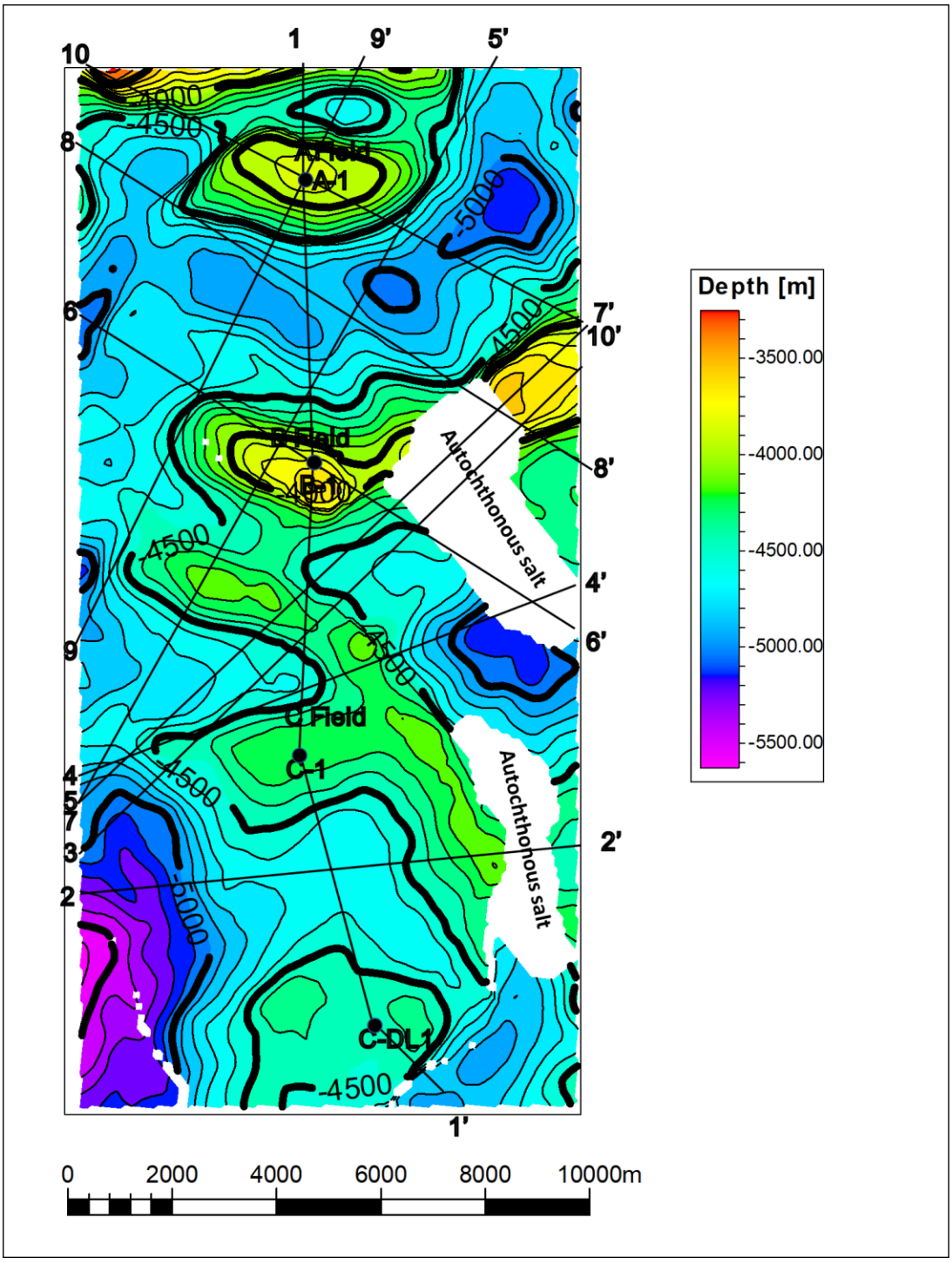


**Figure 1-7.** Structural contour map of the Upper Jurassic surface. For this surface, the structures viewed on the Upper Cretaceous are preserved but, they have a wider amplitude. The autochthonous salt is breaking through a larger zone than in the Upper Cretaceous in the East of the B field. Autochthonous salt is breaking through the East part of field C also, while in Upper Cretaceous is barely present in the same zone. The analyzed cross-sections are shown.

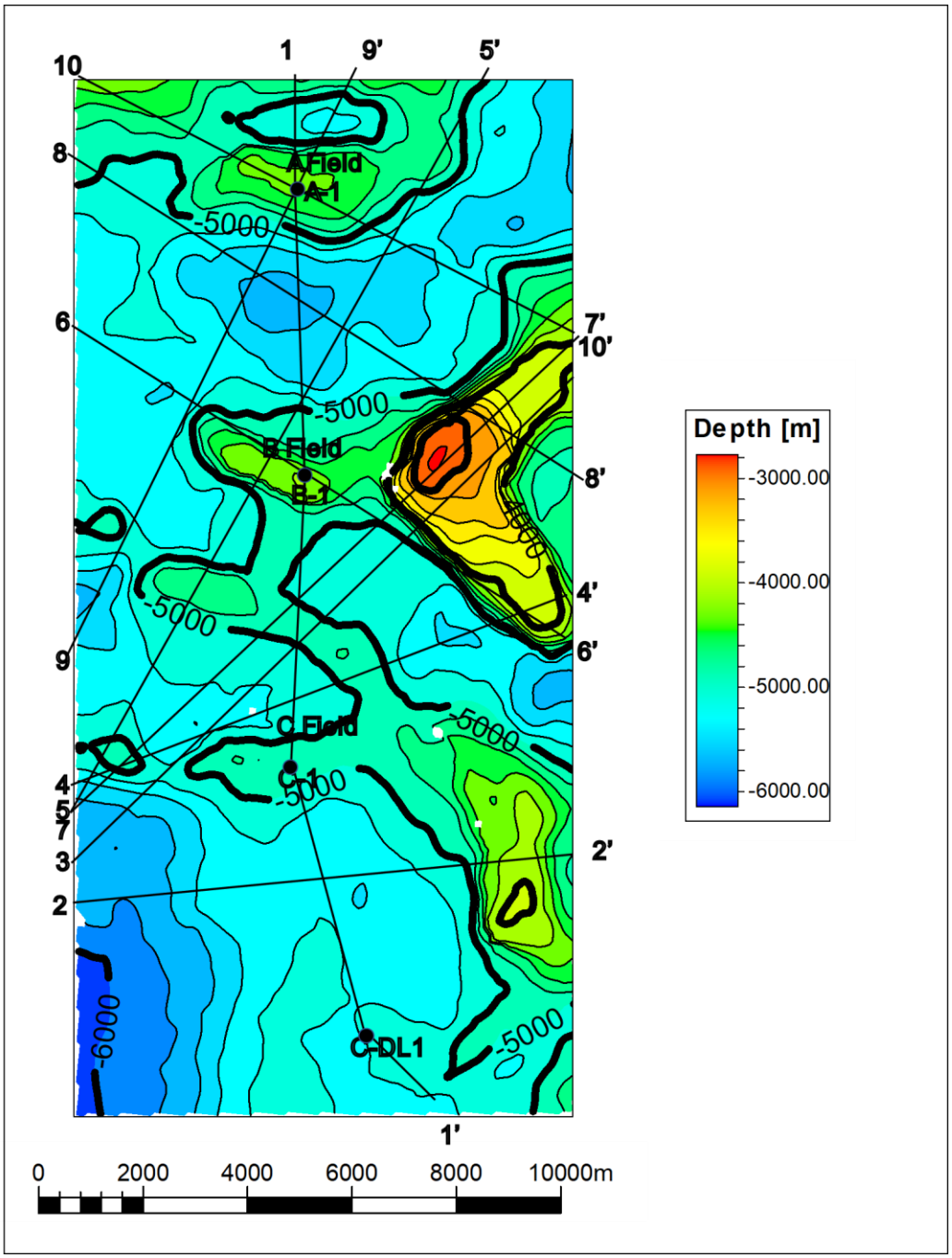


**Figure 1-8.** Structural contour map for autochthonous salt. Autochthonous salt is the detachment zone for the thrust faults on the zone and forms the core for the associated anticlines. Autochthonous salt had a mobility stage on the East part of the zone, breaking through the Cretaceous column and partially the Tertiary column. The analyzed cross-sections are shown.

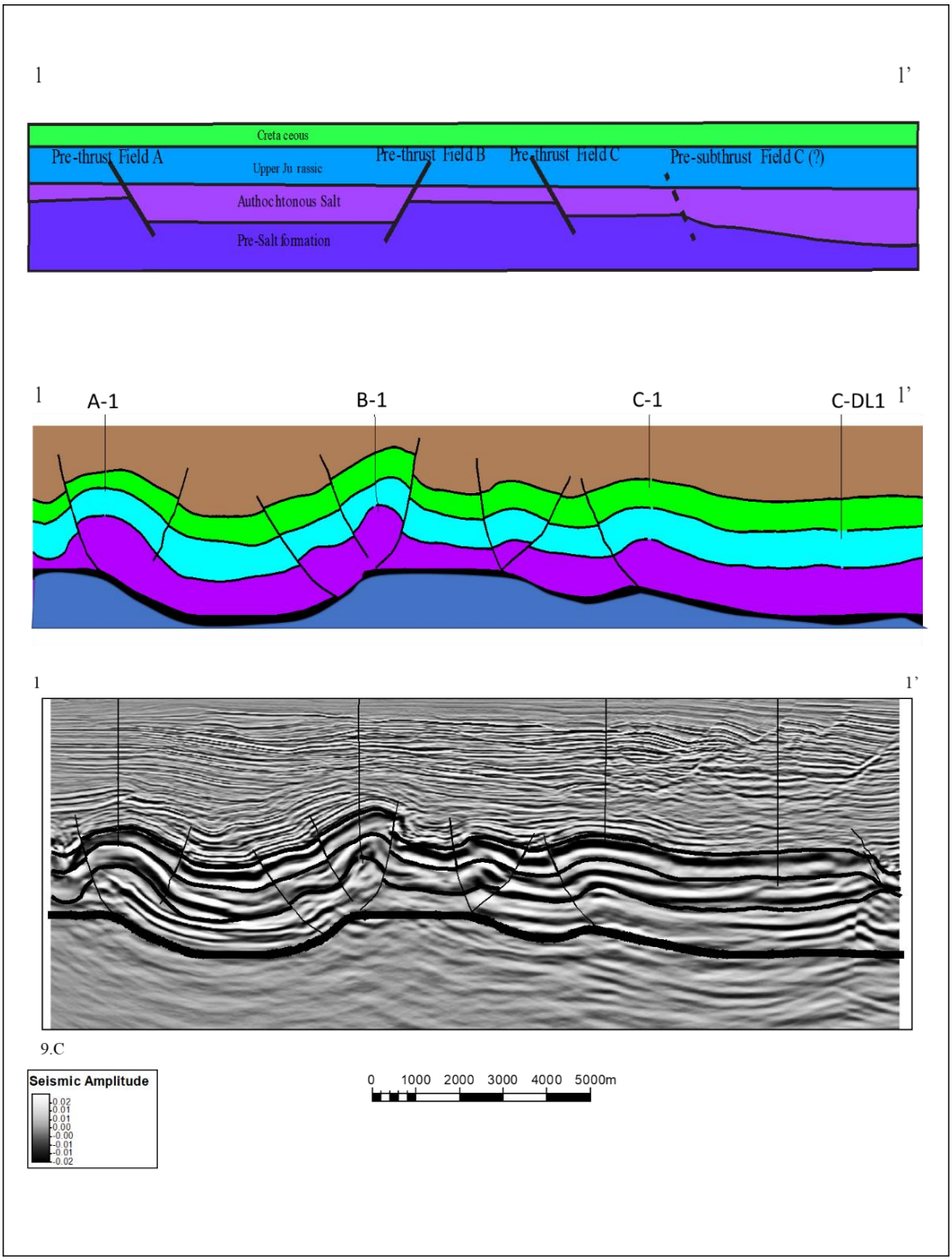


**Figure 1-9.** Cross-section one passing by the wells in the area. The cross-section A is schematic and shows the possible pre-compression faults. The cross-section B shows come from the structural model and present the current compressive structures. In the cross-section C seismic amplitude is presented and the interpretation.

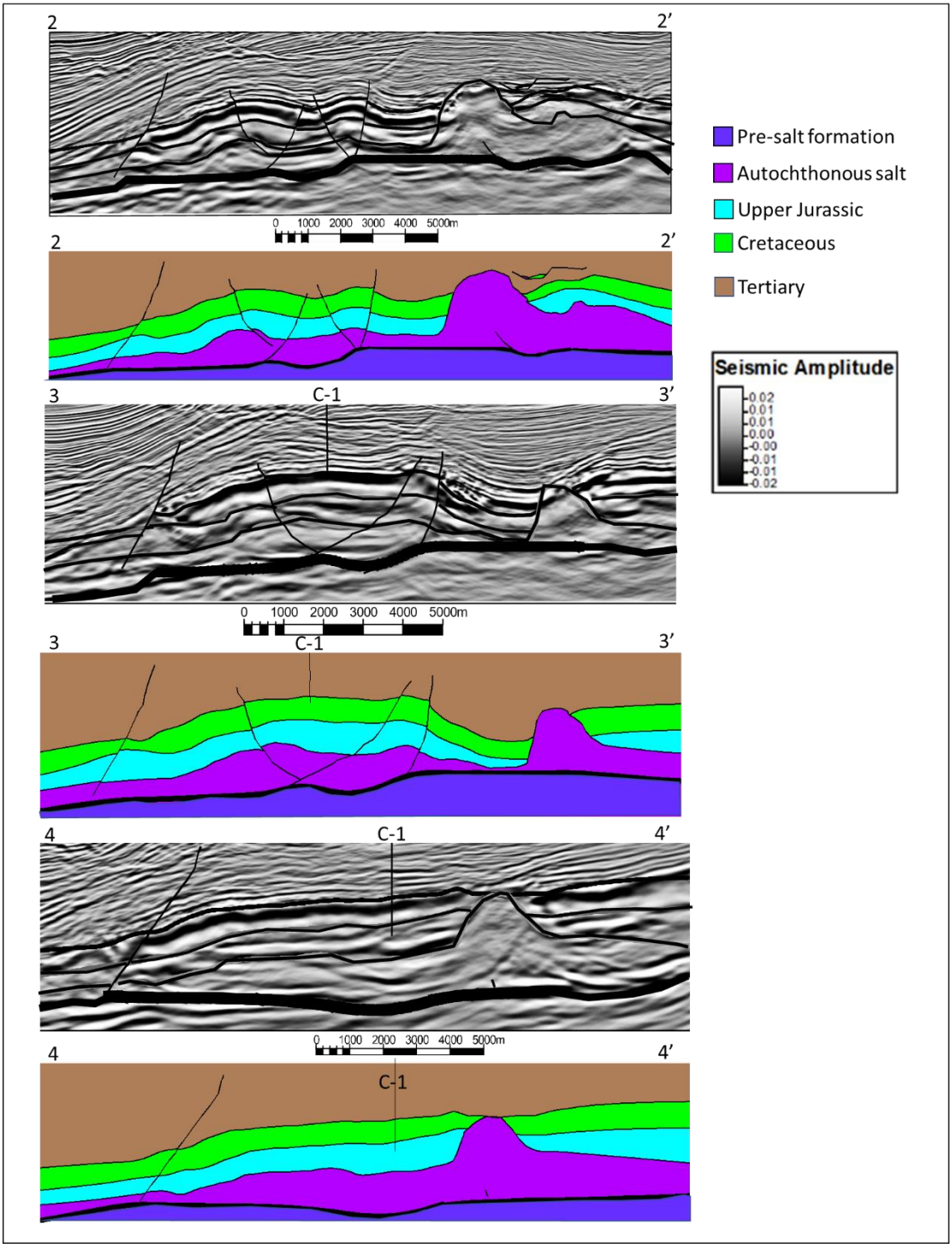


**Figure 1-10.** Cross-sections two, three, and, four illustrating the structural styles for the C field. C field is composed of three anticlines associated with sub-thrusts that are branches of the main thrust. In the east part of this field, a salt body intrudes through the Upper Jurassic, Cretaceous and part of the Tertiary sequence.

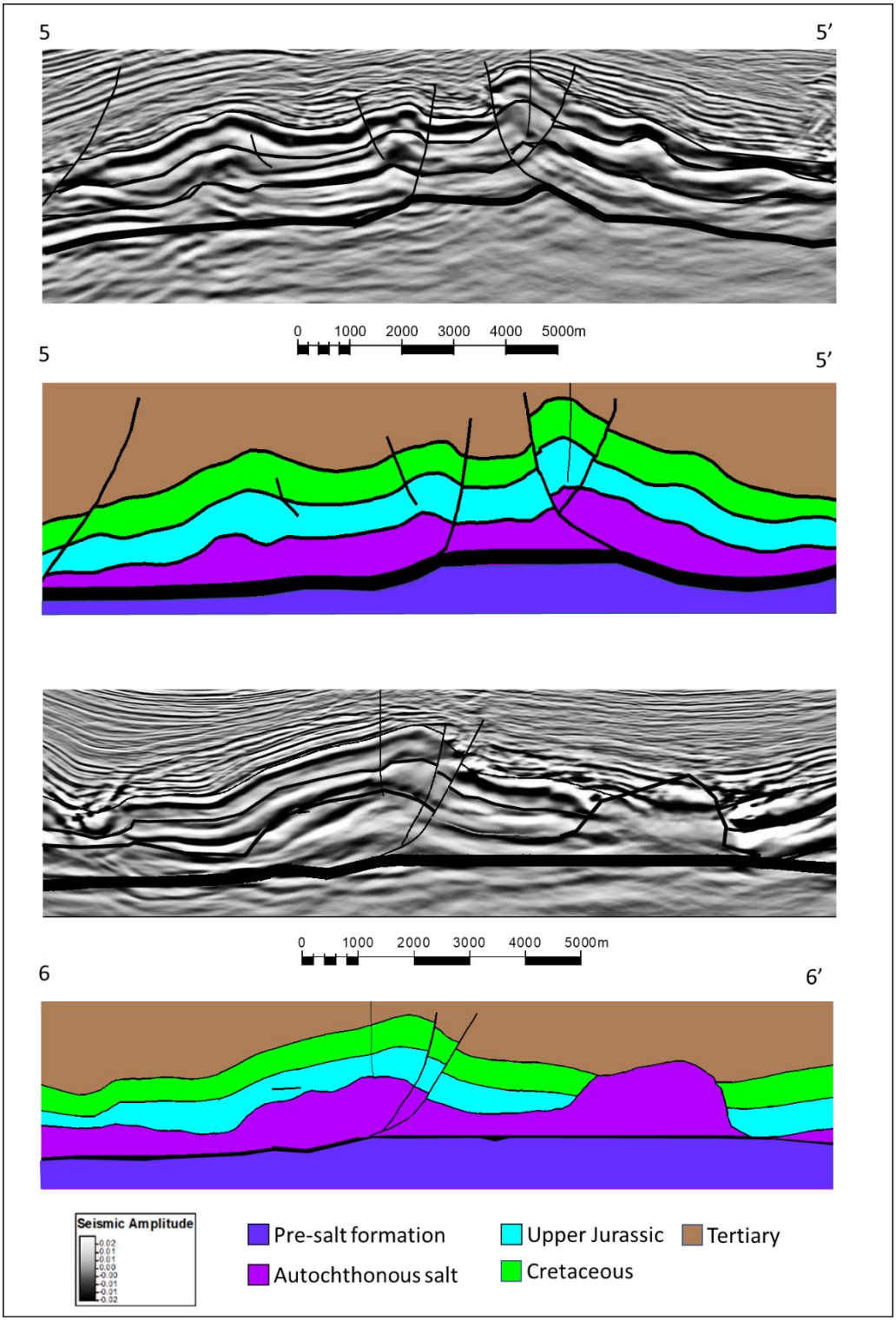


**Figure 1-11.** Cross-sections five and, six illustrating the structural styles for the B field. B field anticline is the structurally highest in the study zone around -2960 m (-9710 ft) TVD. This anticline is associated with a thrust-fault that changes its orientation from NW-SE in the eastern part to SW-NE in the western part.

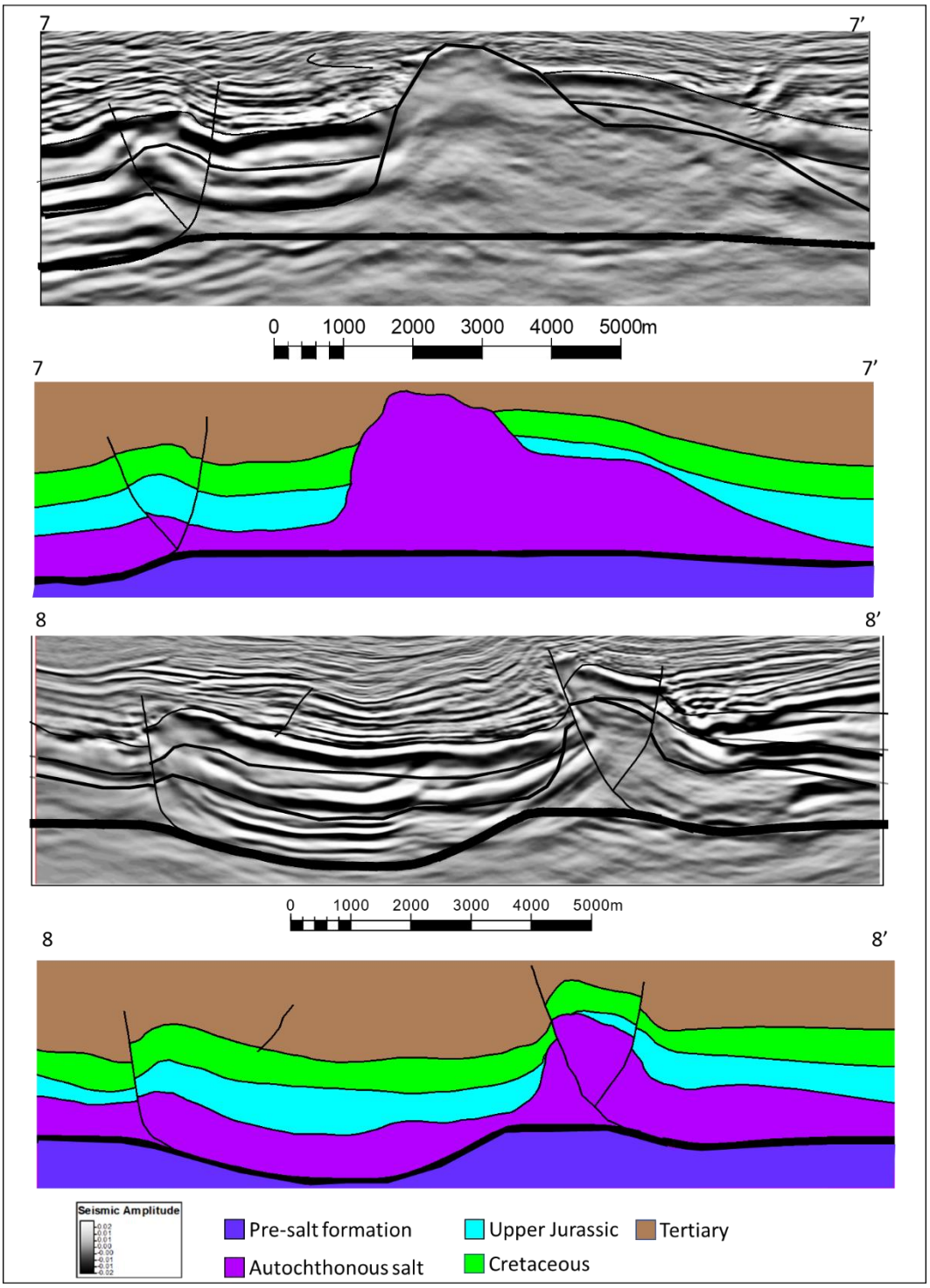


**Figure 1-12.** Cross-sections seven and, eight illustrating the structural styles for the sub-B field. This structure is located to the eastern part of the field B. This is a structurally complex structure because, besides the thrust-fault, part of the salt body breakthrough the southwest part of the structure

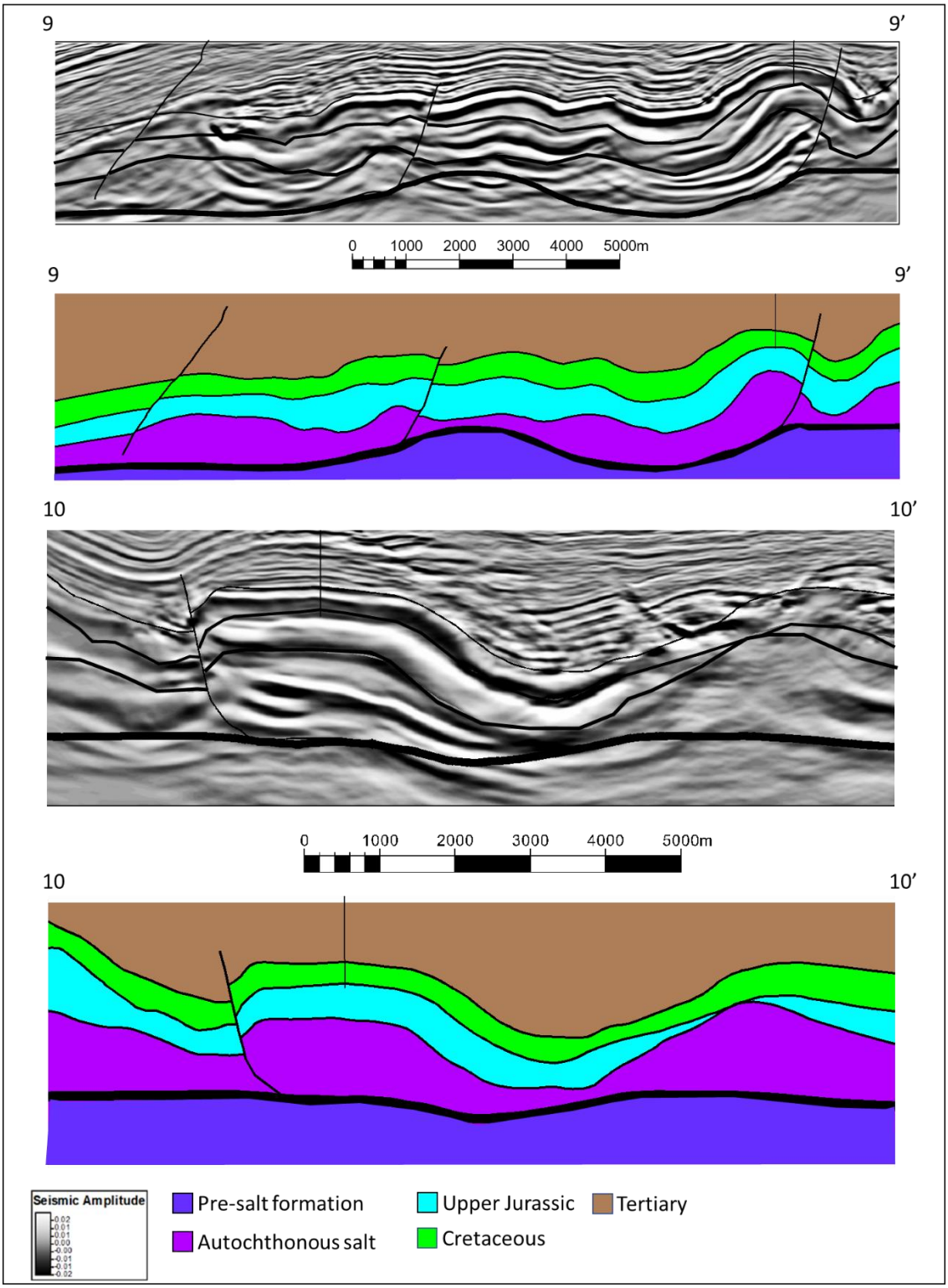


**Figure 1-13.** Cross-sections nine and, ten illustrating the structural styles for the A field. This field is in the north zone in the study area. The thrust associated with this field changes its orientation from NW-SE in the western part to SW-NE in the eastern part.

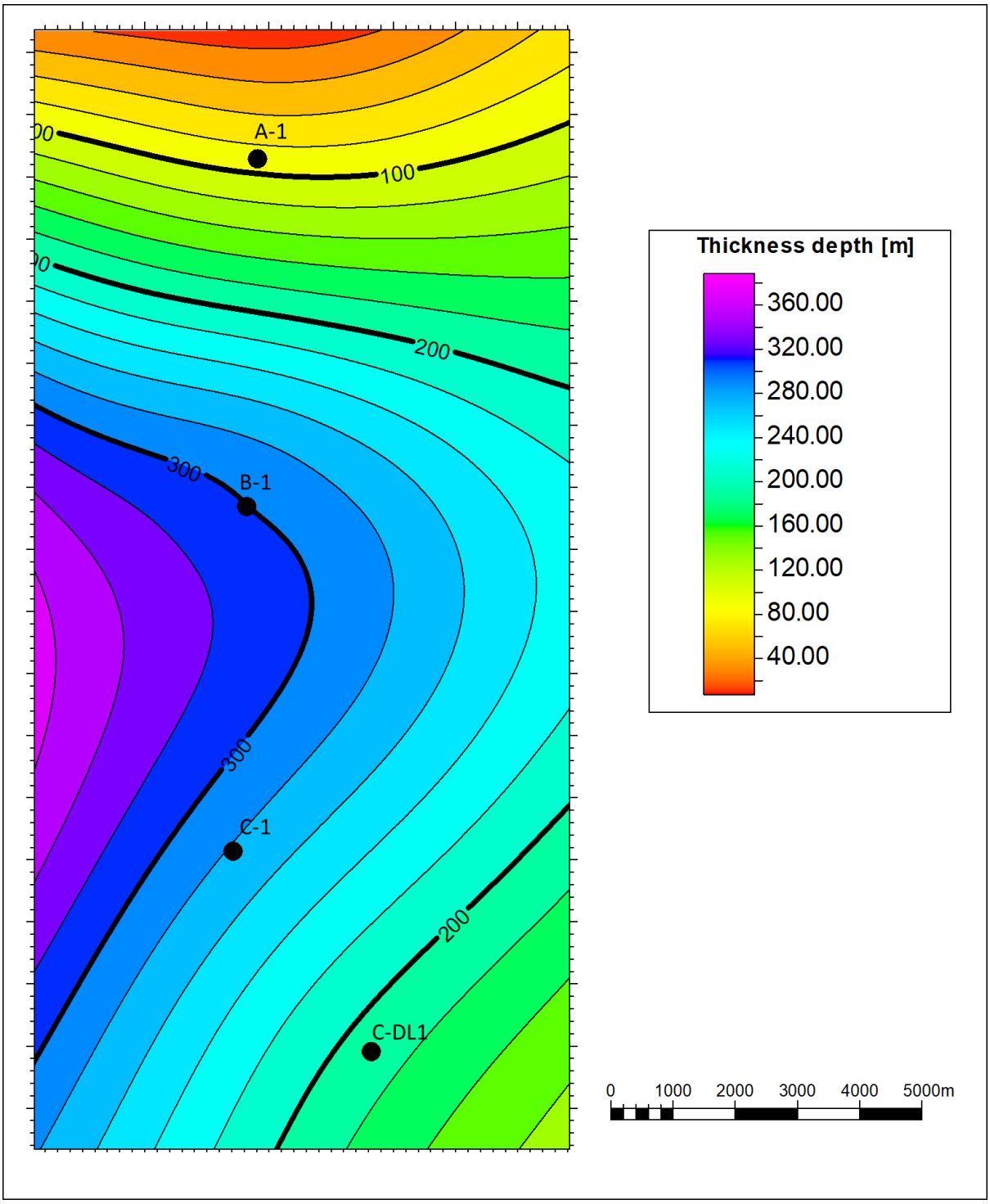


**Figure 1-14.** Isopach Kl map estimated from the top of Kl to the top of Upper Jurassic Tithonian identified in the wells. This unit presents the highest thickness and variability going from less of 100 m in the A-1 to a maximum of 300 m well B-1.

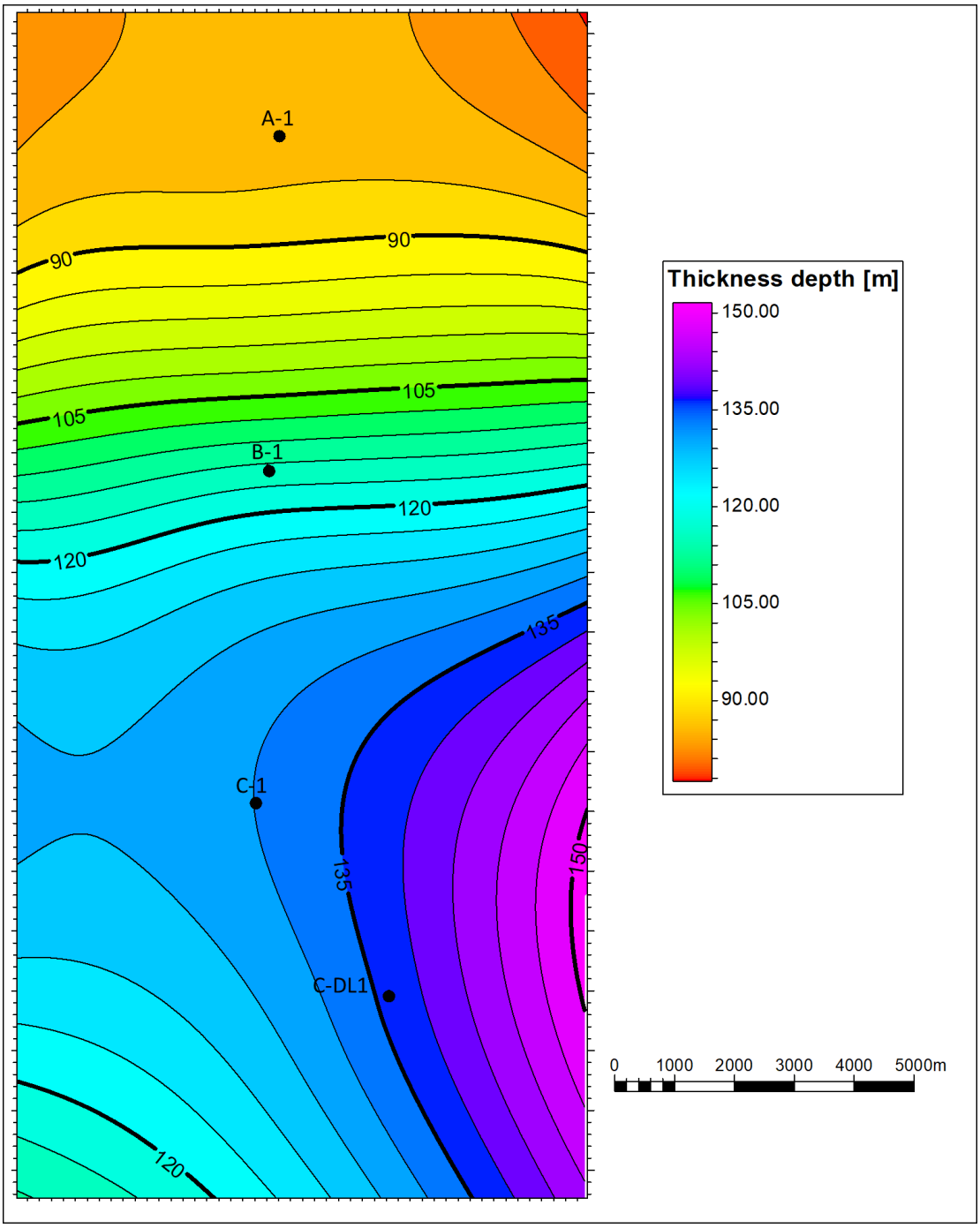


**Figure 1-15.** Isopach Km map estimated from the top of Km to the top of Kl identified in the wells. This unit presents a relative constant thickness related to the other units. Thickness varies from less of 90 m in the well A-1 to higher than 135 m in the well C-DL1.

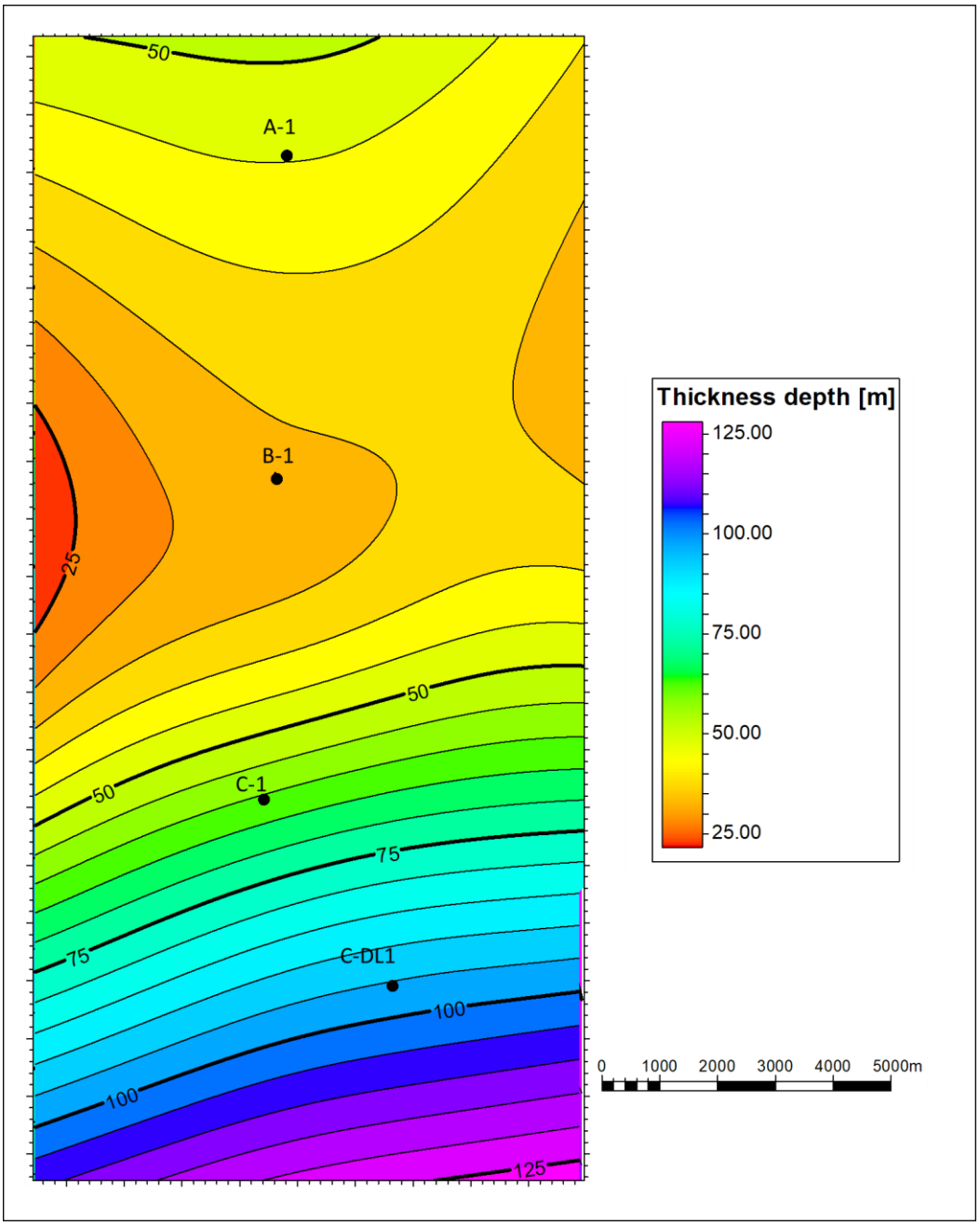


**Figure 1-16.** Isopach Ku-1 map estimated from the top of Ku-1 to the top of Km identified in the wells. This unit presents is one of the thinner units. Thickness varies from less of 55 m in the well A-1 to 95 m in the well C-DL1.

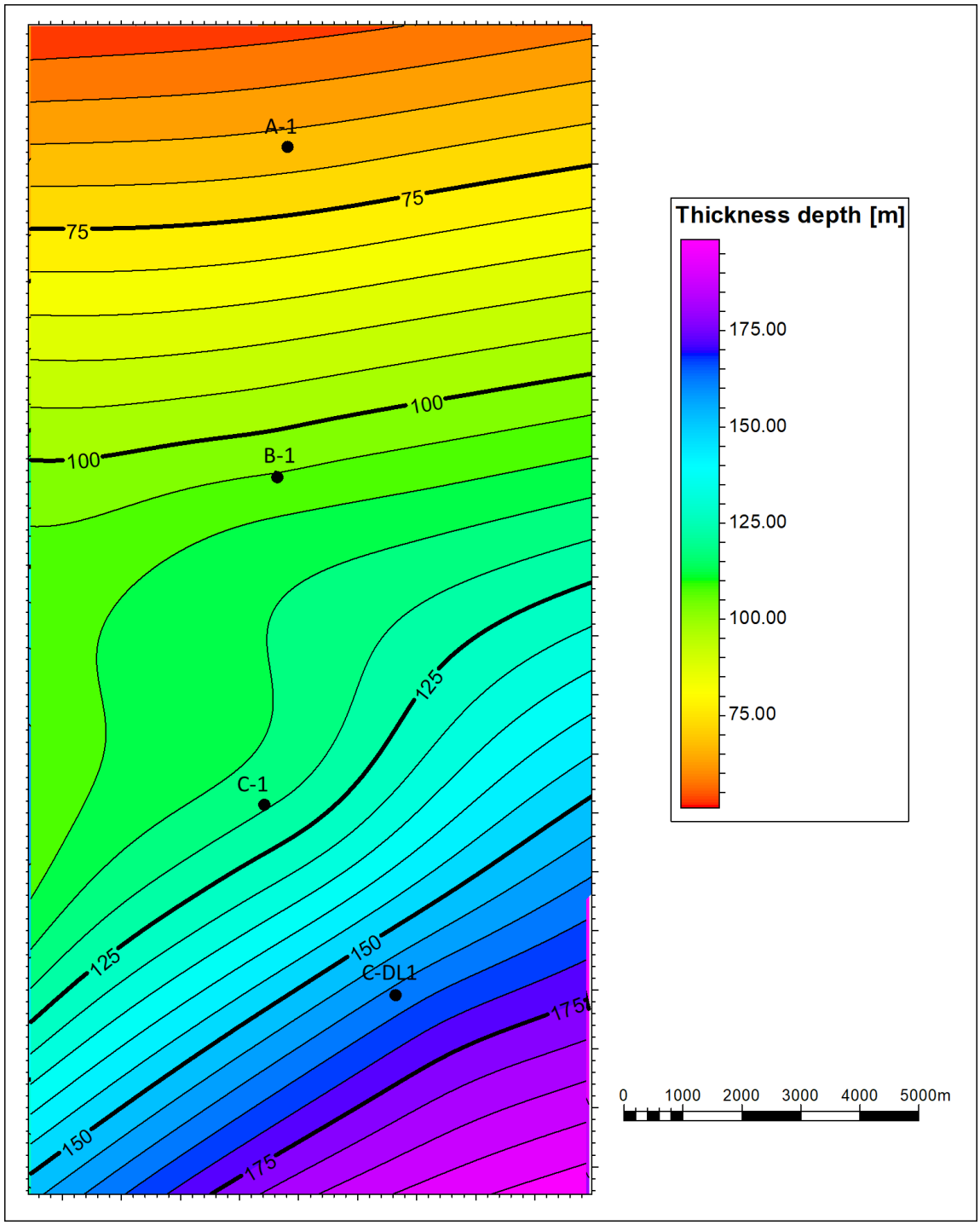


**Figure 1-17.** Isopach Ku-2 map estimated from the top of Ku-2 to the top of Ku-1 identified in the wells. This unit presents an increasing trend of thickness from North to South. Thickness varies from less of 70 m in the well A-1 to 160 m in the well C-DL1.

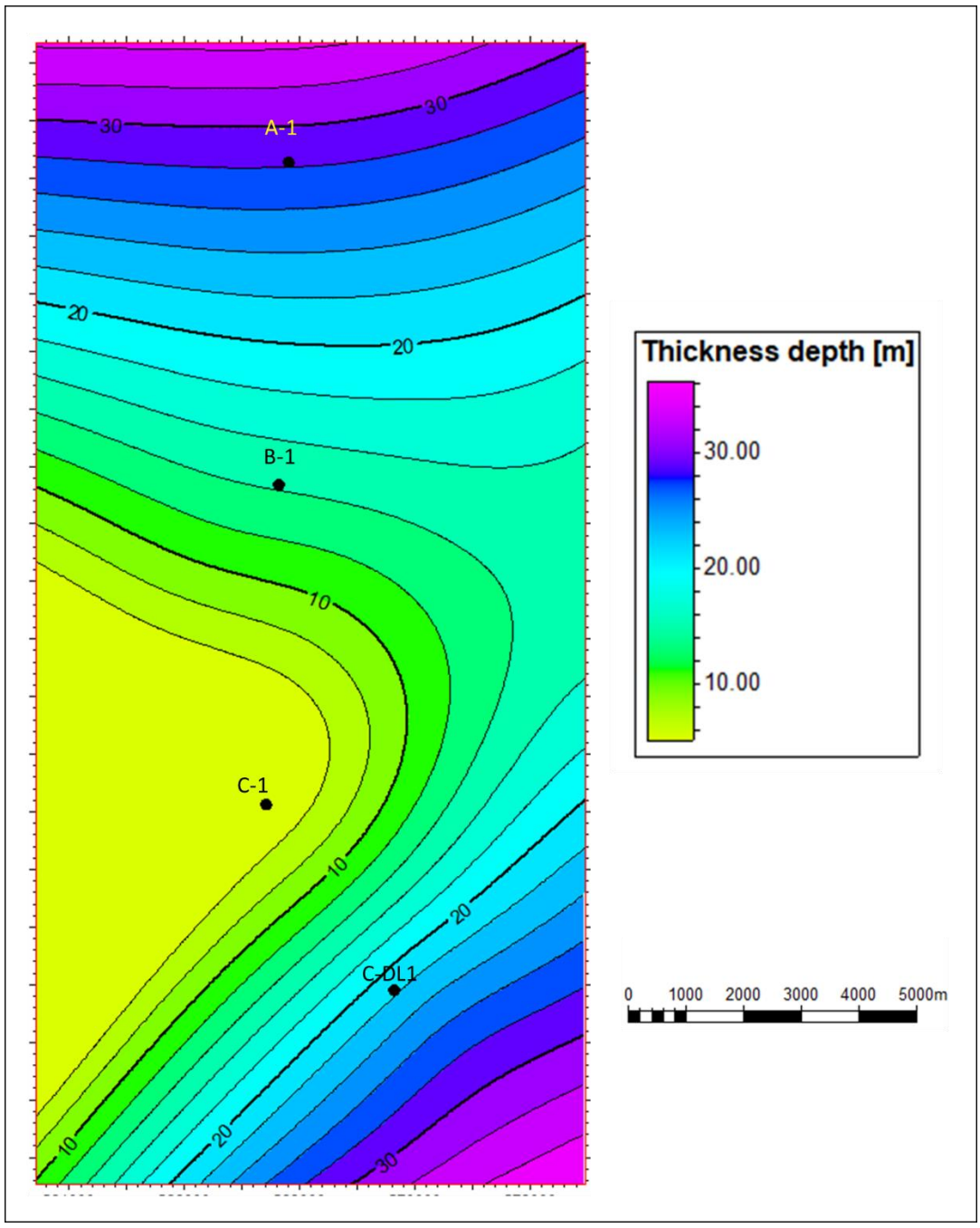


**Figure 1-18** Isopach Ku-2 map estimated from the top of Ku-2 to the top of Ku-1 identified in the wells. This unit presents an increasing trend of thickness from North to South. Thickness varies from less of 70 m in the well A-1 to 160 m in the well C-DL1.

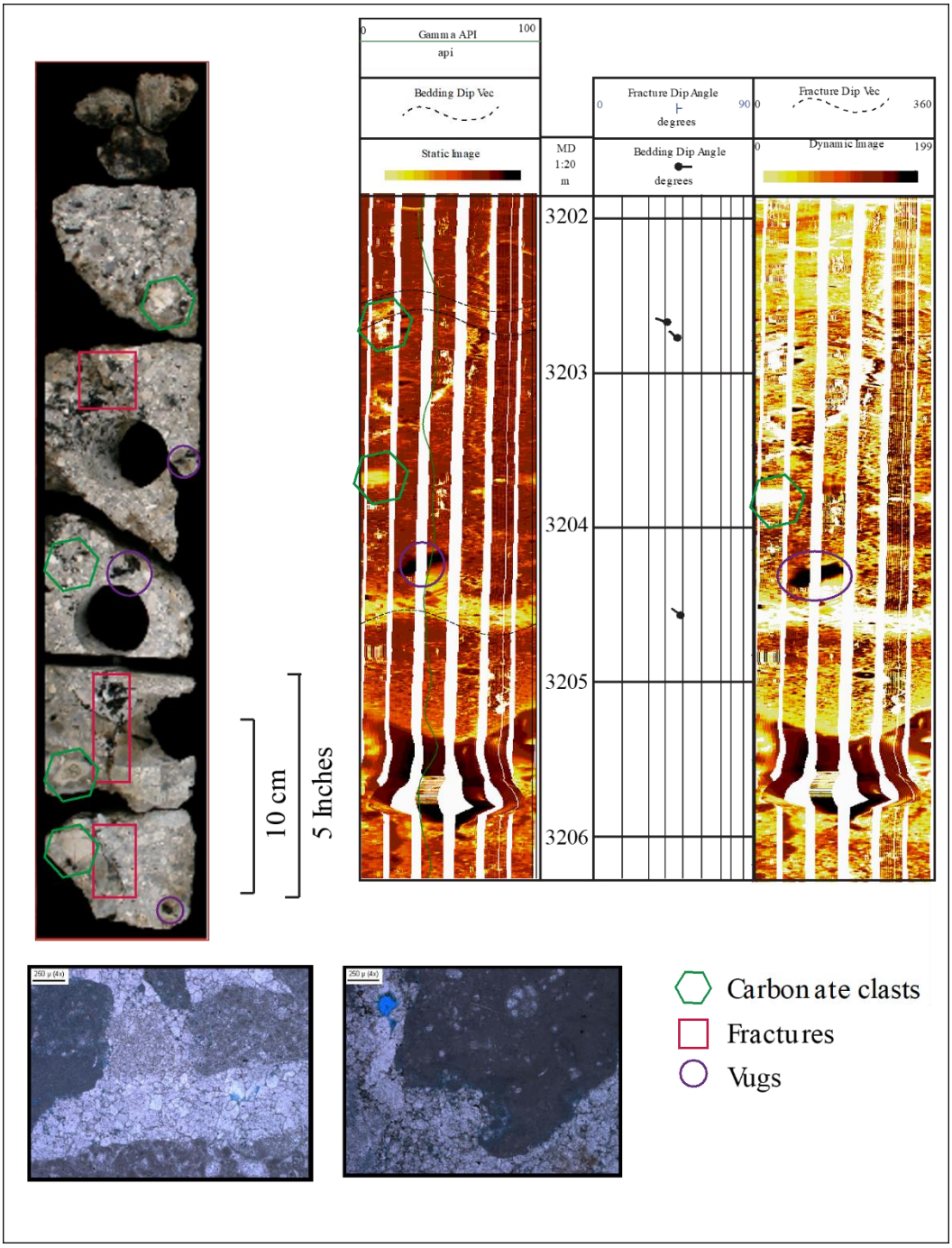


**Figure 1-19.** Fine breccia facies identified in core photography, thin sections, and image log. From the photography, it is possible to identify some carbonate clasts with sizes minor to 10 cm (4 inches) and oil stain. Porosity is in some isolated vugs and minor fractures. Some of these features can be identified in the image-log also, such as fragments and some disperse vugs. Further, in the image-log, it is possible to identify some bedding inside the formation. In the thin sections, it is possible to identify dolomite crystals, vug porosity, and some bioclasts.

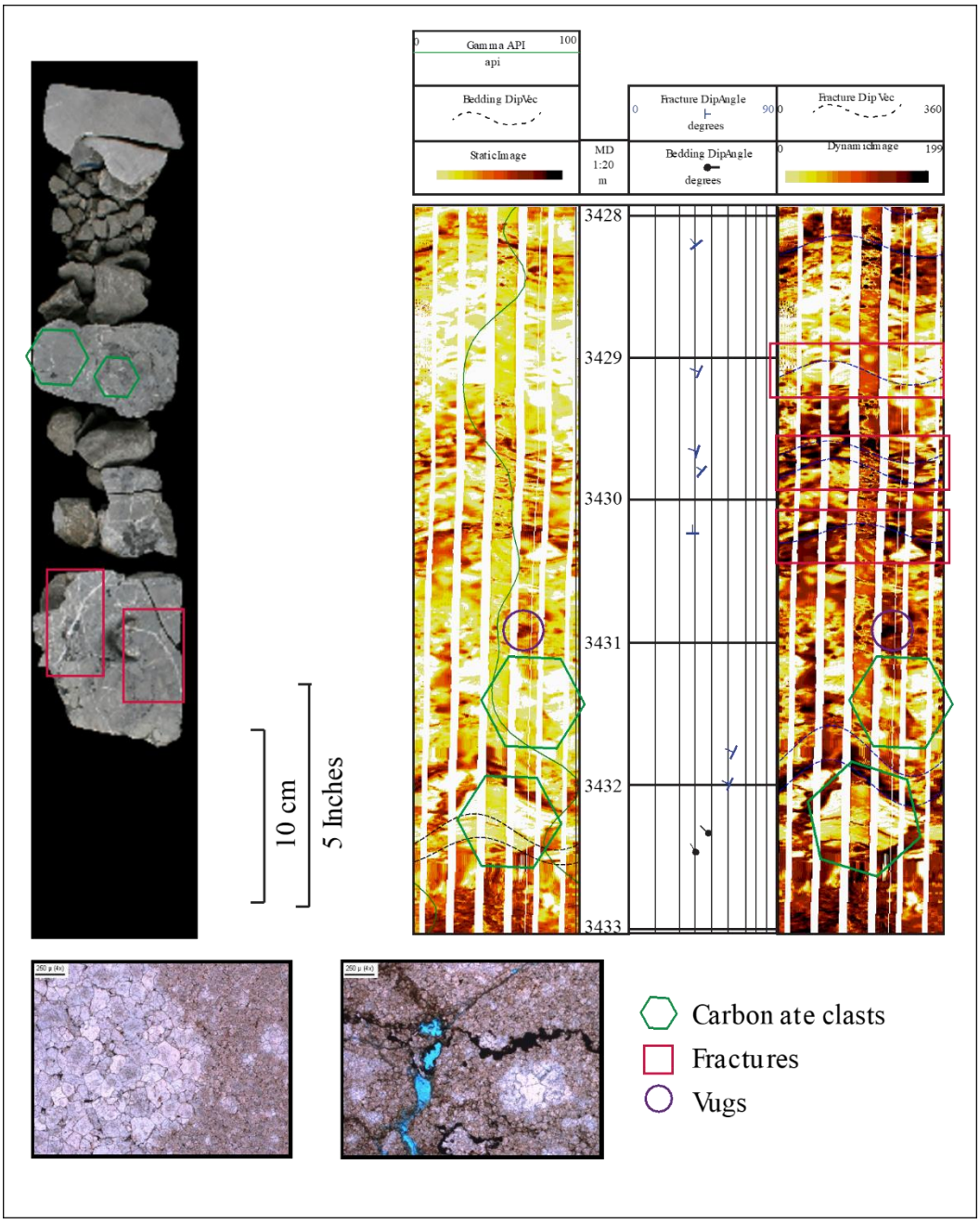


**Figure 1-20.** Laminated fine breccia facies identified in core photography, thin sections, and image log. In photography, it is possible to see carbonate clasts with sizes from one or two centimeters (a half inch) to five to six centimeters (two inches). Fractures are generally filled with calcite. Porosity is in small open fractures. For the image-log, it is possible to see fragments of different sizes, from 10 cm (4 inches) to 30 cm (12 inches). Clasts in image-log have an aspect angulous and oriented. Possible vugs are observed in image-log and, some fractures parallel to the bedding. In the thin sections, it is possible to identify dolomite crystals, vug porosity, and widened fractures for dissolution.

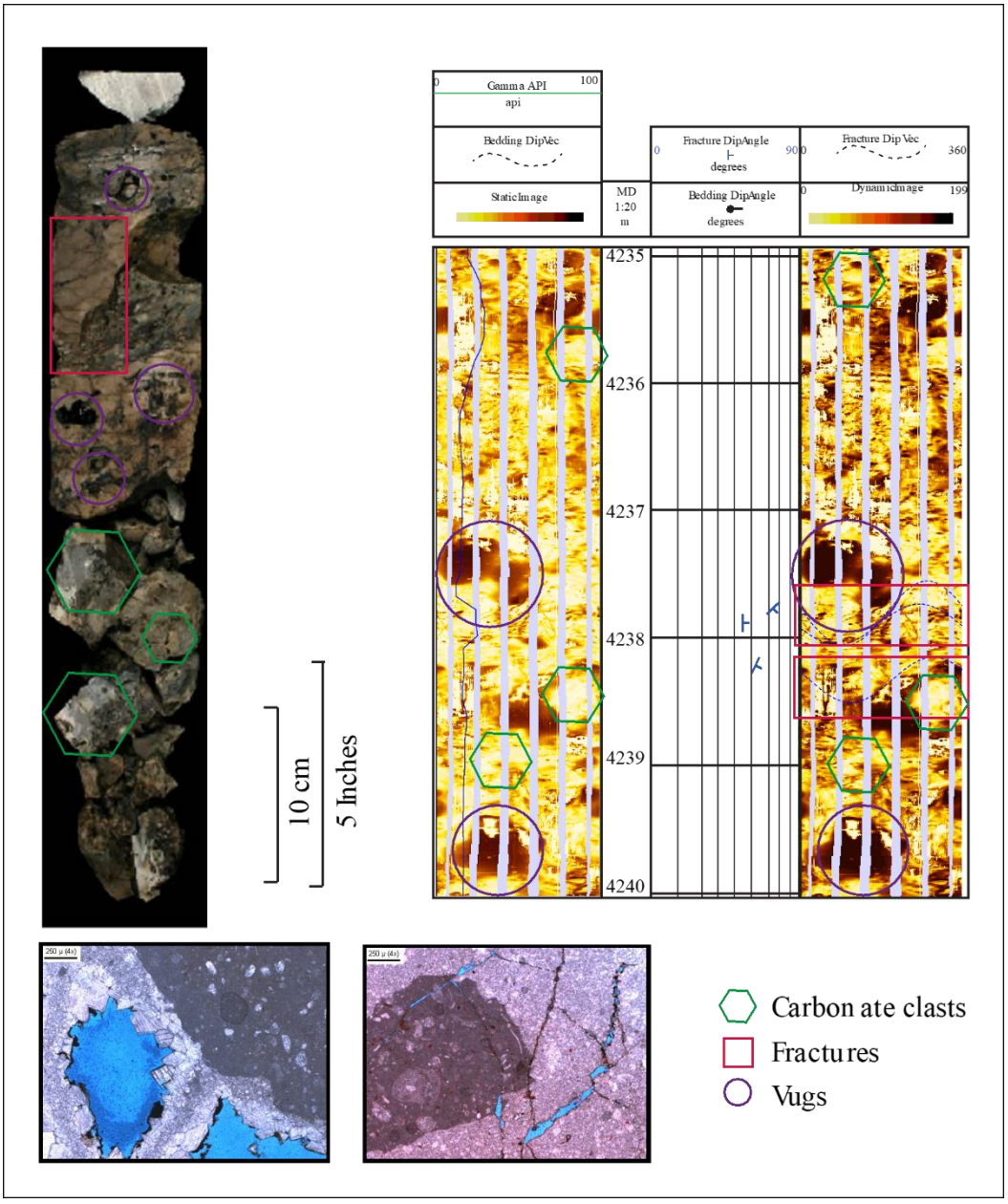


**Figure 1-21** Coarse breccia facies identified in core photography, thin sections, and image log. Because of the abundance of vugs and fractures, core recovery in this facies is low (around 10%). In photography, it is possible to identify both features. The appearance of this facies is generally dark for the oil stain. The clasts have sizes from one centimeter (0.4 inches) to fifteen centimeters (6 inches) in the photography. However, in the image-log is possible to see larger fragments around a half meter. Dissolution cavities reach a size until 20 centimeters (8 inches). In this facies, bedding is absent, and fractures look masked for the dissolution features. In the thin sections, it is possible to identify dolomite crystals, vug porosity, and widened fractures for dissolution.

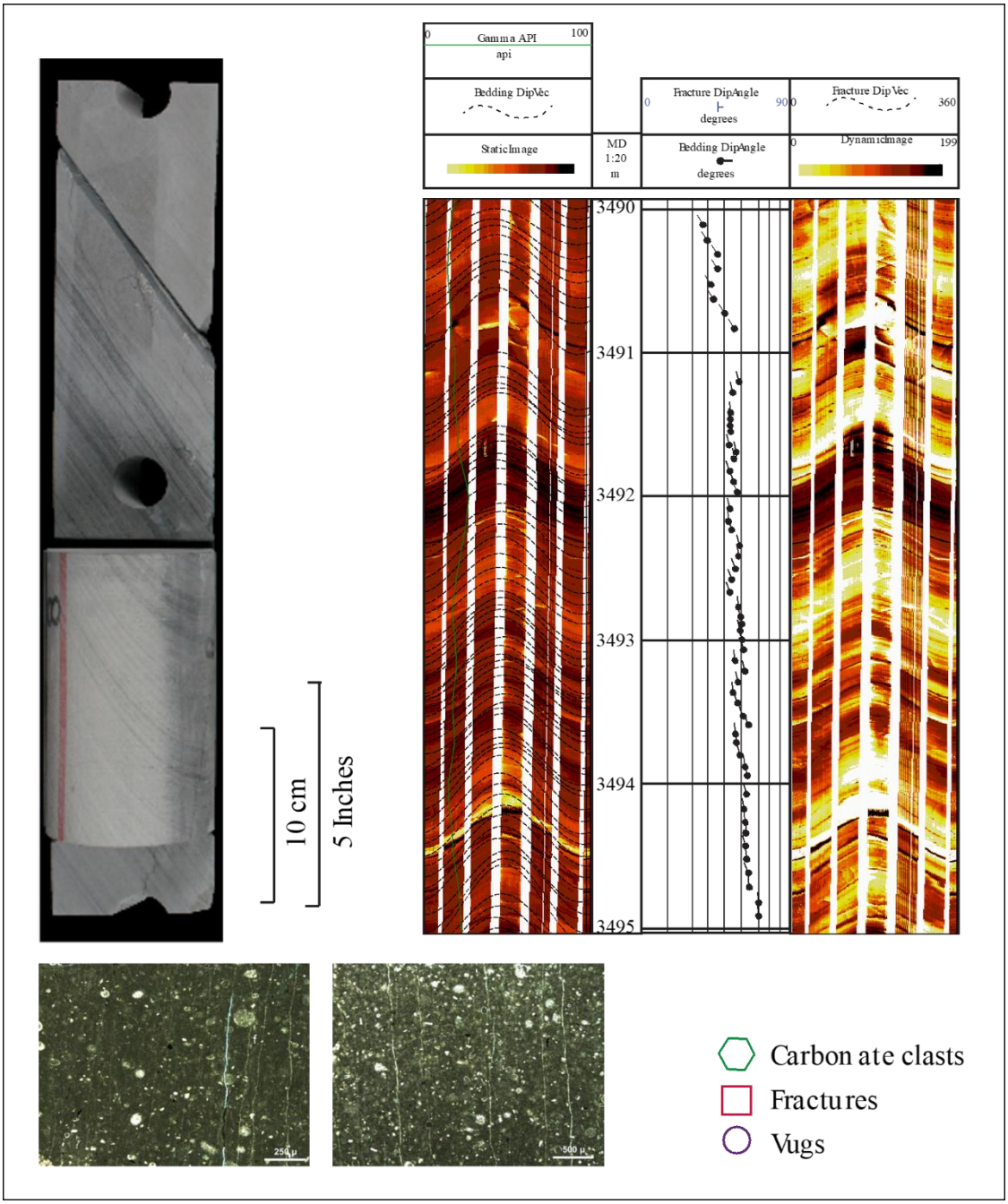


**Figure 1-22** Mudstone-Wackestone facies identified in core photography, thin sections, and image log. In the core photography, it is possible to identify lamination. Porosity is in the matrix, and fractures are absent or filled by calcite. In the image-log, it is possible to identify bedding features. Dissolution features, such as vugs, are absent in this facies. In the thin sections, it is possible to identify bioclasts in a micritic matrix with some fracture filled with calcite.

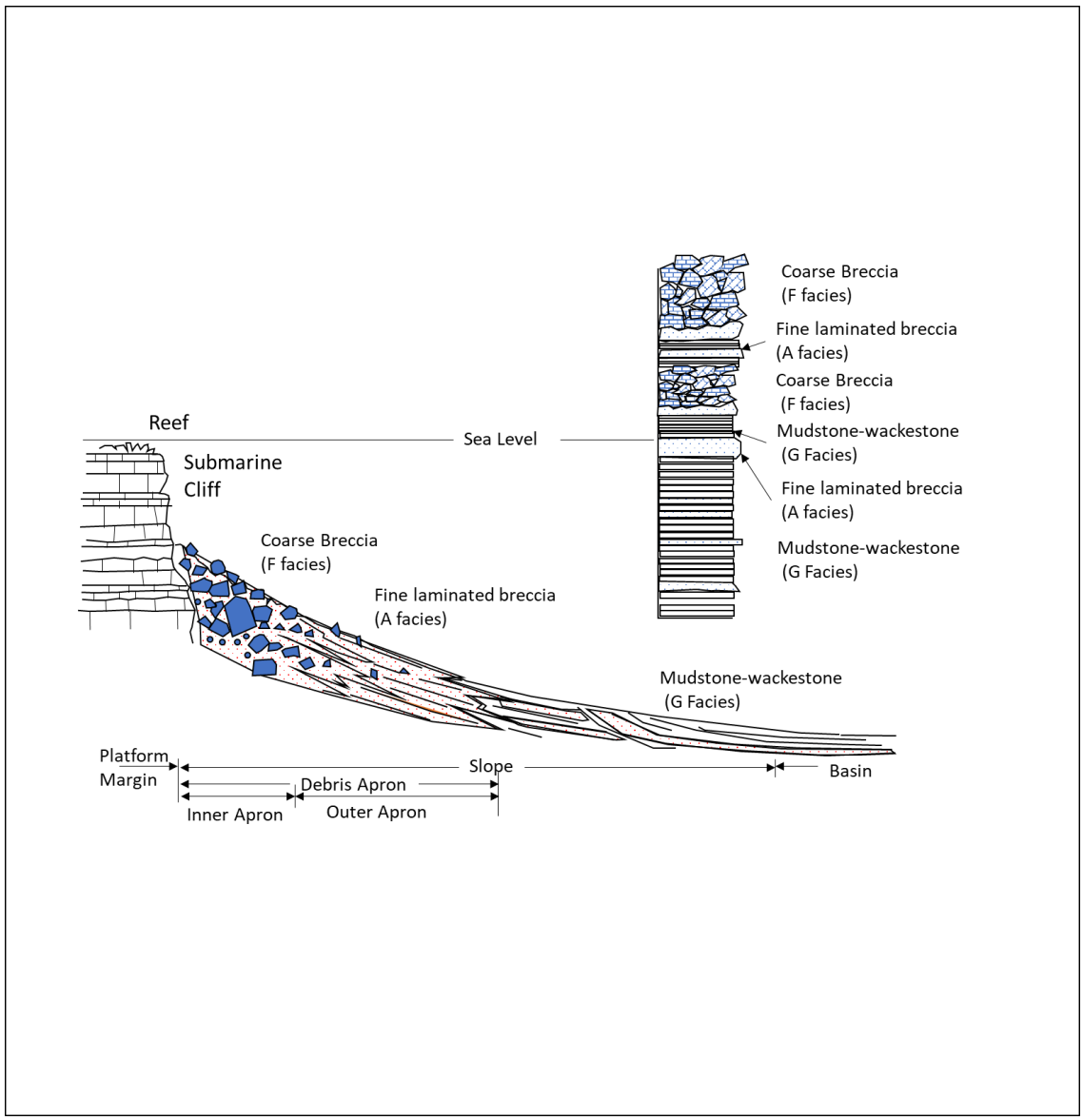


**Figure 1-20.** Schematic sedimentary model for the study zone, in this model the facies classification proposed by Mullins and Cook is related to the facies observed in this study. Coarse breccia facies are located in the inner apron mainly with some presences of fine laminated breccia. Finely laminated breccia facies dominate the outer apron. The mudstone-wackestone facies corresponds to pelagic and hemipelagic sedimentation in the outer slope and basin (After McIlrean and James, 1978).

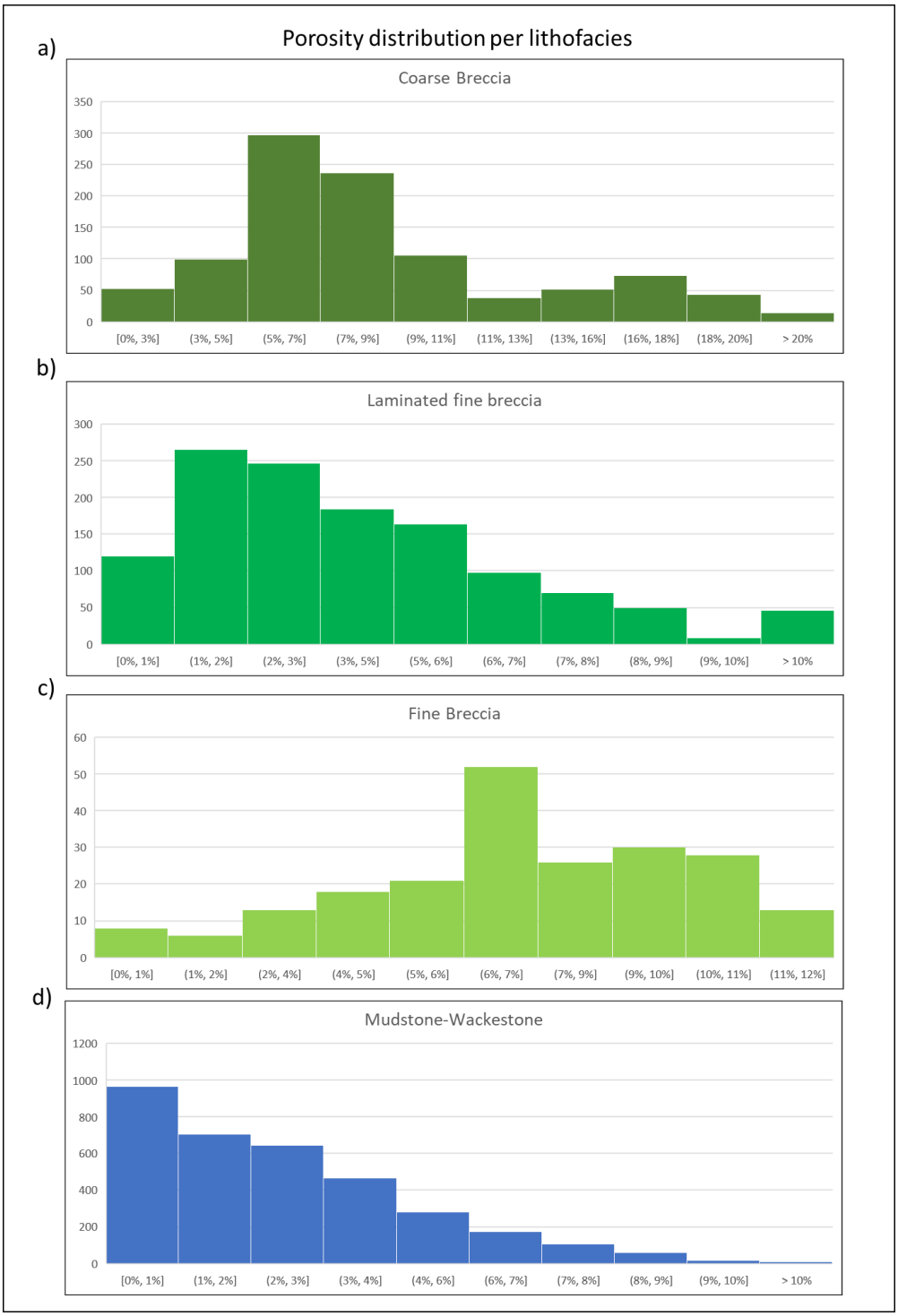


**Figure 1-21.** Porosity distribution histograms per lithofacies. a) Coarse breccia lithofacies present the higher porosity values and a bimodal distribution. b) Laminated fine breccia is shown porosity values between 1 to 6% with a mode in 1 to 3% category. c) Fine breccia has a plateau distribution between 4 to 11% porosity values. d) Mudstone-wackestone lithofacies presents the lower porosity with absolute porosity values below 3%.

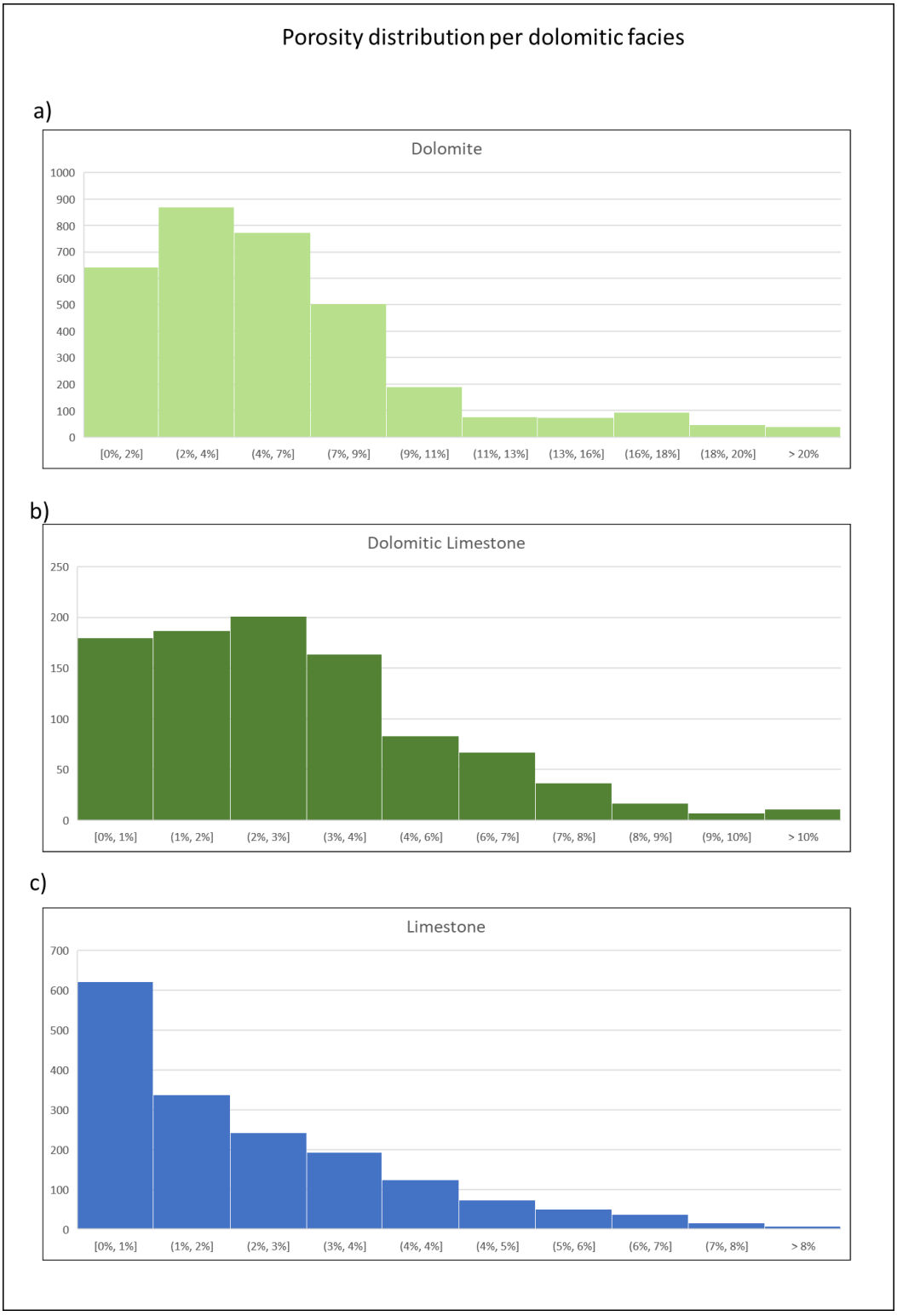


**Figure 1-22.** Porosity distribution per dolomitic facies. a) Dolomite and b) dolomitic limestone have the higher porosity values.

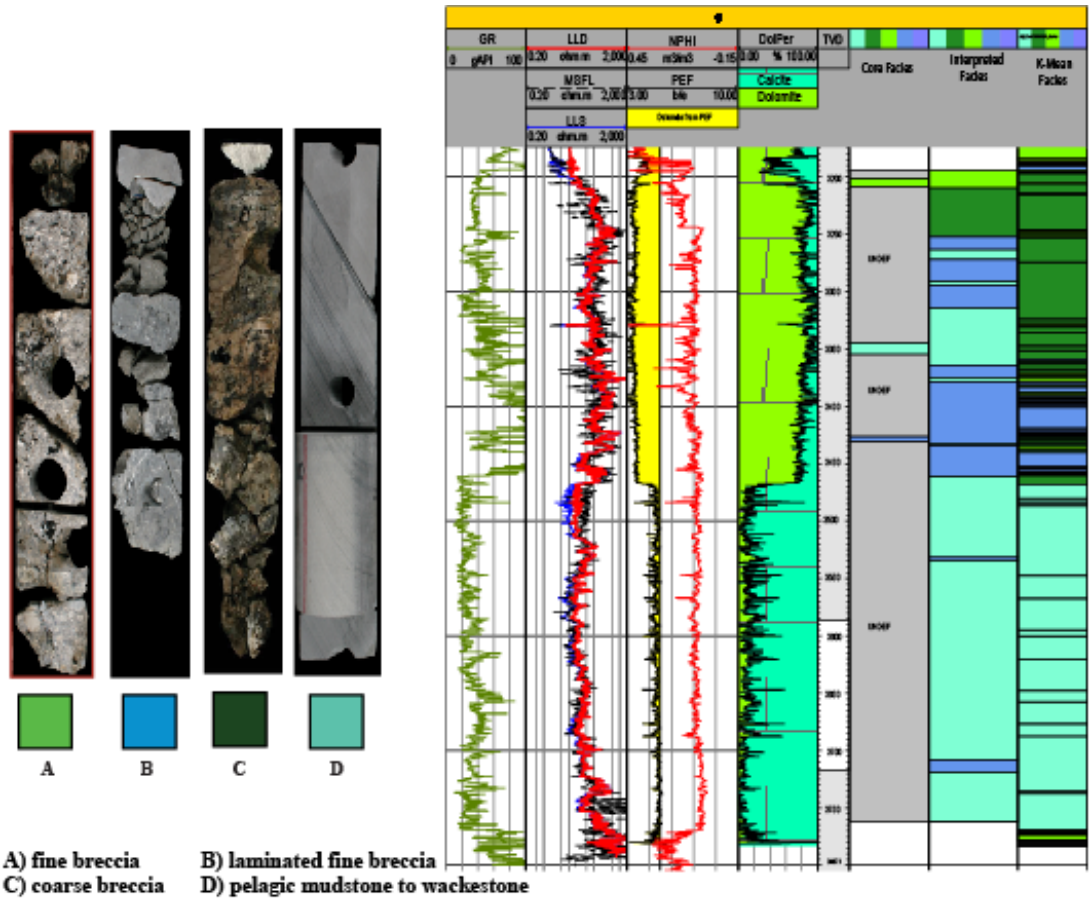


A)

Clusting_3: GR-RESD-NPHI-PEF

| Expected / Predicted | Mudstone-Wackestone | Breccia | Fine Breccia | Laminated Breccia | Truth Overall | User Accuracy (Recall) |
|---|---|---|---|---|---|---|
| Mudstone-Wackestone | 1100 | 0 | 4 | 54 | 1158 | 94.99% |
| Breccia | 266 | 154 | 45 | 319 | 784 | 19.64% |
| Fine Breccia | 23 | 16 | 11 | 57 | 107 | 10.28% |
| Laminated Breccia | 28 | 1 | 0 | 194 | 223 | 87.00% |
| Classification Overall | 1417 | 171 | 60 | 624 | 2272 | |
| Producer Accuracy (Precision) | 77.63% | 90.06% | 18.33% | 31.09% | | |
| | | | | | Overall Accuracy | 64.22% |

B)

**Figure 1-26.** A) Well-log showing the basic logs (first to third track), dolomitization percentage (fourth track) and, the identified facies from cores (sixth track), image logs (seventh track) and, the resulting facies from the K-mean algorithm. B) Confusion matrix showing the accuracy of K-means resulting facies versus the facies described from image-logs and cores. The overall accuracy obtained was 64.22%.

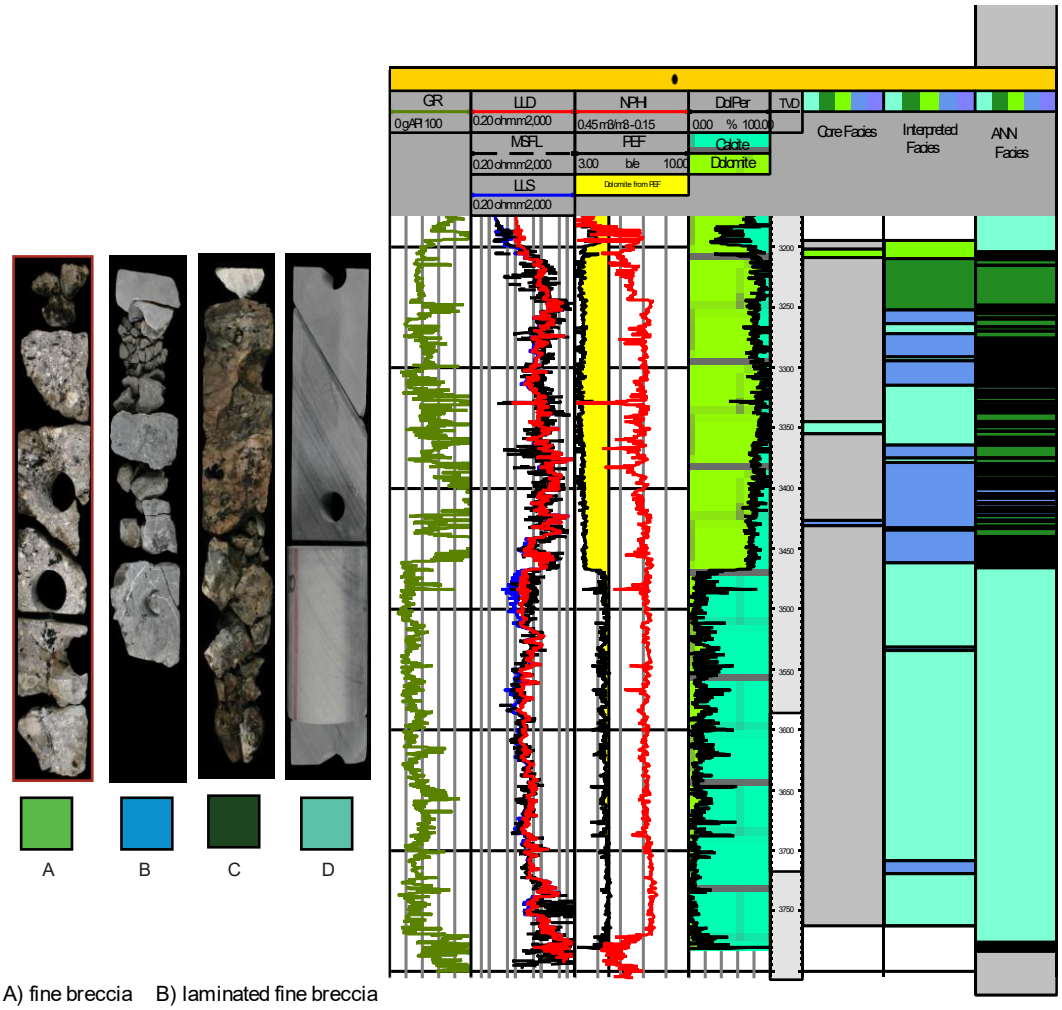


A) fine breccia B) laminated fine breccia
C) coarse breccia D) mudstone to wackestone

A)

| Image-Logs / Expected \ Predicted | Mudstone-Wackestone | Breccia | Fine Breccia | Laminated Breccia | Truth Overall | User Accuracy (Recall) |
|---|---|---|---|---|---|---|
| Mudstone-Wackestone | 1293 | 28 | 28 | 351 | 1700 | 76.06% |
| Breccia | 90 | 142 | 28 | 124 | 384 | 36.98% |
| Fine Breccia | 2 | 0 | 4 | 0 | 6 | 66.67% |
| Laminated Breccia | 32 | 1 | 0 | 149 | 182 | 81.87% |
| Classificat on Overall | 1417 | 171 | 60 | 624 | 2272 | |
| Producer Accuracy (Precision) | 91.25% | 83.04% | 6.67% | 23.88% | | |

ANN2: GR-RESD -NPHI

B)

| Overall Accuracy | 69.89% |
|---|---|

**Figure 1-27** A) Well-log showing the basic logs (first to third track), dolomitization percentage (fourth track) and, the identified facies from cores (sixth track), image logs (seventh track) and, the resulting facies from the ANN algorithm. B) Confusion matrix showing the accuracy of ANN resulting facies versus the facies described from image-logs and cores. The overall accuracy obtained was 69.89%.

# References

Acevedo, J. S., 1980, Giant fields of the Southern Zone, Mexico: Giant Oil and Gas Fields of the Decade 1968-1978, v. 30, p. 339–387.

Al-Dossary, S., and K. J. Marfurt, 2006, 3D volumetric multispectral estimates of reflector curvature and rotation: Geophysics, v. 71, no. 5, p. P41, doi:10.1190/1.2242449.

Angeles-Aquino, F. J., 2006, Monografia petrolera de la zona marina. IN SPANISH. Monograph of the marine zone oil: Boletin de la Asociacion Mexicana de Geologos Petroleros, p. 69.

Cantu-Chapa, A., and R. Landeros-Flores, 2001, The Cretaceous-Paleocene boundary in the subsurface Campeche Shelf, southern Gulf of Mexico: The Western Gulf of Mexico Basin. Tectonics, Sedimentary Basins, and Petroleum Systems., v. 75, p. 389–395.

Chopra, S., and K. J. Marfurt, 2007, Volumetric curvature attributes add value to 3D seismic data interpretation: The Leading Edge, v. 26, no. 7, p. 856, doi:10.1190/1.2756864.

Dunham, R. J., 1962, Classification of carbonate rocks according to depositional texture: Classification of Carbonate Rocks - A Symposium, p. 108–121.

GrajalesNishimura, J M, E CedilloPardo, C RosalesDominguez, D J MoranZenteno, W Alvarez, P Claeys, J RuizMorales, J GarciaHernandez, P PedillaAvila, and A SanchezRios. 2000. “Chicxulub Impact: The Origin of Reservoir and Seal Facies in the Southeastern Mexico Oil Fields (Vol 28, Pg 307, 2000).” Geology 28 (12): 1152. https://doi.org/10.1130/0091-7613(2000)28<307:CITOOR>2.0.CO;2.

Qi, J., G. Machado, and K. Marfurt, 2017, A workflow to skeletonize faults and stratigraphic features: Geophysics, v. 82, no. 4, p. 1–14.

Kumar, M., and D.-H. Han, 2005, Pre shape effect on elastic properties of carbonate rocks, in SEG/Houston 2005 Annual Meeting: p. 1477–1481.

Li, J. 2016, Experimental Modeling of Geometry and Evolution of Structures Aboce Ductile and Frictional Detachments, Master Thesis, University of Oklahoma. https://doi.org/https://doi.org/10.3929/ethz-b-000238666.,

Liu, R. L., N. Li, Q. fu Feng, C. Hai, and K. wen Wang, 2009, Application of the triple porosity model in well-log effectiveness estimation of the carbonate reservoir in Tarim oilfield: Journal of Petroleum Science and Engineering, v. 68, no. 1–2, p. 40–46, doi:10.1016/j.petrol.2009.05.016.

Marfurt, K. J., 2006, Robust estimates of 3D reflector dip and azimuth: Geophysics, v. 71, no. 4, p. 29-40, doi:10.1190/1.2213049.

Mitra, S., G. C. Figueroa, J. H. Garcia, and A. M. Alvarado, 2005, Three-dimensional structural model of the Cantarell and Sihil structures, Campeche Bay, Mexico: AAPG Bulletin, v. 89, no. 1, p. 1–26, doi:10.1306/08310403108.

Mitra, S., J. A. Duran Gonzalez, J. G. Hernandez, S. H. Garcia, and S. Banerjee, 2006, Structural geometry and evolution of the Ku, Zaap, and Maloob structures, Campeche Bay, Mexico: AAPG Bulletin, v. 90, no. 10, p. 1565–1584, doi:10.1306/04240605101.

Mullins, Henry T., and Harry E. Cook. 1986. “Carbonate Apron Models: Alternatives to the Submarine Fan Model for Paleoenvironmental Analysis and Hydrocarbon Exploration.” Sedimentary Geology 48 (1–2): 37–79. https://doi.org/10.1016/0037-0738(86)90080-1.

Murillo-Muñetón, G., J. M. Grajales-Nishimura, E. Cedillo-Pardo, J. García-Hernández, and S. García-Hernández, 2002, Stratigraphic Architecture and Sedimentology of the Main Oil-Producing Stratigraphic Interval at the Cantarell Oil Field: The K/T Boundary Sedimentary

Succession: Proceedings of the SPE International Petroleum Conference and Exhibition of Mexico, p. 643–649.

Santiago, J., and A. Baro, 1992, Mexico's giant fields, 1978-1988 decade, in M. T. Halbouty, ed., Giant oil and gas fields of the decade 1978-1988: AAPG Memoir 54, p. 73-99.

Sinha, S., Devegowda, D., & Deka, B. (2017, July 24). Quantification of Recovery Factors in Downspaced Shale Wells: Application of a Fully Coupled Geomechanical EOS Compositional Simulator. Unconventional Resources Technology Conference. doi:10.15530/URTEC-2017-2697500

Sinha, S., Marfurt, K. J., Devegowda, D., Pires de Lima, R., & Verma, S. (2017, October 9). Seismic Inversion Based SRV and Reserves Estimation for Shale Plays. Society of Petroleum Engineers. doi:10.2118/187137-MS

Sinha, S., Devegowda, D., & Deka, B. (2016, September 13). Multivariate Statistical Analysis for Resource Estimation in Unconventional Plays Application to Eagle Ford Shales. Society of Petroleum Engineers. doi:10.2118/184050-MS

Zapata, Y., T. N. Phan, and Z. A. Reza, 2018, Multi-Physics Pore-Scale Modeling of Particle Plugging Due to Fluid Invasion During Hydraulic Fracturing, in Proceedings of the 6th Unconventional Resources Technology Conference: American Association of Petroleum Geologists, doi:10.15530/urtec-2018-2901340

Zapata, Y., and A. Sakhaee-Pour, 2016, Modeling adsorption–desorption hysteresis in shales: Acyclic pore model: Fuel, v. 181, p. 557–565, doi: 10.1016/J.FUEL.2016.05.002

## Introduction to Chapter 2

In Chapter 1 with a base on the structural model and the stratigraphic model, I was able to define a 3D geo-cellular grid. In this grid are represented all the architectural elements that form the reservoir in its vertical and horizontal boundaries.

In the next Chapter 2, I present the guides to distribute the properties beyond the wells. Because a possible relation between dolomitization and porosity was stated in the last chapter dolomitization was the property that I choose to distribute and use as a base guide for the other properties, total porosity, primary and secondary porosity.

To achieve this objective the workflow that I presented in Chapter 2 was next, in the first step, obtain a set of seismic attributes that could predict dolomitization including a post-stack inversion process. Then, I select the attributes that had a better response to the dolomitization in the wells using cigar-probes. Finally, with these selected attributes I tried three different machine learning processes to select the one with the best dolomitization prediction based on the hard data of the wells and using a well as a blind-test.

Because I have two versions of the seismic data, depth- and time-migrated, I took the opportunity to compare the results and choose what version works better in the study zone.

# Chapter 2: Comparative Analysis of Attributes and Post-stack P-impedance in Time and Depth Domain in a Naturally-Fractured Carbonated Reservoir for Dolomitic Facies Identification in Southeast Gulf of Mexico

Cervantes-Velazquez, Antonio, antonio.cervantes.velazquez-1@ou.edu

Marfurt, Kurt J., kmarfurt@ou.edu

Slatt, Roger M., rslatt@ou.edu

## Abstract

An increasing number of seismic attributes are available for reservoir characterization, providing a means to define structural, sedimentary, and diagenetic features. Unfortunately, there are now so many attributes that it is often challenging to select which attributes best characterize a feature of interest. Further complicating the choice of attributes is that most application are on time-migrated data. In structurally complex areas such as the southeast Gulf of Mexico, depth-migrated seismic data are required to properly image reservoirs in the presence of reverse faulting and salt diapirism. Few published papers address whether attributes applied to depth-migrated volumes are as valuable as those applied to time-migrated volumes.

In this work, we describe an integrated workflow; where we calibrate the attributes and machine learning process with well control to characterize a carbonate reservoir in the southeast Gulf of Mexico. The highest porosity zones in this reservoir are associated with diagenetic processes of fracturing, dolomitization, and dissolution. Because dolomitization provides the

highest values of porosity, distinguishing limestone from dolomite is a key reservoir characterization objective.

We generated a set of seismic attributes including peak magnitude, peak frequency, chaos, total energy, curvature, Sobel filter similarity, P-impedance, and amplitude for both prestack time- and depth-migrated data volumes. Not surprisingly, structural attributes computed from the depth-migrated data provide sharper images with fewer artifacts associated with velocity pull-up and fault shadows. However, because doubling the upper frequency increases the cost of reverse-time prestack depth migration increases by a factor of 16 compared to prestack Kirchhoff time migration, the vertical and lateral resolution of the depth migrated volume is approximately half that of the time migrated volume. The superior resolution of time-migrated volumes therefore provided much more accurate predictions of dolomitization distributions made using a weighted linear combination of peak magnitude and P-impedance PRESTMmeasured in a blind-test well, compared to the other combination of attributes and methods such as artificial neural networks.

.

## Introduction

Seismic attributes such as coherence, curvature, and spectral components are routinely used to map structural, sedimentary, and diagenetic features. Likewise, geomechanical attributes such as impedance are routinely used to estimate lithology or rock properties such as porosity (Latimer, et al., 2002; Kumar, et al., 2016; Khosdel and Riahi, 2011). In structurally complex areas depth-migrated seismic has become the standard such as the Southeastern Gulf of Mexico, providing better focused and less noisy images.

While attributes are often applied to depth migrated data, few papers have qualifiedly compared attributes from time and depth-migrated for the same survey (Figure 2-1). When we convert the PRESTM seismic data to the depth domain, we can compare the differences in the structures related to the structures in PRESDM (Figure 2-2). The anticlines in the PRESTM looks vertically stretched, and the limits of the blocks separated by faults are challenging to identify. For the PRESDM, the structures are softer such as we expected from the geology of the zone and the limits between blocks separated by faults look more defined.

Lin (2016) in his doctoral dissertation estimated spectral and curvature attributes in depth-migrated seismic. For spectral attributes, Lin proposed use dip compensation and short-windows discrete Fourier transform to correct the effects of the dip over the frequency spectrum in depth-migrated seismic. Lin applied this method to time- and depth migrated oilfield of East China, where faults are the main control for reservoirs, obtaining as result attributes where the seismic images were not affected by artifacts associated to lateral variations in velocity as the artifacts calculated in time-migrated seismic. In this dissertation, Lin addressed the issue of "fault whisper", a phenomenon related to distortions in the edges of the faults by velocity changes, applying coherence attributes to PRESDM and PRESTM. Lin observed a better response in the PRESDM coherence where the artifacts caused by horizontal velocity variation were removed. A method to work with multiple attributes is using machine-learning algorithms because they can combine many attributes to identify specific features of a reservoir. But some attributes could highlight the features, and other attributes could mask the features. In this work, we suggest an integral view, where along with the attributes and machine learning process we use a previous selection analysis with cigar- and well-probe methods. We applied these methods for the characterization of a carbonate reservoir in the southeast Gulf of Mexico (**Figure 2-3**).

This reservoir has a low API gravity around 11º, so this reservoir depends on high porosity sweet spots to be productive. The highest porosity zones are associated with diagenetic processes, such as fracturing, dolomitization, and dissolution. Of these three processes, dolomitization processes gives the highest values of porosity. For this reason, our main objective is to distinguish between limestone and dolomite.

Using a post-stack seismic survey of the study area, we generate two spectral attributes, peak frequency and, peak magnitude; and four geometric attributes, chaos, total energy, maximum positive curvature and, Sobel filter similarity. All these attributes were generated in the two versions available of this post-stack, time-migrated (PRESTM) and depth-migrated (PRESDM) seismic. We performed a post-stack impedance inversion in both seismic versions also, to incorporate its results to the machine learning processes. We used the data from five wells in the area, four of these wells have a complete set of basic logs (resistivity, gamma ray, litho-density, neutron porosity, and PEF) The lithology in the wells was identified using the PEF log, separating limestone from dolomite. Then cigar-probes for every lithology were performed on the wells, obtaining the weighted average values for every attribute in a 50 m radio around the well. These values were plotted with the lithological changes identified in the wells. This way it was possible to observe the response of the attributes to the lithological changes and made a preliminary selection of attributes for the subsequent processes. These selected attributes were used as an input for the next machine learning processes, artificial neural network (ANN), weighted linear combination (WLN) and, generative topographic mapping (GTM). All these processes were applied to the PRESDM and PRESTM set of attributes to compare the results.

To verify the efficacy of the machine learning processes, we stated constraints to accomplished by the learning machine processes. These constraints were based on the geological

knowledge of the area. Besides, we reserved one of the wells than not participated in the P-impedance inversion process and in the supervised machine learning process. To use this well as a blind test.

## Geologic Setting

The stratigraphy of the area was described by Angeles-Aquino (2006), identifying the main units from the Jurassic to the Cenozoic. The reservoir rock is Cretaceous in age. According to Angeles-Aquino's work, the Cretaceous formation is divided into Upper, Middle, and Lower Cretaceous intervals (F. J. Angeles-Aquino 2006). These formations in our study area are represented by bentonitic mudstone, intraclastic mudstone to wackestone and limestones, and micro-dolomites.

The main reservoir rock consists of Upper Cretaceous carbonate debris flows that were deposited on the Yucatan Peninsula slope. The debris flows consist of heterogeneous carbonate clasts in a carbonate matrix. The formation is diagenetically altered through a sequence of dolomitization, dissolution, and fracturing. The diagenetic processes developed a complex porosity system where three (3) types of pores, intercrystalline pores associated with the dolomitic matrix, vugs, and fractures, are equally important.

Related to dolomitization we subdivided the formations described by Angeles-Aquino (2006) into five units inside the geo-cellular model (Figure 2-4. ),

- ***Unit Ki*** corresponds to Lower Cretaceous is limestone in all the wells in the study zone.

- ***Unit Km*** corresponds to dolomized Middle Cretaceous in all the wells in the study zone.
- ***Unit Ku-1*** corresponds to the lower part of the Upper Cretaceous and is always dolomized in all the wells in the study zone.
- ***Unit Ku-2*** corresponds to the middle part of the Upper Cretaceous. This unit is dolomitized in all the wells excepting the well C-DL1.

Near the study area, structural analyses of the Cantarell and Sihil fields were conducted by Mitra et al. (2005) and later for the Ku, Zaap, and Maloob fields (Mitra et al., 2006). These analyses described the main deformation episodes for the area, identifying three main episodes of deformation: (1) a Jurassic to Early Cretaceous extensional event; (2) a Miocene compressive phase, during which the main trap-forming structures were formed; and (3) a Pliocene to Holocene extensional event, resulting in several listric-growth faults.

The study area is composed of three anticline structures related to thrusting. According to the events described for Mitra (2005; 2006), these structures were generated in the Miocene compressive phase. In this study, the fields related to these thrusting structures are called, from north to south, fields A, B, and C. The structural trend of the thrusts has a general east-west orientation dipping to the south for fields A and C. However, structure B is dipping toward the north (Figure 2-5. ).

## Methods

The products of a seismic inversion process can be related to petrophysical properties to differentiate limestone and dolostone. A seismic survey is composed by acoustic impedance (AI) values and these values comes from the product of the rock density and P-wave velocity. As

such, the AI is a function of the rock matrix lithology, porosity and fluid content. In the post-stack impedance exists the assumption that each seismic trace is a result product of a reflectivity series and a wavelet (Zhang et al., 2017). Then, an inversion process estimates reflectivity or impedance from seismic data (Zhang et al., 2017). From these premises, Calcite has a density value in logs of 2.71 g/cm3 and the density value for dolomite is 2.88 gr/cm3 (Gardner, 1980). We generated cross-plots to verify the response of lithological properties, such as density and porosity, to elastic properties, such as velocity and impedance, and its relationship with the dolomitic facies. For the impedance vs. porosity cross-plot, dolomite and dolomitized limestone are equal 10% porosity and P-impedance is, in general, below 0.08 [(m/s) gr/cm3)] (Figure 2-6 ). For density vs. velocity, the distinction is not so clear, only can be distinguished that the values for limestone are in a band between 2.5 and 2.75 g/cm3. On the basis of these relations, applying an inversion-seismic process could be a valid option to distribute the dolomized facies. The chosen method for inversion was a model-based inversion (Hampson and Russell, 1991).

For the PRESDM version of the seismic data, we converted this data set to the time domain to make comparisons to the inversion in time and preserve the wavelet properties. The first pass for seismic inversion is tying the seismic to the wells with a cross-correlation. This tie was performed trying different wavelets extracted from the wells. These parameters for the wavelet were varied until finding the optimal wavelet for the tie (Figure 2-7 ). The second step was building a background model on the basis of the tied wells and the top and base of the reservoir. Low wavenumbers were incorporated from the logs (Figure 2-8 ) and an initial strata model was generated (Figure 2-9 ). The analysis before inversion indicates a correlation in the wells with the inversion between 75% to 96%. However, the error varies between 27% to 74% for PRESDM. For PRESTM the correlation values are from 89% to 99% and the error is from

15% to 44% (Figure 2-10 ). Then, the correlation is good but, the uncertainty is considerable for PRESDM, in another PRESTM case uncertainty is lower.

According to Lin (2016) found that PRESDM corrects many of the “fault whisper” artifacts described by Hatchell (2000), resulting in a single coherence anomaly without a fault whisper coherence artifact. This phenomenon generates transmission distortions related to changes in velocity over the trajectory of the faults. Because dolomitization could be related to faults in the area, we generated four geometric attributes, chaos, total energy, maximum positive curvature (K1) and Sobel filter similarity. Therefore, from the paper of Lin (2016), we could expect a better response from geometric attributes in PRESDM than in PRESTM.

Additionally, we calculate two spectral attributes, peak frequency, and peak magnitude. These attributes were calculated both in PSDTM and PRESDM as well for comparison purposes.

We implemented two methods to filter and select the attributes to characterize dolomitization in the study area, cigar probe and well probe.

With cigar probe, we generated a 50 meter cylinder around the wells (Figure 2-11). These cigar-probes provide us with weighted values of all the generated attributes for every dolomitic facies around the well. In this way, we can select the attributes that have a better response to dolomitization changes for machine learning methods.

On the basis of the response of the attributes to the changes on lithology, three values were assigned to the different responses observed from the weighted averages, 1 for a remarkable response, 0.5 for mild response and 0 for a no visible response (Table 2-1).

From these selected attributes from the cigar-probe process, we generated well-probes of rendered attributes in pairs (Figure 2-12 ). On the basis of these well-probes cross-plots were

built to identify the attributes that better separates limestone from dolomite. The attributes selected in this method were used as inputs for a machine learning process.

In this research three methods were implemented and compared to generate dolomitization trends, supervised artificial neural network (ANN), weighted linear combination (WLC), and generative topographic maps (GTM). Below is description of these methods.

A neural network is a group of interconnected processing elements (West, et al., 2002; Lima et al., 2018). The advantage of the neural nets is in the process to learn or modify the weight between the connections to produce the desired result (West, et al., 2002). The connectivity of the neural net modifies an input vector of attributes and passes the modified values to the next layer of the network (West, et al., 2002). Once sufficiently trained to match on a calibrated objective set of data the neural network can be applied to the rest of the data to classify (West, et al., 2002). In the case of this study, the learning data were the dolomitic facies defined in the wells.

a)

| | Spectral Attributes | | Geometric Attributes | | | | Seismic Inversion | |
|---|---|---|---|---|---|---|---|---|
| Well | Peak Freq | Peak Mag | Chaos | Total Energy | Maximum positive Curvature | Sobel Filter | P-Impedance | Amplitude |
| A-1 | 0.5 | 1 | 1 | 0.5 | 0 | 1 | 1 | 0.5 |
| B-1 | 0 | 0 | 0 | 1 | 1 | 0 | 0 | 1 |
| C-DL1 | 1 | 1 | 1 | 0.5 | 1 | 1 | 1 | 1 |
| Total | 1.5 | 2 | 2 | 2 | 2 | 2 | 2 | 2.5 |

b)

| | Spectral Attributes | | Geometric Attributes | | | | Seismic Inversion | |
|---|---|---|---|---|---|---|---|---|
| Well | Peak Freq | Peak Mag | Chaos | Total Energy | Maximum positive Curvature | Sobel Filter | P-Impedance | Amplitude |
| A-1 | 1 | 1 | 1 | 0.5 | 1 | 1 | 1 | 1 |
| B-1 | 0.5 | 0.5 | 0.5 | 0.5 | 0.5 | 0 | 1 | 1 |
| C-DL1 | 1 | 1 | 1 | 1 | 1 | 1 | 1 | 1 |
| Total | 2.5 | 2.5 | 2.5 | 2 | 2.5 | 2 | 3 | 3 |

**Table 2-1.** Three values were assigned to the different responses observed from the weighted averages, 1 for a remarkable response, 0.5 for mild response and 0 for no visible response. a) In this table, the results for PRESDM are presented. b) The attributes from PRESTM showed a better response to the lithological changes. Amplitude, total energy, and P-impedance were selected for machine learning processes.

WLC is based on the concept of a weighted average in which continuous criteria are standardized to a common numeric range, and then combined by means of a weighted average (Drobne and Lisec, 2009). In this case, the numeric range represents the dolomite percentage

based on the information from the wells. The data combined were the selected attributes sampled to the geo-cellular model. The weights were assigned from the correlation with the dolomitization related to the PEF log. Then the weights were adjusted until the result was closest possible to the stated premises.

GTM is a probabilistic process that reduces non-linearly multidimensional data vectors to a reduced representation. This reduced representation is projected on a latent lower dimension space (Bishop et al., 1998). GTM is a process where a constrained mixture of Gaussians is modeled by parameters determined by a maximum likelihood by an expectation algorithm (EM). The first step is defining a set of points $\{x_i\}$ over a latent space with a set of basis functions $\{\phi_j(x)\}$. Then, the constrained mixture of Gaussians is defined by the adaptive parameters **W** and $\beta$, where centers are given by $\mathbf{W}\phi(x_i)$ and a covariance matrix is given by $\beta^{-1}\mathbf{I}$. After initializing **W** and $\beta$ posterior probability is calculated and evaluated. From the result of posterior probability **W** and $\beta$ are updated. An evaluation function of the likelihood is used at the end of each cycle until reaching the convergence.

For our research we considerate our latent space bi-dimensional. Then the mean of the posterior probability vector is projected onto the latent space in two-axis, axis-1, and axis-2 projections. We can combine these two projections using WLC, making this process supervised by the PEF log used as an index of dolomitization.

In this way we feed GTM algorithm with the attributes selected by cigar-probe and well-probe and the resulting projections in the bidimensional space were combined in a supervised way with WLC and we made tries for PRESDM and PRESTM as well. The summarized workflow is illustrated in Figure 2-13. .

# Results

To evaluate the efficacy of the machine learning process applied to PRESDM and PRESTM attributes, we established some constraints based on the geological knowledge described in the geologic settings part (Figure 2-14. ). The constraints are,

- Ku-3 and Ku-2 units are dolomitized in all the wells.
- Ku-1 unit is not dolomized only in the area of well C-DL1
- Km unit is always dolomitized.
- Ki unit is never dolomitized.

Based on these constraints, the machine learning process that can be achieved them will be suitable to characterize dolomitization in this reservoir.

Besides these constraints, we left out of all the processes the B-DL1 well blind-test. This well B-DL1 is almost all dolomite, excepting a body of 20 m (65 ft) of limestone in the lower part of the well, dolomite is at the bottom of the well is again. Variations in the well are good indicators about of the efficiency of the machine learning process of classifying dolomitization.

The result for ANN in PRESDM attributes was very poor (Figure 2-15. ). The result covered some of the premises, such as Ku-3 and Ku-2 zones dolomized. K-1 unit is dolomized also, but the limestone body of C-DL1 it wasn’t identified. There are more limestone and

dolomitic limestone in the Ki zone than in the PRESTM version. The result of the blind-test well was not satisfactory, ANN showed almost, all the zone as dolomized.

The result of ANN in PRESTM, ANN did not classify well (Figure 2-16. ). It shows dolomitization in some parts of the Ki zone such as in the syncline between A-1 and B-1 and in the C-1 zone. For the C-DL1 zone, there is no dolomitization in many areas of the Ku units. For the blind-test well, ANN works relatively well. ANN was capable of identifying dolomitization zones and the thin limestone zone in the lower part of the well, becomes dolomite again in the bottom of the well.

For the WLC process in PRESDM, are covered almost all the constraints (Figure 2-17 ). Except for the syncline between well A-1 and well B-1 where the upper part of the Ki zone is dolomitized. For the C-DL1 zone, the limestone in the third unit was identified, but with sections mostly dolomized. For the test-well, all the zone was dolomized, but the limestone in the lower part was not identified.

WLC in PRESTM covered all the constraints (Figure 2-18.). Units Ku-3 and Ku-2 are always dolomized, the Ku-1 unit is not dolomized in the C-DL1 well area and Ki unit is never dolomized, except in the syncline between field B and field C. We assigned the weights for WLC through try and error until we found the combination of weights that best fit the geology of the area. The response in the blind-test well was good as well. WLC covered the constraints and was able to identify the limestone body in the lower part of the well.

For GTM, we applied WLC over the axis projections from GMT (Figure 2-19. ). The only goal that was not completely accomplished was the limestone in the unit Ku-1. For the

blind-test well zone, the transition between the dolomite from Km and, limestone from Ki was well delimited. But it was not able to identify the limestone in the lower part of the well.

For GTM combined with WLC in PRESTM, we obtained an acceptable result, where almost all the constraints were achieved (Figure 2-20. ). The only zone where dolomite that was not completely identified was zone Ku-1, wherein the well C-DL1 is not completely limestone. The area of the blind-test well is not bad, but the limestone in the lower part of the well was not identified.

## Conclusions

In the southeast Gulf of Mexico, the best carbonate reservoirs are dolomitic, occur in structural highs, and exhibit four-way closure. Because the cost of reverse-time PreSDM increases as the fourth power of the maximum frequency imaged, the PreSDM images exhibit lower vertical resolution than the corresponding PreSTM images. However, the PreSDM migration images are far superior in imaging faults, suppressing fault shadow and velocity pull up artifacts, and in mapping reflector configurations, even in the easier-to-image Tertiary section. For these same reasons geometric attribute images such as coherence and curvature computed from the PreSDM volumes are sharper and less ambiguous than those generated from the corresponding PreSTM volumes.

By design, all six wells in the survey targeted broad structural highs, away from the complications of faulting and inaccurate imaging. In these zones, the higher frequency PreSTM images exhibit not only more seismic events and a statistically better well tie.  Using one well as

a blind test, we evaluated alternative combination of attributes and unsupervised and supervised machine learning techniques to predict the dolomitic facies of interest. For this reservoir, the lower resolution PreSDM attributes were not able to predict the relatively thin dolomitic zone in the blind test well. In contrast, the higher frequency PreSTM attributes (P-wave impedance, peak-spectral magnitude, and positive curvature) provided good predictions. For unsupervised learning, generative topographic mapping provided better clustering than k-means, identifying three major facies. For supervised learning, the weighted linear correlation method provided results superior to artificial neural network in predicting the dolomitic facies in the blind test well.

In summary, when imaging complex structure similar to that of the southeastern Gulf of Mexico, prestack depth migration provides images with sharper discontinuities, reduced velocity artifacts, and reduced migration noise than prestack time migration. Good structural imaging does not guarantee good amplitude preservation. Either because of less accurate amplitude preservation, or in our opinion, because of the lower spectral content of the PreSDM volume, we obtained better well ties and better lithologic predictions using the PreSTM volume.

# Chapter 2 Figures

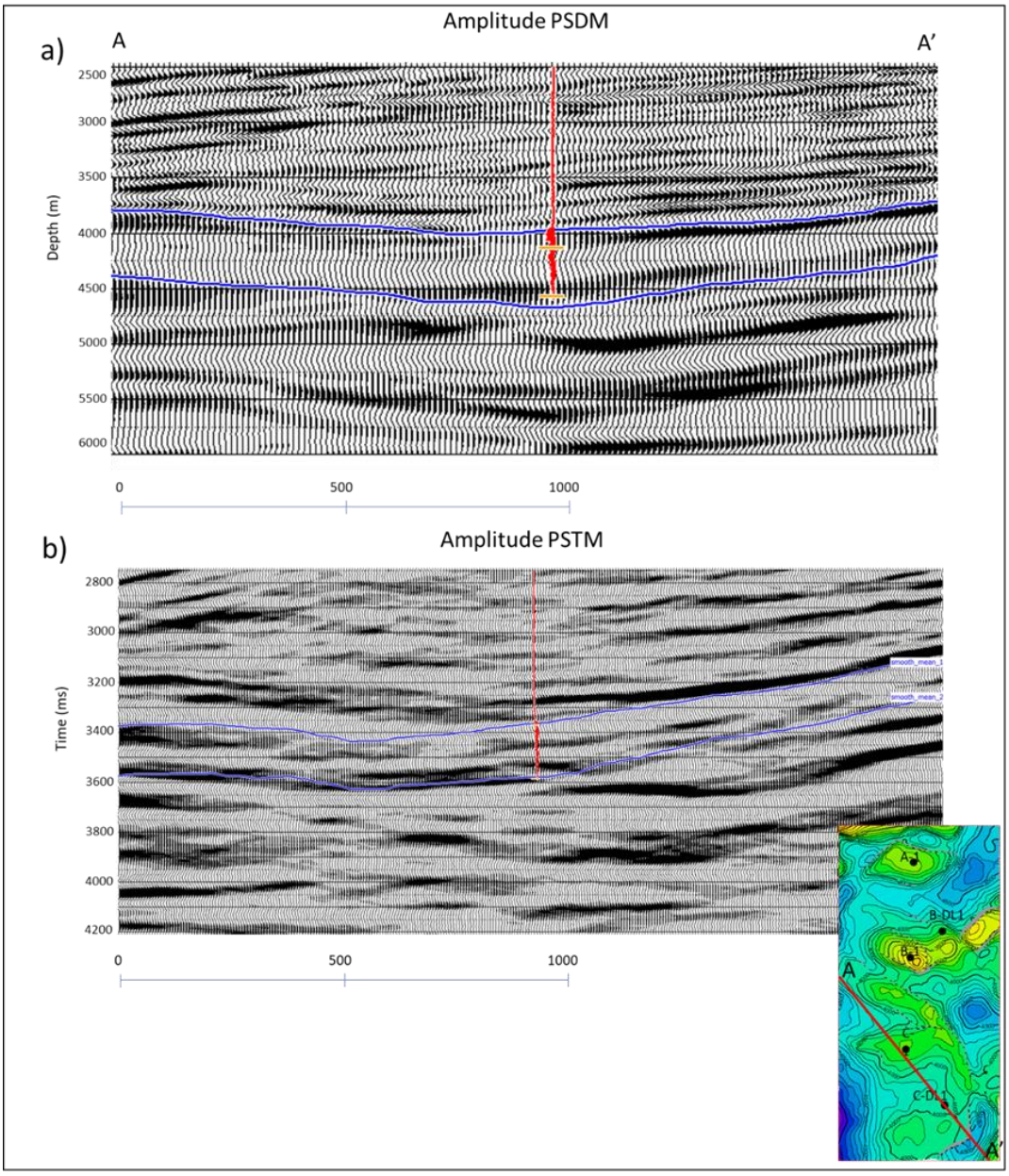


**Figure 2-1.** For this work, we have a wide-azimuth seismic survey that has been imaged using (a) a prestack depth- and (b) prestack time-migrated (PRESDM, PRESTM.) Before conversion to depth, the time-migrated volume appears to dip to the left northwest different structure for the reservoir delineated by the blue horizon picks. Note that there are more reflection events within the target zone for the PreSTM data volume. The lower frequency resolution is due to the cost of the algorithm used, rather than to the algorithm itself, where it is common to control the cost of imaging by reducing the value of the highest frequency used.is unlike also. Therefore, it is possible to identify more events in the same interval in PSTM, than PSDM version.

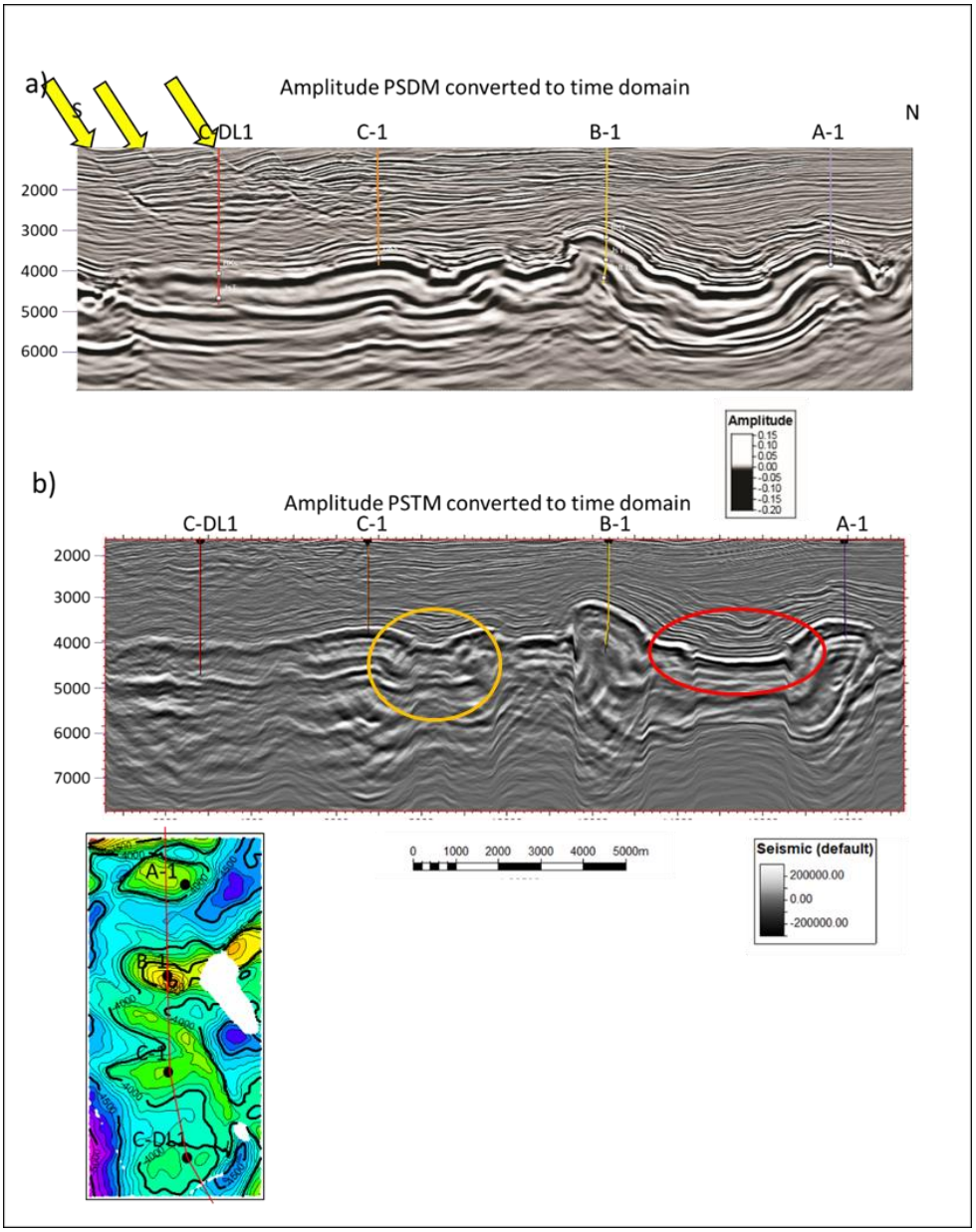


**Figure 2-2.** A vertical line connecting the four wells in the study zone through the (a) prestack depth- and (b) prestack time-migrated data volumes showing the structural complexity of the area. Yellows arrows indicate steeply dipping fault-plane reflectors that are imaged by PreSDM but not by PreSTM. The reverse fault beneath well B-1 is also better imaged by PreSDM. The fault block indicated by the orange ellipse is more tightly focused by PreSDM with the deeper reflectors appearing planar and of near constant amplitude. The fault block indicated by the red ellipse is considerably wider in the PreSTM image where velocity pull-up makes the fault look vertical where PreSDM shows it to be a reverse fault dipping towards the south. Although the structural imaging of PreSDM is superior to that of PreSTM, the PreSTM used all the frequency content in the original unmigrated data and thus exhibits higher resolution within the red ellipse. Well locations shown on the inset.

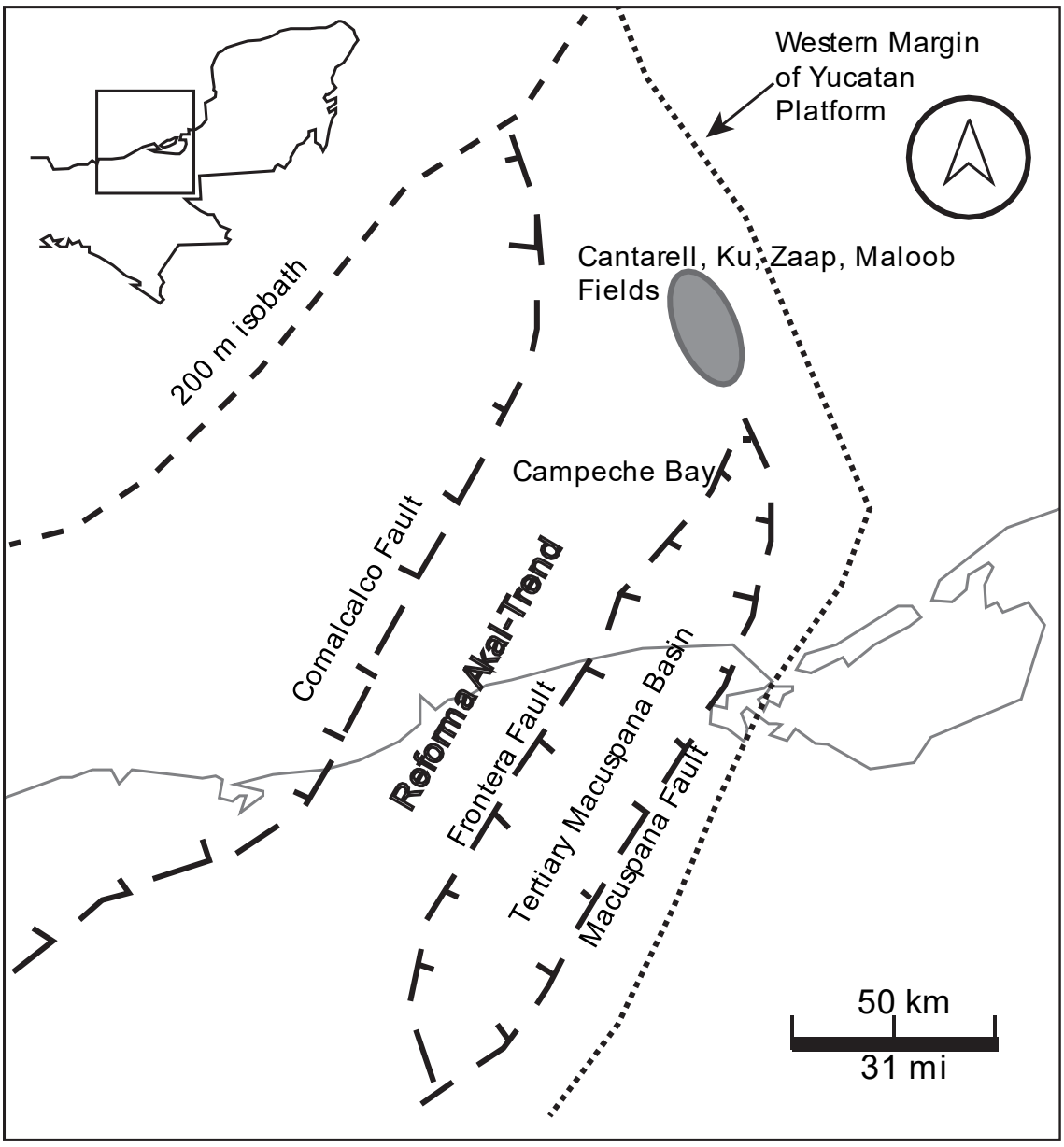


**Figure 2-3**. Location of the study area showing the main structural features. Study area shares the depositional, tectonic and diagenetic history with the Cantarell, Ku, Maloob, and, Zaap oil fields. (after Murillo-Muñeton et al., 2002).

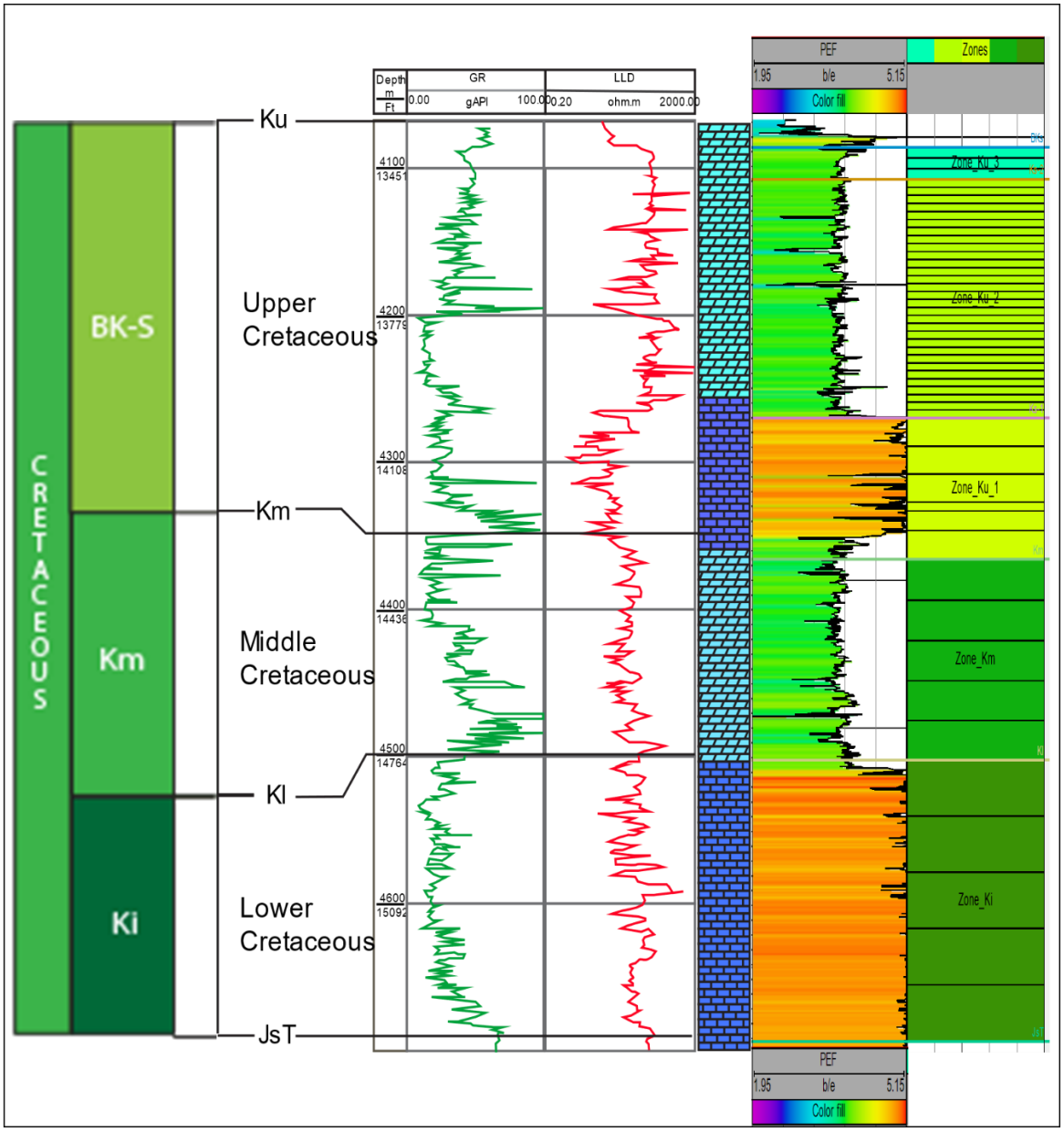


**Figure 2-4.** Type-column for the study area and corresponding well-log response showing the reservoir rock ranging from Lower Cretaceous to Upper Cretaceous. The dolomites generally exhibit better porosity and permeability than the limestones. Generally, more intense dolomitization occurs in the breccias of the Upper Cretaceous upper zone. The last track shows the zones and layers used to construct the cellular model. (After Angeles-Aquino et al., 2006).

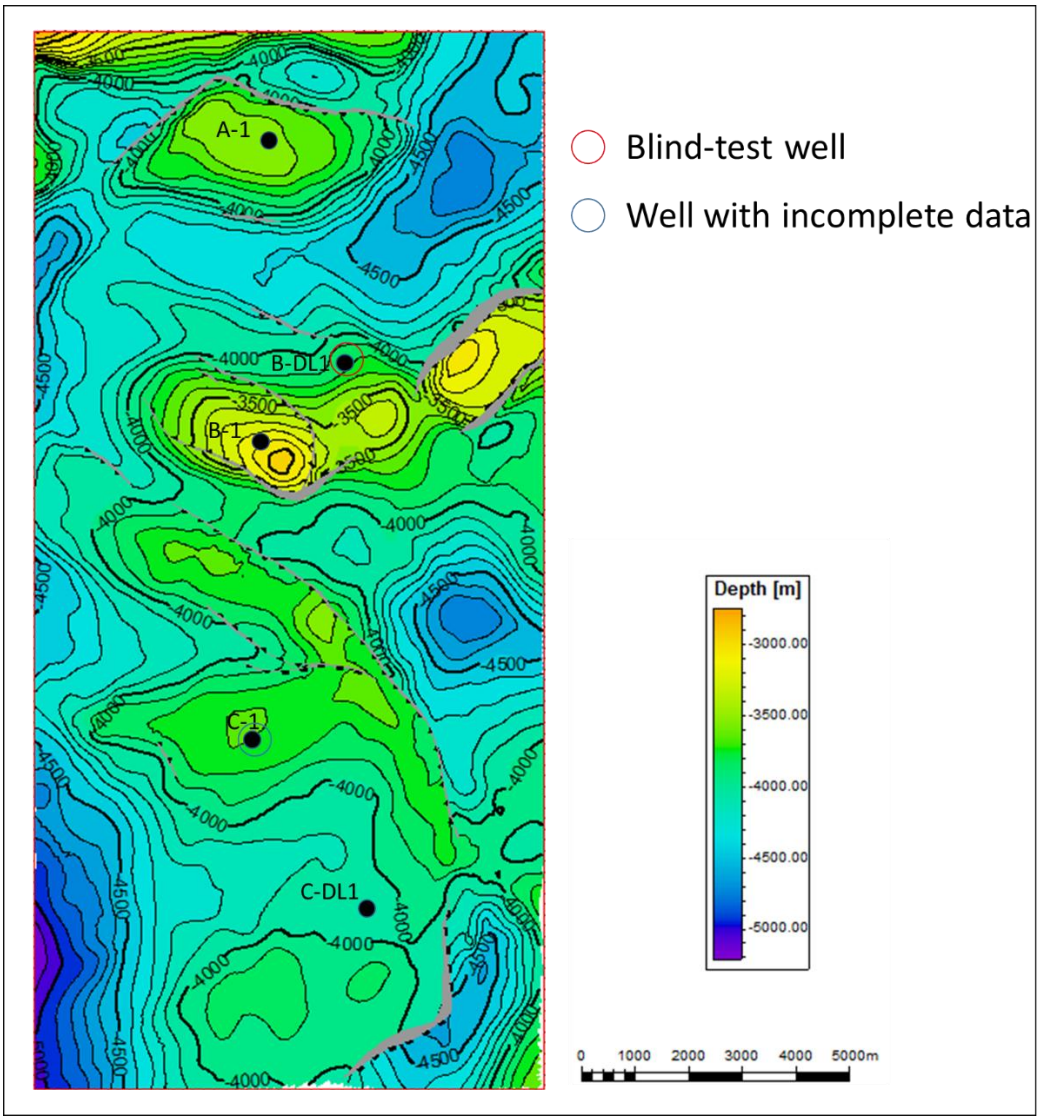


**Figure 2-5.** Map of the top of the reservoir. The study area is composed of three fields, named from North to South as A, B, and C. Field A was discovered by well A-1. Field B has two wells, with well B-1 the discovery well and well B-DL1 an appraisal well. This latter well will be used as a blind test well. Field C has two wells: C-1 was the discovery well but only drilled into the top 120 of the reservoir, while C-DL1 was an appraisal well.

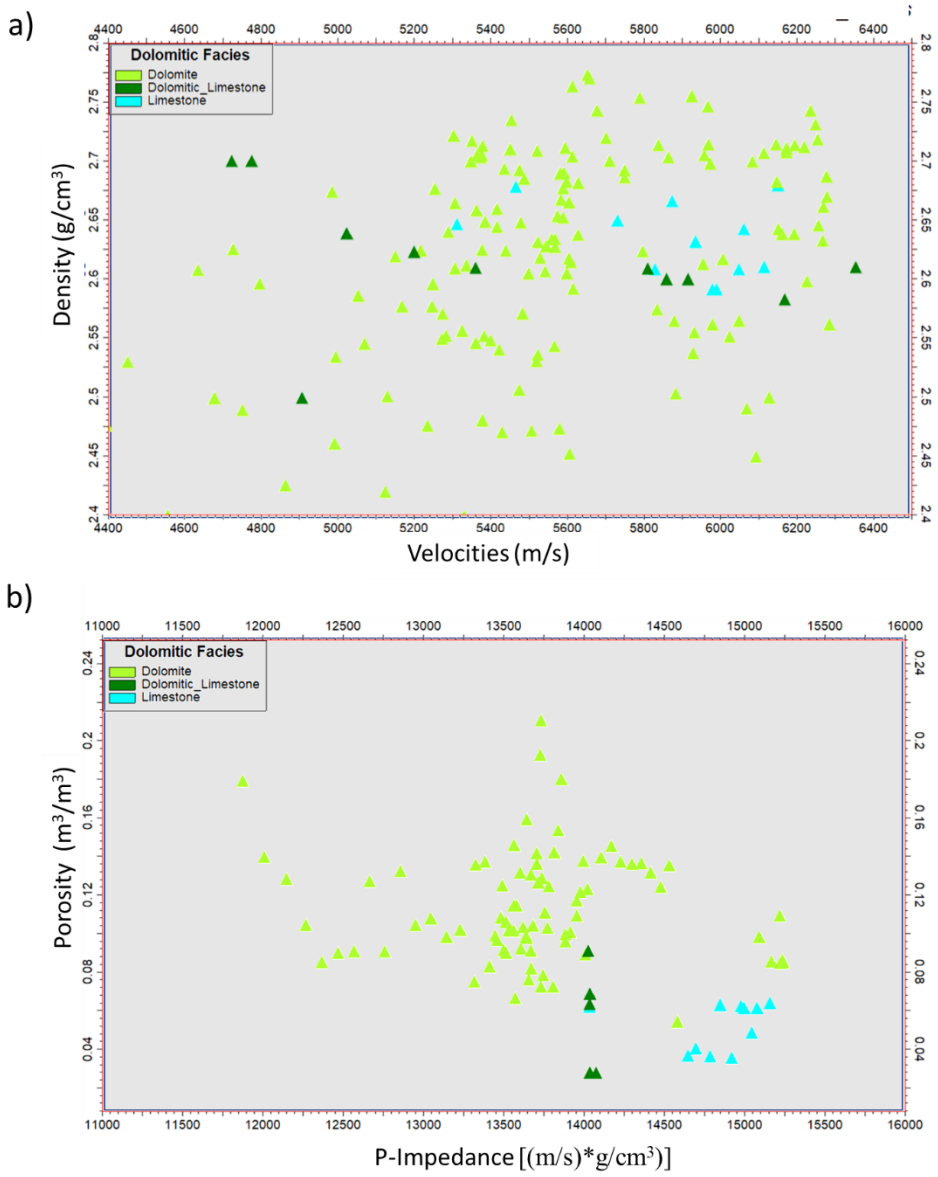


**Figure 2-6** a) Velocity vs. density cross-plot for the three facies, based on well-logs from the study area. Velocities are less sensitive to the facies than density, (b) where the dolomitic facies density mainly limited to the range from 2.6 to 2.72 (g/cm$^3$), where porosity increases and P-impedance.

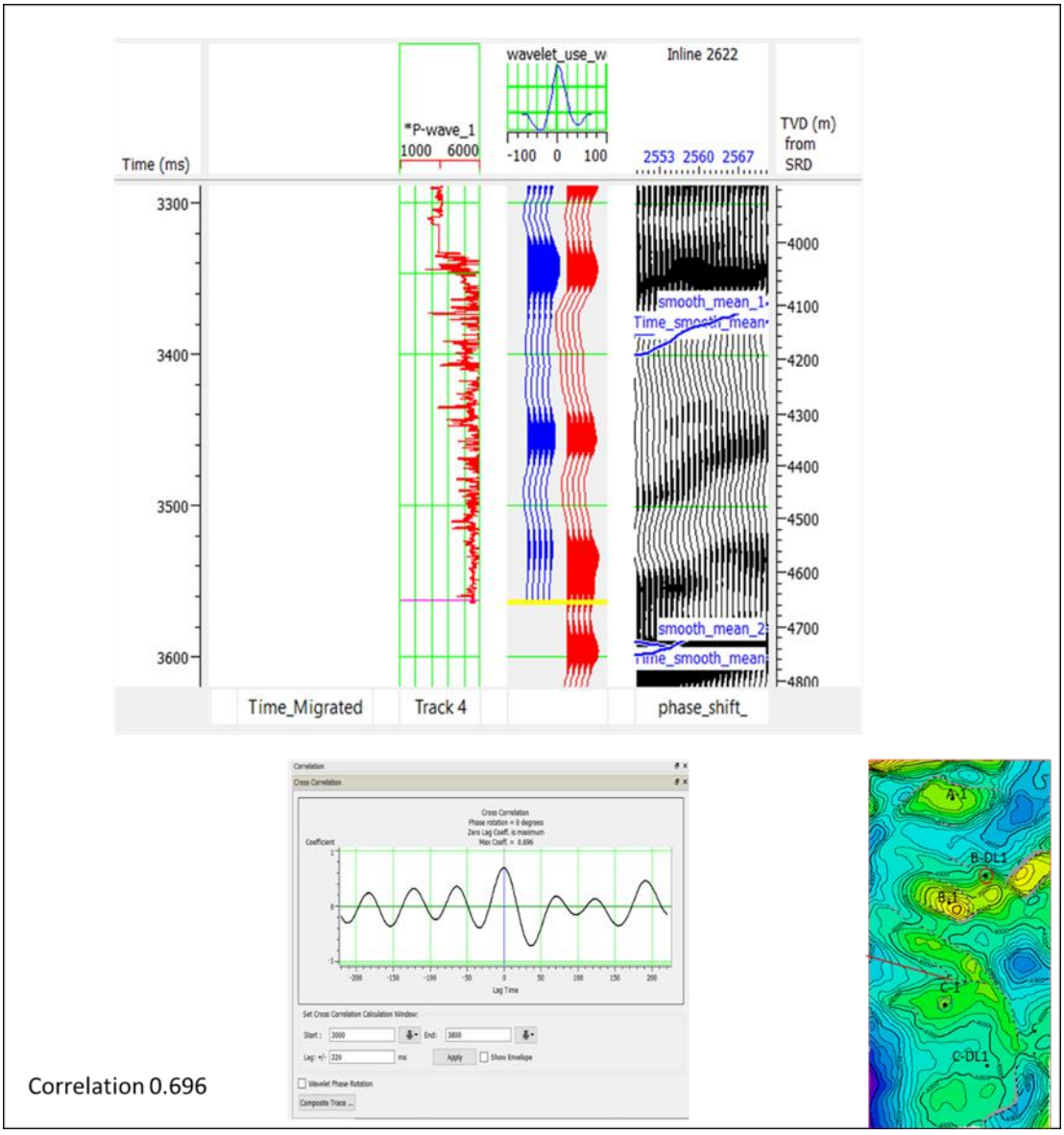


**Figure 2-7** Figure illustrating the well-seismic tie process for well C-DL1. The correlation values for the wells, in general, were around 0.6. Because changes in velocity result in variable seismic wavelet in time, all the correlations were performed in the time domain by converting the PRESDM data resulting in a stationary wavelet.

a)

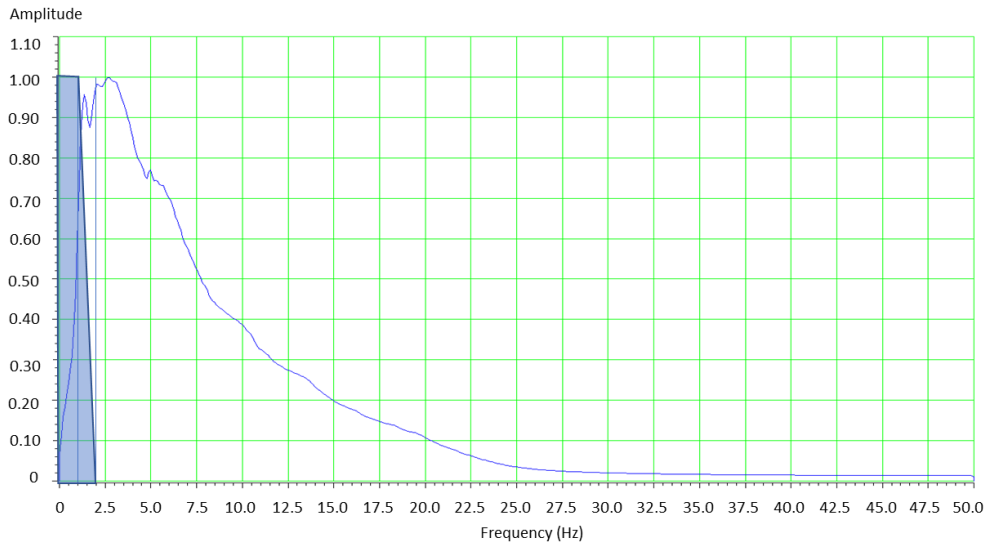


b)

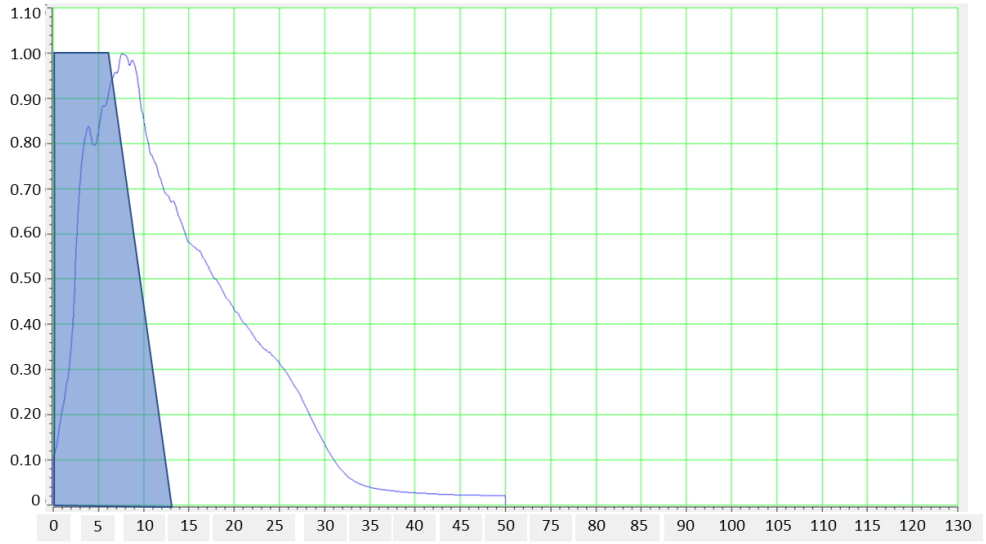


**Figure 2-8** (a) Figure illustrating the spectrum of low-frequency tomographic velocity model derived for PreSTM. Low-frequency values were incorporated from well-logs with a high cut filter rolling off between 1 to 2 cycles/km. (b) The same model for PreSDM converted to time. The corresponding high cut filter now rolls off between 4 to 14 Hz.

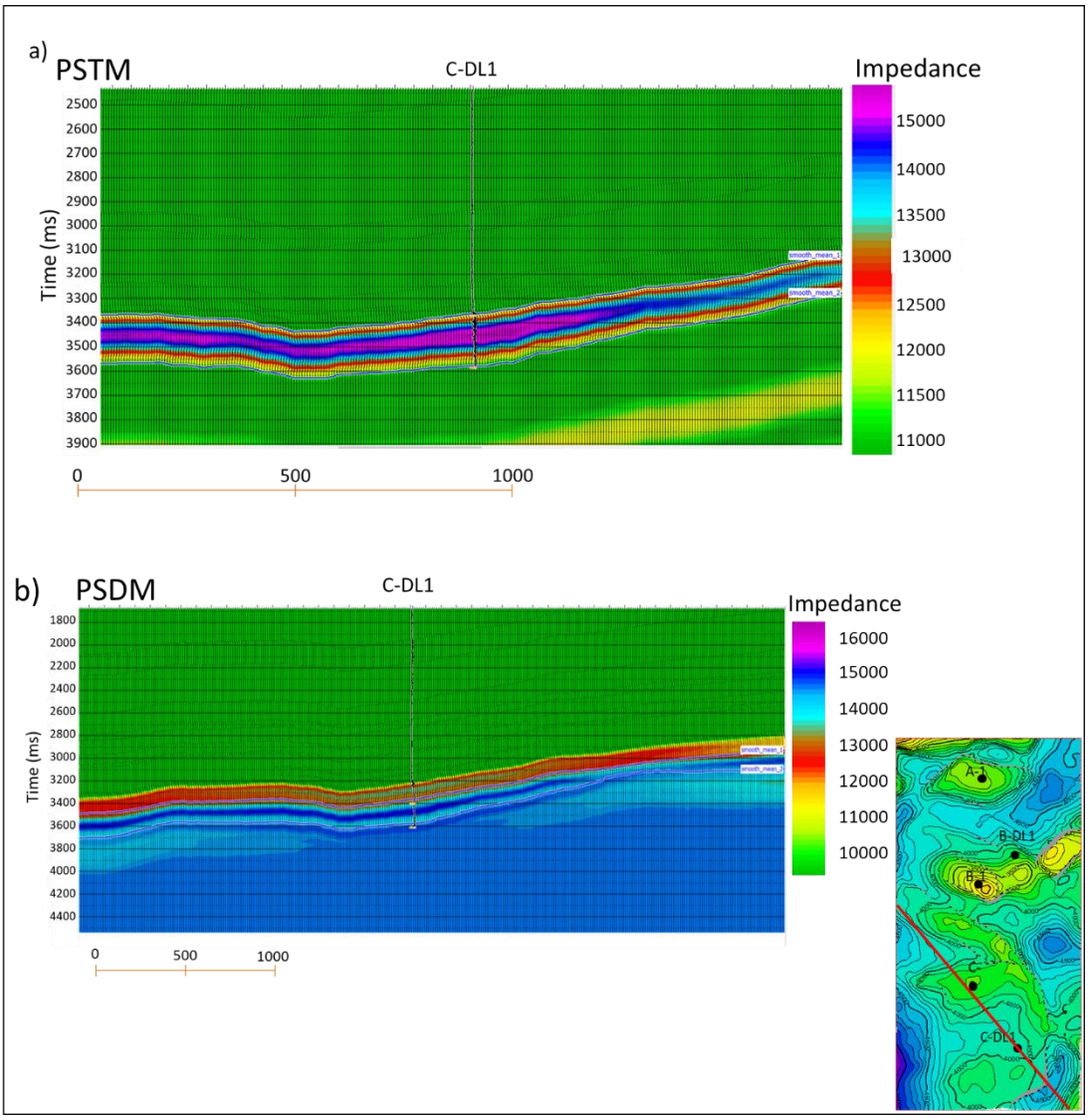


**Figure 2-9** (a) Vertical slice cutting well C-DL1 through of the low-frequency P-impedance background model. The strata model was focused to the reservoir zone limited for the horizons interpreted in the PRESTM version. Impedance values in the reservoir zone range from 12,500 to 15,000 (m/s)*g/cm$^3$). (b) The same model for PRESDM converted to time. Impedance values in the reservoir zone ranges from 14,000 to 15,000 (m/s)*g/cm$^3$).

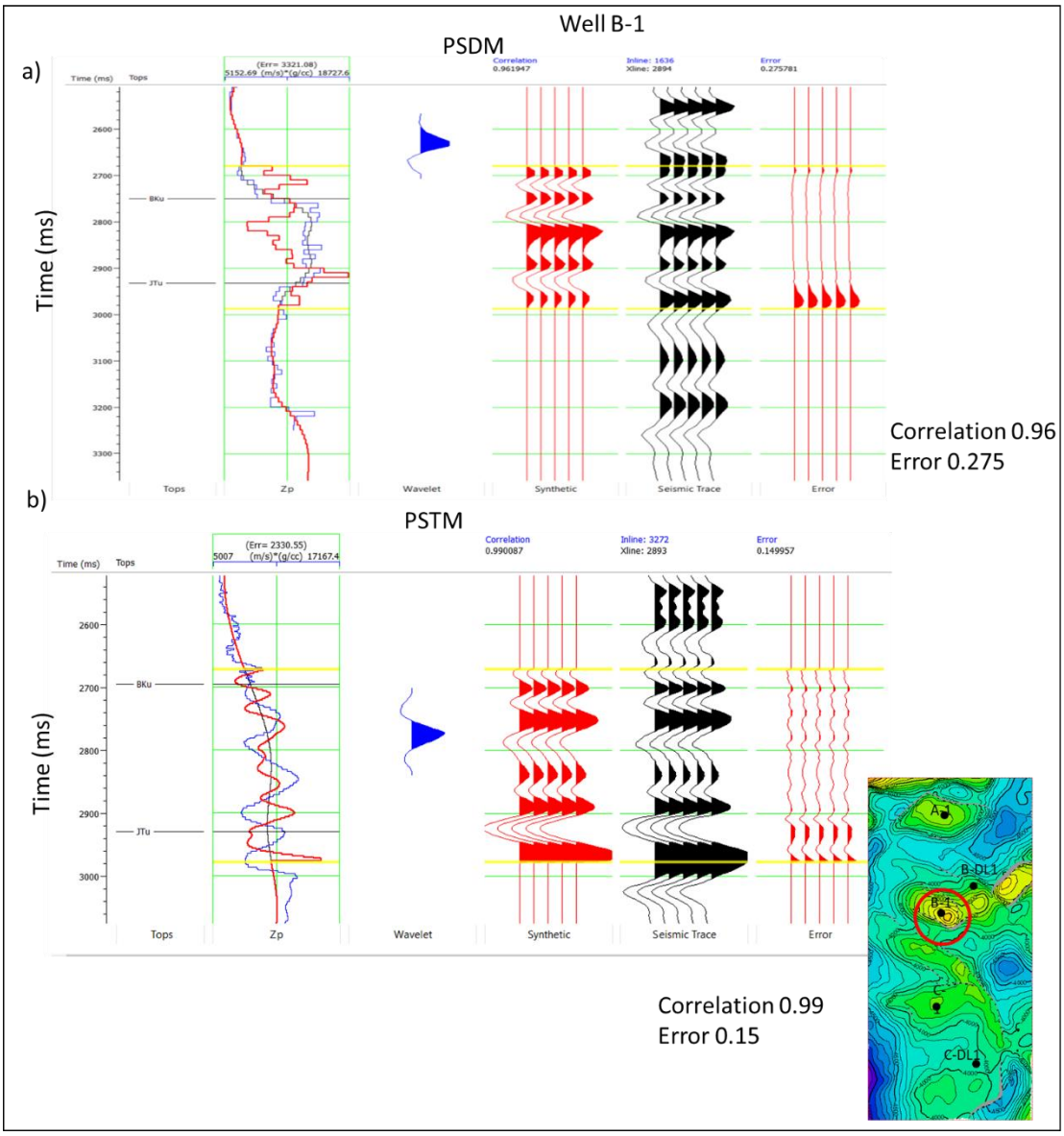


**Figure 2-10** (a) Results of the previous analysis to post-stack inversion for the B-1 well in PRESDM converted to time. The correlation for this model is 0.96 and the error is 0.275. (b) Previous analysis to post-stack inversion for PRESTM. Correlation is higher than PRESDM correlation, the error is lower.

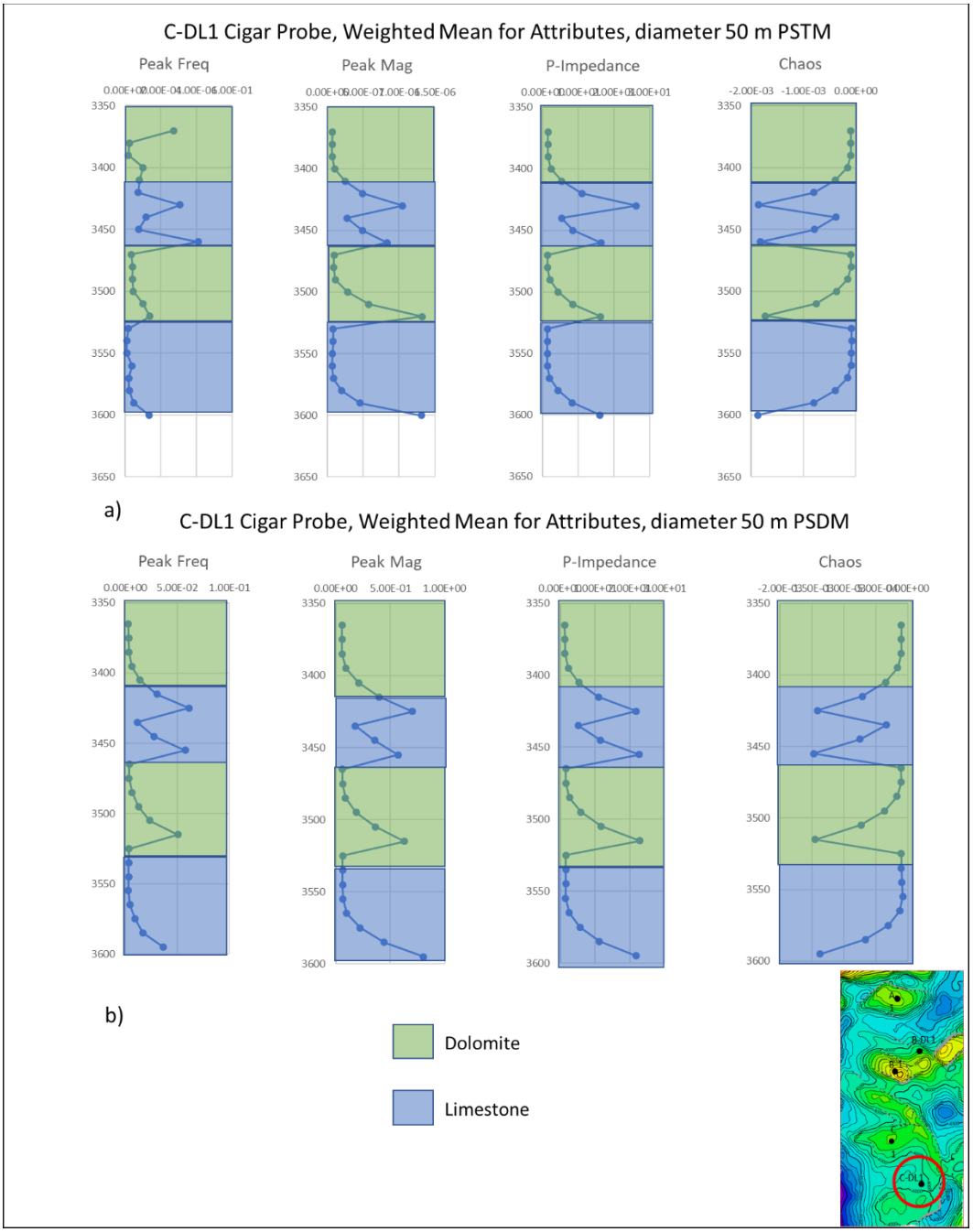


**Figure 2-11. .** Weighted mean from the attributes generated using cigar-probe in a neighborhood of 50 m around the well C-DL1 for PRESTM (a) and PRESDM (b). These probes were generated for the three wells and contrasted with the lithology to select the attributes with a better response to changes in lithology.

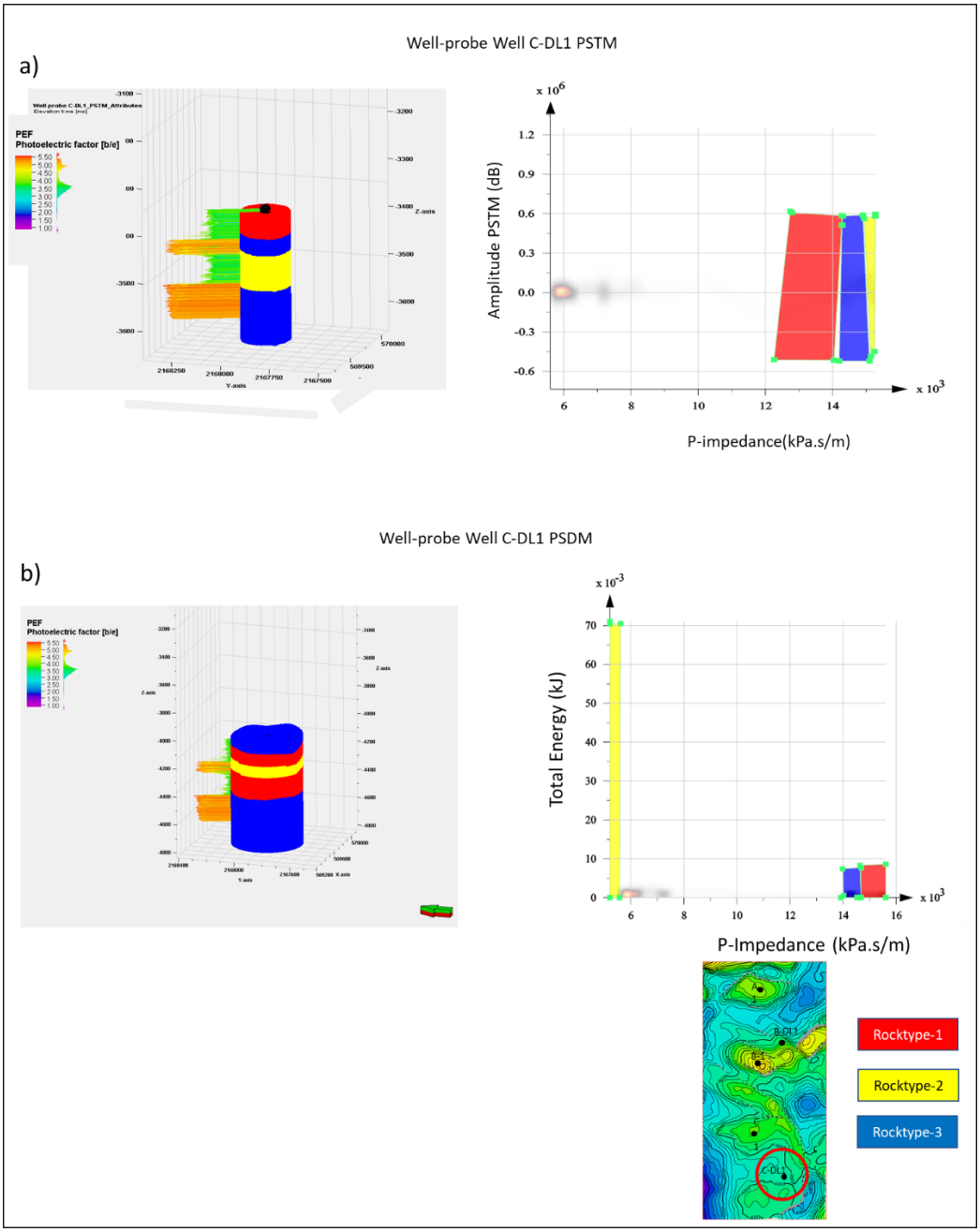


**Figure 2-12** Well-probes were generated in pairs of attributes and using cross-plots to verify the capability of the attributes to separate lithofacies. For PRESTM (a) some combination of attributes, such as illustrated, were able to distinguish between the upper dolomite in red, and the lower dolomite in yellow in the well C-DL1. For PRESDM (b) some combinations were able to separate limestone from dolomite.

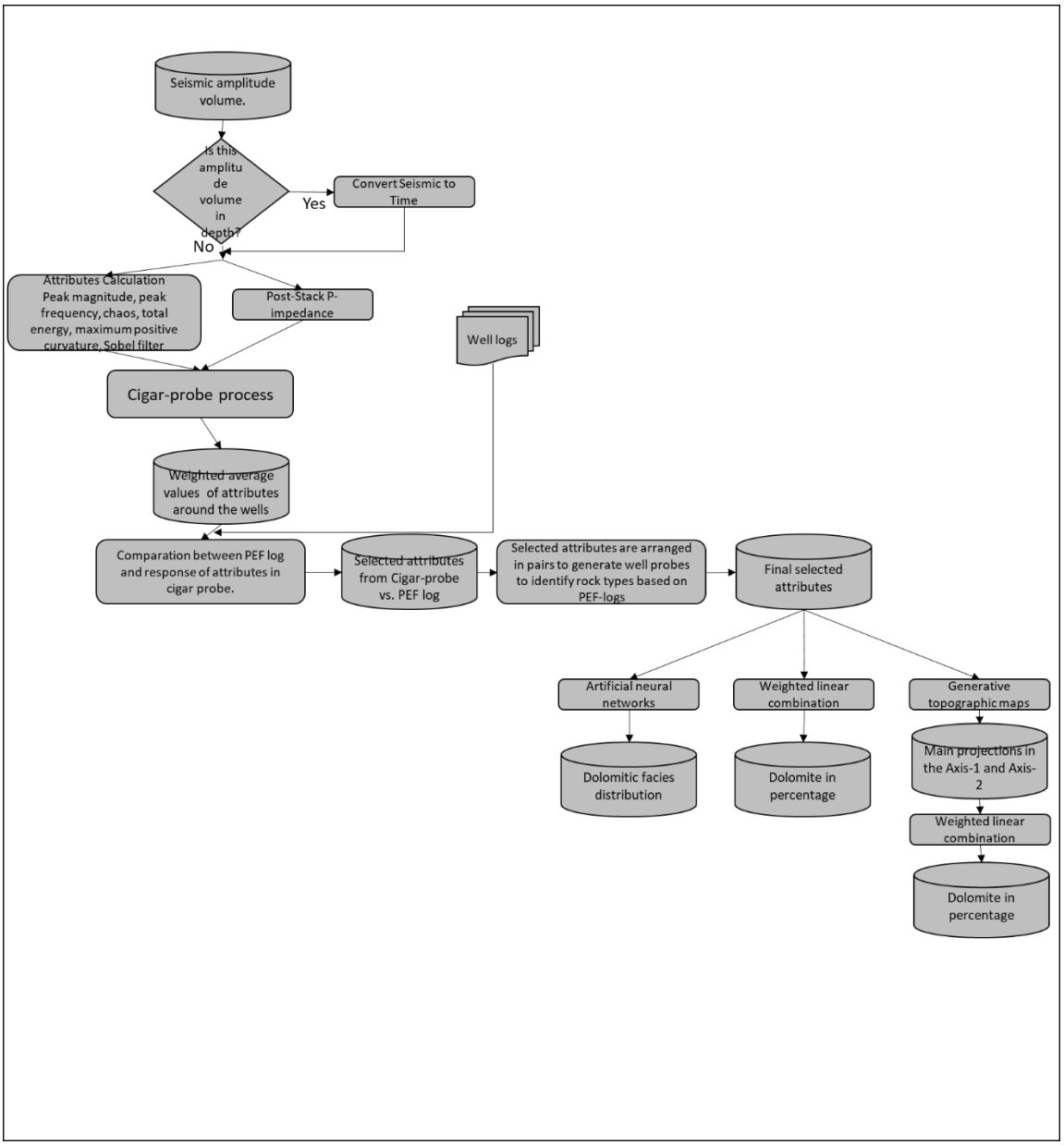


**Figure 2-13.** The flowchart illustrating the proposed workflow.

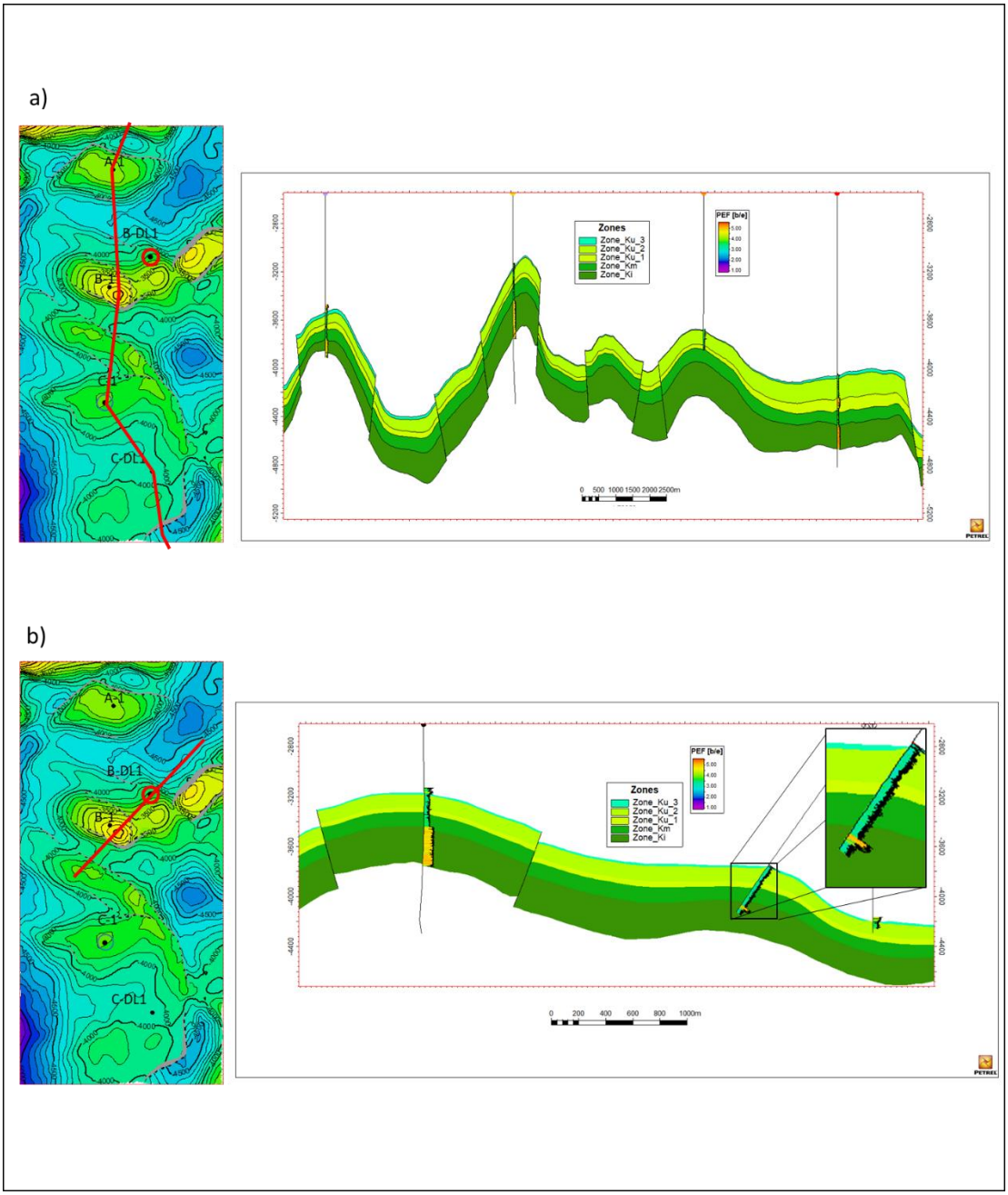


**Figure 2-14.** (a) Cross-section through the wells illustrating the zones in the model. According to the geological knowledge of the zone it is expected that Ki is limestone in all the model and in Ku-1 zone in the neighborhood of well also C-DL1. (b) The cross-section in the blind-test well B-DL1 shows the zones in the model. In the blind-test well there is a dolomitized zone in the Ki.

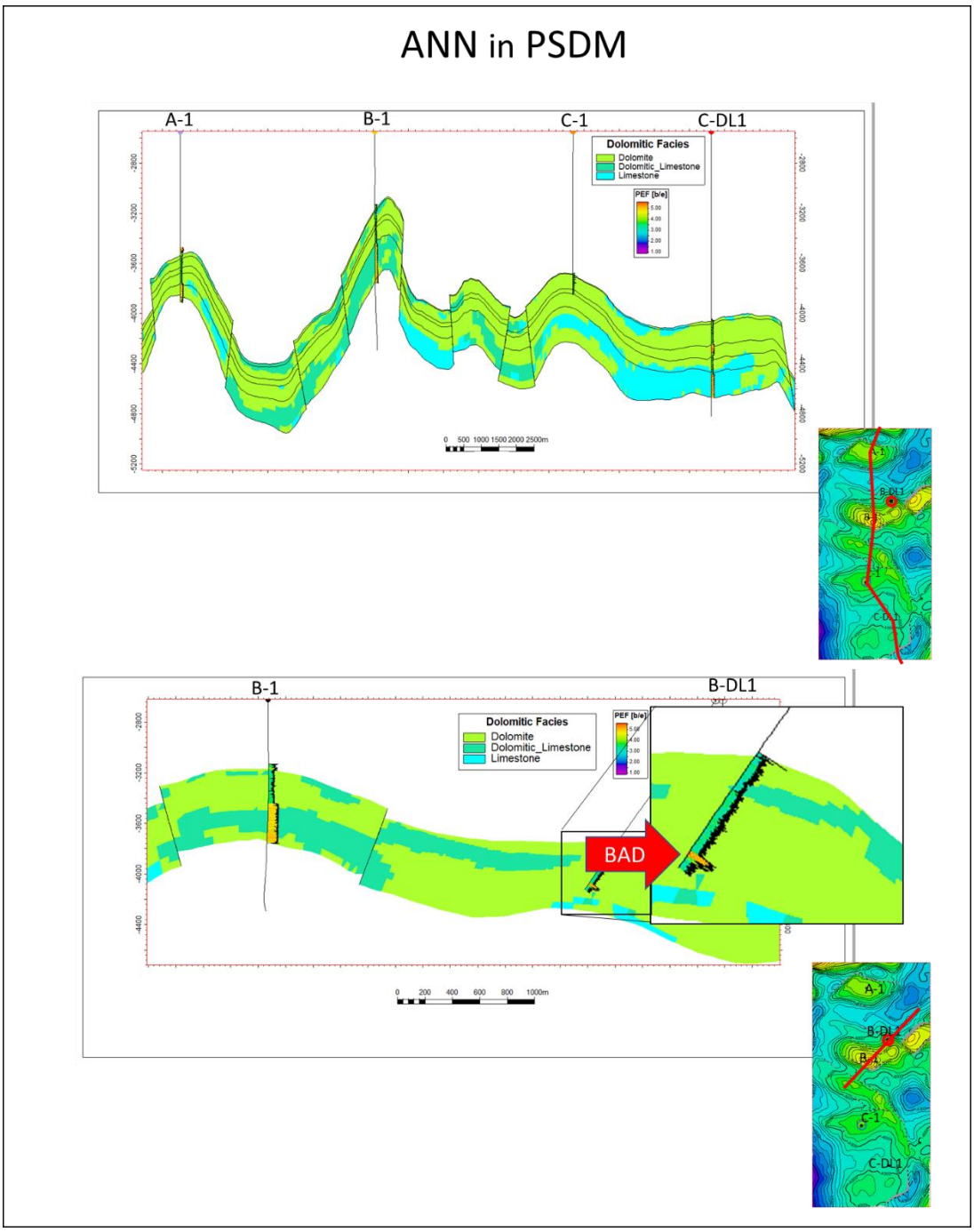


**Figure 2-15. .** Result for ANN process in the PRESDM attributes. (a) The result covered some of the constrains, such as Ku-3 and Ku-2 dolomized zones. K-1 unit is dolomized also, but the limestone body in the C-DL1 zone it was not identified. (b) The result of the blind-test well was not good. ANN showed almost as all the zone dolomized.

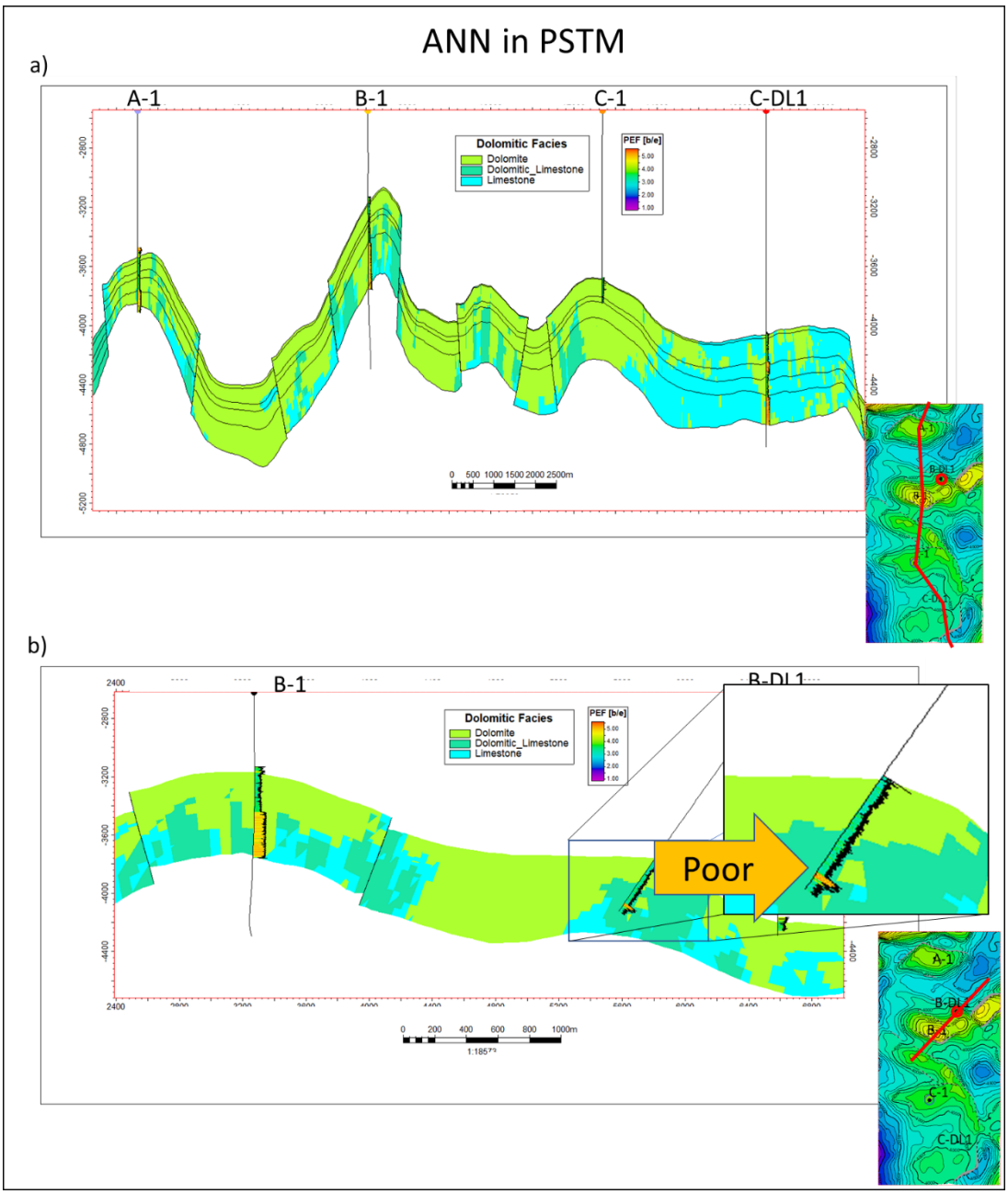


**Figure 2-16.** Result for ANN in PRESTM, ANN does not work well for classification. (a) The cross-section shows dolomitization in some parts of the Ki zone at the syncline between A-1 and B-1 and in the zone of C-1. For the blind-test well (b), ANN works relatively well and was capable of identify dolomitization zone and the thin limestone zone on the lower part of the well, that changes to dolomite again on the bottom of the well.

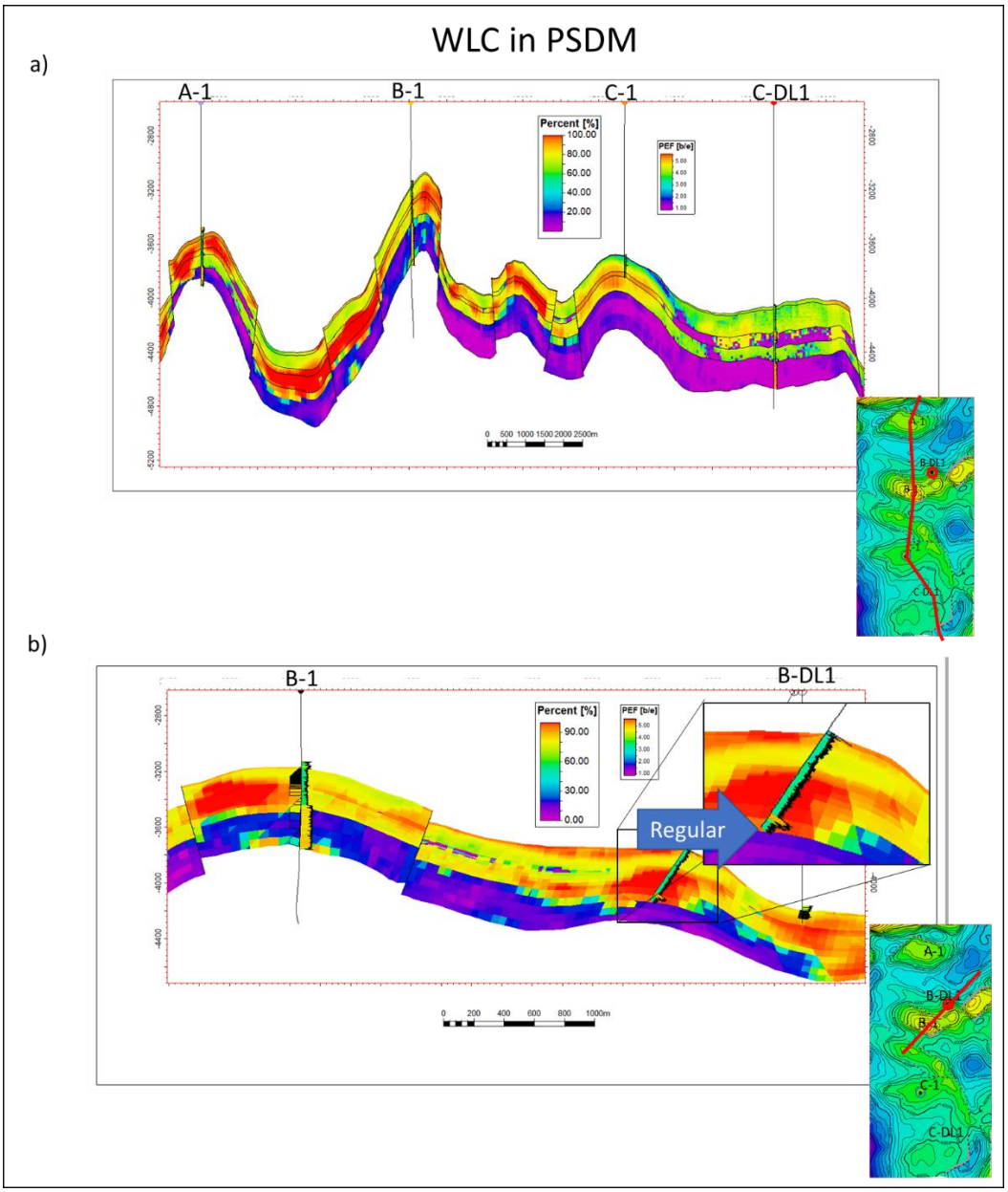


**Figure 2-17** Result for WLC process in the PRESDM attributes. For the WLC, PRESDM covered almost all the constraints. (a) For the B-DL1 zone, the limestone in the third unit was identified. (b) For the test-well all the nearby zones were dolomized. The limestone in the lower part was not identified, as the zone appears dolomitized.

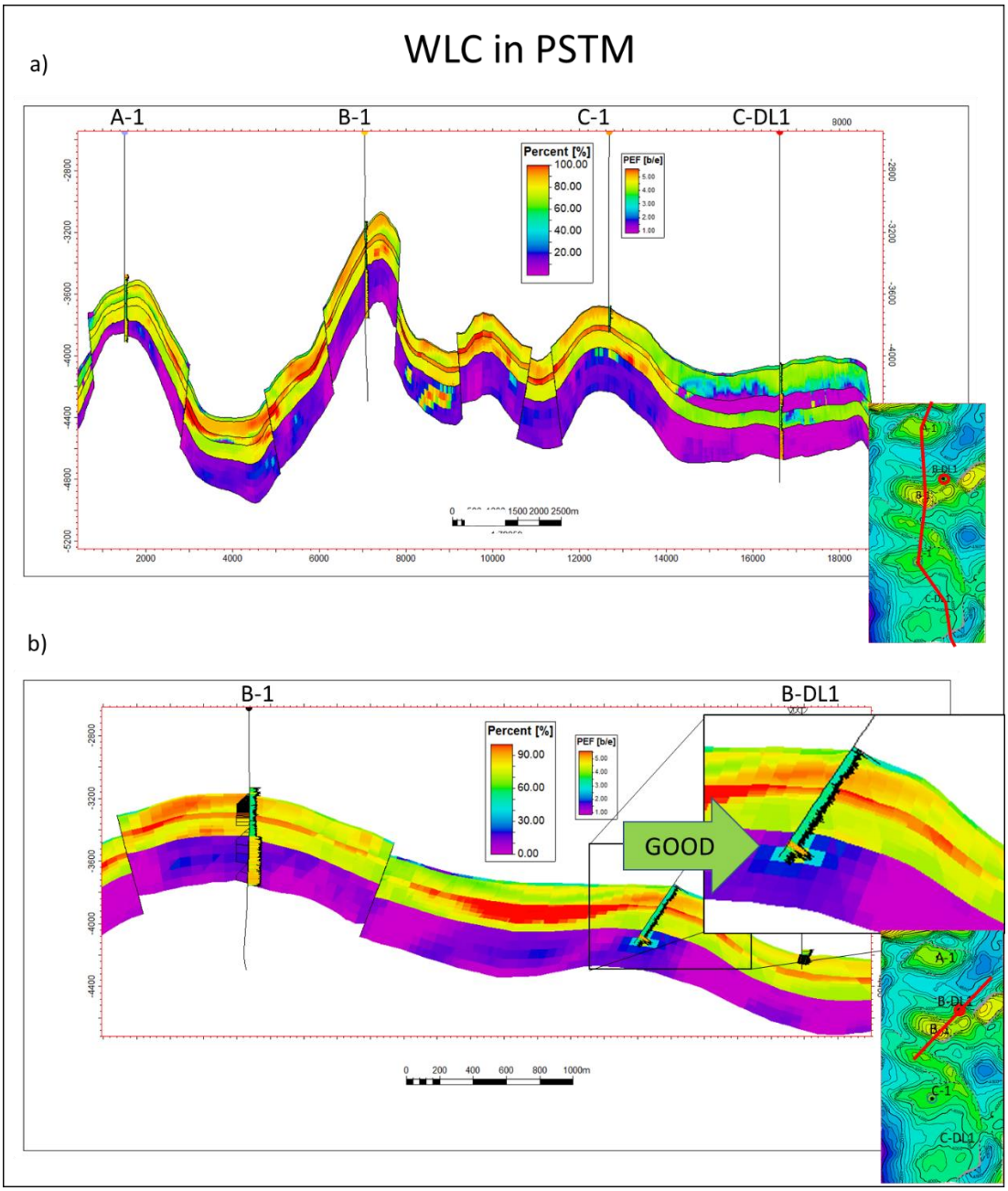


**Figure 2-18.** For WLC in PRESTM, the result is much better. WLC covered all the constraints. (a) Units Ku-3 and Ku-2 are always dolomized, the Ku-1 unit is not dolomized in the C-DL1 well area and, Ki unit is never dolomized, except in the syncline between field B and field C. (b) The response in the blind test well was good too. WLC covered the constraints and was able to identify the limestone body in the lower part of the well.

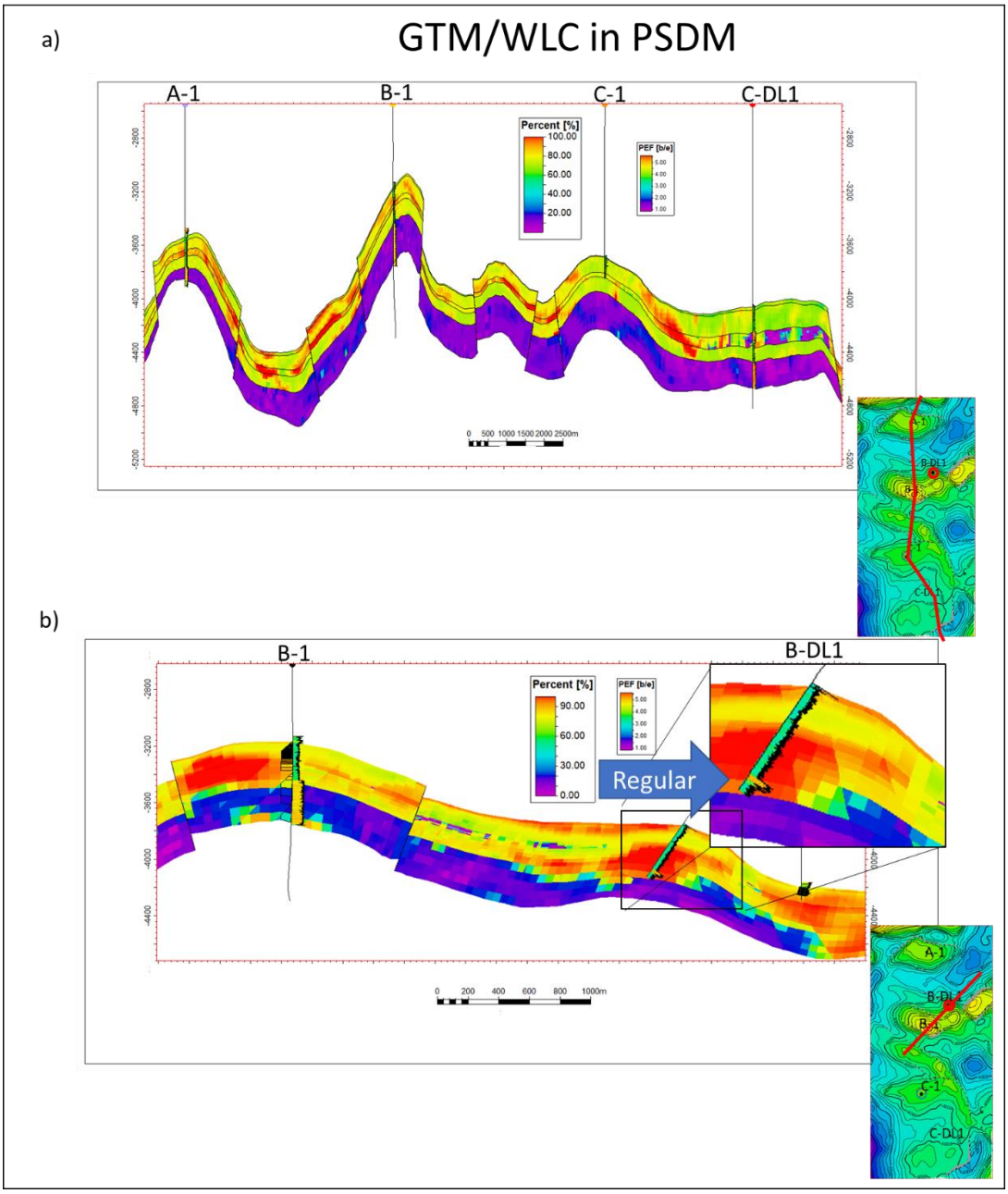


**Figure 2-19.** (a) For GMT/WLC the only constraint that is not completely accomplished was the limestone in the unit Ku-1. (b) For the test well zone, the transition between the dolomite from Km and, limestone from Ki was well delimited. But it was not able to identify the limestone in the lower part of the well.

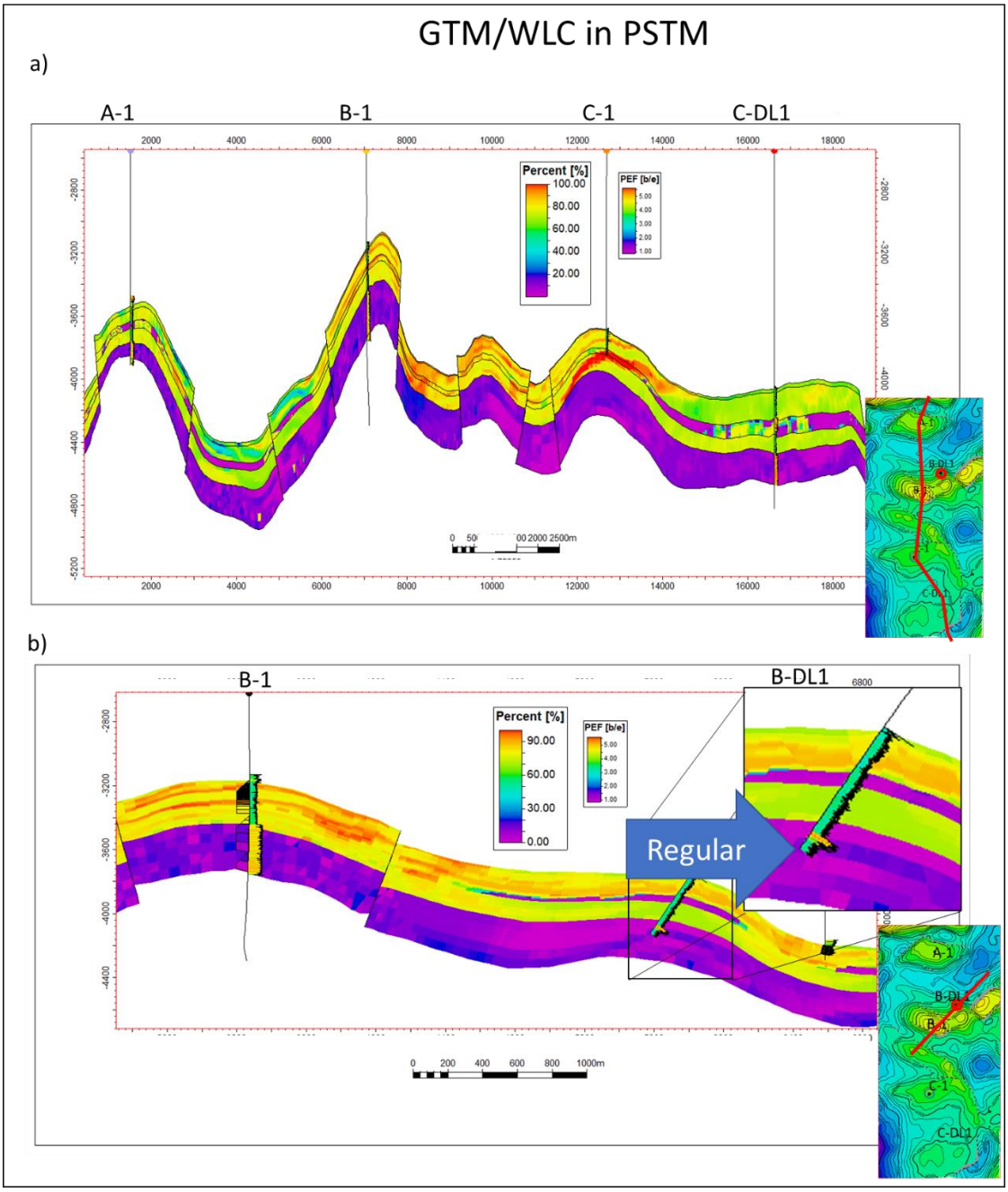


**Figure 2-20.** (a) For GTM/WLC, we obtained an acceptable result, where almost all the constraints were accomplished. The only zone with issues was zone Ku-1, wherein the C-DL1 well is not completely limestone. (b) For the area of the blind-test well it was not able to identify the limestone in the lower part of the well.

# References

Angeles-Aquino, F. J,. 2006, Monografia Petrolera De La Zona Marina. IN SPANISH. Monograph of the Marine Zone Oil. *Boletin de La Asociacion Mexicana de Geologos Petroleros*, 69.

Bishop, C. M., M. Svensén, and C. K. Williams, 1998, GTM: The Generative Topographic Mapping. Neural Computation, 10(1), 215-234.

Drobne, S., and A. Lisec, 2009, Multi-Attribute Decision Analysis in GIS: Weighted Linear Combination and Ordered Weighted Averaging. Informatica, 33, 459–74. https://doi.org/10.1017/CBO9781107415324.004.

Gardner, J.S. and J. L. Dumanoir, 1980, Litho-Density Log Interpretation: SPWLA Twenty-First Annual Logging Symposium. Society of Petrophysicists and Well-Log Analysists.

Khoshdel, H., and M. A. Riahi, 2011, Multi Attribute Transform and Neural Network in Porosity Estimation of an Offshore Oil Field - A Case Study. Journal of Petroleum Science and Engineering, 78 (3–4) 740–47. https://doi.org/10.1016/j.petrol.2011.08.016.

Kumar, R. B. Das, R. Chatterjee, and K. Sain, 2016, A Methodology of Porosity Estimation from Inversion of Post-Stack Seismic Data. Journal of Natural Gas Science and Engineering, 28, 356–64. https://doi.org/10.1016/j.jngse.2015.12.028.

Latimer, R. Buxton, R. Davidson, and P. van Riel, 2002, An Interpreter's Guide to Understanding and Working with Seismic-Derived Acoustic Impedance Data. The Leading Edge 19 (3): 242–56. https://doi.org/10.1190/1.1438580.

Lima, R. P., and K. J. Marfurt, 2018, Principal component analysis and K-means analysis of airborne gamma-ray spectrometry surveys: 88th Annual International Meeting of the Society of Exploration Geophysicists, Expanded Abstracts, 2277–2281, doi:10.1190/segam2018-2996506.1

Lodha, G.S. 1974, Quantitative Interpretation of Airborne Electromagnetic Response for a Spherical Model. M.S. thesis, University of Toronto.

Mitra, S. G. Correa Figueroa, J. Hernandez Garcia, and A. Murillo Alvarado, 2005, Three-Dimensional Structural Model of the Cantarell and Sihil Structures, Campeche Bay, Mexico. AAPG Bulletin 89 (1): 1–26. https://doi.org/10.1306/08310403108.

Mitra, S., J. A. Duran Gonzalez, J. Garcia Hernandez, S. Hernandez Garcia, and S. Banerjee, 2006, Structural Geometry and Evolution of the Ku, Zaap, and Maloob Structures, Campeche Bay, Mexico. AAPG Bulletin 90 (10): 1565–84. https://doi.org/10.1306/04240605101.

Murillo-Muñetón G., J. M. Grajales-Nishimura, E. Cedillo-Pardo, J. García-Hernández, and S. García-Hernández, 2002, Stratigraphic Architecture and Sedimentology of the Main Oil-Producing Stratigraphic Interval at the Cantarell Oil Field: The K/T Boundary Sedimentary Succession. Proceedings of the SPE International Petroleum Conference and Exhibition of

Mexico, 643–49. http://www.scopus.com/inward/record.url?eid=2-s2.0-1642564036&partnerID=tZOtx3y1

Russell, B., and D. Hampson, 1991, Comparison of poststack seismic inversion methods: 61st Annual International Meeting of the SEG, Expanded Abstracts, 876-878.

Lin, T., 2016, Seismic Attribute Analysis of Depth-Migrated Data. Ph.D. dissertation, University of Oklahoma.

West, B., P. Brian, S. R. May, J. E. Eastwood, and C. Rossen, 2002, Interactive seismic facies classification using textural attributes and neural networks: The Leading Edge, **21,**1042–49. https://doi.org/10.1190/1.1518444.

Zhang, R., K. Zhang, and J. E. Alekhue, 2017, Depth-domain seismic reflectivity inversion with compressed sensing technique: Interpretation, **5** (1): 1–9.

## Introduction to Chapter 3

In Chapter 2, I obtained a guide based on the dolomitization. This guide was obtained using a machine learning process (weighted linear combination) where I combined a set of attributes in time.

In the next Chapter 3, I made petrophysical estimations to split the total porosity in primary porosity (intercrystalline porosity, isolated vugs, minor fractures) and secondary porosity (vugs and fractures). This split was performed using image logs and nuclear resonance magnetic logs. Besides, I tried analytical methods based on basic well-logs to choose a method to use in future wells where probably image logs and NRM logs will be no available.

In the second part of Chapter 3, I am using the dolomitization trend as a second variable for sequential Gaussian function simulation process I distribute total porosity. Then, based on this distribution I use sequential indicator simulation to distribute the lithofacies described in Chapter one with total porosity as a guide. Then I assigned a probability distribution of secondary porosity for every lithofacies, and I use these distributions in a sequential Gaussian function simulation to distribute secondary porosity.

Finally based on the results of this process I was able to propose a location for a new producer well.

# CHAPTER 3: Petrophysical Properties Distribution for a 3d Geo-cellular Model For A Dual Porosity Carbonate Reservoir In The Southeast Gulf Of Mexico.

Cervantes-Velazquez, Antonio, antonio.cervantes.velazquez-1@ou.edu

Jose M. Morales-Ramirez.

Slatt, Roger M., rslatt@ou.edu

## Abstract

The porous system in carbonate reservoirs is complex to model because of the different types of porosity that exist in carbonates. Different petrophysical solutions have been proposed to characterize the porous system of this of reservoirs. But these solutions can show a better performance in some fields, but not so good in others. The reason for this complexity is because the final porous system is the result of a unique history of different secondary processes such as fracturing, dolomitization and, dissolution.

Advanced well-log tools can be useful to this objective. Nuclear magnetic resonance tools can discriminate pore size and, image-logs are useful to visually identify secondary porosity. However, because of the cost of these tools it is not possible to run them in all the wells in a development project. Hence, to develop a method to characterize secondary porosity from basic well-logs is important. We tried some of the methods traditionally used to estimate dual porosity in a Southeast Gulf of Mexico field, applied to a field in a stage of planning and we verified its performance, with the result of a split porosity estimated from nuclear magnetic resonance (NMR) and image log interpretation. This field has a secondary porosity related to the

process above described, but the porous system shows a dependence related to the stratigraphy and the original rock fabric also.

After the petrophysical part of this work, the secondary porosity was distributed in a 3D geo-cellular model. The method for this distribution is presented next. First, with the previously estimated dolomite percentage estimated from seismic attributes, we found a relation between effective porosity and dolomite percentage. We applied a Gaussian random simulation with co-kriging algorithm to distribute effective porosity with dolomitization as a second variable to guide the distribution. The second step was to associate the resulting total porosity to the lithofacies previously described in the wells. With this association we applied a sequential indicator algorithm to distribute the interpreted facies. Then the two porosities estimated from petrophysics, matrix, and fracture were constrained by this lithofacies distribution.

In the end, we found the methods to estimate secondary porosity that best fit to the study area and, based on the distribution of secondary porosity, we proposed the sweet spots that indicate where to locate the next wells.

## Introduction

In this work, we propose a workflow to characterize complex porous system carbonate reservoirs into a 3D geo-cellular model. In the first part, we characterized the porous system in the wells by trying analytical methods available in the petrophysical literature. The objective for this part was to determine the analytical method based on basic well-logs to split total porosity into primary and, secondary porosity. For our case of study, we have a heterogenous carbonate reservoir in the Southeast Gulf of Mexico (Figure 3-1) and we verify its performance based on the result of an estimated secondary porosity from nuclear magnetic resonance (NMR) and

image logs. At that point, we identified the method that best suits the reservoir case of study. For the second part, we distributed the total porosity, primary porosity, and secondary porosity by using geostatistical methods using dolomitization trends previously estimated by machine-learning processes fed with seismic attributes (Chapter 2). Additionally, porosities were constrained to the facies identified in the wells for its distribution. For this study our dataset was composed of a basic well-log set (gamma ray, litho-density and, sonic) for three wells in the zone, well A-1, B-1 and C-DL1. For the same wells, we had nuclear magnetic resonance (NMR) and image logs (Figure 3-2). We had a geo-cellular 3D model also that covers three fields divided into five units and a 3D trend of dolomitization previously estimated from seismic attributes (Chapter 1).

## Petrophysical background in double-porosity estimation

In Archie´s equation, a relation between the formation resistivity factor F and the porosity system was stated through the "m" and "a" constants The "m" constant is known as the cementation factor and "a" as the tortuosity factor and they represent the slope and intercept from a linear regression from empirical data. Furthermore, the "m" value for a reservoir can provide information about the porous system. Because of these different analytical methods for calculating "m", Aguilera (1976), Gomez-Rivero (1981) and, Lopez and Viro (2002). Aguilera (1974) developed a theoretical model based on parallelepipeds where the spaces between them represented the fractures, and an equation was proposed to estimate a dual-porosity value of m from resistivity and sonic logs. In a later work, Aguilera (1976) made an extension of this method to use resistivity logs as an alternative to estimate dual-porosity m. Gómez-Rivero (1978) proposed an analytical estimation of variable m from his observations from cores in the

Mexican Republic and the southeast United States. In his subsequent work, Gomez-Rivero provided an empirical equation to differentiate secondary porosity in vuggy fractured carbonates from their variable parameter, using a partition coefficient v also estimated from well-logs (Rivero, 1981). In particular, he corroborates that the porosity from litho-density well-log lectures to total porosity and the sonic log to matrix porosity. Based on Gomez-Rivero´s work, Lopez and Viro (2002) proposed a specific ”m” variable equation from well-logs for vuggy and fractured carbonates for a field in Southeast Gulf of Mexico. The resulting m from this equation was called m-pivot. This equation is based on assuming that any secondary-porosity above 7% corresponds to vuggy porosity and the porosity below this value is fracture porosity. This assumption was supported with capillary pressure studies from cores in the Taratunich field located in the southeast Gulf of Mexico area.

The porous system in our study area varies from fracture, vuggy and, intercrystalline porosity in dolomized zones to a limited matrix intercrystalline porosity in a non-dolomized zone. Dolomitization is a major process related to the generation of secondary porosity. However, we observed that the original fabric of the rock has a role in the secondary porosity also. Furthermore, the zones where the original rock was a carbonate breccia develop bigger vugs and more connected fractures than where the original rocks correspond to mudstone-wackestone textures. To select a method to suit with this heterogeneity we tried these three methods to estimate "m" and split porosity in primary and secondary porosity. We validated the results through the interpretation of the image well-logs, nuclear magnetic resonance logs and core studies available from three wells distributed in three fields in the study zone. Chang, et al., (1994), found a relation between the relaxation time (T2) and the pore types in carbonates microporosity and free fluid porosity. Chang et al., (1994) were able to find a cutoff for vug

porosity, all this calibrated with NMR measurements in cores. We stated cutoffs for the wells in the study area based on the visual percentage of vugs and fractures taking them as secondary porosity observed in the image-well logs. With this secondary porosity as a parameter, we can compare it with the results from the methods of Aguilera (1976), Gomez-Rivero (1981) and Lopez and Viro (2002). Finally, we selected the methods for characterizing the porous system for future wells in these fields.

**Property distribution background.**

For the distribution of the total porosity and double porosity in the 3D model, we used Gaussian random function simulation (GRFS) with a collocated co-kriging (Daly, et al., 2010). This algorithm is based on the traditional sequence gaussian simulation (SGS) but incorporates a fast Fourier transform to reduce the variability in the output of SGS and improve the calculation velocity. The second variable for GRFS was a dolomitization trend property estimated previously from a linear weighted combination of seismic attributes (Chapter 2). We used the total porosity property as a function of probability of occurrence for every litho-facies using sequential indicator simulation (SIS). These lithofacies were previously described in the wells of the zone (Chapter 1). Finally, secondary porosity then was distributed using the lithofacies, assigning a higher distribution of porosity to the lithofacies where the fractures and vugs were observed in image-logs and cores, for the facies with a low incidence of secondary porosity lower porosity distribution were assigned.

## Geologic Setting

The stratigraphy of the area was described by Angeles-Aquino (2006), identifying the main units from the Jurassic to the Cenozoic. The reservoir rock is Cretaceous in age. According to Angeles-Aquino's work (2006), the Cretaceous formation is divided into Upper, Middle, and Lower Cretaceous intervals (F. J. Angeles-Aquino 2006).

We used the stratigraphic subdivision in units and the lithofacies classification proposed in the Chapter 1 for the study area. From Chapter 1, Lower Cretaceous (Kl) is a unique unit as well as the Middle Cretaceous (Km) and, Upper Cretaceous (Ku) is subdivided into three units (Figure 3-3).

These units can be related to the lithofacies.

- ***Unit Kl*** the dominant lithofacies corresponds to mudstone-wackestone carbonate with some presence of layered carbonate breccia.
- ***Unit Km*** is dominated by layered carbonate breccia with some presence of mudstone-wackestone limestone. This unit is always dolomitized in the described wells.
- ***Unit Ku-1***. This unit is formed by mudstone-wackestone and is dolomitized in all the wells in the area, excepting well C-DL1.
- ***Unit Ku-2***. This unit is composed by a coarse dolomitized carbonate breccia.
- ***Unit Ku-3*** is formed by a fine layered breccia with low dolomitization and represents the top of the Upper Cretaceous. Because this unit is considered part of the seal of the reservoir along with the tertiary column, we are not considering this unit in this study.

The main reservoir rock corresponds to the Ku-2 unit of the Upper Cretaceous carbonate debris flows that were deposited on the Yucatan Peninsula slope. The debris flows consist of heterogeneous carbonate clasts in a carbonate matrix. The formation is diagenetically altered

through a sequence of dolomitization, dissolution, and fracturing. The diagenetic processes developed a complex porosity system where three (3) types of pores, intercrystalline pores associated with the dolomitic matrix, vugs, and fractures, are equally important.

Near the study area, structural analyses of the Cantarell and Sihil fields were conducted by Mitra et al. (2005) and later for the Ku, Zaap, and Maloob fields (Mitra et al., 2006). These analyses described the main deformation episodes for the area, identifying three main episodes of deformation: (1) a Jurassic to Early Cretaceous extensional event; (2) a Miocene compressive phase, during which the main trap-forming structures were formed; and (3) a Pliocene to Holocene extensional event, resulting in several listric-growth faults.

The study area is composed of three anticline structures related to thrusting. According to the events described by Mitra (2005; 2006), these structures were generated in the Miocene compressive phase. In this study, the fields related to these thrusting structures are called, from north to south, fields A, B, and C. The structural trend of the thrusts has a general east-west orientation dipping to the south for fields A and C. However, structure B is dipping toward the north (Figure 3-2).

## Methods

First, we used Archie equations for effective porosity and water saturation from the basic well-logs. The results were calibrated with the core studies available, for these wells and the total porosity from NMR logs (Figure 3-4, 3-5 and, 3-6). In order to obtain a parameter to validate the methods to split porosity, we estimate the porosity types using image and NMR-logs based on the Chang, et al., (1994) method mentioned in the introduction. First, porosity types were identified visually from well image-logs then, from these visual inspection percentages of ratios

of secondary porosity (fractures and connected vugs) vs. primary porosity (isolated vugs and matrix porosity). Based on this percentage, cut-offs were stated on the porosity bins in the NMR to split the porosity types for the three wells. Then, values of "m" and the corresponding porosity split were estimated with the methods proposed by Aguilera (1976), Gómez-Rivero (1981) and, Lopez and Viro (2002).

With the split porosity, we distributed the estimated porosities in the 3D-model. To do this, the first step was distributing total effective porosity. We applied a Gaussian random function simulation with a collocated co-kriging. For the co-kriging we used a previously estimated property of dolomitization, which related higher dolomitization to higher porosity. Formerly, we distributed the interpreted litho-facies in the wells with a sequential indicator simulation using the final total porosity property as a probability constraint, so the distribution of probability of porosity values was associated to any facie.

Secondary porosity was distributed using Gaussian random function simulation but was applied using a probability distribution of porosity according to the facies previously distributed. Finally, to obtain matrix porosity we calculated the difference between total effective porosity and secondary porosity.

The applied workflow is shown in Figure 3-7.

# Results

### Petrophysical model results.

The average values of percentage proportion of secondary porosity for well and unit are presented in the Table 3-1. From the results of the secondary porosity based on NMR, we observed that the Ku-2 unit has a major proportion of secondary porosity overall. Ku-1 has a

lower proportion of secondary porosity, even in the dolomitized zones. The zone Ku-1 is a layered mudstone-wackestone that could be dolomitized as in the well C-DL1, while Ku-2 is a carbonated breccia. This could imply that there exists a textural component controlling the secondary porosity in Ku-1 unit, beside the dolomitization. Km unit has a slight increment in the proportion of secondary porosity, this could be related to the original texture also. This unit is formed by a most homogenous layered breccia compared to Ku-2, that is a poorly sorted, chaotic breccia. For Kl unit the proportion of secondary porosity is scarce; the only method with a significative proportion of secondary porosity was the secondary porosity from NMR.

To evaluate the porosity split based on basic well-logs we plotted the values of the secondary porosity from NMR with the secondary porosity from the analytic methods. Then, we made a linear regression as an indicative of likeness, where the closer the slope is to one, the closer will be to the expected result from NMR.

| Secondary porosity well A-1 | | | | | |
|---|---|---|---|---|---|
| Unit | Percentage of Secondary porosity from image logs | Percentage of Secondary porosity from CMR | Percentage of secondary porosity from Lopez and Viro (2002) | Percentage of secondary porosity from Gomez-Rivero (1981) | Percentage of secondary porosity from Aguilera (1976) |
| Ku-2 | 36.87% | 55.37% | 4.99% | 20.70% | 22.69% |
| Ku-1 | 11.48% | 22.73% | 2.21% | 12.34% | 12.34% |
| Km | 24.97% | 30.81% | 3.50% | 16.53% | 12.13% |
| Ki | 2.58% | 15.90% | 2.04% | 6.55% | 6.74% |

A)

| Secondary porosity well B-1 | | | | | |
|---|---|---|---|---|---|
| Unit | Percentage of Secondary porosity from image logs | Percentage of Secondary porosity from CMR | Percentage of secondary porosity from Lopez and Viro (2002) | Percentage of secondary porosity from Gomez-Rivero (1981) | Percentage of secondary porosity from Aguilera (1976) |
| Ku-2 | 32.57% | 45.19% | 7.76% | 30.98% | 40.55% |
| Ku-1 | 6.67% | 16.19% | 4.45% | 13.00% | 17.10% |
| Km | 33.52% | 39.98% | 4.82% | 16.44% | 21.30% |
| Ki | 6.59% | 3.20% | 3.65% | 10.15% | 13.49% |

B)

| Secondary porosity well C-DL1 | | | | | |
|---|---|---|---|---|---|
| Unit | Percentage of Secondary porosity from image logs | Percentage of Secondary porosity from CMR | Percentage of secondary porosity from Lopez and Viro (2002) | Percentage of secondary porosity from Gomez-Rivero (1981) | Percentage of secondary porosity from Aguilera (1976) |
| Ku-2 | 25.19% | 50.85% | 4.76% | 29.00% | 28.99% |
| Ku-1 | 7.19% | 28.54% | 2.20% | 11.23% | 13.40% |
| Km | 24.38% | 50.60% | 3.13% | 11.59% | 9.81% |
| Ki | 8.84% | 43.64% | 3.54% | 9.86% | 7.70% |

C)

**Table 3-1.** The average proportion of secondary porosity by well and unit. We estimated these values using the ratio of the average secondary porosity related to the average total porosity in every unit and well. The higher proportions are presents in the Ku-2 unit and in the Km. Kl and Ku-1 have a minor proportion of secondary porosity.

In a comprehensive view, we found a significant difference between the results from Lopez and Viro (2002) and the results from NMR (Figure 3-8). The proportion of secondary porosity was constantly less than secondary porosity in NMR. For the cross-plot, the slope of the

linear regression had a value of 0.1081. Gómez-Rivero (1981) and Aguilera (1976) were similar in results and closer to the split porosity estimated from NMR. Aguilera has a slightly closer slope close to one (0.7081) than Gómez-Rivero (1981) (0.7272).

In the field we found diverse results depending on the methods and the fields themselves. In Figure 3-9, 3-10, and 3-11, we present the results of the partition in well-log mode for the well A-1 for the applied methods. The Lopez-Viro method in general presents low secondary proportion related to the NMR parametric curve. On the other hand, Aguilera and Gomez Rivero have a similar result of secondary porosity proportion. In Figure 3-12 we present the secondary porosity cross-plots for every method compared to the NMR secondary porosity. Well A-1 has the lowest approximation to the NMR partition, being the lowest approximation the results from Lopez and Viro (2002) method (m=0.1). In field A, the results between Gomez-Rivero (1981) and Aguilera (1976) have a significative difference, m= 0.38 for Gómez-Rivero and m=0.5033 for Aguilera.

For the well B-1 we present the result of the porosity partition in Figure 3-13, 3-14 and, 3-15. This well has the highest porosity values in the study area of the upper part of the Ku-2 zone. In Figure 3-16 are the cross-plots of secondary porosity for every method. For well B-1, the Lopez and Viro (2002) method had the lowest likeness with a value of m=0.18. For this field, the difference between Gomez-Rivero and Aguilera increased considerably, the magnitude of m, were m=0.75 for Gomez-Rivero and m=0.98 for Aguilera. This last m magnitude from Aguilera is remarkable because this value is the closest to one in the study zone.

For well C-DL1 we present the result of the porosity partition in Figure 3-17, 3-18 and, 3-19. This well has a notable drop of porosity in the Ku-1 zone. In Figure 3-20 are the cross-plots of secondary porosity for every method. For Field C, once more Lopez and Viro provided the

lowest likeness to NMR with m=0.1. This field was the only one where Gomez-Rivero had a higher likeness than Aguilera, although the difference was minor, m=0.79 for Gomez-Rivero (1976) and m=0.75 for Aguilera.

The case for Unit Ku-2 (Figure 3-21) is important because this is the main reservoir rock in the field. The Lopez and Viro (2002) method were of steady value, being the lowest value in likeness m=0.1315. For Gomez-Rivero and Aguilar had a good performance with a high likeness value to the NMR and split with a little higher likeness of Aguilera (m=1.0137) than Gomez Rivero (m=0.9573).

The unit Ku-1 (Figure 3-22) generally presents low secondary porosity values relatively to Ku-2 and Km units. Ku-1 is the only unit that varies in its dolomitization, being the area around the well C-DL1 which is not dolomitized at all. All the methods resulted in values of secondary porosity below the estimated from the NMR log. The Gomez-Rivera method gave the highest value (m=0.7049), followed by Aguilera (m=0.5691) and Lopez and Viro (0.0856).

For Km unit generally, the proportion of secondary porosity increases relatively to Ku-1 (Figure 3-23). All the methods estimate the secondary porosity below the values of the NMR estimated secondary porosity, from Lopez and Viro that have the lowest likeness value (m=0.1027) to Gomez-Rivero with a value of m=0.669, and finally, the closest value comes from Aguilera (1976) with a value of m=0.7125.

The Ki unit (Figure 3-24) is the lowest part of the reservoir and is not a producer. All the methods have secondary porosity values under the estimated values of porosity from NMR. However, the difference between the results was minimal between the methods from m=0.0638 for Lopez and Viro, to 0.0967 for Gomez-Rivero and finally Aguilera with 0.1531. While Ki is

not considered a producer in the zone, characterizing it as second porosity in this unit is important because this type of porosity could be a way for a possible water irruption.

**Property distribution in geo-cellular model.**

Total porosity distribution performed by the dolomitization trend honored the effective porosity estimated from the well-logs (Figure 3-25). In general, the distribution is close to the expected result, where the higher porosity is concentrated in the Ku-2 unit with a low porosity decrement for Ku-1 zone and slightly increment for the Ku-1 zone and, low porosity for the Kl unit.

We generated average porosity maps for every zone. For the Ku-2 unit (Figure 3-26) the porosity distribution is triangular, and in the study area, is concentrated in the central part.

Ku-1 unit has a semi-log like distribution (Figure 3-27) and the predominant frequency is in low porosity values. In the study area on the map, the higher porosities are located in the central part of the study area also.

Km unit (Figure 3-28) has a porosity distribution of the frequency lightly biased to the left part, where the low porosity values are found. From the map, the higher porosity values in the study area are consistently located in the central part.

Kl unit (Figure 3-29) has the lowest porosity values in the area, and their distribution is almost homogenous.

The facies distribution in the geo-cellular model based on the total porosity honored the facies described in the wells and was consistent with the expected stratigraphic distribution (Figure 3-30). To present the distribution for the unit we generated facies maps. These maps

were calculated generating surfaces between the top and the base of the units and we extracted the property values from the lithofacies property along the calculated surface.

The predominant facies in the unit Ks-2 (Figure 3-31) corresponds to the Coarse Breccia, but this unit has the presence of another facies, dolomitized mudstone to wackestone and layered fine breccia. A possible explanation for this might be that this unit was not formed by a unique process (massive transport deposit), otherwise the resting facies, mudstone-wackestone could be deposited as pelagic sediments and the finely laminated breccia as another kind of gravitational deposition.

Unit Ku-1 (Figure 3-32) is formed by two facies related in their origin, the first corresponds to a mudstone-wackestone limestone and, a dolomitized mudstone-wackestone. The presence of these two different facies, related to the dolomitization in the same unit, indicates that the dolomitization process was not so homogeneous as in the Ku-2 and Km units.

Unit Km (Figure 3-33) is composed of two facies, dolomitized mudstone to wackestone and layered fine breccia. Dolomitized mudstone-wackestone lithofacies were predominant over the finely layered breccia.

Unit Kl (Figure 3-34) is all formed by the mudstone-wackestone facies and, the dolomitization process is not present in this zone.

For the secondary porosity distribution, the low porosity values are predominant in the total model (Figure 3-35). However, the distribution into the zones is not homogenous, which will be explained further.

For the Ku-2 unit (Figure 3-36), the secondary porosity property had a wide porosity value distribution. In the map, the higher porosity values are concentrated in the southwest of the study area. This is different from the total porosity distribution, where most of the higher values

are in the central part. This difference could be related to the thickness of this unit in the southeast zone as in the C-DL1 well.

In the Ku-1 unit (Figure 3-37), the low porosity distribution values have a higher frequency. The concentration of higher values in the area coincides with the anticline structures. Therefore, the secondary porosity could be related to the structural trend of the zone.

For the Km unit (Figure 3-38), secondary porosity has a broader frequency distribution of values. The average porosity map does not show a clear trend of distribution. However, Km unit had a concentration of higher porosity values limited to a zone in the southwest part.

For the unit Kl (Figure 3-39), the porosity values are low and, just a slight increment in the southeast part can be observed.

## Conclusions

A secondary porosity estimation was performed based on NMR and image logs in a complex carbonate reservoir in southeast Gulf of Mexico. Three methods to split porosity in a matrix and a secondary porosity based on basic well-logs were applied to the same fields. This was to determine what is the best method to apply in the area. As a result, the proposed method by Aguilera (1976) had better performance over Gómez-Rivero (1981) method. On the other hand, the Lopez and Viro (2002) method underestimated the proportion of secondary porosity. However, depending on the fields in the area and the units, the results varyed significantly. The most concordant results by the methods were obtained in the Ku-2 unit, the main producer unit in the reservoir. This is remarkable in the well-B zone, where the Aguilera method was closer to the parametric secondary porosity from NMR. We can observe a possible correlation between the bigger and abundant secondary porosity from vugs and fractures and the capability of the well-log sensitivity that permits its identification.

Because Ku-1 could work as a flow barrier between the units Ku and Km units, characterizing the possible connection between these units through secondary porosity is important. This unit is the only one where the Gomez -Rivero method was closer to the parametric NMR secondary porosity.

Km is the second-best unit in the reservoir and the Aguilera method had an acceptable result to characterize this unit.

The secondary porosity in the Kl unit, in general, is very low and is not considered a possible reservoir rock. For this unit, the methods used to estimate secondary porosity from good logs underestimated the secondary porosity calculated from NMR.

In the light of these results we recommend using the Aguilera method for units Ks-2 and Km and Gomez Rivero for Ks-1.

The secondary porosity distribution based on facies was useful to limit the probabilities of occurrence of secondary porosity to the facies where previously this porosity was identified. In this way, uncertainty was reduced for the geological knowledge and facilitates future updating in the model because the probability functions are already defined. These probability functions can be incorporated into the facies identified in future wells

The main concentration of secondary porosity is in the central anticline of the field C. If we superimpose this distribution on the structural map, we can define possible opportunity zones to locate new producer wells. The central anticline itself is attractive, but the zone next to the main fault in this anticline has an attractive potential from the structural point of view, being that primary and secondary porosity values are high. We illustrate in Figure 3-40, a cross section through well C-1 to a proposed well in this zone. We can appreciate that the high values of

secondary porosity reach 10%. The northern anticline in C field has potential also, with secondary porosity values between 4 and 6% and a high structure that forms a trap.

# Figures Chapter 3

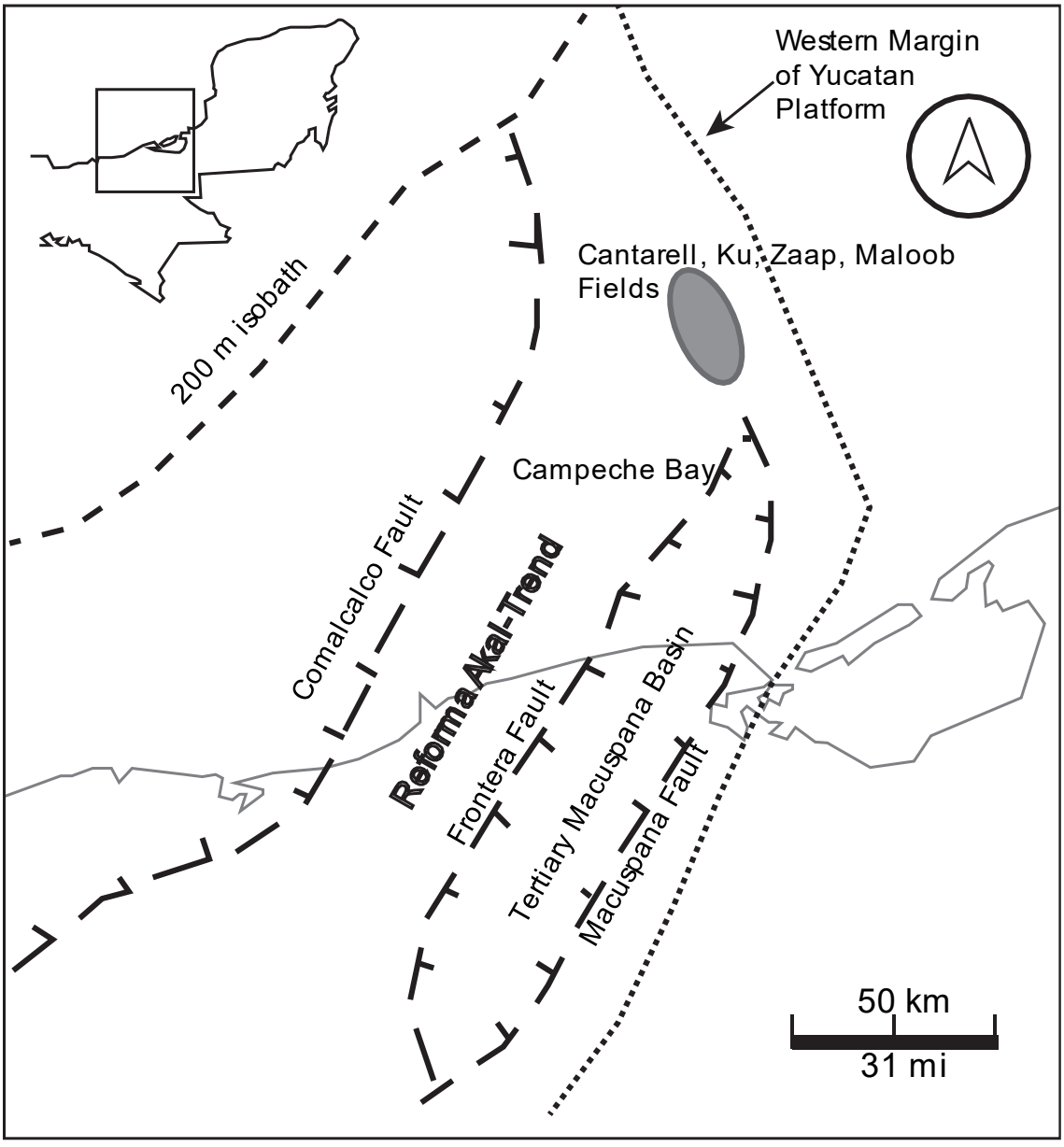


**Figure 3-1.** Location of the study area and the main structural features in the zone. The study area shares the geological history and several features with the major fields in the Gulf of Mexico including Cantarell, Ku, Maloob, and, Zaap. (after Murillo-Muñeton et al., 2002).

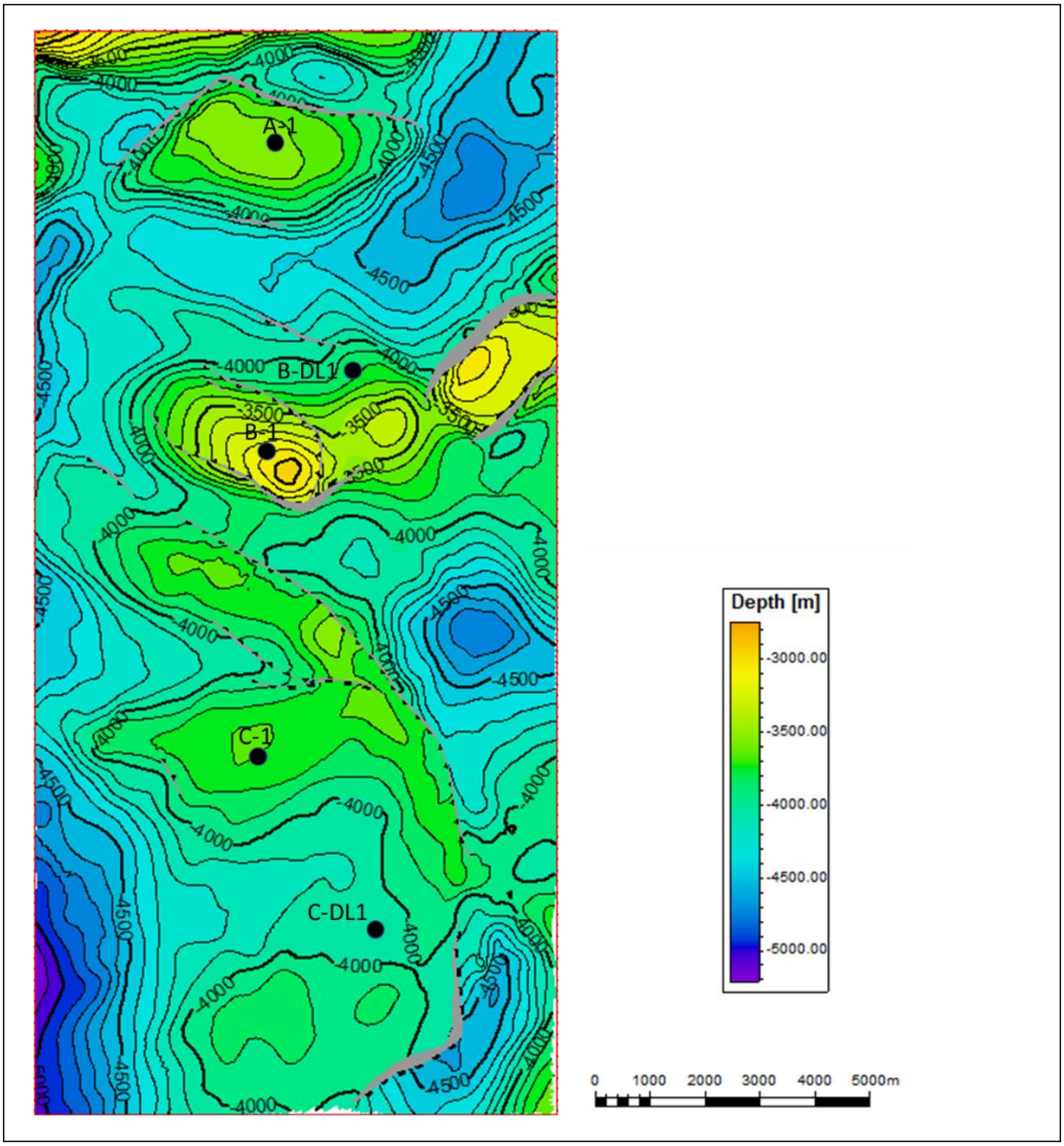


**Figure 3-2.** Map of the top of the reservoir. The study area is composed of three fields, named from North to South as A, B, and C. Field A was discovered by well A-1. Field B has two wells, with well B-1 the discovery well and well B-DL1 an appraisal well. This latter well was used as a blind test well. The C field has two wells, C-1 was the discovery well but only drilled 120 m inside the reservoir. C-DL1 was an appraisal well.

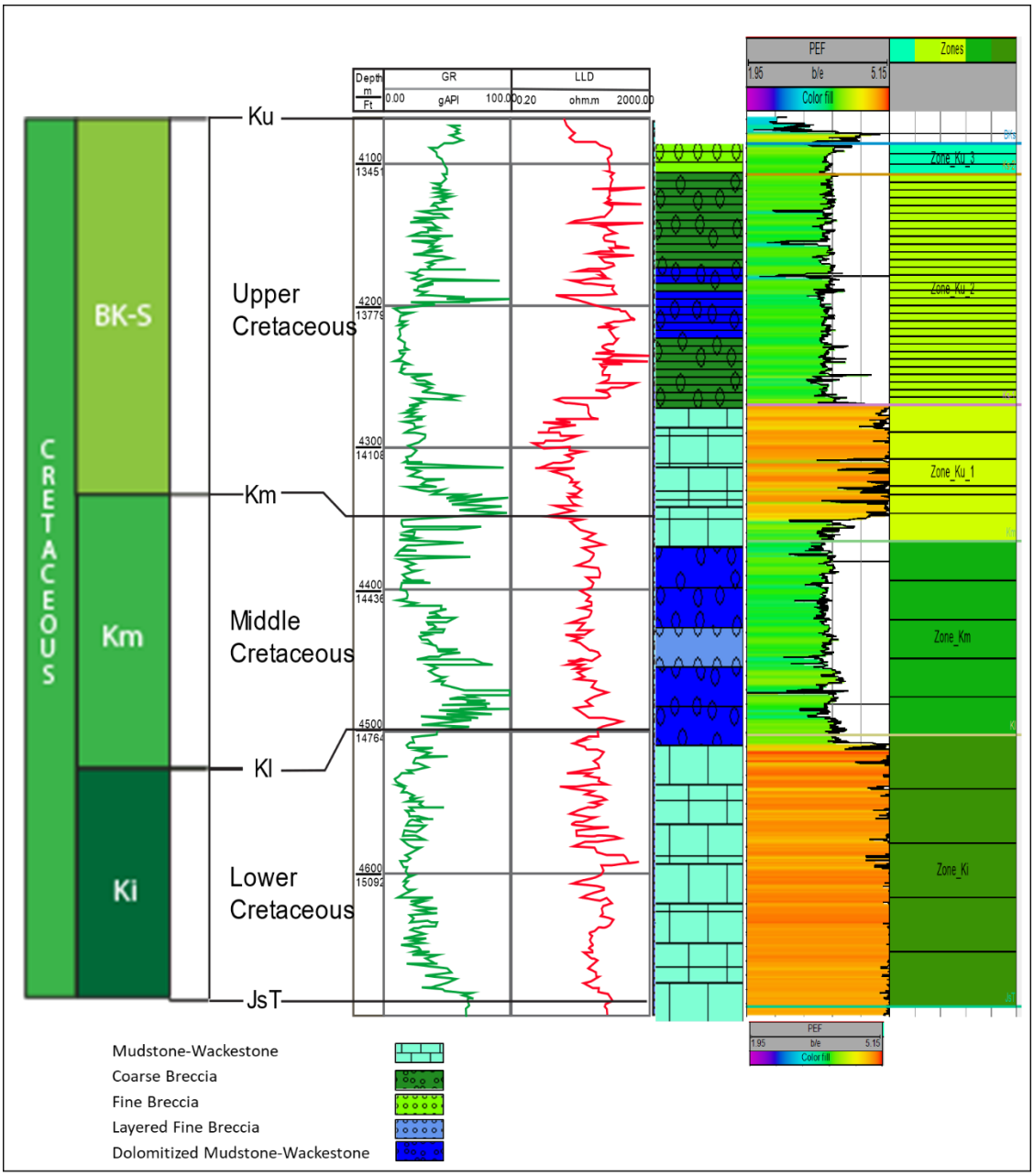


**Figure 3-3.** Type-column for the study area and corresponding well-log response showing the reservoir rock ranging from Lower Cretaceous to Upper Cretaceous. This lithofacies description is incorporated from the previous work in the area (Velazquez et al., 2017). In this column, the zones and layers dividing the cellular model are shown in the last track. (After Angeles-Aquino et al., 2006).

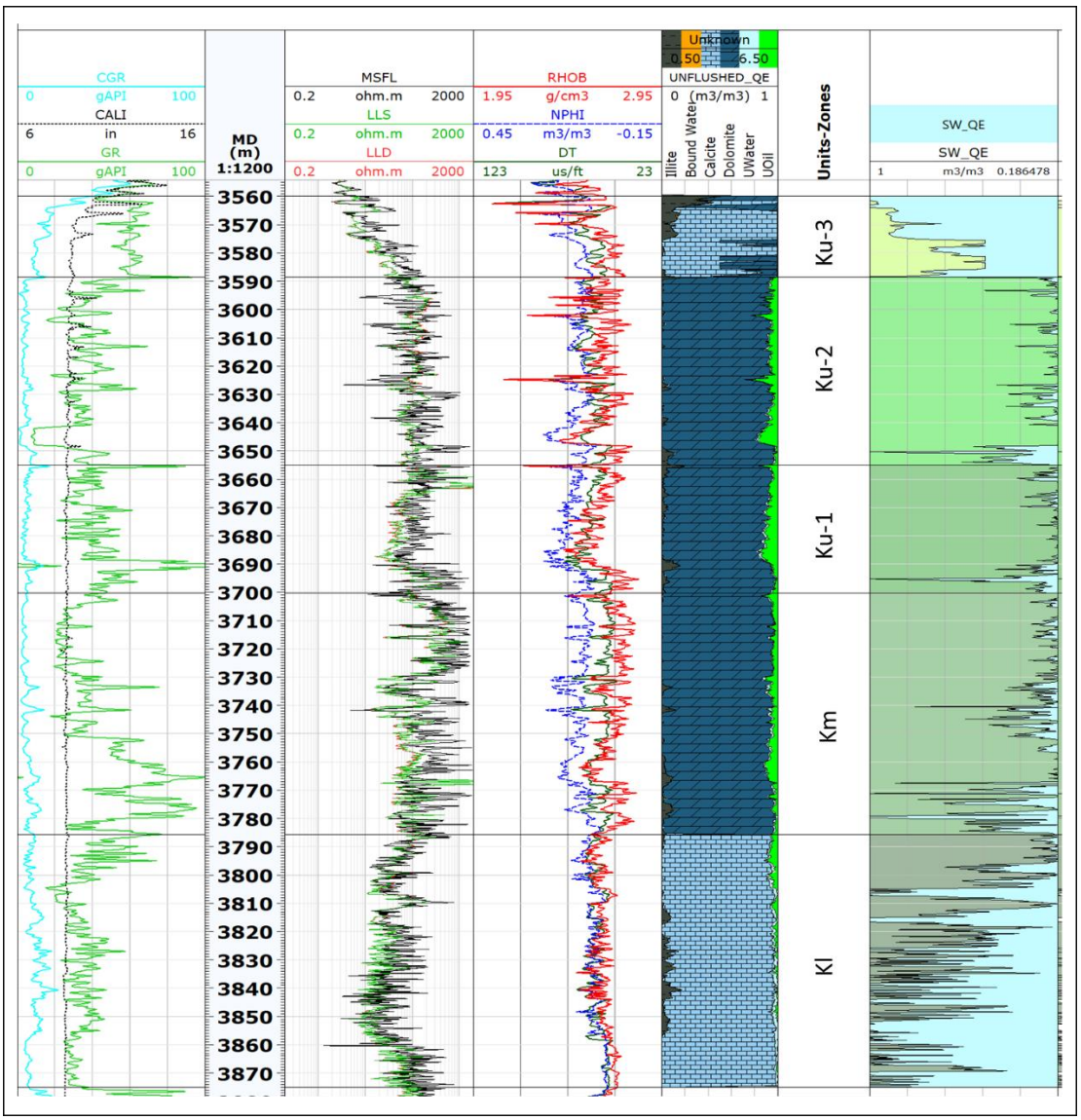


**Figure 3-4** Basic well-logs for A-1 well and the result of basic petrophysical analysis were effective porosity and water saturation was estimated. This will have the minimum thickness for the Cretaceous, particularly in the Kl zone. The caliper log shows some washouts, they exist in the Ku-2 zone mainly this is reflected as spikes in the basic logs. Low resistivity values on the upper zone could be indicative of low compacity related to the Km unit.

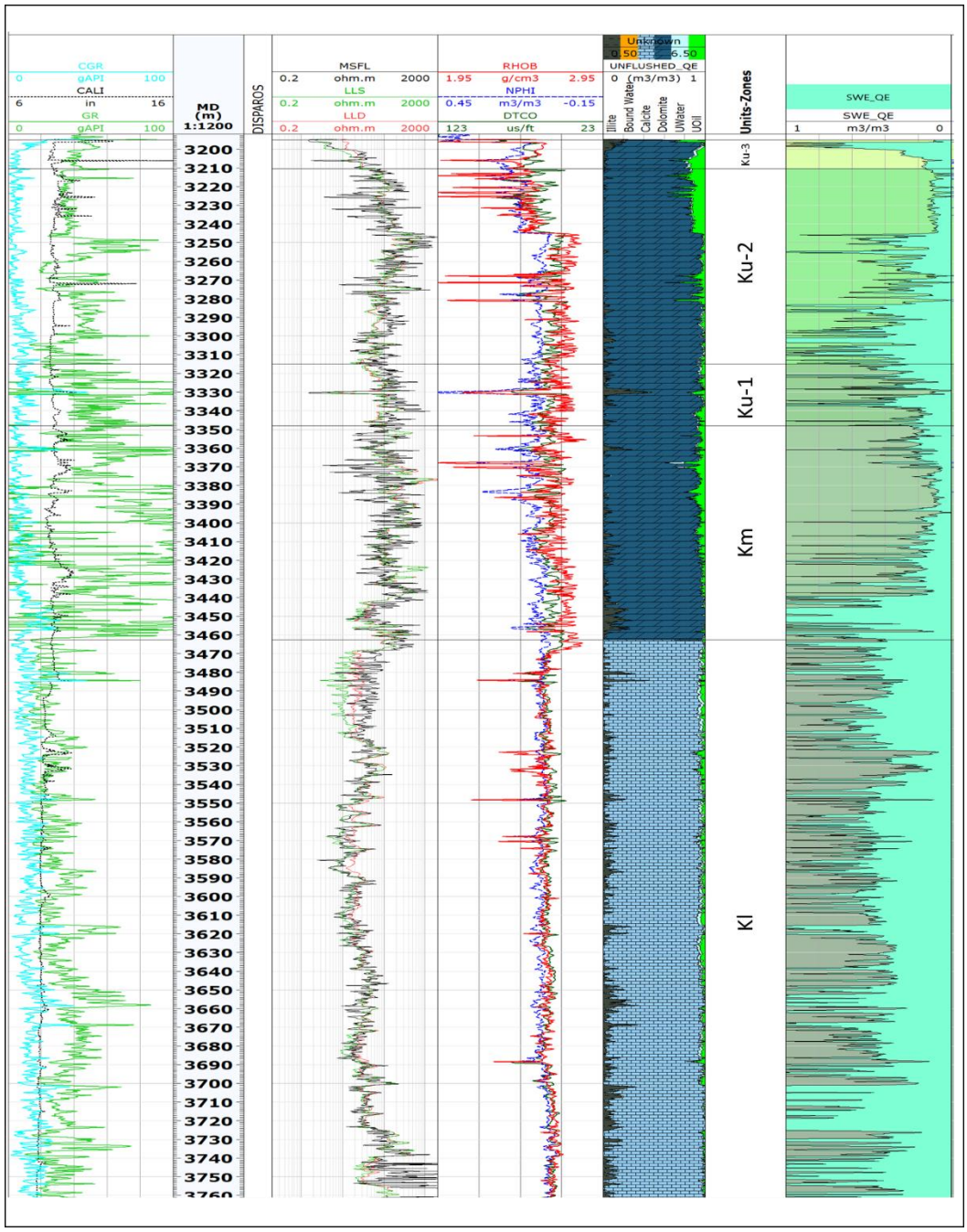


**Figure 3-5.** Basic well-logs for B-1well and the result of basic petrophysical analysis where effective porosity and water saturation were estimated. Well B-1 had the highest porosity values, around 18%.

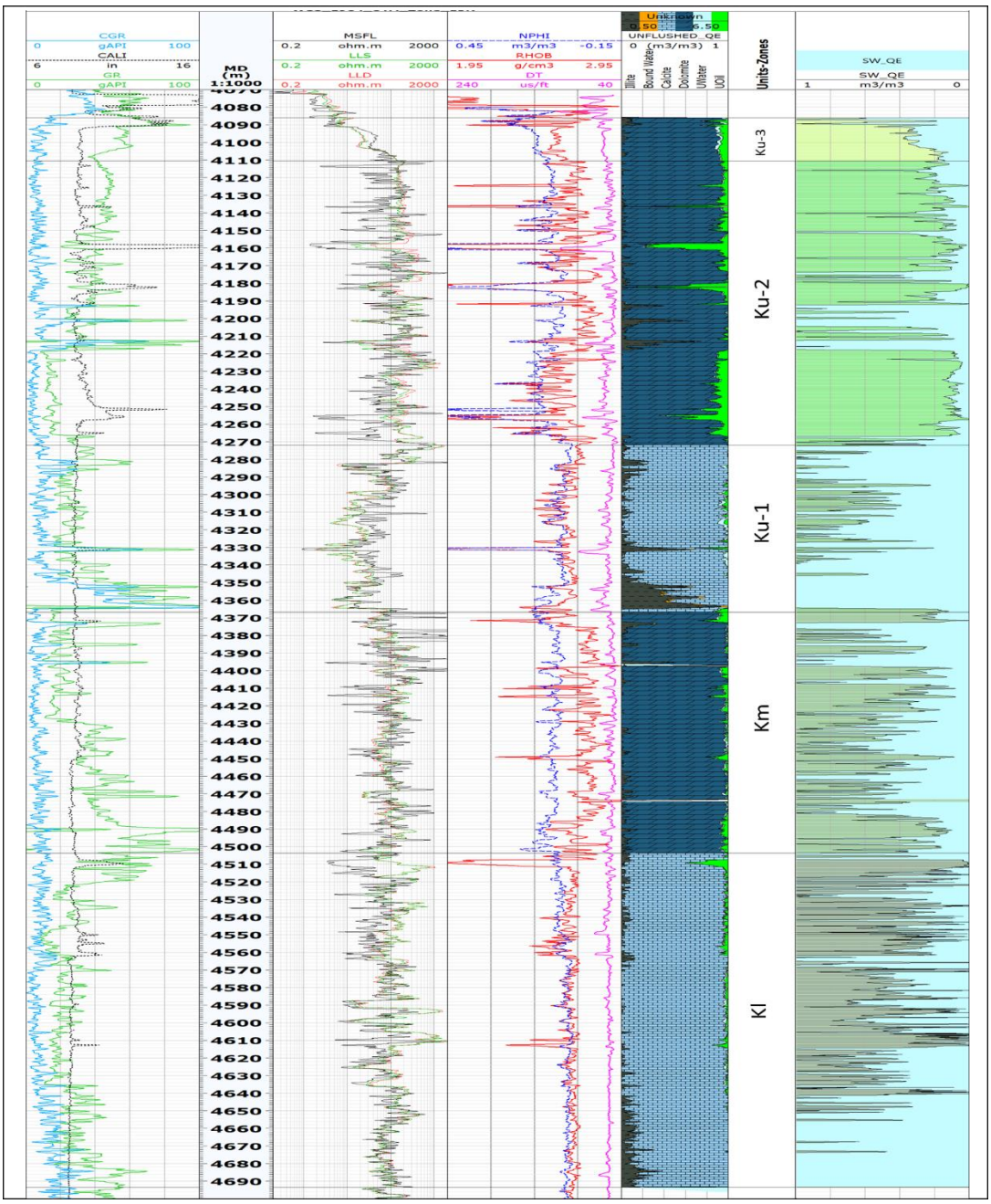


**Figure 3-6.** Basic well-logs for C-DL 1well and the result of basic petrophysical analysis where effective porosity and water saturation were estimated. Well C-DL1 is the only where the Ku-1 unit is not dolomitized, total porosity value falls in this unit. Caliper-log shows washouts in the Ku-2 unit mainly, affecting the basic well-logs.

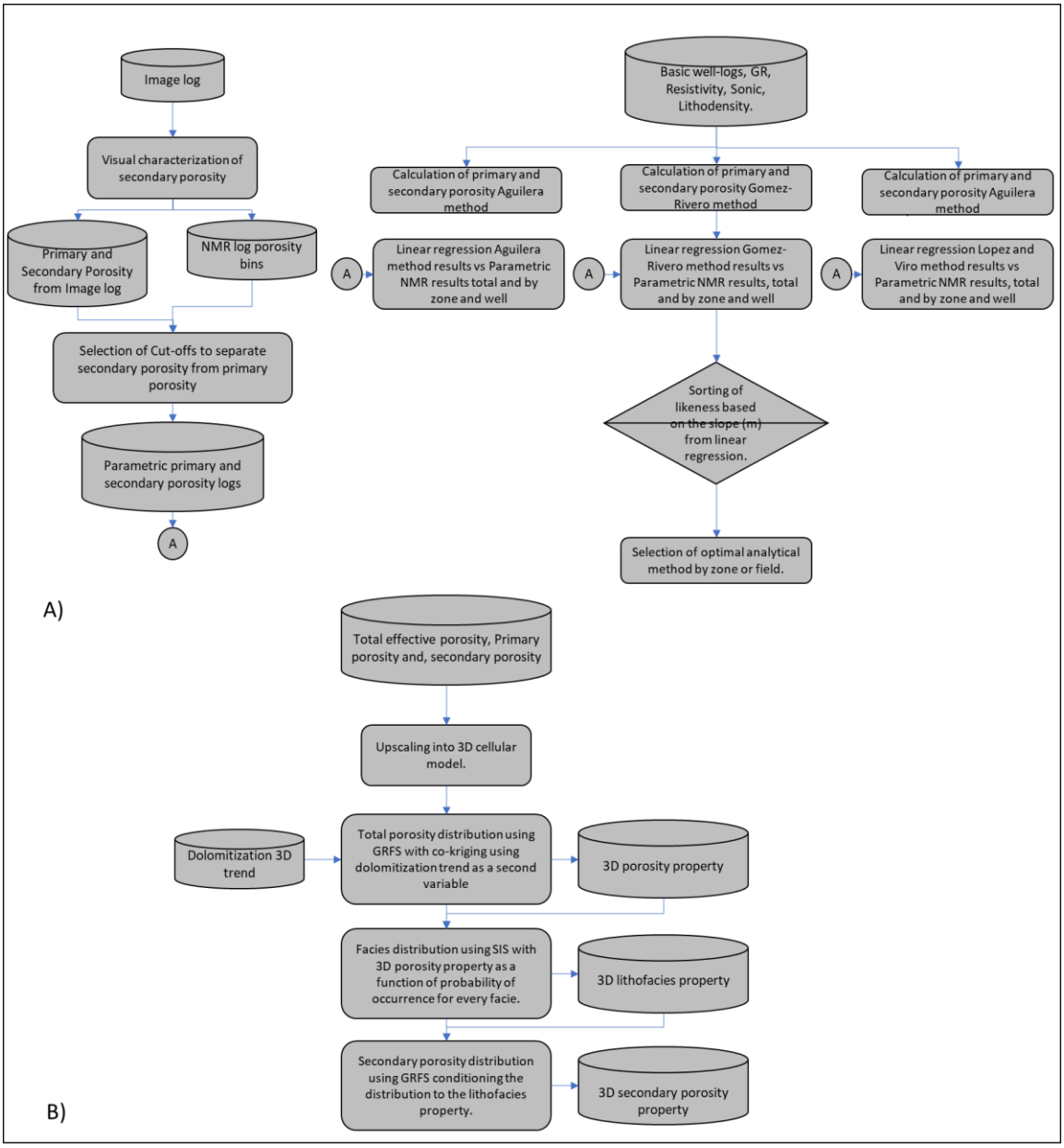


**Figure 3-7.** The flowchart illustrating the proposed workflow for (A) selection of an analytical method to estimate double porosity from well-logs and, (B) distribution of dual porosity in the 3D geo-cellular model.

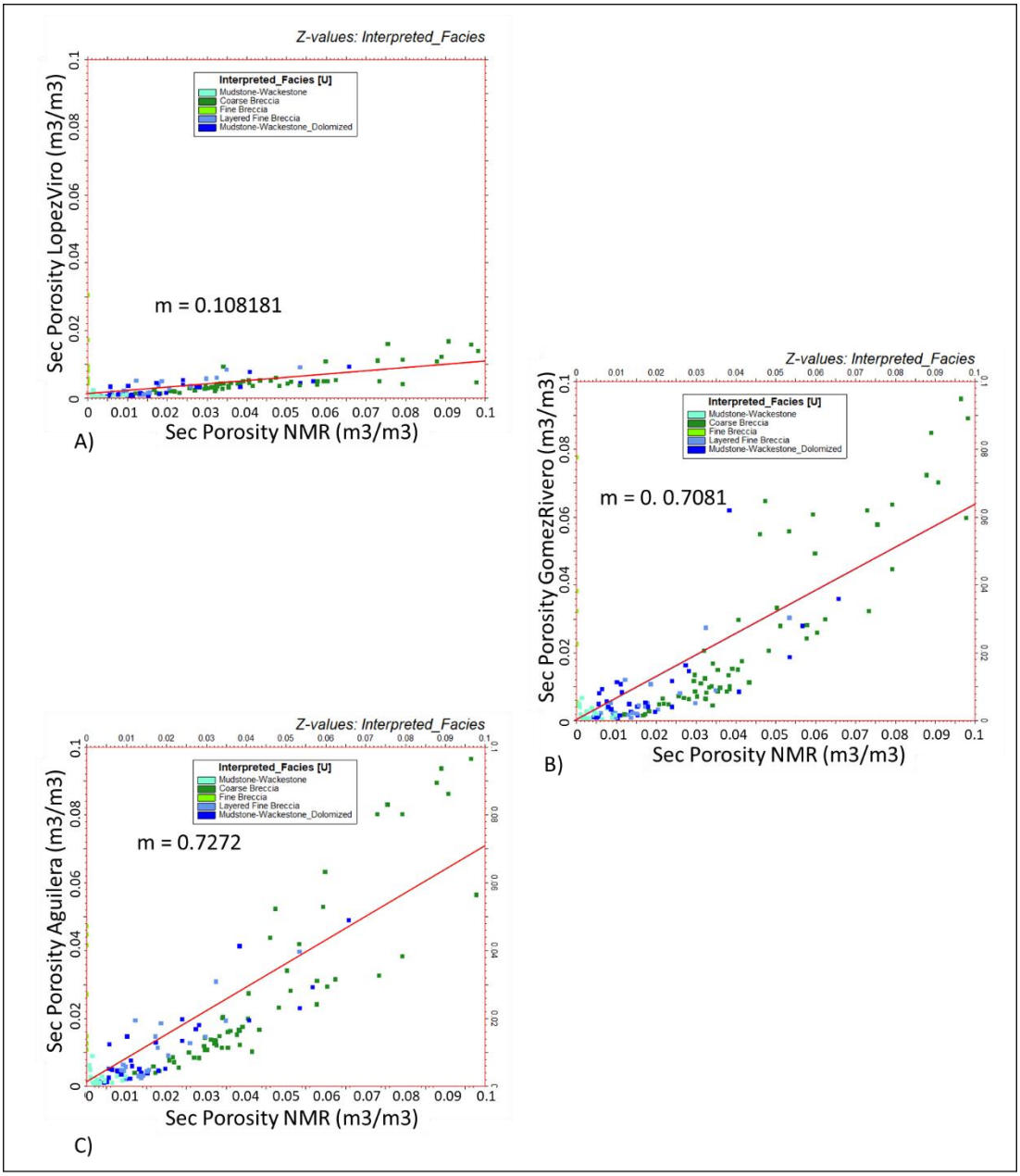


**Figure 3-8.** Cross-plot of the secondary porosity log upscaled to the model from NMR vs Lopez and Viro (2002) (pivot method) (A), vs Gomez-Rivero (1981) (B) and, vs Aguilera (1976) (C). We calculated a linear regression and we used the resulting slope as an indicator of likeness.

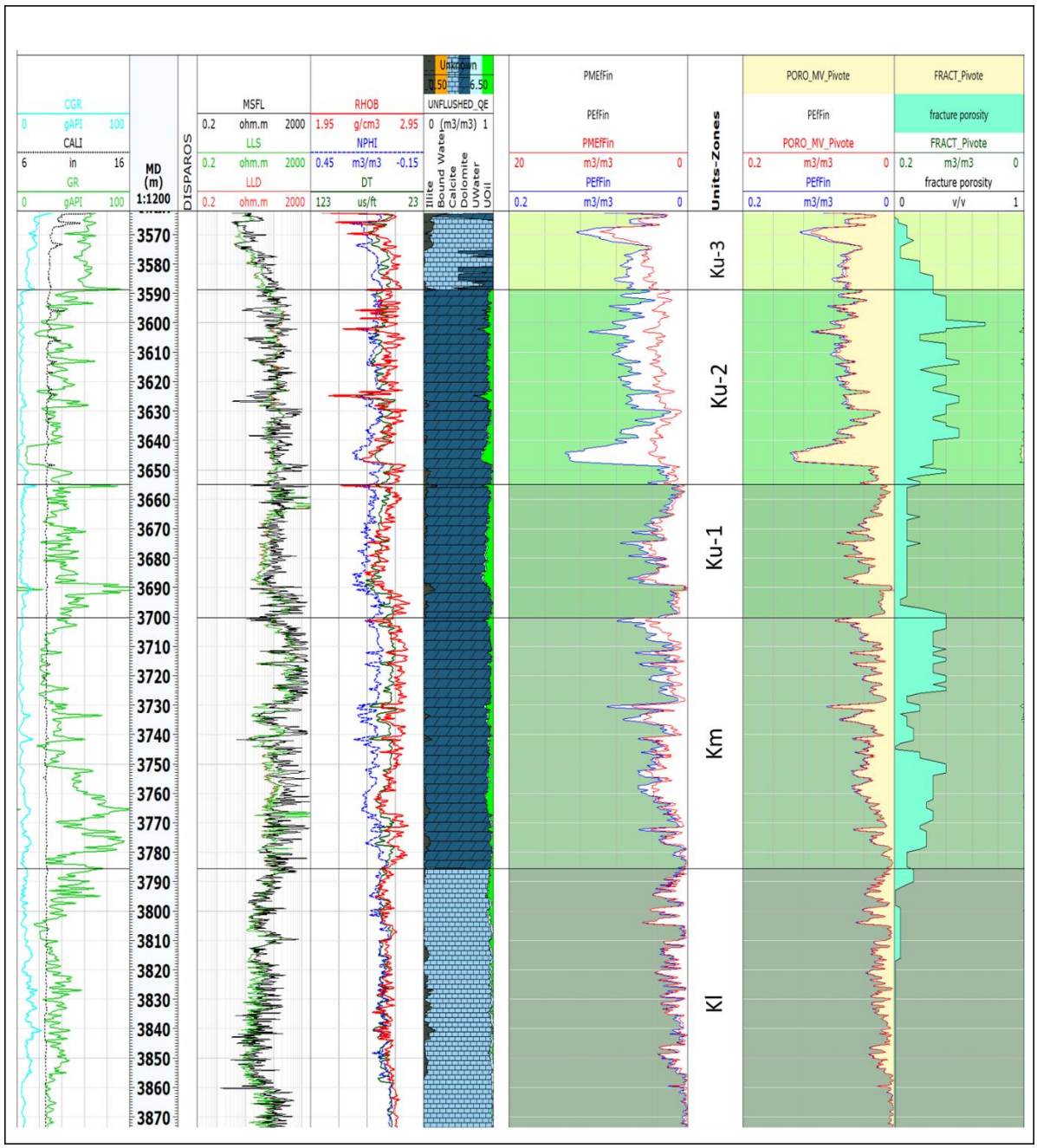


**Figure 3-9.** Porosity partition for well A-1. In the 6th track from left to right, is the partition from NMR log. In the 7th track is the partition from the Lopez and Viro (2002) method. And in the last track is the proportion of secondary porosity in the left side of the track from image logs and, the secondary porosity from Lopez and Viro (2002) in the right side of the same track.

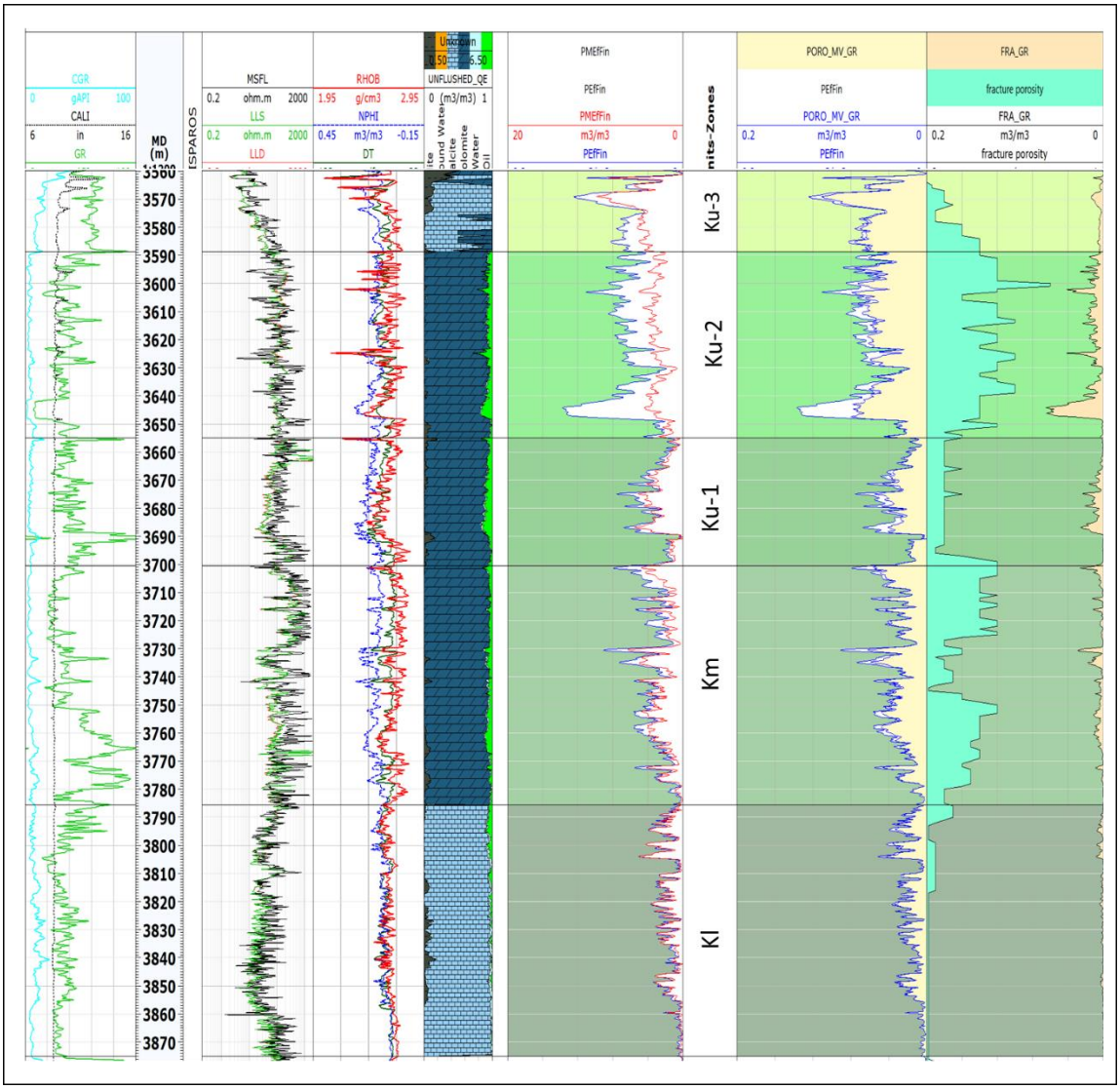


**Figure 3-10.** Porosity partition for well A-1. In the 6th track from left to right, is the partition from NMR log. In the 7th track is the partition from Gomez-Rivero (1981) method. And in the last track is the proportion of secondary porosity in the left side of the track from image logs and, the secondary porosity from Gomez-Rivero (1981) in the right side of the last track.

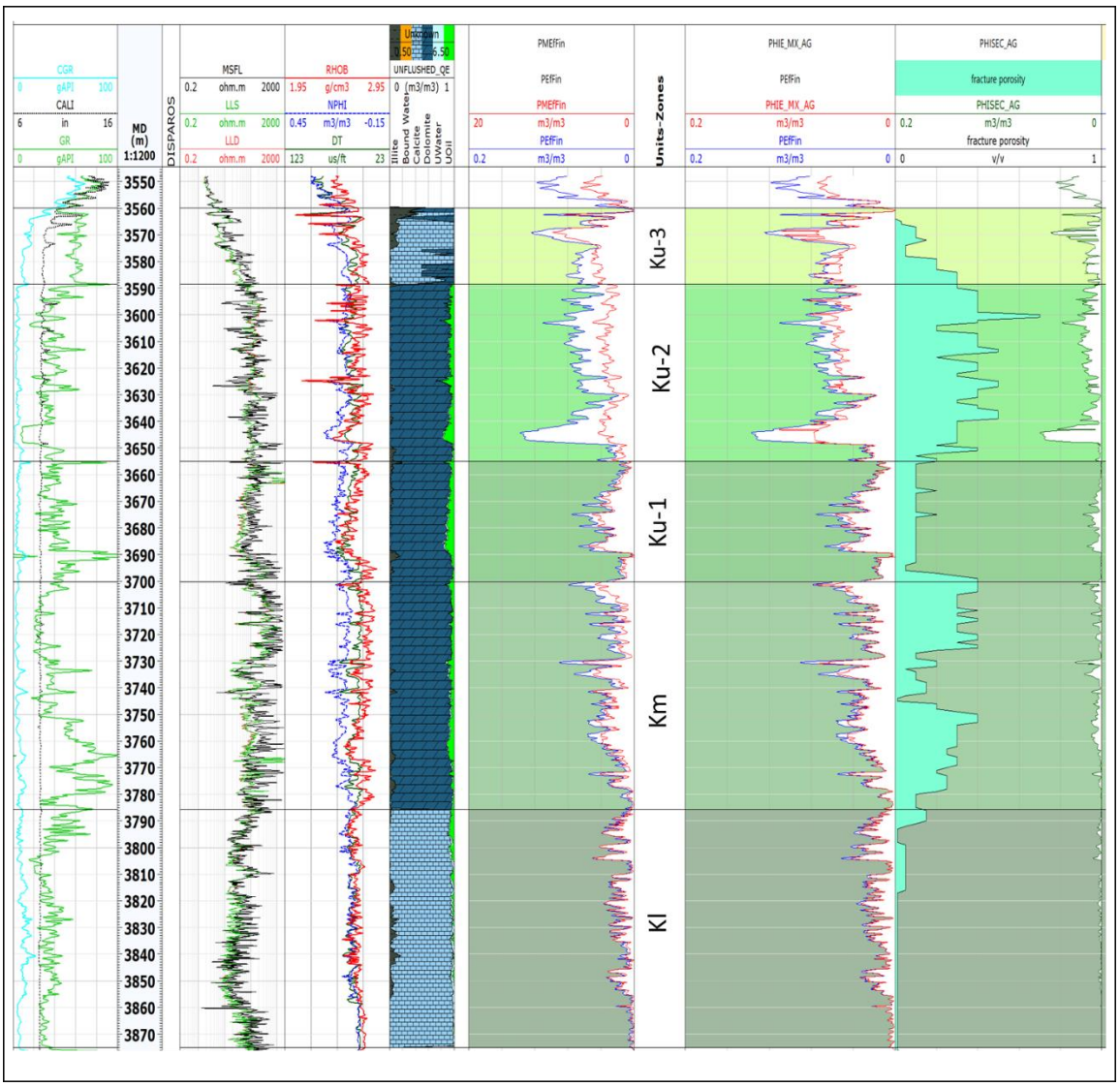


**Figure 3-11.** Porosity partition for well A-1, in the 6th track from left to right, is the partition from NMR log. In the 7th track is the partition from Aguilera (1976) method. And in the last track is the proportion of secondary porosity in the left side of the track from image logs and, the secondary porosity from Aguilera (1976).

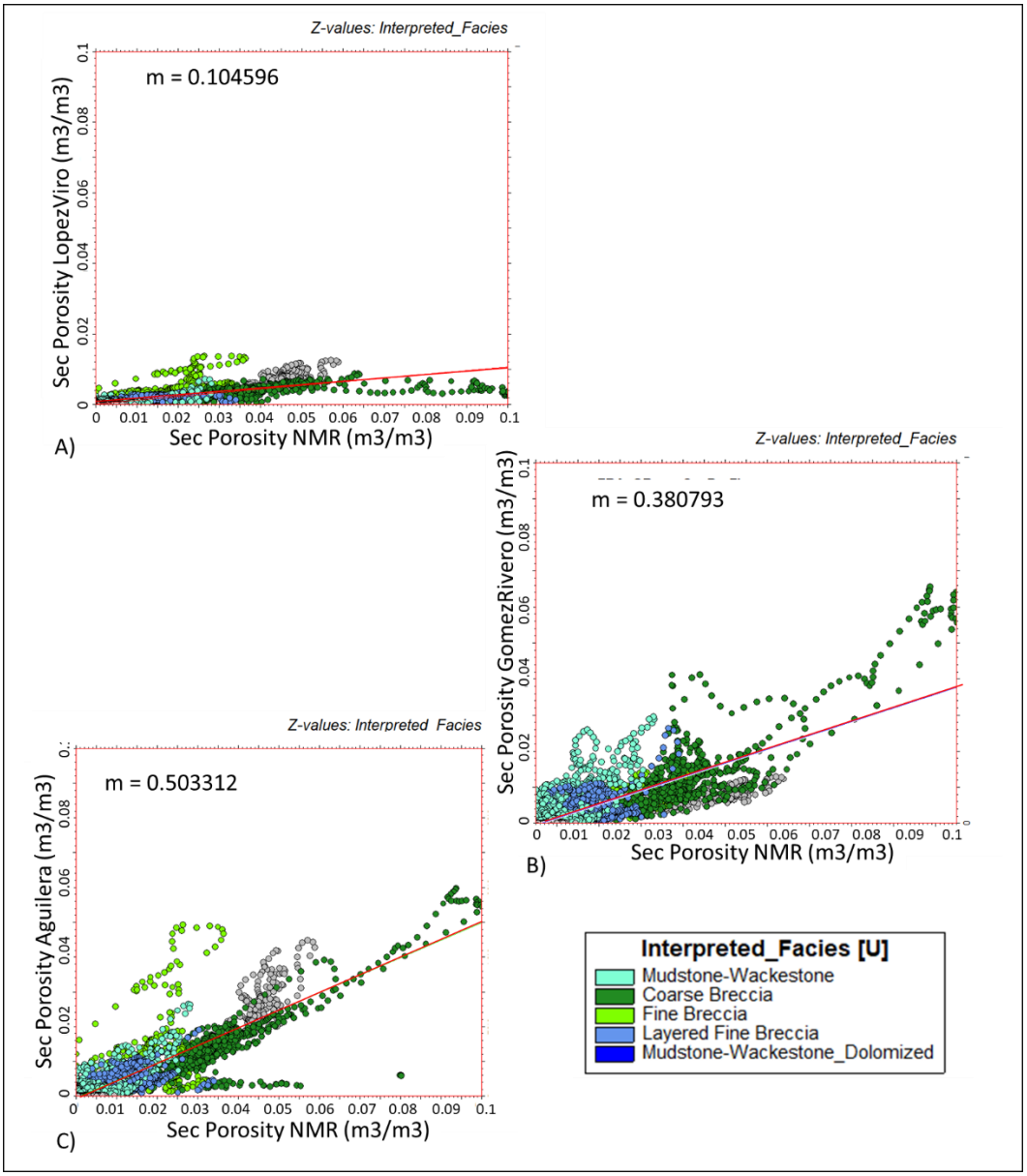


**Figure 3-12.** Cross-plots of Secondary Porosity for the Well A-1 from NMR with vs Lopez and Viro (2002) (pivot method) (A), vs Gomez-Rivero (1981) (B) and, vs Aguilera (1976) (C). For this well, Aguilera method had a higher likeness.

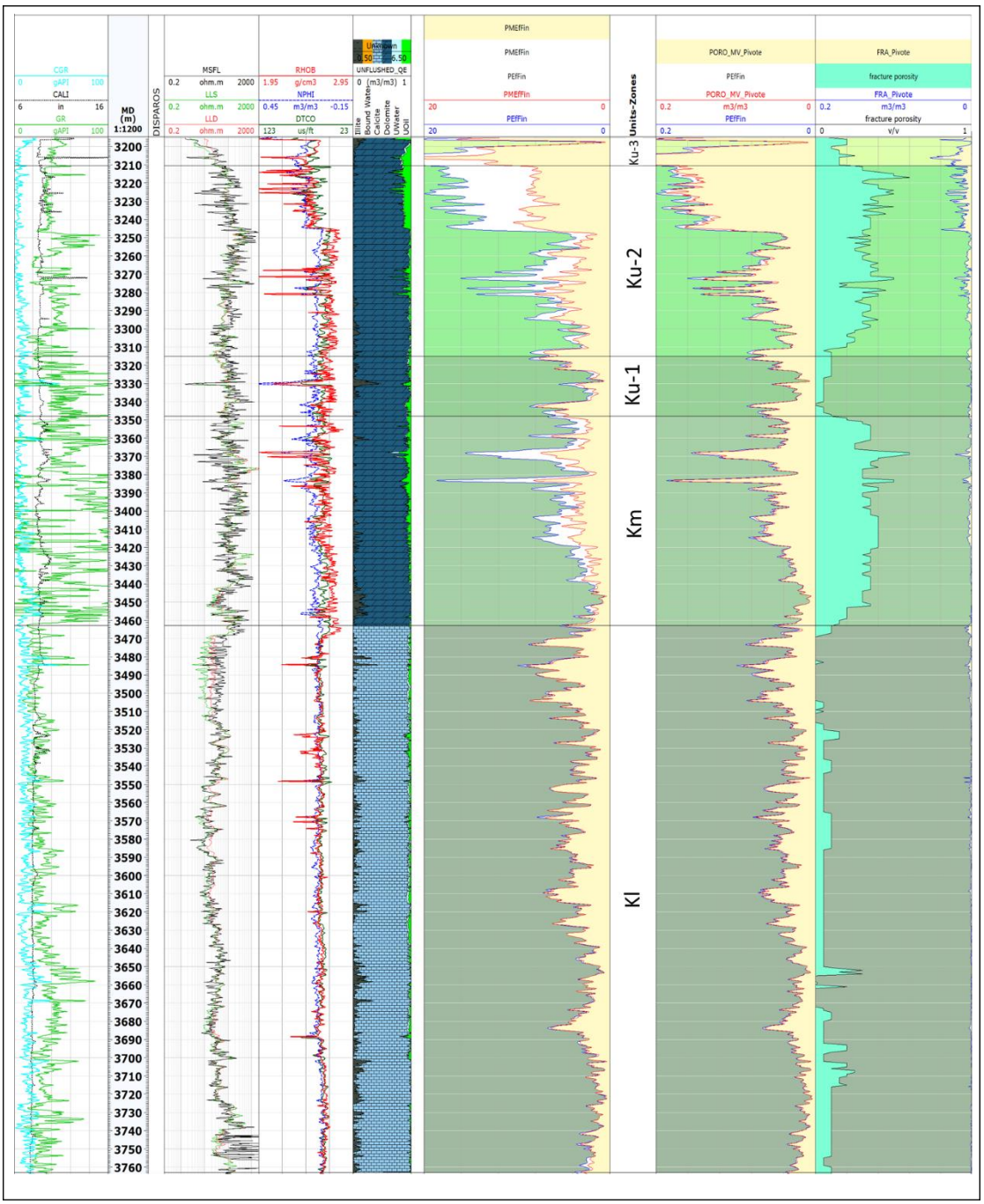


**Figure 3-13.** Porosity partition for well B-1. In the 6th track from left to right, is the partition from NMR log. In the 7th track is the partition from the Lopez and Viro (2002) method. And in the last track is the proportion of secondary porosity in the left side of the track from image logs and, the secondary porosity from Lopez and Viro (2002) in the right side.

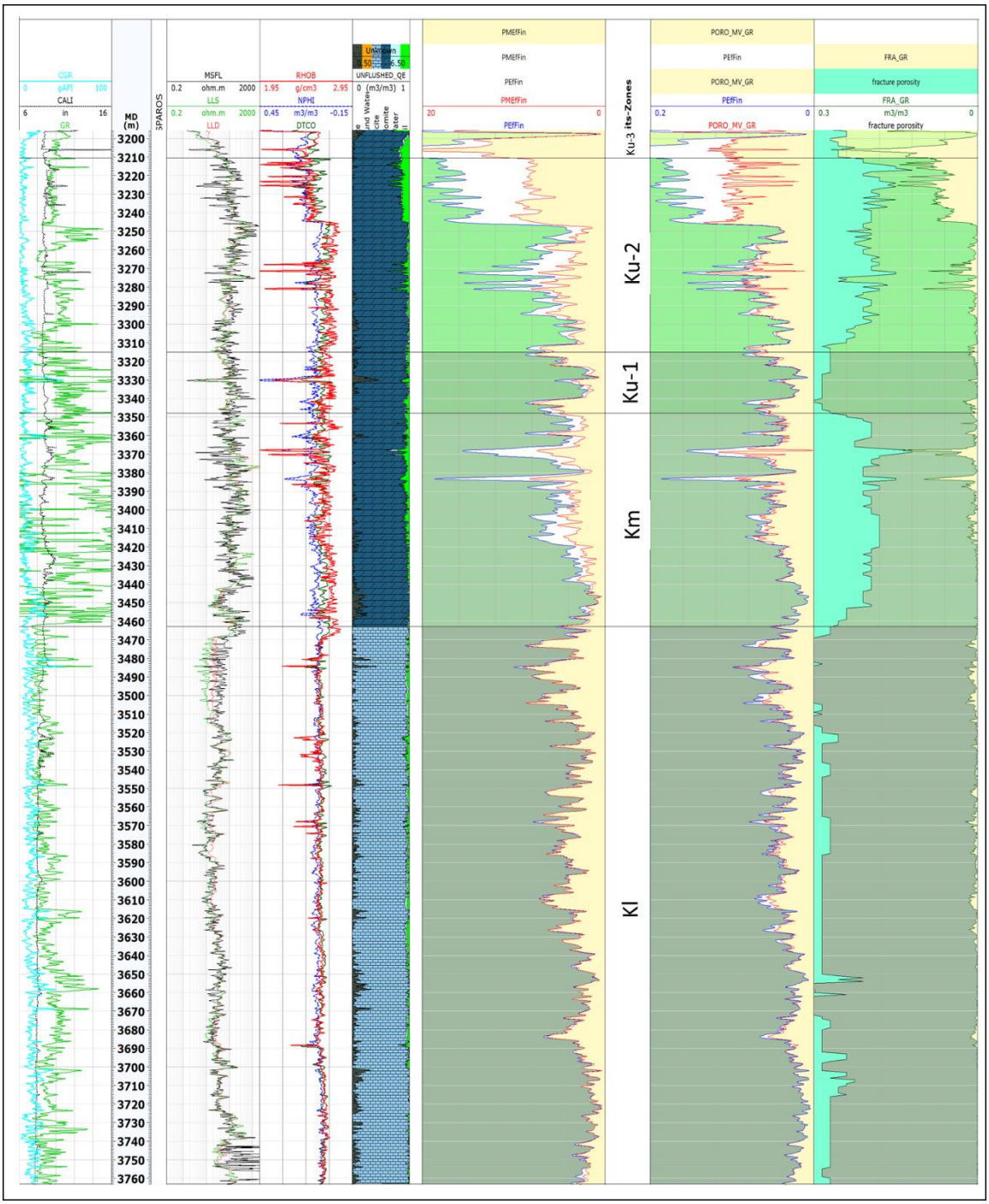


**Figure 3-14.** Porosity partition for well B-1. In the 6th track from left to right, is the partition from NMR log. In the 7th track is the partition from the Gomez-Rivero (1981) method. And in the last track is the proportion of secondary porosity in the left side of the track from image logs and, the secondary porosity from Gomez-Rivero (1981) in the right side of the track.

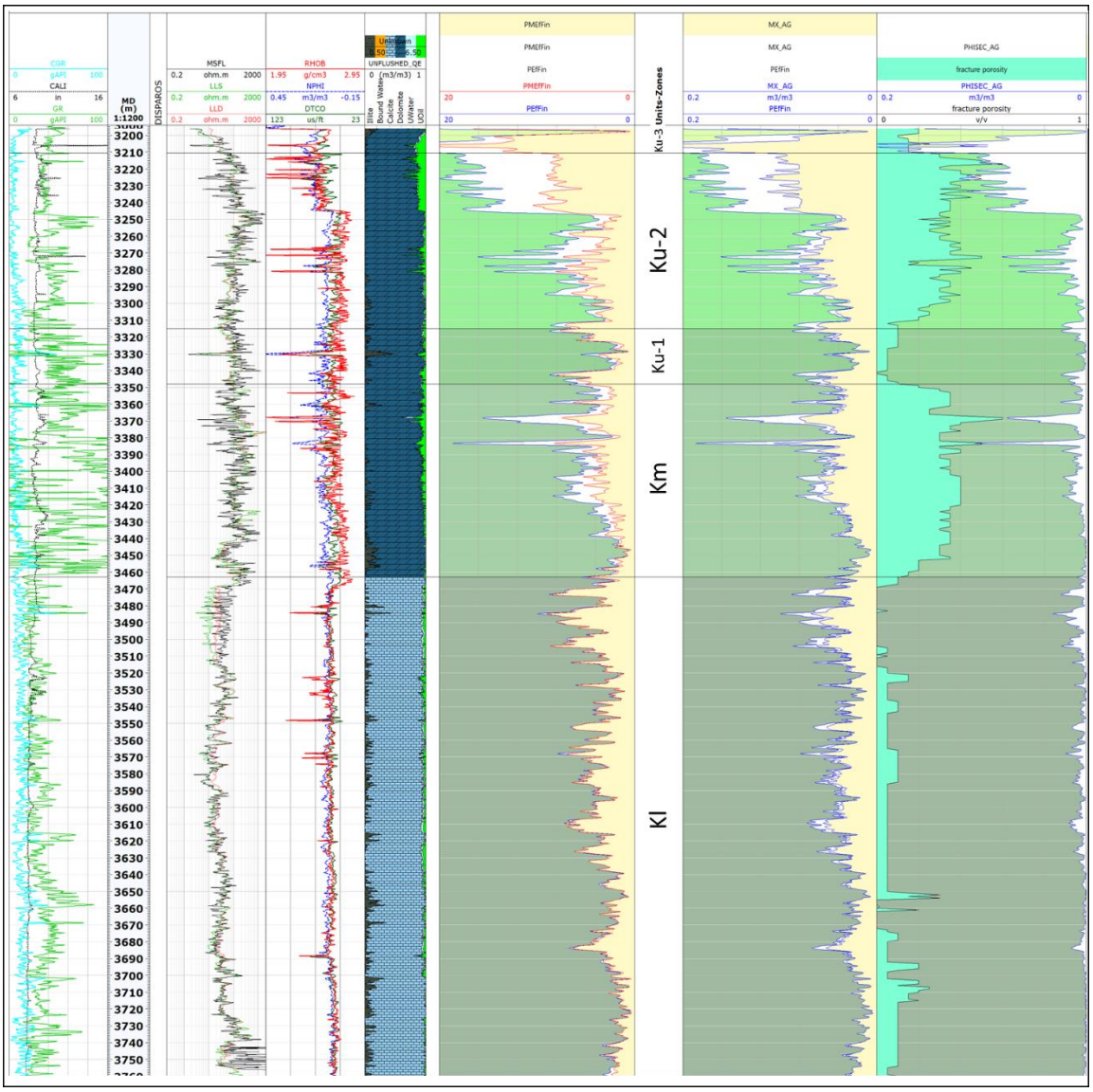


**Figure 3-15** Porosity partition for well B-1. In the 6th track from left to right, is the partition from NMR log. In the 7th track is the partition from the Aguilera (1976) method. And in the last track is the proportion of secondary porosity in the left side of the track from image logs and, the secondary porosity from Aguilera (1976) in the right side.

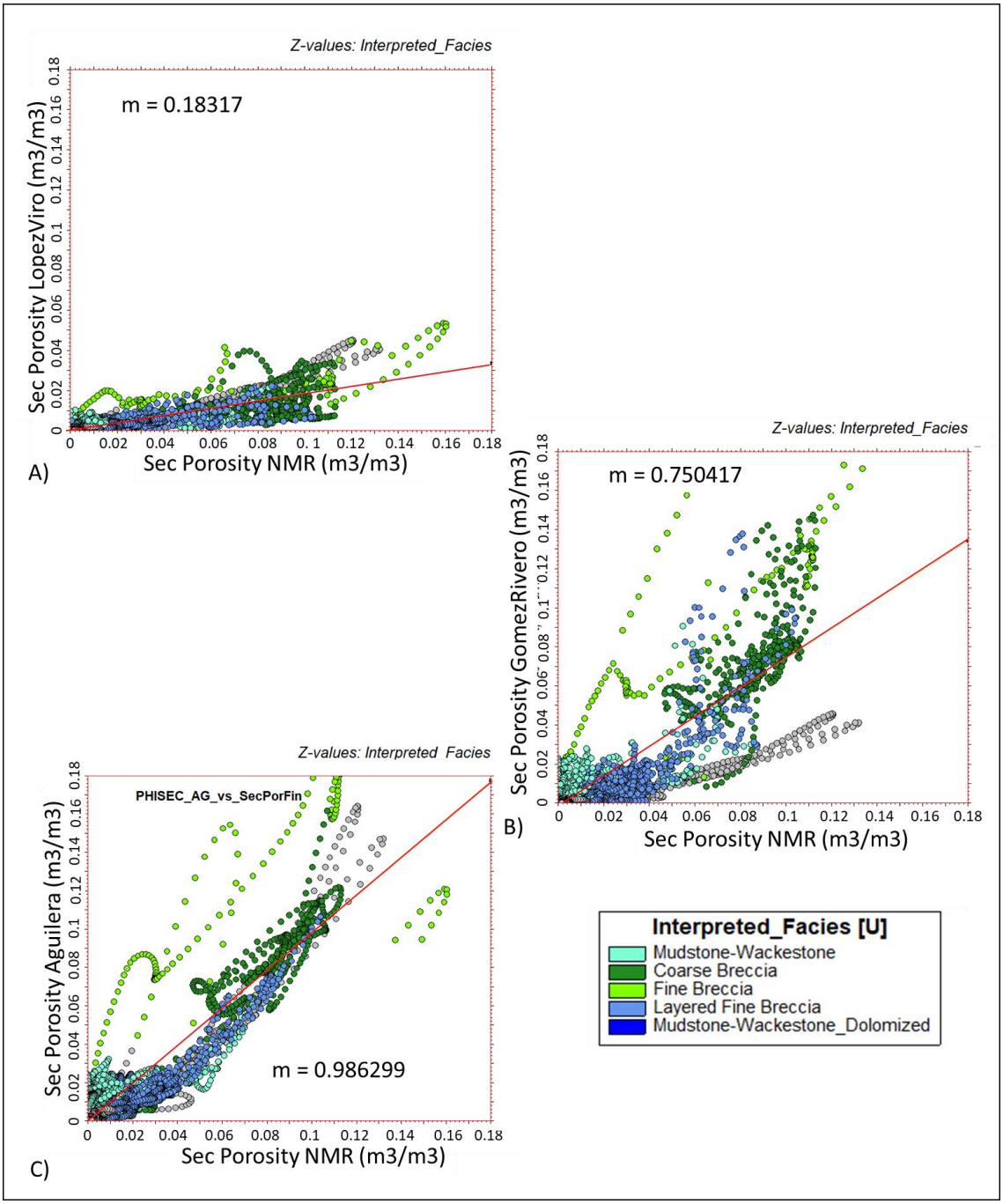


**Figure 3-16.** Cross-plots for the Well B-1 of Secondary Porosity from NMR with vs Lopez and Viro (2002) (pivot method) (A), vs Gomez-Rivero (1981) (B) and, vs Aguilera (1976) (C). For this well, the Aguilera method had a higher likeness and the highest value overall (m=0.986299).

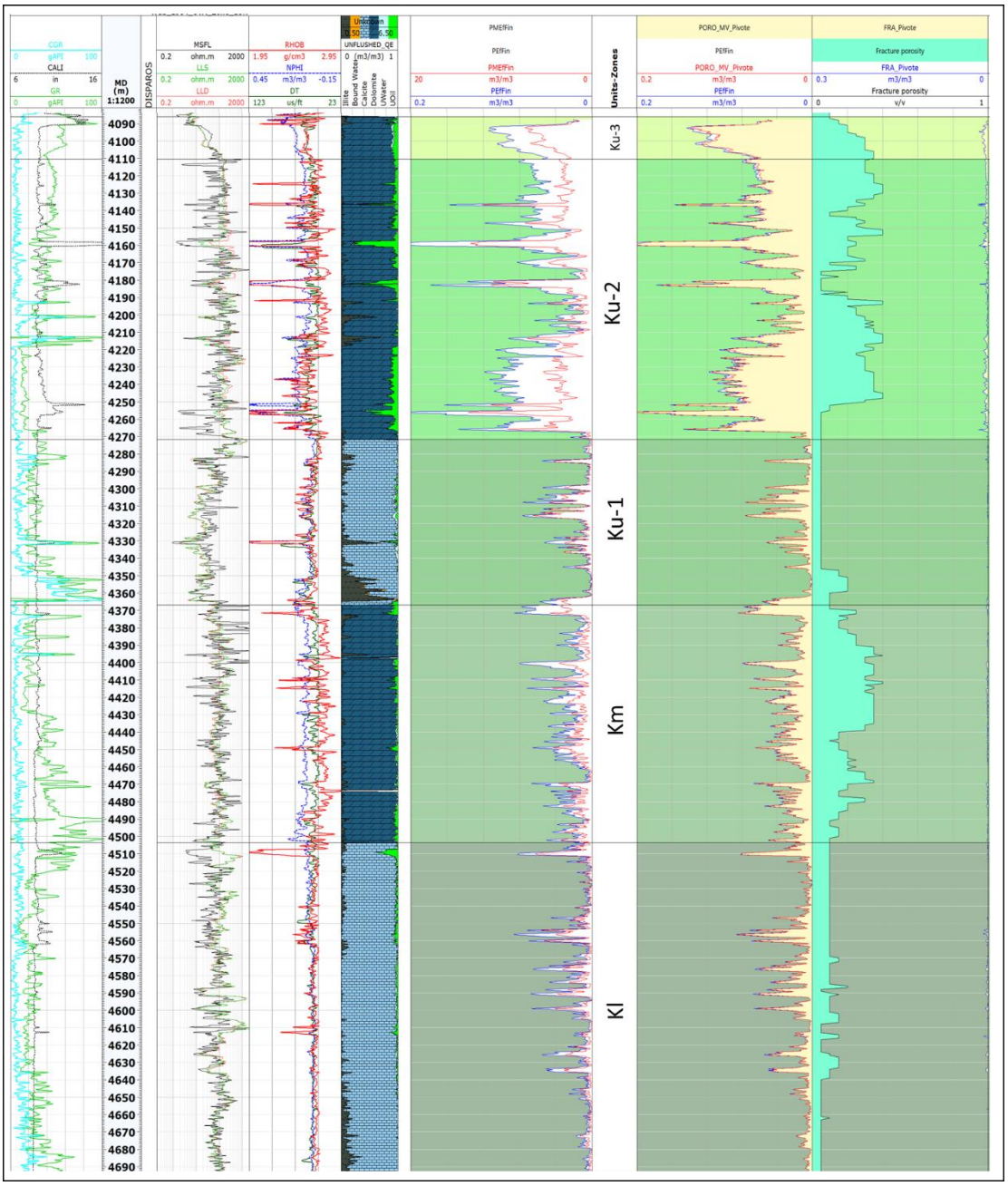


**Figure 3-17.** Porosity partition for well C-DL1, in the 6th track from left to right, is the partition from NMR log. In the 7th track is the partition from the Lopez and Viro (2002) method. In the right side of the last track is the proportion of secondary porosity from Lopez and Viro (2002). In the same track in the left side of the track is the secondary porosity proportion from image logs.

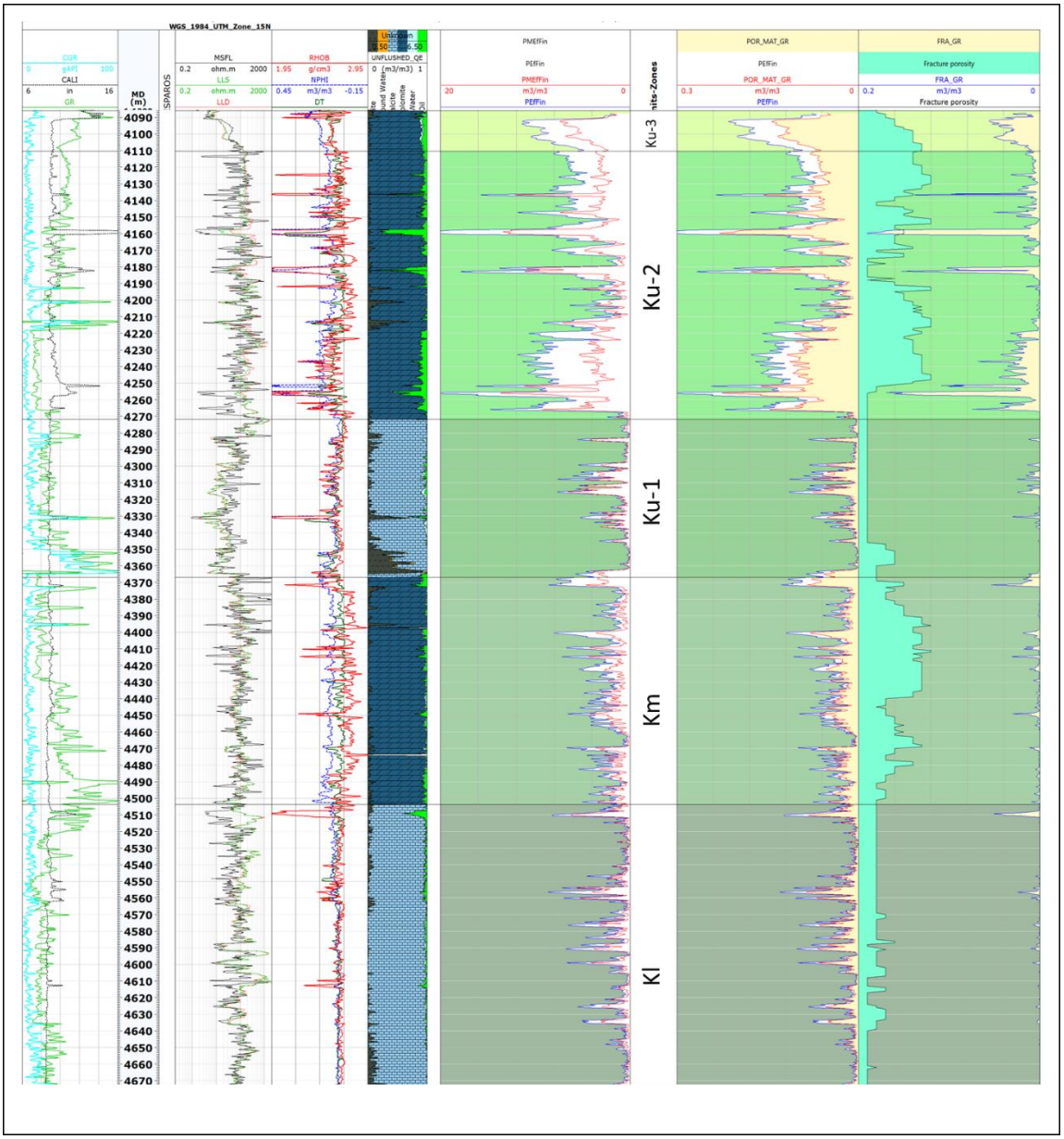


**Figure 3-18.** Porosity partition for well C-DL1, in the 6th track from left to right, is the partition from NMR log. In the 7th track is the partition from Gomez-Rivero (1981) method. And in the last track is the proportion of secondary porosity in the left side of the track from image logs and, the secondary porosity from Gomez-Rivero (1981).

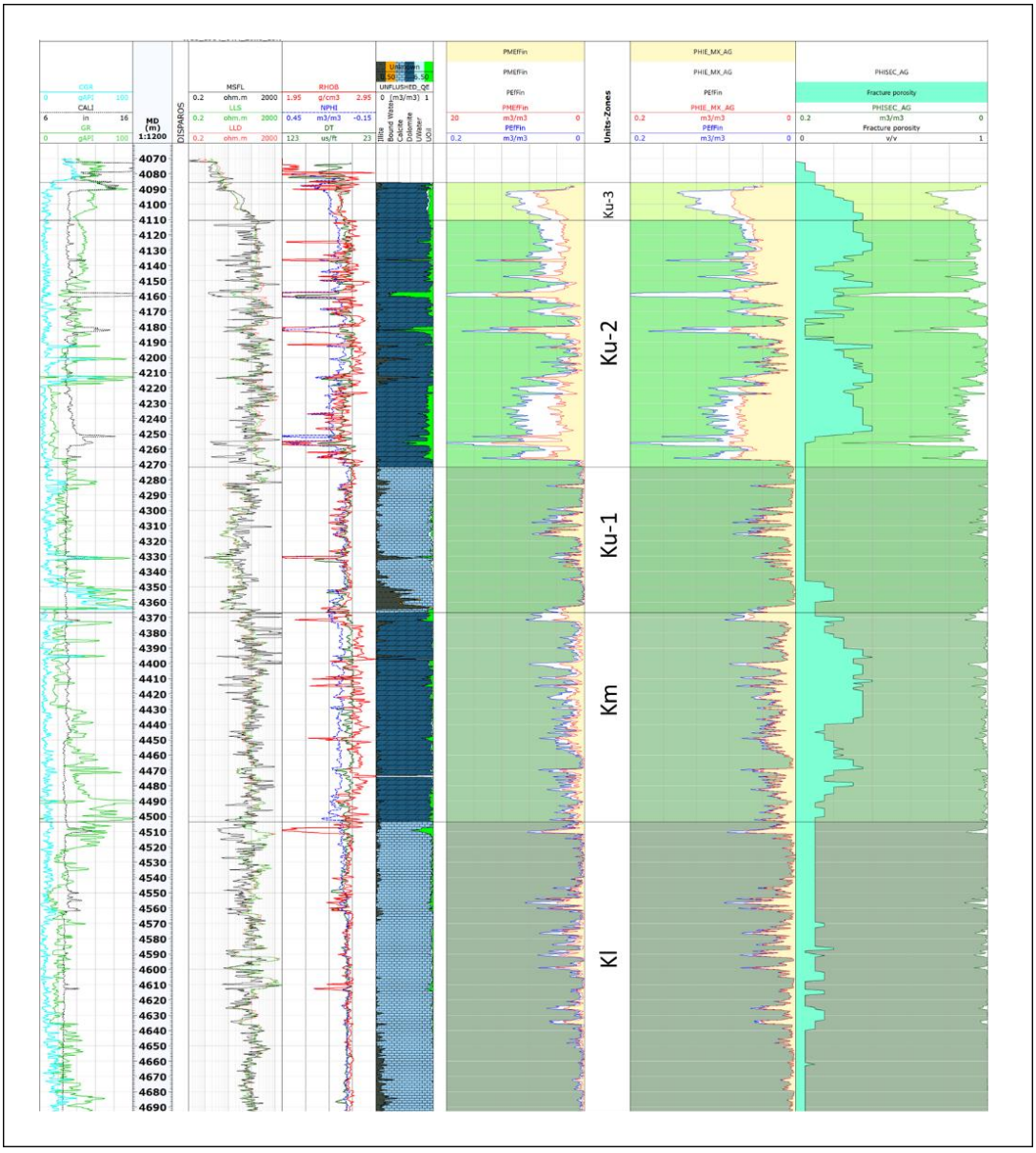


**Figure 3-19.** Porosity partition for well C-DL1, in the 6th track from left to right,is the partition from NMR log. In the 7th track is the partition from Aguilera (1976) method. And in the last track is the proportion of secondary porosity in the left side of the track from image logs and, the secondary porosity from Aguilera (1976).

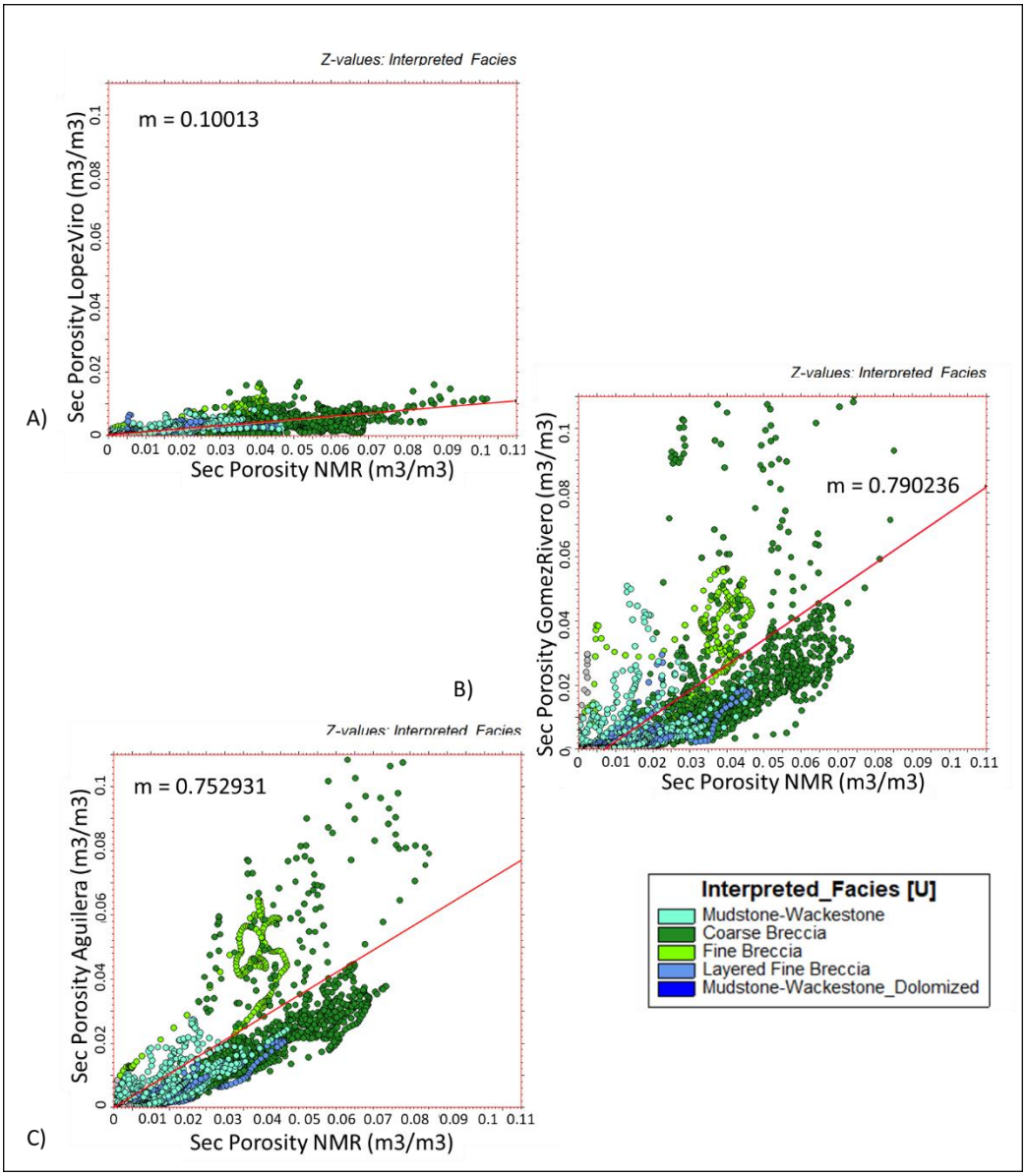


**Figure 3-20.** Cross-plots for the Well C-DL1 of Secondary Porosity form NMR with vs Lopez and Viro (2002) (pivot method) (A), vs Gomez-Rivero (1981) (B) and, vs Aguilera (1976) (C). This well was the only one where Gomez-Rivero method had a higher likeness than Aguilera method.

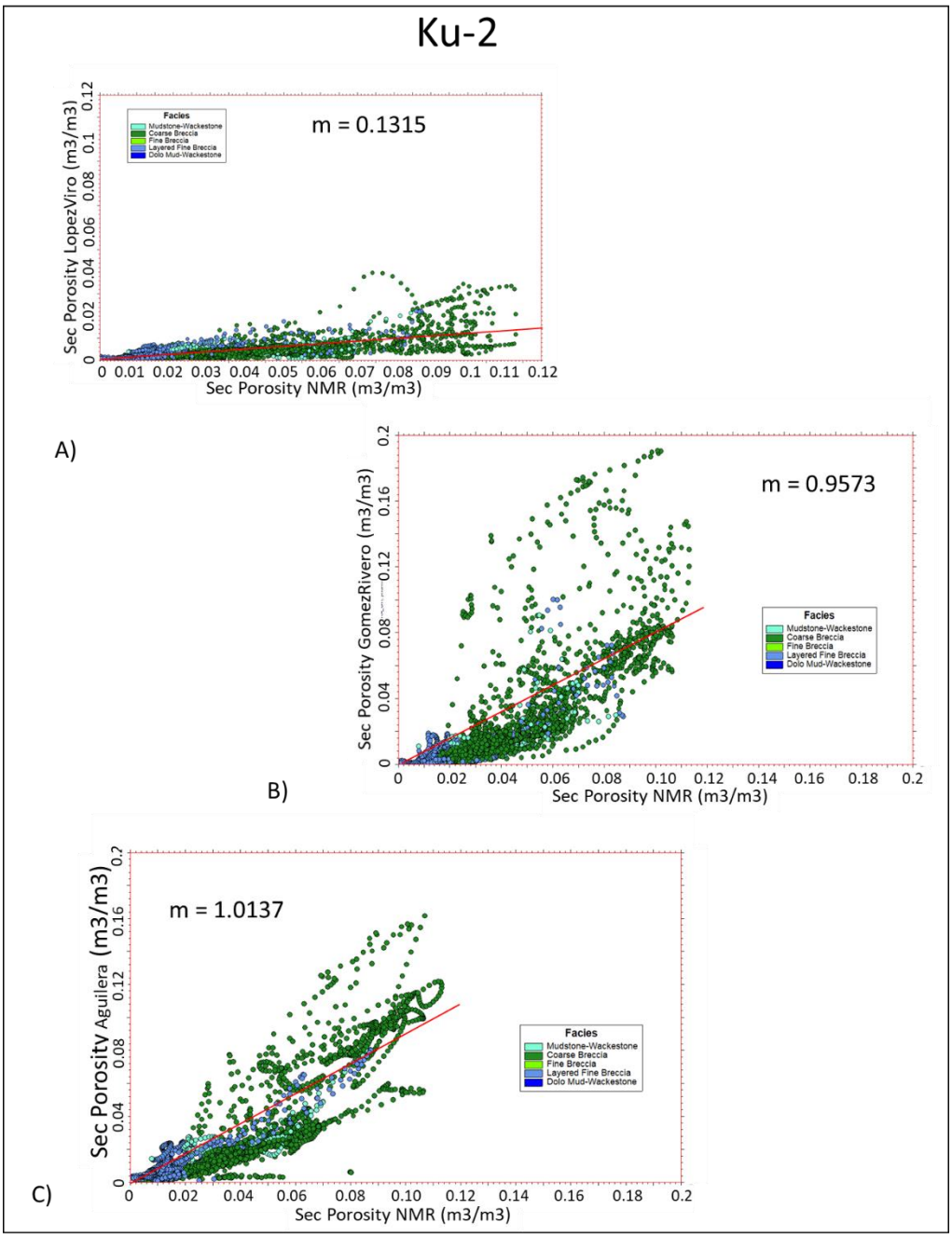


**Figure 3-21.** Cross-plot for the unit Ks-2, of Secondary Porosity from NMR with vs Lopez and Viro (2002) (pivot method) (A), vs Gomez-Rivero (1981) (B) and, vs Aguilera (1976) (C). Aguilera and Gomez-Rivero had a good performance for this unit with a slope value very close to m=1.

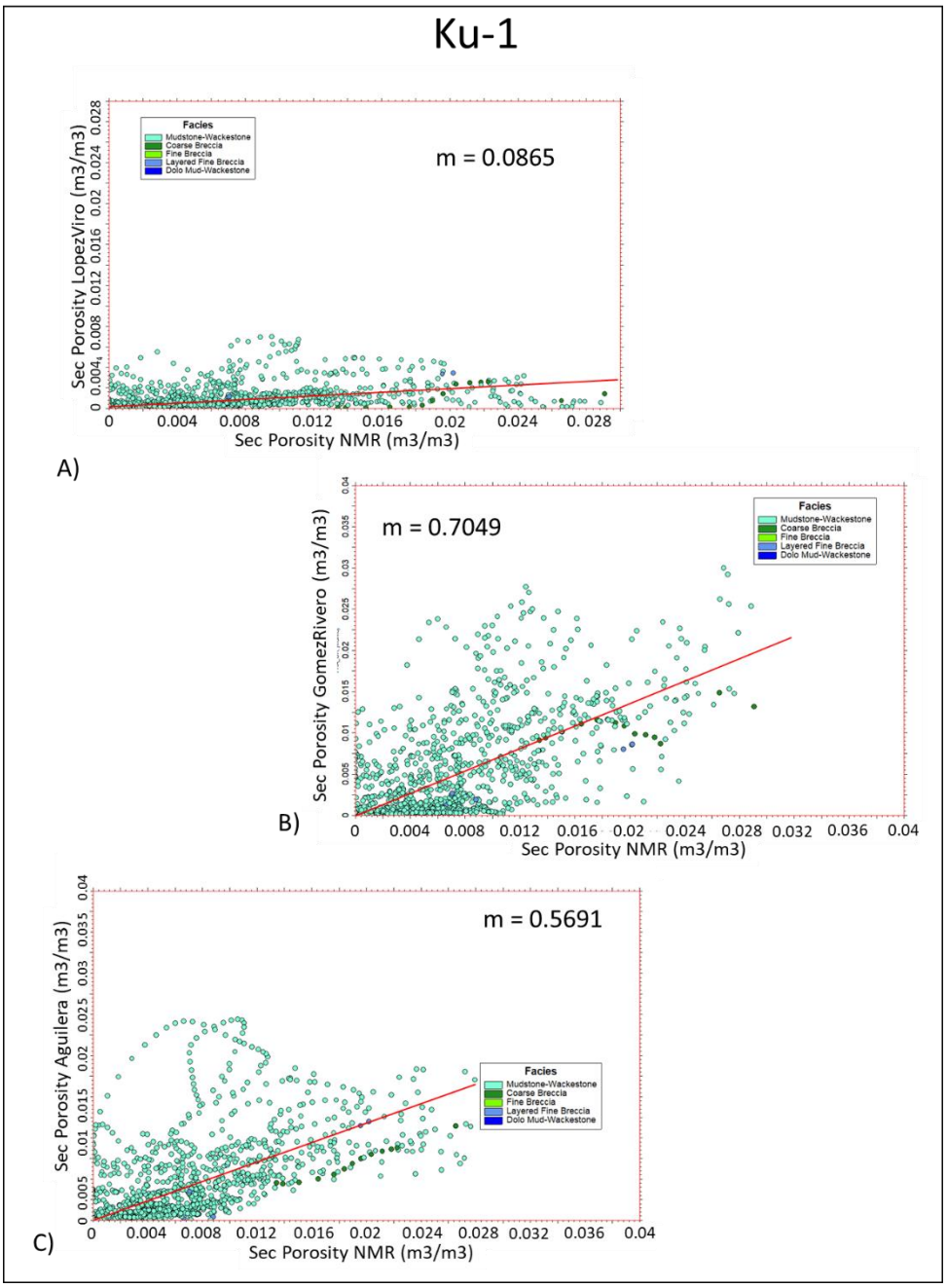


**Figure 3-22.** Cross-plot for the unit Ks-1, of Secondary Porosity from NMR with vs Lopez and Viro (2002) (pivot method) (A), vs Gomez-Rivero (1981) (B) and, vs Aguilera (1976) (C). Gomez-Rivero had the best performance for this unit with a slope m=0.7049.

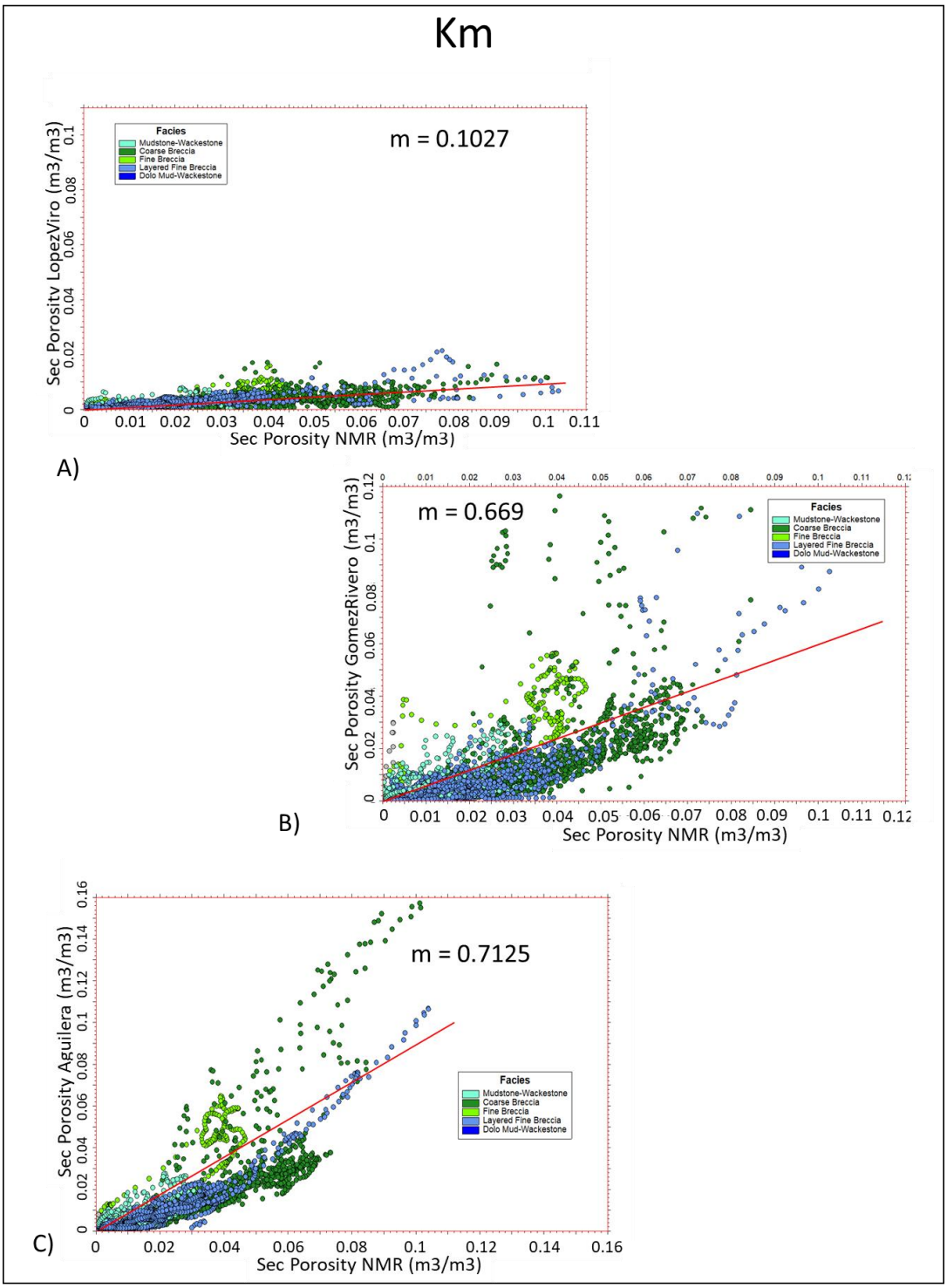


**Figure 3-23.** Cross-plot for the unit Km, of Secondary Porosity from NMR with vs Lopez and Viro (2002) (pivot method) (A), vs Gomez-Rivero (1981) (B) and, vs Aguilera (1976) (C). Aguilera had the best performance for this unit with a slope m=0.7125.

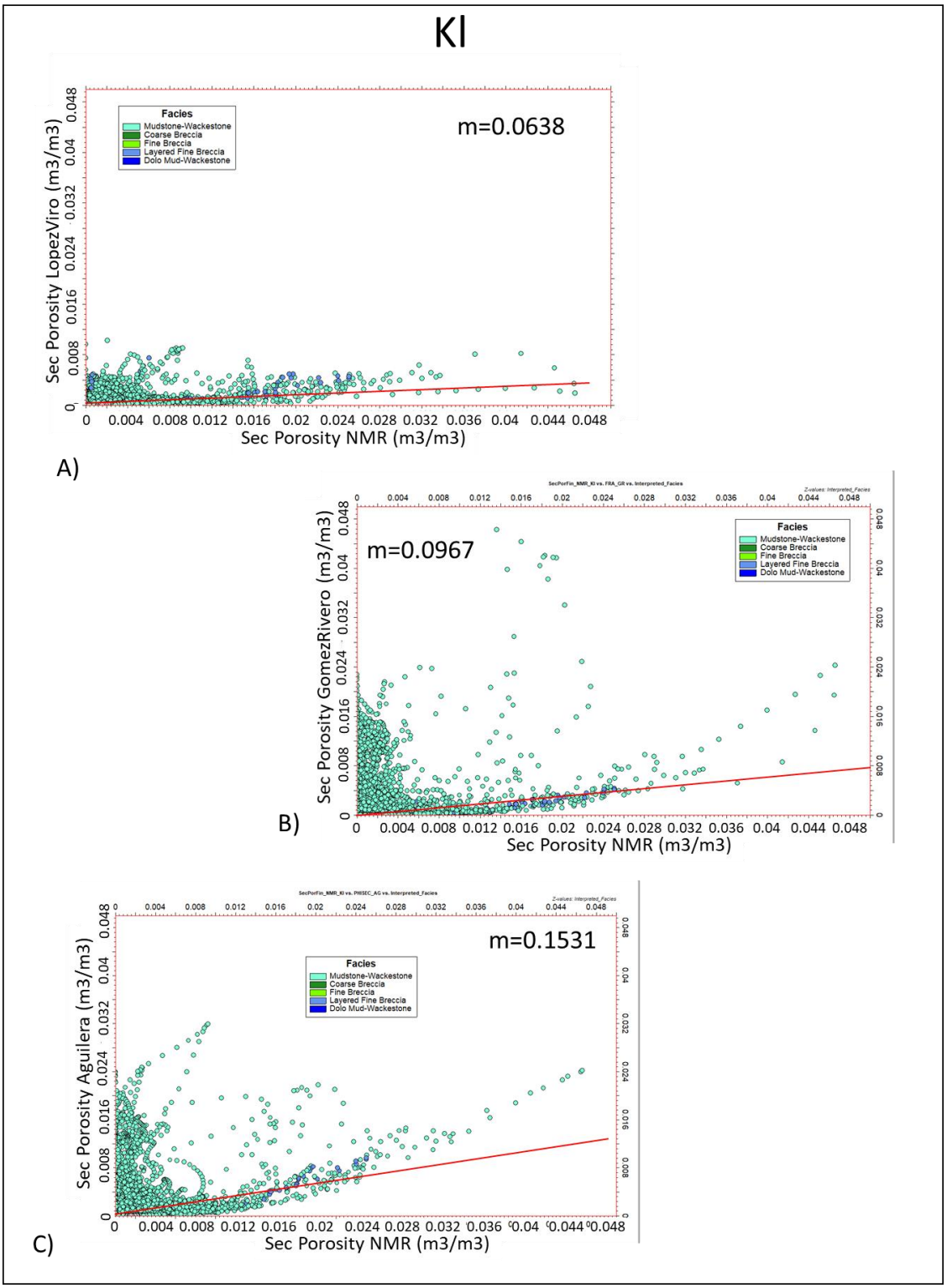


**Figure 3-24.** Cross-plots for the unit Ki, Secondary Porosity from NMR vs Lopez and Viro (2002) (pivot method) (A), vs Gomez-Rivero (1981) (B) and, vs Aguilera (1976) (C). This unit had the poorest likeness. The Aguilera method had the best performance for this unit with a low slope value m=0.1531.

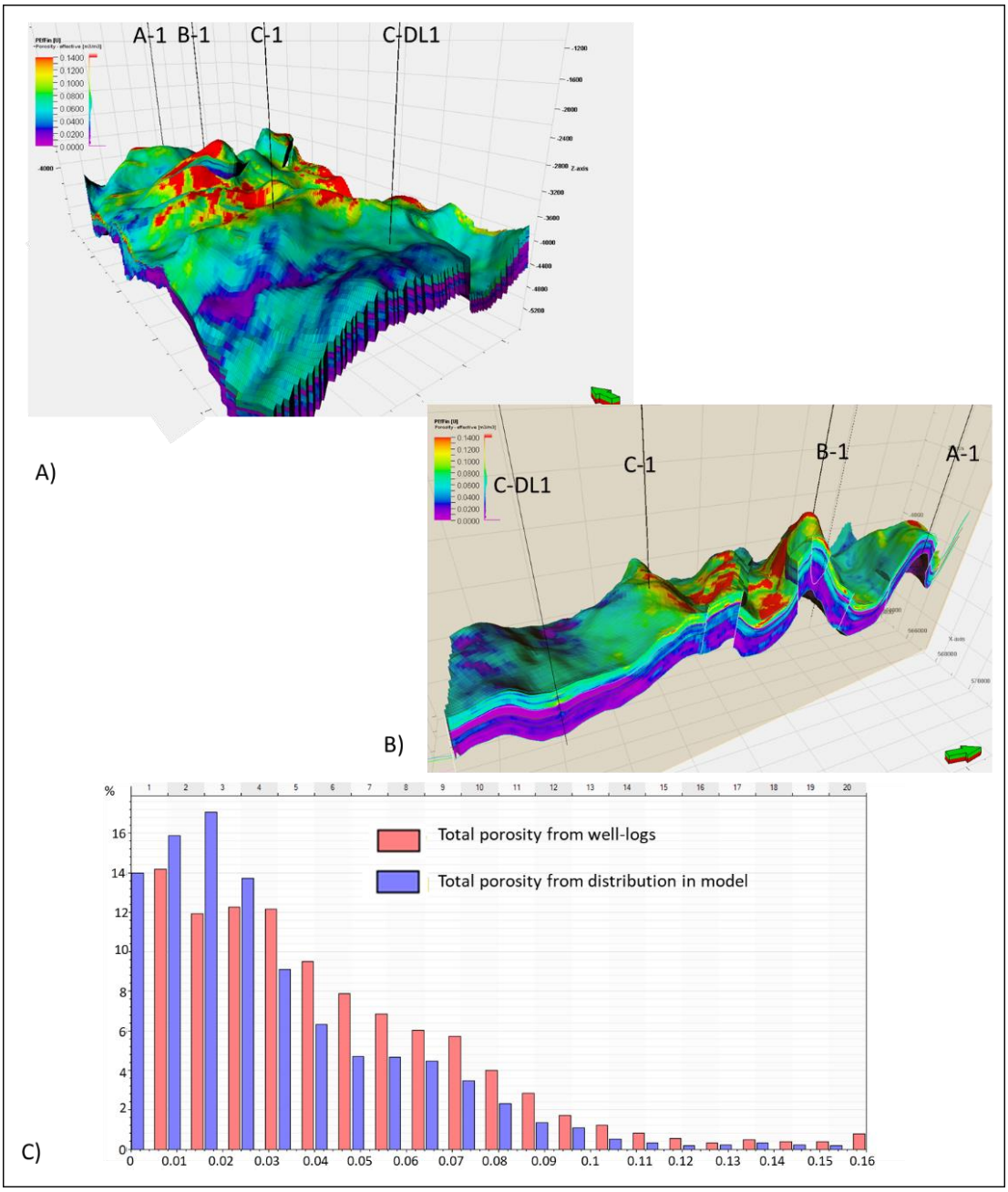


**Figure 3-25.** Total effective porosity in the 3D geo-cellular model. A) A general isometric view of the total porosity property. Higher values are located in the central and northern parts of the model. B) Cut across the model higher porosity values are in the upper part of the model and the lowest is located in the bottom part. C) Histogram of the porosity values in the model and in the original petrophysical estimation. The distribution is honoring the original values from petrophysics.

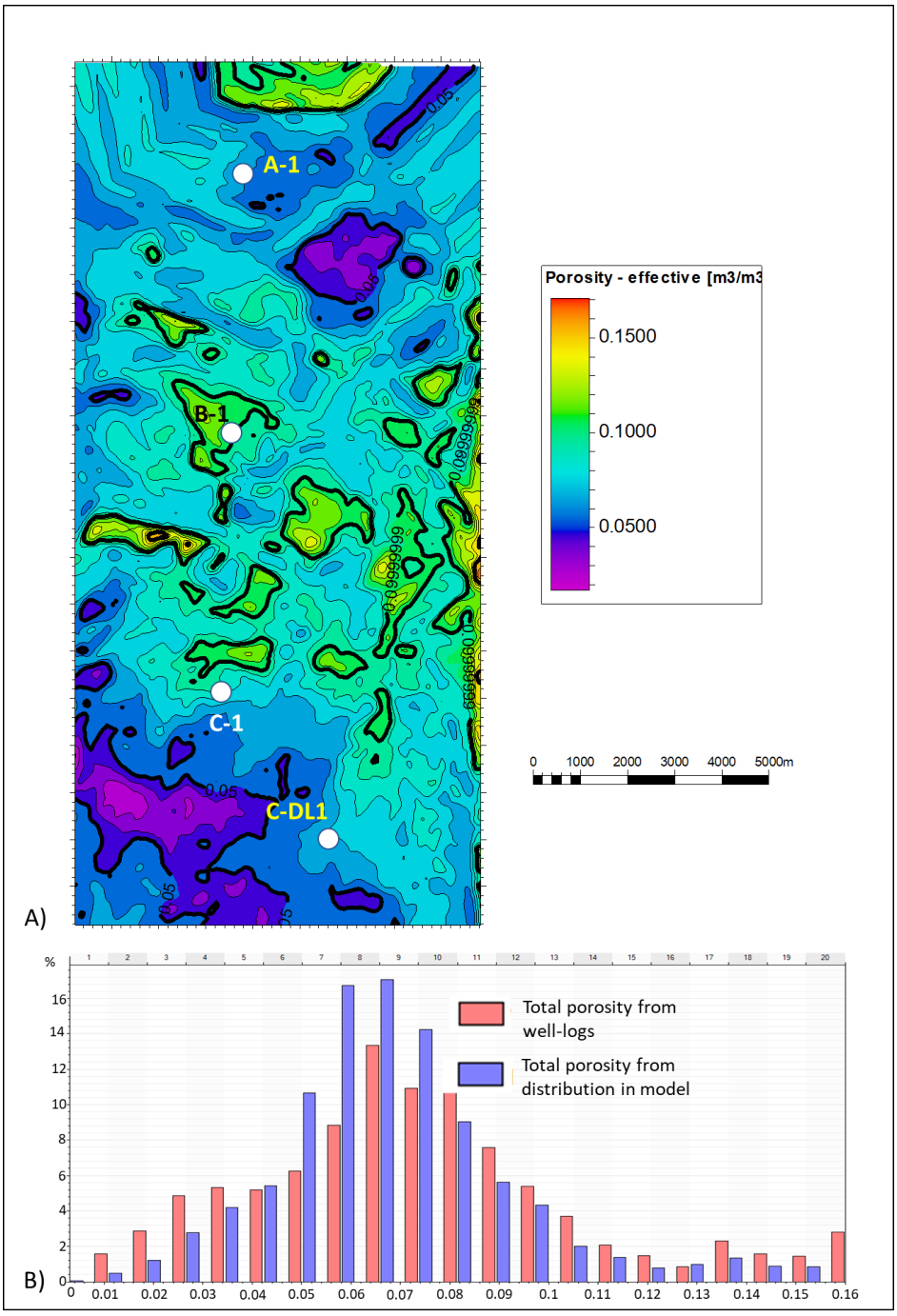


**Figure 3-26.** A) Map of average total effective porosity for Ku-2 zone. Higher values are presents in the central part of the area. B) Histogram of the distribution from the model and the original porosity from petrophysics. The distribution honors the original porosity from petrophysics.

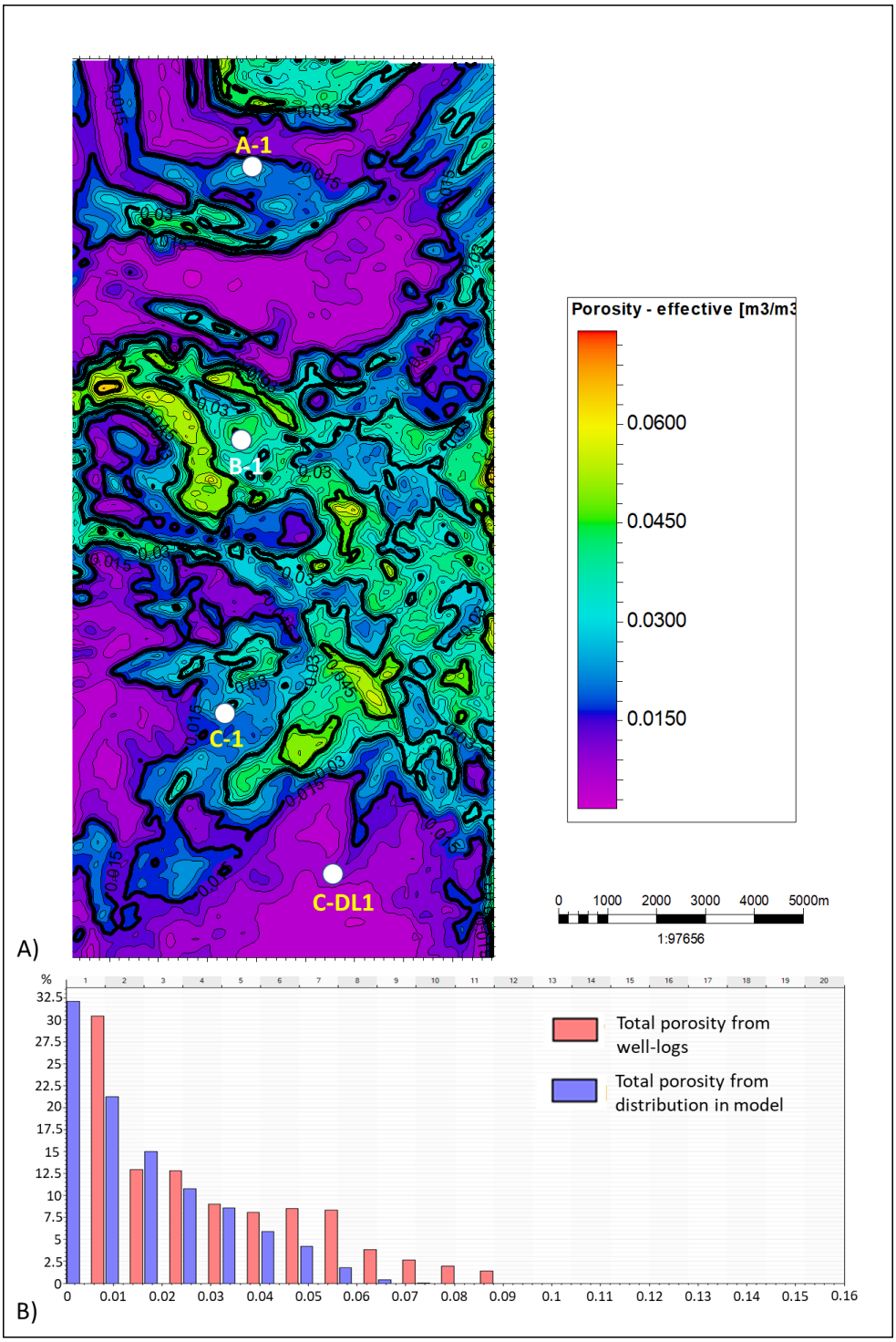


**Figure 3-27.** A) Map of average total effective porosity for Ku-1 zone. Higher values look oriented to the structural features of the area. B) Histogram of the distribution from the model and the original porosity from petrophysics. The distribution honors the original porosity from petrophysics.

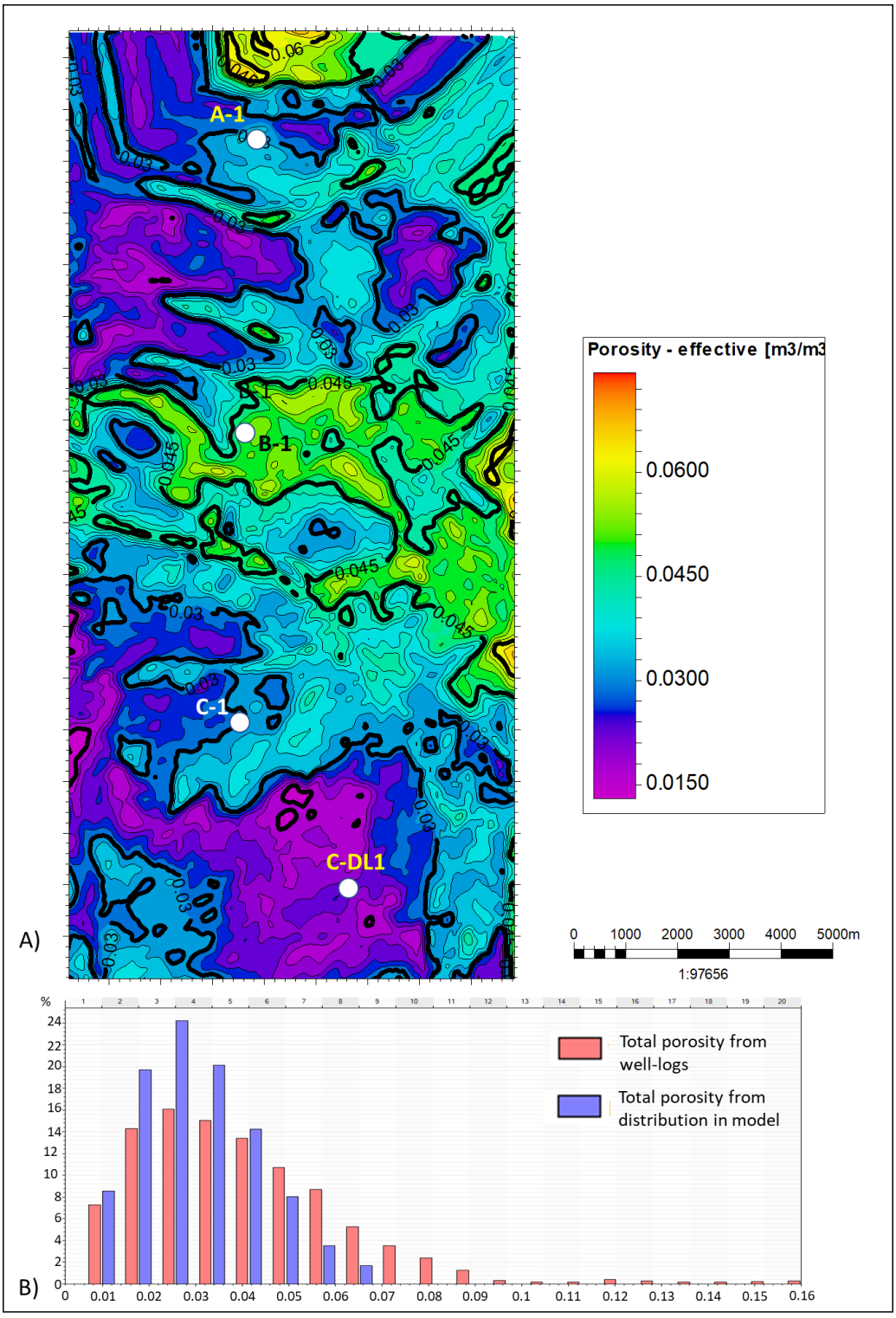


**Figure 3-28.** A) Map of average total effective porosity for Km zone. Higher values are located in the north and center of the study area, similar to the distribution of Ku-2 zone. B) Histogram of the distribution from the model and the original porosity from petrophysics. The distribution honors the original porosity from petrophysics.

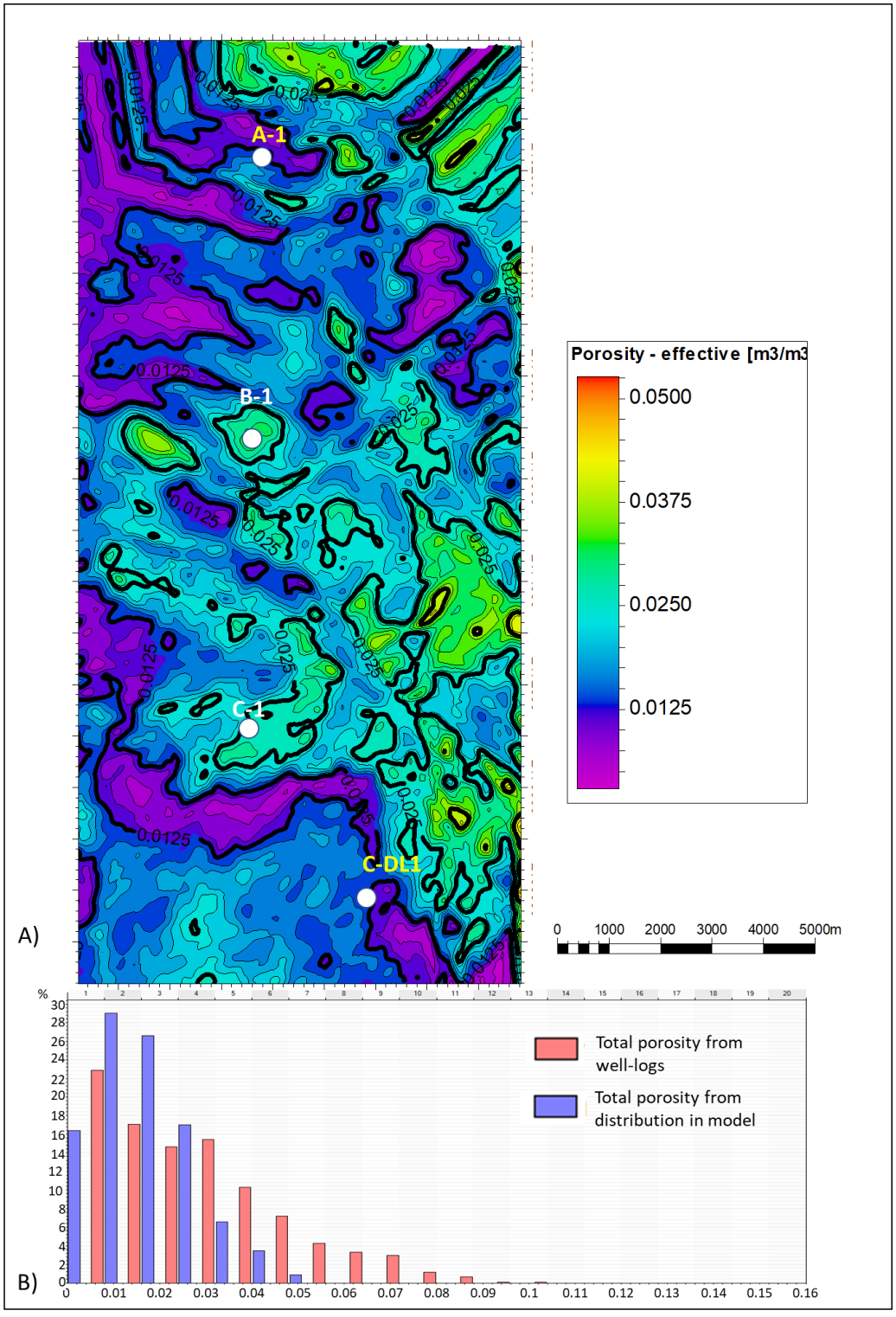


**Figure 3-29.** A) Map of average total effective porosity for Kl zone. In a similar way to the Km zone, higher values look oriented to the structural features of the area. B) Histogram of the distribution from the model and the original porosity from petrophysics. The distribution honors the original porosity from petrophysics.

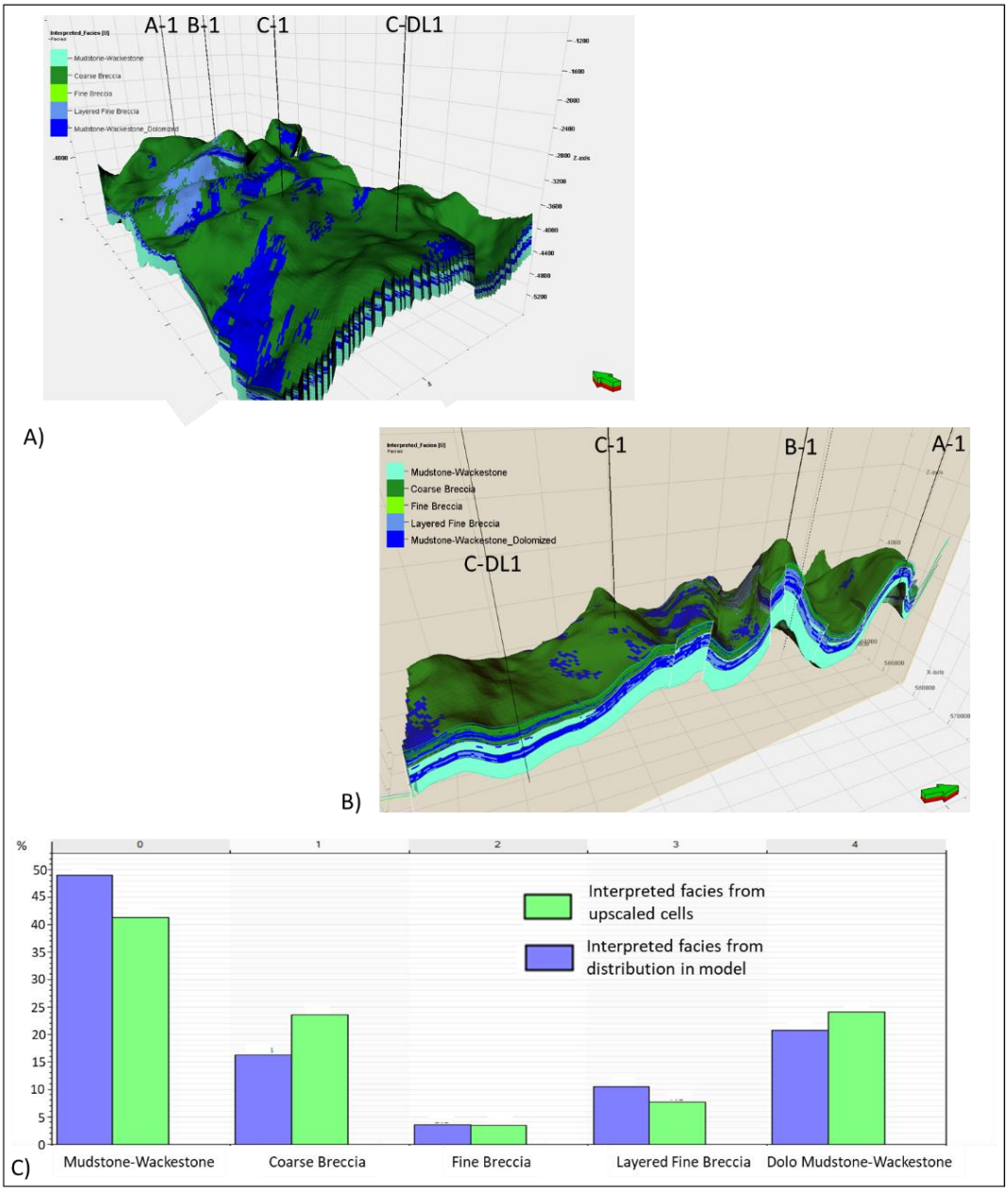


**Figure 3-30.** Lithofacies distribution in the 3D geo-cellular model. A) A general isometric view of the lithofacies, Coarse breccia facies predominates in the upper part of the model. However, there exists a presence of layered fine breccia and dolomitized mudstone-wackestone. B) Cut across the model, the distribution of facies corresponds to the expected geology. C) Histogram of the porosity values in the model and in the original petrophysical estimation. The distribution is honoring the original values from petrophysics.

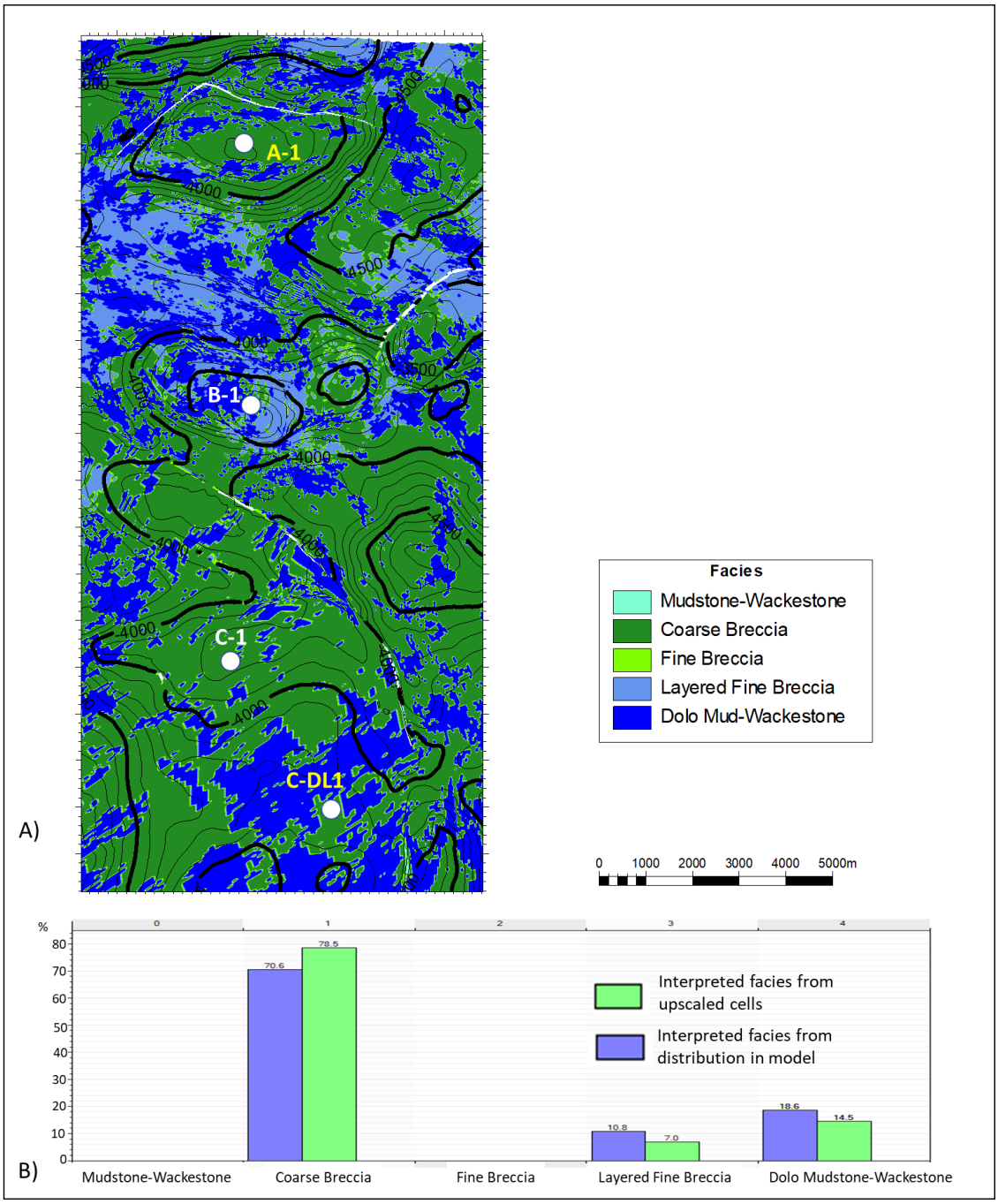


**Figure 3-31.** Lithofacies map for the unit Ku-2. The map shows the heterogeneity of this unit. Coarse breccia facie could be deposited over the mudstone-wackestone facie and the presence of layered fine breccia could indicate a different transport process along the one that deposits the coarse breccia. B) Histogram of the distribution from the model and the original lithofacies interpretation from the wells. The distribution honors the original lithofacies interpretation.

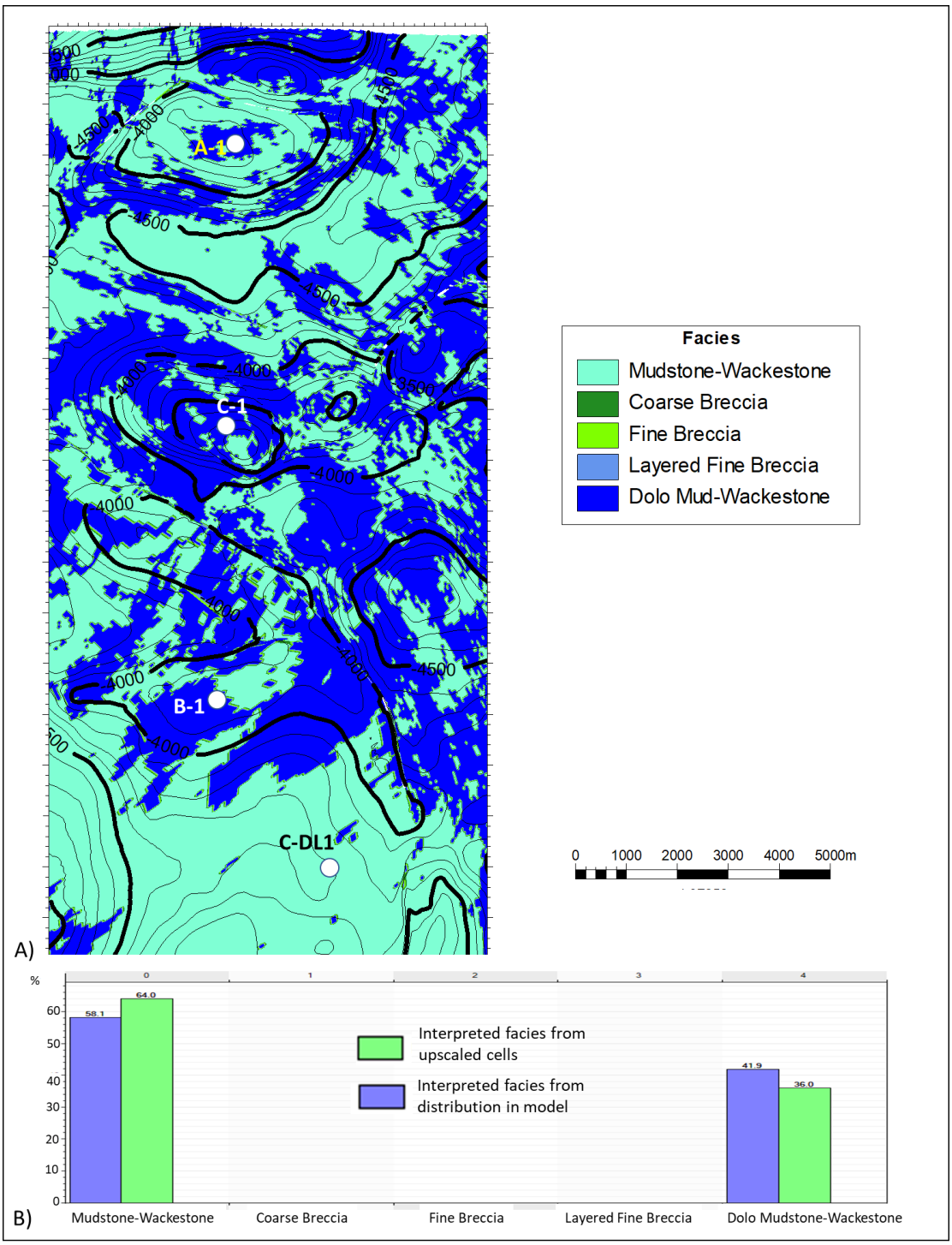


**Figure 3-32.** Lithofacies map for the unit Ku-1. The map shows two facies with a similar origin, with the only difference is the dolomitization process. B) Histogram of the distribution from the model and the original lithofacies interpretation from the wells. The distribution honors the original lithofacies interpretation.

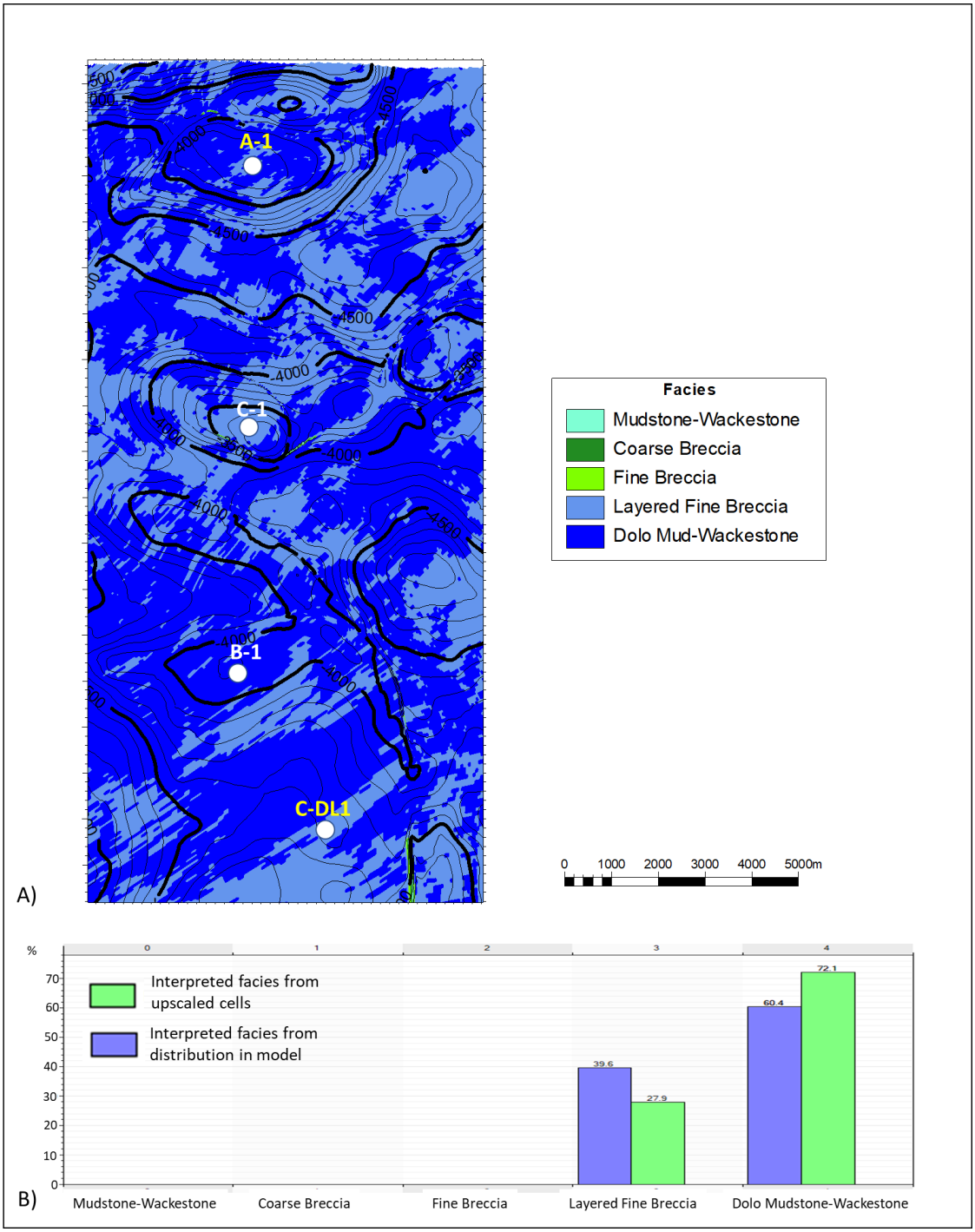


**Figure 3-33.** Lithofacies map for the unit Km. The map shows two facies mudstone-wackestone and the layered fine breccia. This breccia possibly was deposited in various episodes. B) Histogram of the distribution from the model and, the original lithofacies interpretation from the wells. from this histogram, we can observe that the distribution honors the original lithofacies interpretation.

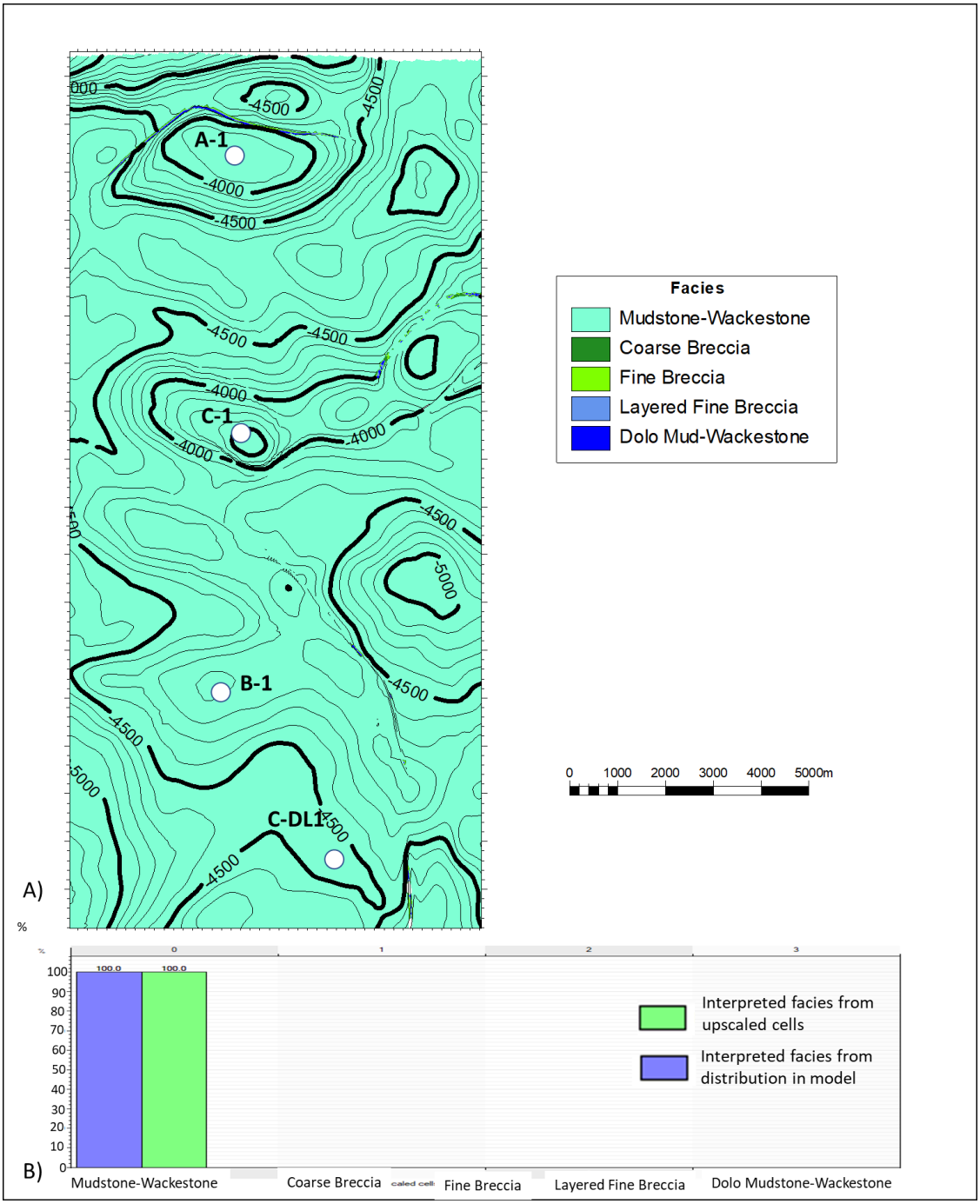


**Figure 3-34.** Lithofacies map for the unit Kl. The map shows that this unit for only one facie. B) Histogram of the distribution from the model and the original lithofacies interpretation from the wells. The distribution honors the original lithofacies interpretation.

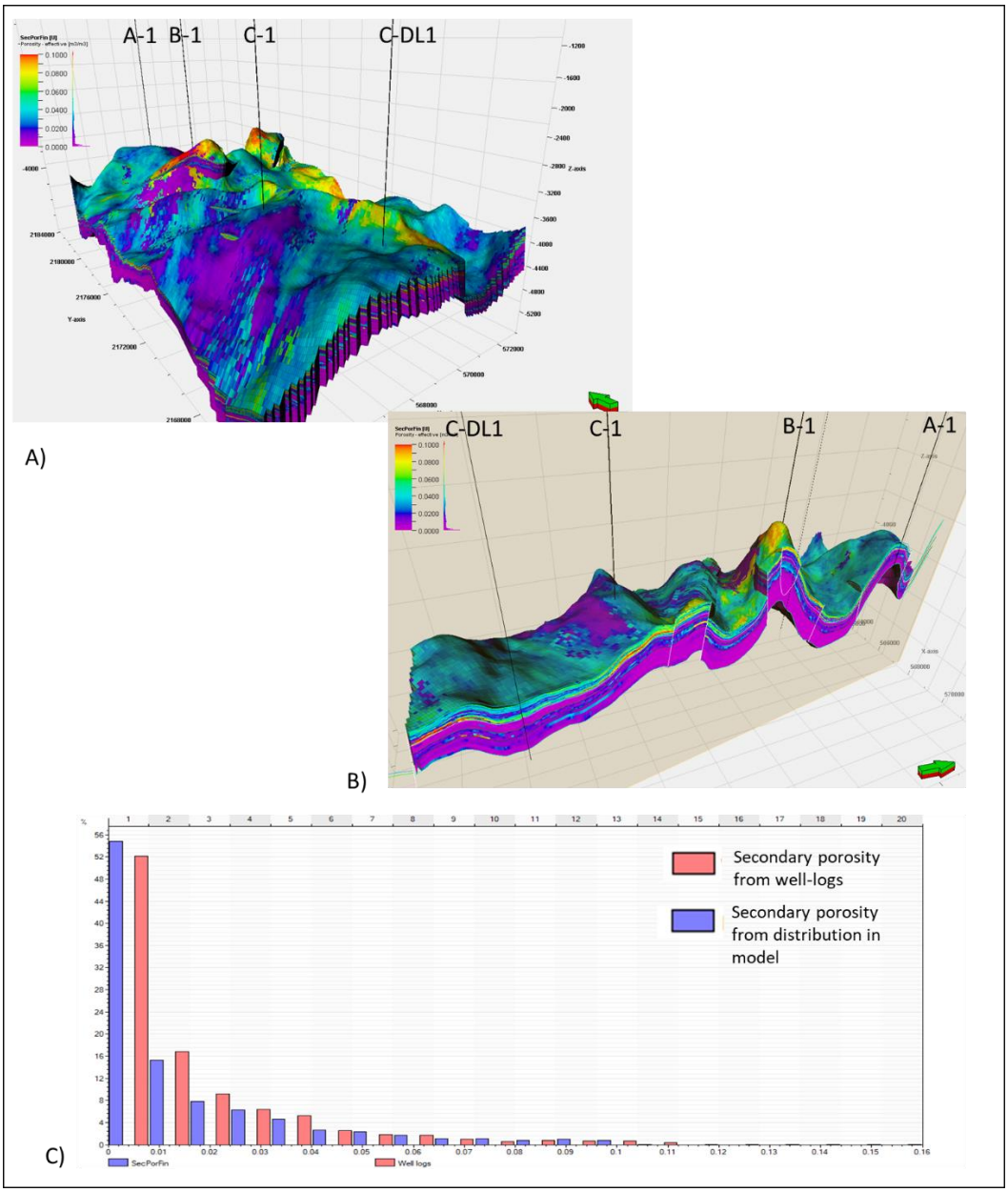


**Figure 3-35.** Secondary porosity in the 3D geo-cellular model. A) A general isometric view of the secondary porosity property, for the upper part of the model higher values are located in the well-B zone. B) Cut across the model higher secondary porosity values are in the upper part of the model and the lowest is located in the bottom part. C) Histogram of the porosity values in the model and in the original petrophysical estimation. The distribution is honoring the original values from petrophysics.

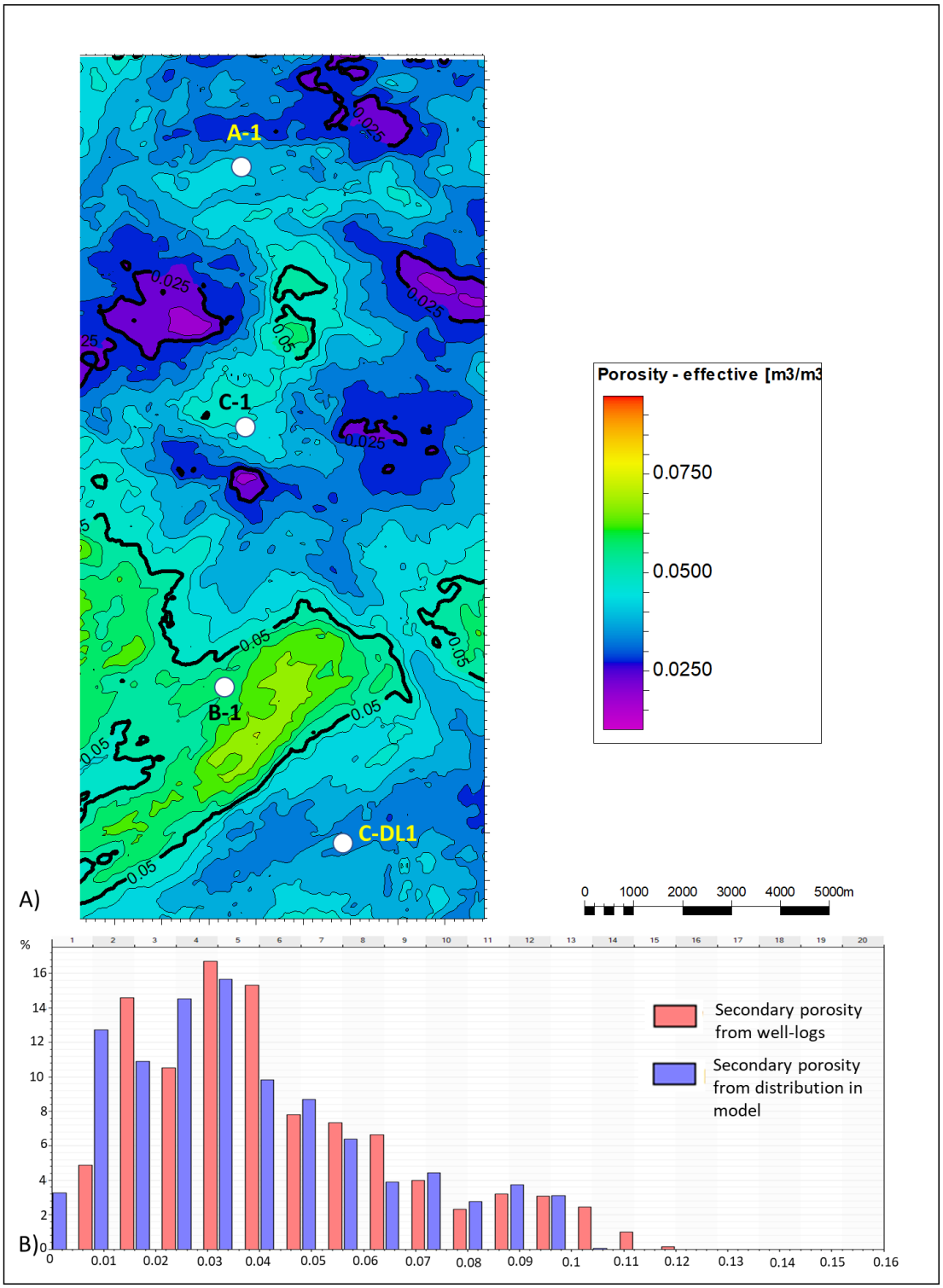


**Figure 3-36.** A) Map of average secondary porosity for Ku-2 zone. Higher values are presents in the central part and the southwest of the area. B) Histogram of the distribution from the model and the original porosity from petrophysics. The higher secondary porosity is in this unit. The distribution honors the original porosity from petrophysics.

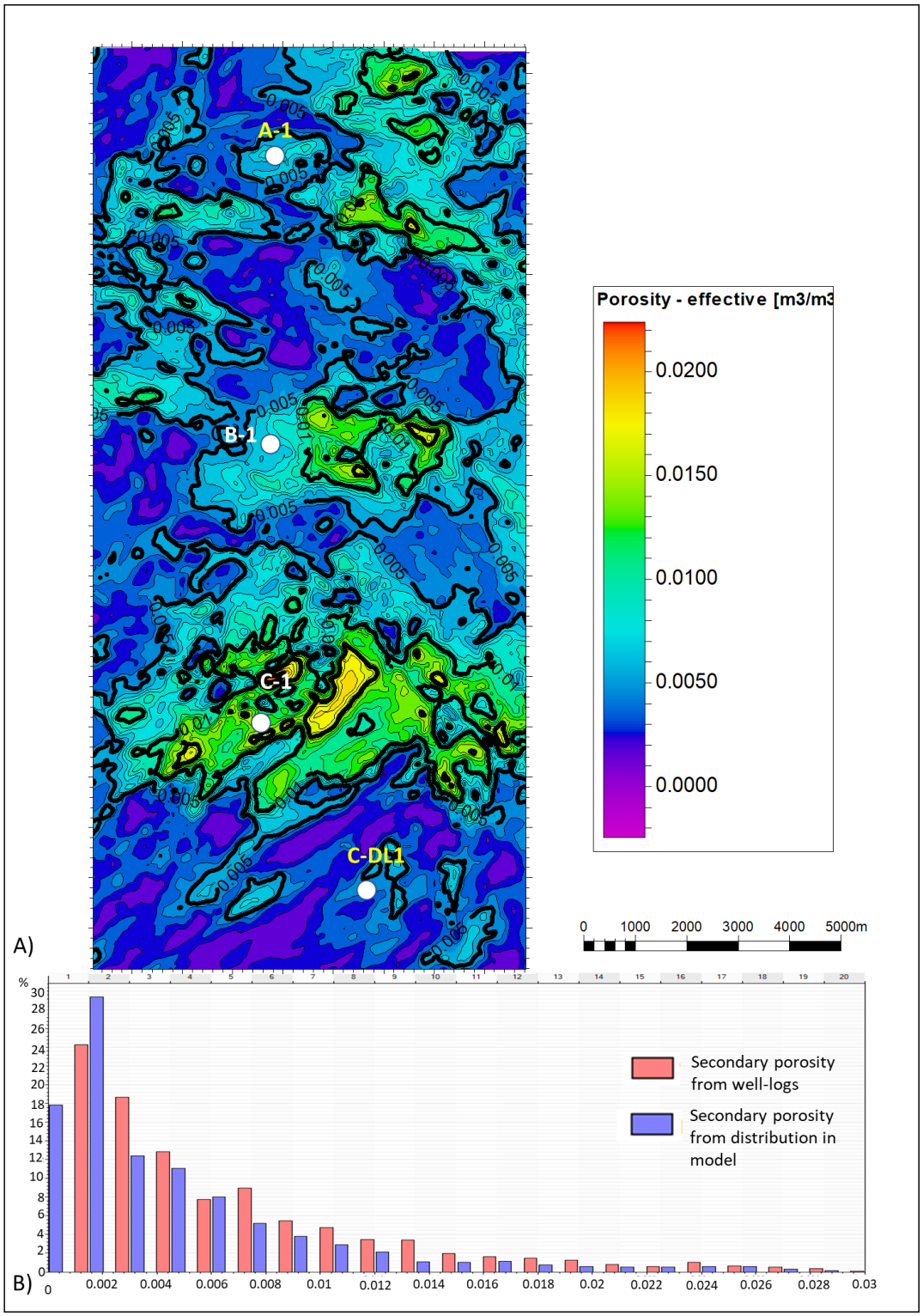


**Figure 3-37.** A) Map of average secondary porosity for Ku-1 zone. Higher values look oriented to the structural features of the area. B) Histogram of the distribution from the model and the original porosity from petrophysics. The distribution honors the original porosity from petrophysics.

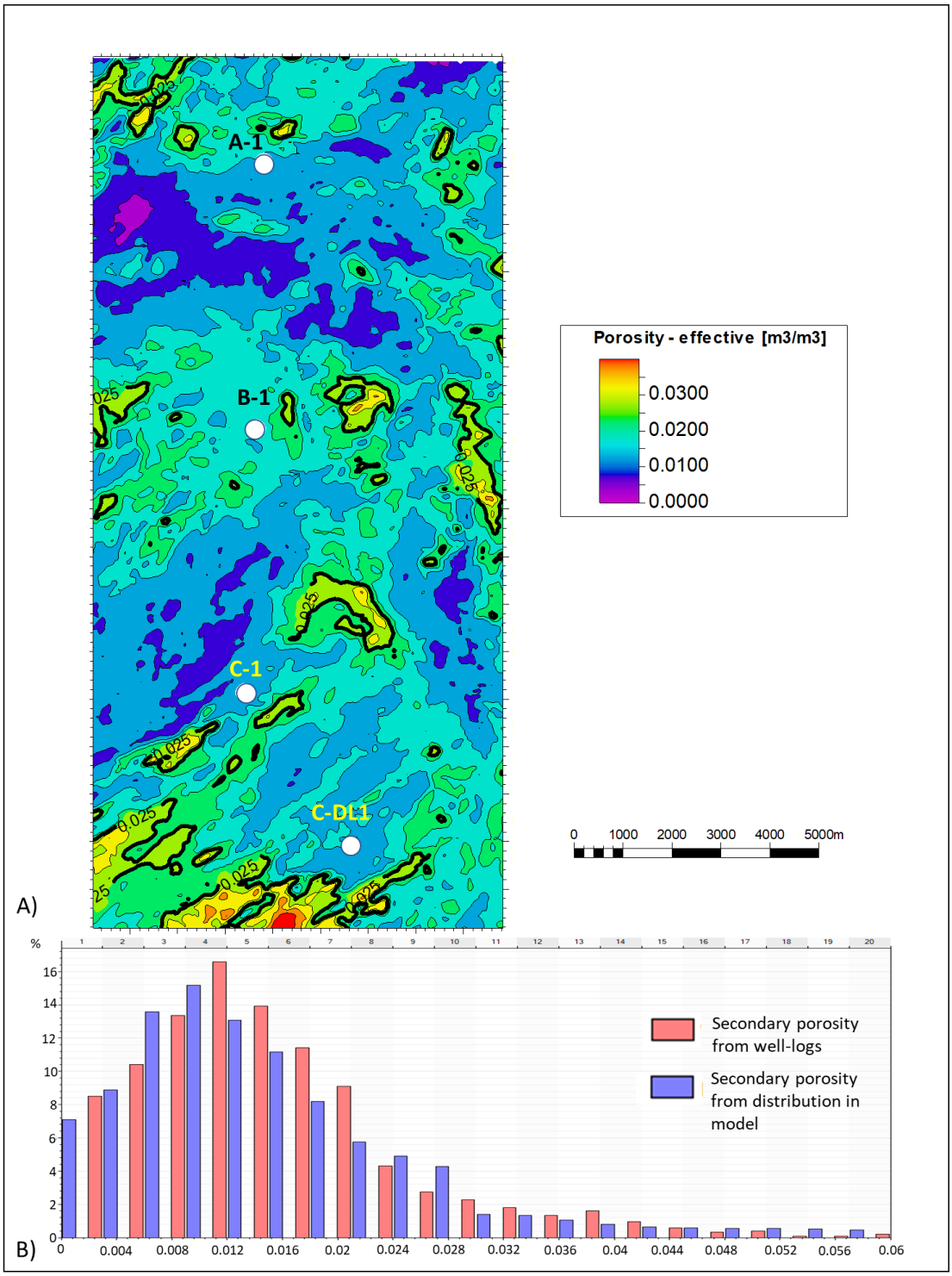


**Figure 3-38.** A) Map of average total effective porosity for Km zone. Higher values are located in the southeast of the study area, similar to the distribution of Km zone. B) Histogram of the distribution from the model and the original porosity from petrophysics. The distribution honors the original porosity from petrophysics.

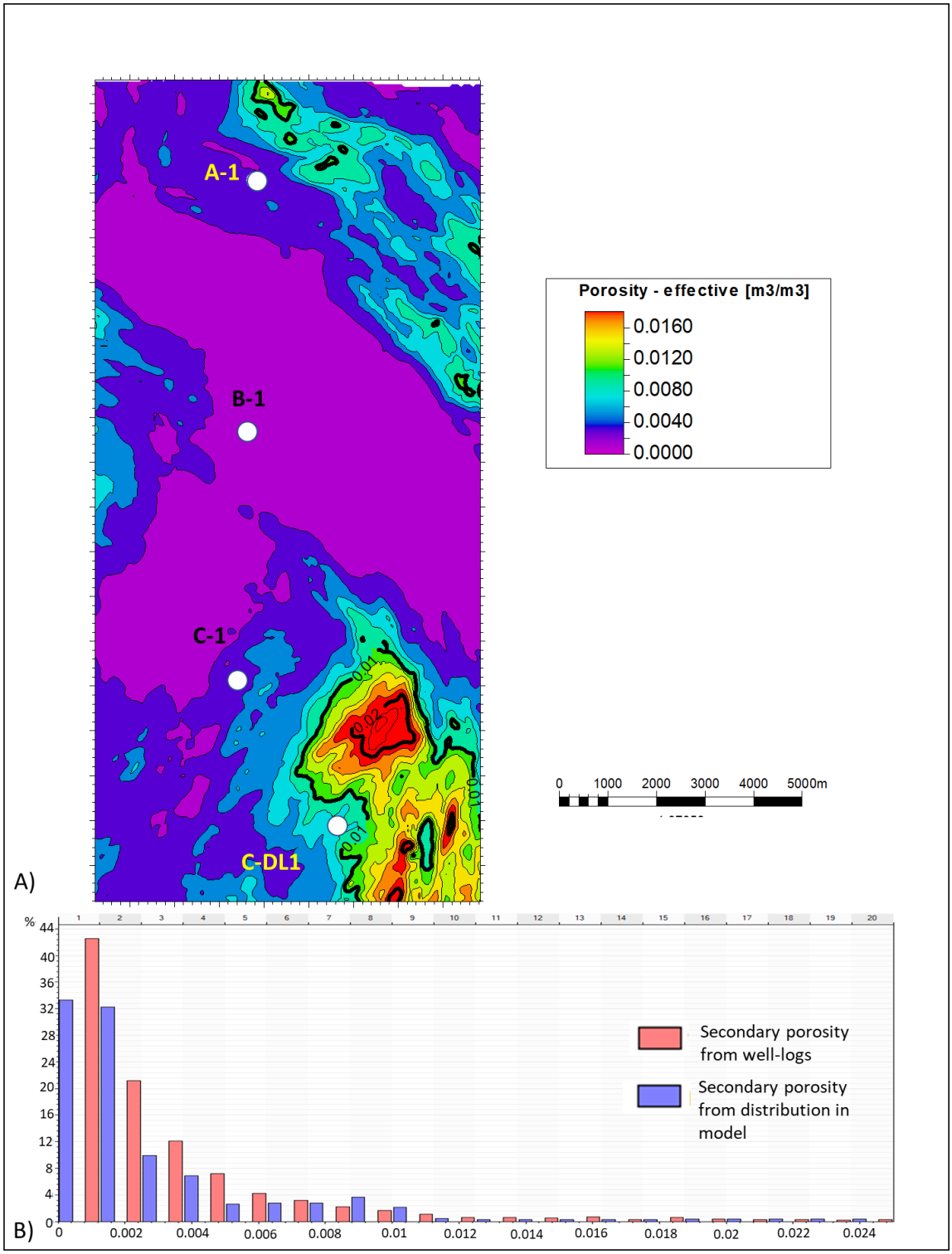


**Figure 3-39.** A) Map of average total effective porosity for Kl zone. In a similar way than Kl zone, higher values are located in the southeast part of the model. B) Histogram of the distribution from the model and the original porosity from petrophysics. The distribution honors the original porosity from petrophysics.

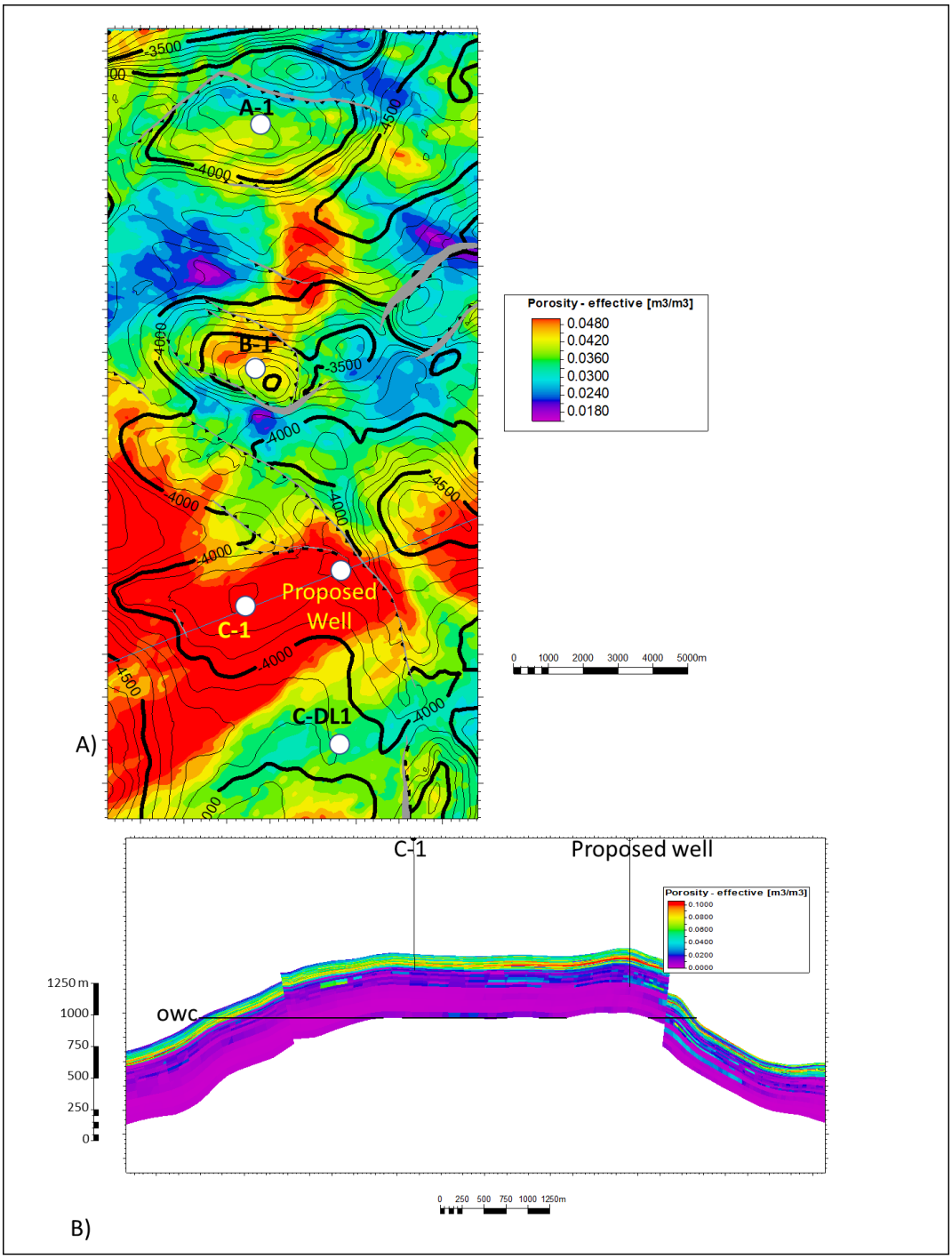


**Figure 3-40.** A) Map of secondary porosity superimposed on the structural B) Cross-section across the secondary porosity model well C-1 and the proposed well, in the proposed well zone is the highest structural part in the C field and the secondary porosity have the highest values also.

# References

Angeles-Aquino, Francisco J. 2006. “Monografia Petrolera De La Zona Marina. IN SPANISH. Monograph Of The Marine Zone Oil.” Boletin de La Asociacion Mexicana de Geologos Petroleros, 69.

Aguilera, Roberto. 1974. “Analysis of Naturally Fractured Reservoirs From Sonic and Resistivity Logs.” Journal of Petroleum Technology 26 (11): 1233–38. https://doi.org/SPE-4398-PA.

Aguilera, Roberto. 1976. “Analysis of Naturally Fractured Reservoir From Conventional Well Logs.” Journal of Petroleum Geology 7 (28): 764–72.

Chang, Dahai, HJ Vinegar, and CE Morriss. 1994. “Effective Porosity, Producible Fluid and Permeability Carbonate in Carbonates from NMR Logging.” SPWLA 35th Annual Logging Symposium, 1–21. http://www.onepetro.org/mslib/servlet/onepetropreview?id=SPWLA-1994-A&soc=SPWLA&speAppNameCookie=ONEPETRO.

Daly Schlumberger, Colin, Darcy Novak Schlumberger, and Canada Calgary. 2010. “A Faster, More Accurate Gaussian Simulation Introduction to Gaussian Random Function Simulation,” 1–5.

Gomez-Rivero, Orlando G (Pemex). 1976. “A Practical Method for Determining Cementation Exponents and Some Other Parameters As an Aid in Well Log Analysis.” The log analyist 17 (05).

Lopez, Dario Oscar Lopez, and Viro, Eduardo. 2002. “A Saturation Model for Complex Carbonates in Mexico.” SPWLA 43rd Annual Logging Symposium 2002, 1–14.

Mitra, Shankar, Gerardo Correa Figueroa, Jesus Hernandez Garcia, and Antonio Murillo Alvarado. 2005. “Three-Dimensional Structural Model of the Cantarell and Sihil Structures, Campeche Bay, Mexico.” AAPG Bulletin 89 (1): 1–26. https://doi.org/10.1306/08310403108.

Mitra, Shankar, Juan A. Duran Gonzalez, Jesus Garcia Hernandez, Sergio Hernandez Garcia, and Subhotosh Banerjee. 2006. “Structural Geometry and Evolution of the Ku, Zaap, and Maloob Structures, Campeche Bay, Mexico.” AAPG Bulletin 90 (10): 1565–84. https://doi.org/10.1306/04240605101.

Murillo-Muñetón, G., J. M. Grajales-Nishimura, E. Cedillo-Pardo, J. García-Hernández, and S. García-Hernández. 2002. “Stratigraphic Architecture and Sedimentology of the Main Oil-Producing Stratigraphic Interval at the Cantarell Oil Field: The K/T Boundary Sedimentary Succession.” Proceedings of the SPE International Petroleum Conference and Exhibition of Mexico, 643–49. https://doi.org/10.2118/74431-MS.

Rivero, Orlando Gomez. 1981. “A Conciliating Porosity Relationship: Its Application to Practical Well Log Analysis.” In SPWLA Twenty-Second Annual Logging Symposium., 19. Mexico City.

West, Brian P., Steve R. May, John E. Eastwood, and Christine Rossen. 2002. “Interactive Seismic Facies Classification Using Textural Attributes and Neural Networks.” The Leading Edge 21 (10): 1042–49. https://doi.org/10.1190/1.1518444.

Zhang, Rui, Kui Zhang, and Jude E Alekhue. 2017. “Technical Papers Depth-Domain Seismic Reflectivity Inversion with Compressed Sensing Technique” 5 (1): 1–9.

## Summary

The carbonate reservoirs analyzed in this dissertation have a complex geological history; this includes a compressive regime that generated thrust-faults and folding. Diagenesis was another critical process that formed different types of porosity such as vug, fractures and intercrystalline porosity. A better prediction of these features contributes to more efficient production planning.

Because of its shared geological background with relevant producer fields in the zone as supergiant Cantarell field, characterize these fields is essential and is an economic opportunity also.

In this dissertation, I defined a structural model, a 3D-grid model, a stratigraphic model, a facies model and made a distribution of petrophysical properties based on machine learning processes, seismic attributes, and analytical methods. All this, honoring the hard data provided by the wells in the zone and bolstered by indirect methods as seismic data migrated in time and depth domain.